

The broadband spectra of infrared-faint radio sources

By

Andreas Herzog

Dissertation
zur Erlangung des Grades
eines Doktors der Naturwissenschaften
in der Fakultät für Physik und Astronomie
der Ruhr-Universität Bochum

A thesis submitted to Macquarie University
for the degree of Doctor of Philosophy
Department of Physics and Astronomy

Completed under a program of joint doctoral supervision
between Ruhr-Universität Bochum and Macquarie University



August 2015

Except where acknowledged in the customary manner, the material presented in this thesis is, to the best of my knowledge, original. In particular, this is a thesis by publication. Chapters 2, 3, 4, and 5 contain the following four manuscripts:

- Herzog, A., Middelberg, E., Norris, R. P., et al., 2014, Infrared-faint radio sources are at high redshifts: Spectroscopic redshift determination of infrared-faint radio sources using the Very Large Telescope, *Astronomy & Astrophysics*, 567, A104.
- Herzog, A., Middelberg, E., Norris, R. P., et al., 2015, Active galactic nuclei cores in infrared-faint radio sources: Very long baseline interferometry observations using the Very Long Baseline Array, *Astronomy & Astrophysics*, 578, A67.
- Herzog, A., Norris, R. P., Middelberg, E., et al., 2015, Infrared-faint radio sources remain undetected at far-infrared wavelengths: Deep photometric observations using the *Herschel* Space Observatory, *Astronomy & Astrophysics*, 580, A7.
- Herzog, A., Norris, R. P., Middelberg, E., et al., 2015, The radio spectral energy distribution of infrared-faint radio sources, submitted for publication in *Astronomy & Astrophysics*.

My contribution and the contribution of co-authors to the manuscripts are described in the respective chapters. This thesis has not been submitted in whole or part for a degree in any other university or institution than Macquarie University and Ruhr-Universität Bochum.

Andreas Herzog

Abstract

Infrared-faint radio sources (IFRSs) are objects found a decade ago that are characterised by their infrared faintness and enormously high radio-to-infrared flux density ratios. The nature of this extreme class of object was uncertain and several scenarios have previously been suggested. This thesis presents new multi-wavelength data in the optical, far-infrared, and radio regime that are used to study unexplored regimes of the spectral energy distribution (SED) of IFRSs, crucially narrowing down the nature of this class of objects.

Optical spectroscopic data are used to measure spectroscopic redshifts of three IFRSs, showing that these sources are at cosmologically relevant redshifts. Further, the spectra themselves and the first redshift-based SED modelling show IFRSs to be consistent with radio-loud active galactic nuclei (AGNs). The suggested presence of AGNs in IFRSs is confirmed based on very long baseline interferometry observations of a large sample of IFRSs in the radio regime. Based on these data, it is also argued that IFRSs might be AGNs in their earliest evolutionary stages. This suggestion is consistent with the results from a detailed radio SED study over a wide frequency range presented in this thesis, finding steep and a few curved radio SEDs. In the first far-infrared observations of IFRSs, all six targeted sources remained undetected. The resulting flux density limits provide crucial constraints for a comprehensive broadband SED modelling, showing that only high-redshift radio galaxies (HzRGs) can reproduce the characteristics of IFRSs. Estimated limits of the infrared luminosity, star formation and black hole accretion rates are also found to be consistent with the corresponding properties of HzRGs.

The thesis adds significant support to the suggestion that IFRSs are radio-loud AGNs at high redshifts ($z \gtrsim 2$) and similar to HzRGs, whereas other objects like heavily obscured star forming galaxies or galactic objects could explicitly be ruled out. Further, it hypothesises that IFRSs are young AGNs.

Acknowledgements

Working on my PhD project at three different institutions—Ruhr-Universität Bochum, Macquarie University, and CSIRO Astronomy & Space Science—, I had the pleasure to meet and work with many different people. This cooperation had significant impact on my PhD project and thus the resulting thesis. I am very grateful for all the advice and support given and opportunities opened.

Enno Middelberg awakened my interest and fascination for the class of IFRSs and gave me the opportunity to work on my PhD project under his supervision. He introduced me to radio astronomy and python with giving me helpful advice in many computational issues. I am thankful for amazing observational data that he successfully proposed before the start of my PhD project. This paved the road for my work. Lee Spitler supervised my work with deep interest. I am very thankful for his radio-unbiased view on my project and lots of valuable, complementing suggestions, extending far beyond scientific questions. Weekly meetings with Ray Norris were highly productive and our stimulating and open-minded discussions had crucial impact on my work. I very much appreciate his supervision. However, most of all, I thank him for discovering the first IFRSs a decade ago and so establishing the basis for my PhD project in the first place. Without Quentin Parker's support, I would not have had the chance to work on my PhD project co-supervised by Ruhr-Universität Bochum and Macquarie University, spending time at either of the two universities. I highly appreciate this experience and the resulting valuable contacts, and I thank Quentin for his efforts regarding my residence in Australia. I am also grateful to Ralf-Jürgen Dettmar and Julia Tjus for advice and support.

I appreciate insightful discussions, talks, and meetings in the Galaxiengruppe at Ruhr-Universität Bochum, in the ExGal group at Macquarie University, and with the ATLAS team

at CSIRO Astronomy & Space Science. In particular, thanks go to Nick Seymour, Peter Zinn, Jordan Collier, and Tom Franzen for valued scientific input and advice. The working environment at all three institutions was very productive and appreciated. In particular, I want to thank my office mates Marek Weźgowiec, Shi Dai, and Alessandro Maini.

My PhD project greatly benefitted from my status as cotutelle PhD student jointly supervised by scientists from all three institutions. I am very grateful to Higher Degree Research (HDR) at Macquarie University in general for advancing cotutelle programmes and specifically for enabling my stay in Australia. As cotutelle programmes include administrative challenges, I appreciate contributions from Ruhr-Universität Bochum and Macquarie University for the realisation of my cotutelle project. In particular, I want to thank Ivonne Möller for her continuing support.

I acknowledge funding support from Bundesministerium für Wirtschaft und Technologie under the label 50OR1202 and from a CSIRO Astronomy & Space Science, Australia Telescope National Facility Graduate Research Scholarship.

Support and interest from family and friends helped me significantly in meeting all the challenges of my PhD project.

Contents

Abstract	v
Acknowledgements	vii
Contents	ix
List of figures	xi
List of tables	xi
List of acronyms	xiii
List of units and constants	xvii
1 Introduction	1
1.1 The Australia Telescope Large Area Survey	3
1.2 Active galactic nuclei	4
1.2.1 The standard unified AGN model	4
1.2.2 SMBHs and their host galaxies	12
1.3 Infrared-faint radio sources	15
1.3.1 Samples of IFRSs in different survey fields	16
1.3.2 Deep infrared faintness of IFRSs	19
1.3.3 IFRSs in the optical and X-ray regime	19
1.3.4 Radio properties of IFRSs	20
1.3.5 Connection between IFRSs and other classes of objects	22
1.3.6 Remaining explanations for the characteristics of IFRSs	25
1.4 Motivation and outline	26
1.5 Technical remarks	28
2 Infrared-faint radio sources are at high redshifts	29
3 Active galactic nuclei cores in infrared-faint radio sources	43
4 Infrared-faint radio sources remain undetected at far-infrared wavelengths	69
5 The radio spectral energy distribution of infrared-faint radio sources	95
6 Conclusion and outlook	127
References	133

Scientific curriculum vitae	147
List of publications	149

List of figures

1.1	Illustration of the standard unified model of AGNs	6
1.2	Qualitative representation of different AGN subclasses in the three-dimensional parameter space of emission line width, nuclear luminosity, and radio power	11
1.3	Illustration of the standard AGN feedback model	14
1.4	Two examples of the class of IFRSs	16
1.5	Radio-to-IR flux density ratio as a function of redshift for different classes of objects	24
3.1	Observed near-IR 3.6 μm flux density as a function of redshift for all IFRSs with known spectroscopic redshifts	49
4.1	Broadband SED modelling for the IFRSs observed with <i>Herschel</i> , using no scaling and no added extinction	74
4.2	Broadband SED modelling for the IFRSs observed with <i>Herschel</i> with no scaling but additional extinction	77
5.1	Scale as a function of redshift in standard ΛCDM cosmology	97

List of tables

3.1	Spectroscopic redshift information for IFRSs from SDSS DR10	48
6.1	Broadband characteristics of IFRS in the ATLAS fields	130

List of acronyms

- 3CRR** Revised Revised Third Cambridge Catalogue. 22, 70
- AGN** active galactic nucleus. v, xi, 2–17, 20, 21, 23–27, 29–33, 43, 44, 46, 47, 50, 52, 54, 71–73, 76, 96, 98, 99, 101, 127–132
- AIPS** Astronomical Image and Processing System. 54
- ALMA** Atacama Large Millimeter Array. 32, 72, 128
- ASKAP** Australia Square Kilometre Array Pathfinder. 2, 3, 101
- ATCA** Australia Telescope Compact Array. 3, 21, 72
- ATLAS** Australia Telescope Large Area Survey. vii, xi, 2–4, 15–17, 19, 21, 23, 27, 31–34, 46, 95, 96, 101, 127, 129, 130
- BLR** broad-line region. 6, 7, 9, 12, 51
- BLRG** broad-line region galaxy. 9
- CANDELS** Cosmic Assembly Near-infrared Deep Extragalactic Legacy Survey. 129
- CDFS** Chandra Deep Field-South. 3, 15, 16, 18–21, 31, 45, 101
- CDM** cold dark matter. xi, 13, 28, 96, 97
- CDQ** core-dominated quasar. 10
- CMB** cosmic microwave background. 2, 28
- COSMOS** Cosmological Evolution Survey. 18, 20
- CSS** compact steep-spectrum. 27, 33, 34, 97–99, 101, 128
- DOG** dust-obscured galaxy. 25
- DR** data release. xi, 3, 16, 17, 47–52, 54, 96, 101
- eCDFS** extended Chandra Deep Field-South. 19, 31
- ELAIS-N1** European Large Area Infrared space observatory Survey-North 1. 17, 18
- ELAIS-S1** European Large Area Infrared space observatory Survey-South 1. 3, 16, 18, 20, 21, 45

- EMU** Evolutionary Map of the Universe. 2, 3
- FFA** free-free absorption. 98, 99
- FIR** far-infrared. 27, 72, 73, 75, 78, 95, 96, 101, 129
- FIRST** Faint Images of the Radio Sky at Twenty cm survey. 18, 48
- FR** Fanaroff-Riley. 5, 11, 12, 22, 33, 34, 47, 96, 97, 99, 130
- FSRQ** flat-spectrum radio quasar. 10
- FWHM** full width at half maximum. 51
- GB6** Green Bank 6 cm survey. 18
- GILDAS** Grenoble Image and Line Data Analysis Software. 101
- GPS** GHz peaked-spectrum. 27, 97–99, 101, 128
- HerMES** *Herschel* Multi-tiered Extragalactic Survey. 1, 129
- HFP** high-frequency peaker. 97, 98
- HIPE** *Herschel* Interactive Processing Environment. 78
- HPQ** highly polarized quasar. 10
- HyLIRG** hyper-luminous infrared galaxy. 70, 75
- HzRG** high-redshift radio galaxy. v, 23–25, 27, 30, 32, 34, 49–52, 70–72, 78, 129, 131
- ICM** intracluster medium. 8
- IFRS** infrared-faint radio source. v, vii, xi, 4, 15–27, 29–34, 43–54, 69–78, 95–101, 127–132
- IGM** intergalactic medium. 8, 98
- IR** infrared. xi, 3–5, 7, 9–11, 15–20, 22–27, 29–34, 49, 50, 69–73, 75, 76, 78, 95, 96, 100, 127–131
- IRAC** Infrared Array Camera. 3
- ISM** interstellar medium. 98
- LBA** Australian Long Baseline Array. 21, 45, 46
- LH** Lockman Hole. 18
- LINER** low-ionisation nuclear emission-line region galaxy. 10
- LIRG** luminous infrared galaxy. 24, 70
- LOFAR** LOw Frequency ARray. 128

- LSST** Large Synoptic Survey Telescope. 2
- MIPS** Multiband Imaging Photometer for *Spitzer*. 3
- MSSS** Multifrequency Snapshot Sky Survey. 128
- MWA** Murchison Widefield Array. 101
- NLR** narrow-line region. 7, 9, 12, 97, 98
- NLRG** narrow-line region galaxy. 9
- NLXG** narrow-line X-ray galaxy. 10
- NVSS** NRAO Very Large Array Sky Survey. 1, 18
- OIRS** optically invisible radio source. 23
- OVV** optically violently variable. 10
- PACS** Photodetecting Array Camera and Spectrometer. 73, 129
- PdBI** Plateau de Bure Interferometer. 101
- PEP** PACS Evolutionary Probe. 129
- QSO** quasi-stellar object. 5, 24, 50, 51
- RL** radio-loud. 10–12, 14–17, 22–27, 30, 31, 33, 34, 43, 47, 69, 73, 75, 76, 99, 101, 127, 129–131
- RLQ** radio-loud quasar. 11
- RQ** radio-quiet. 10, 12, 23, 24, 69
- RQQ** radio-quiet quasar. 11
- S/N** signal-to-noise ratio. 16, 17
- SDSS** Sloan Digital Sky Survey. xi, 1, 32, 47–54, 131
- SED** spectral energy distribution. v, xi, 4, 21, 22, 26, 27, 29–31, 33, 34, 43, 52, 73–78, 96–101, 128–131
- SERVS** *Spitzer* Extragalactic Representative Volume Survey. 18, 19, 30, 32
- SFR** star formation rate. 1, 23, 24, 70–72, 78, 131
- SKA** Square Kilometre Array. 2, 3
- SMBH** supermassive black hole. 5–8, 12–15, 70, 72
- SMG** sub-mm galaxy. 24

- SPIRE** Spectral and Photometric Imaging Receiver. 73
- SSA** synchrotron self absorption. 98, 99
- SWIRE** *Spitzer* Wide-area Infrared Explorer. 3, 4, 15–17, 19, 23, 31, 32
- ULIRG** ultra-luminous infrared galaxy. 22, 24, 70
- URC** Unified Radio Catalogue. 18
- UV** ultraviolet. 7, 9–11
- VLA** Very Large Array. 16, 72
- VLBA** Very Long Baseline Array. 44, 46, 47, 52–54, 128
- VLBI** very long baseline interferometry. 20, 21, 25–27, 44–47, 54, 72, 128–130
- VLT** Very Large Telescope. 31, 34
- WENSS** Westerbork Northern Sky Survey. 18
- WISE** Wide-field Infrared Survey Explorer. 1, 18
- WTF** Widefield ouTlier Finder. 2
- xFLS** *Spitzer* First Look Survey. 16, 18, 19, 95, 97
- XMM-LSS** XMM-Newton Large Scale Structure Survey. 18

List of units and constants

List of units

Unit	SI equivalent	Name
Å	10^{-10} m	Ångström
AU	1.496×10^{11} m	astronomical unit
Jy	10^{-26} W m ⁻² Hz ⁻¹	Jansky
pc	3.086×10^{16} m	parsec

List of constants

Constant	SI equivalent	Name
L_{\odot}	3.9×10^{26} W	solar luminosity
M_{\odot}	1.99×10^{30} kg	solar mass

1

Introduction

How did the global star formation rate (SFR) change with cosmic time? What is the luminosity function of galaxies with active cores and of star forming galaxies depending on the redshift? When did the first galaxies form and how did they evolve until the present day? What is the distribution of galaxies in the universe? These are some of the crucial questions driving current astronomy. Qualitative and quantitative answers are sought out in order to reach a better understanding of the universe. The open questions can be addressed using astronomical surveys, deeply targeting an appropriate area of the sky.

Several large survey projects have been accomplished during the past decades in different wavelength regimes: the broadband optical Sloan Digital Sky Survey (SDSS; York et al., 2000), the Wide-field Infrared Survey Explorer (WISE; Wright et al., 2010), the far-infrared *Herschel* Multi-tiered Extragalactic Survey (HerMES; Oliver et al., 2012), the *Chandra* X-ray observatory surveys (Xue et al., 2011), or the NRAO Very Large Array Sky Survey (NVSS; Condon et al., 1998), among many others. Such surveys provide rich data sets

over wide areas of the sky and enable many astronomers to address open issues in understanding the universe and its evolution.

The successes of the early surveys has spurred the establishment of some very large surveys using multi-million dollar facilities, scheduled to start operation in the next decade: the optical and near-infrared Large Synoptic Survey Telescope (LSST; Ivezić et al., 2008) or the radio Square Kilometre Array (SKA; Dewdney et al., 2009). Data from these telescopes will help answer known outstanding questions about the universe. However, answering open questions is not the only—and potentially not even the most important—contribution from astronomical surveys. The history of astronomy shows that several major discoveries have been made unexpectedly as discussed by Ekers (2009): unexpected discoveries that were not listed as science goal of any telescope proposal, survey description, or project plan. Examples include the discovery of pulsars (see Bell Burnell, 2009 for a review), of the cosmic microwave background (CMB; Penzias and Wilson, 1965), or of dark energy (Riess et al., 1998; Perlmutter et al., 1999). There is no reason why the next surveys should not provide such “unexpected surprises” hidden in their data. Therefore, next-generation survey projects will only spread their full impact if approaches are found how to track down these “unknown unknowns” in complex and huge data sets. For example in the Evolutionary Map of the Universe (EMU; Norris et al., 2011b) radio continuum survey—one of two key science projects of the Australia SKA Pathfinder (ASKAP; Johnston et al., 2007, 2008; DeBoer et al., 2009)—, this issue is addressed in the data mining project Widefield outlier Finder (WTF), considering approaches like the k nearest neighbours (e.g. Polsterer et al., 2013) or citizen science (“zoo”) projects (Lintott et al., 2008).

The Australia Telescope Large Area Survey¹ (ATLAS) is one of the widest deep radio surveys accomplished so far and revealed one of these “unknown unknowns”: the class of infrared-faint radio sources, topic of this thesis. The ATLAS survey is briefly summarised in section 1.1. An overview of active galactic nuclei (AGNs) is given in section 1.2 and the class of infrared-faint radio sources is presented in section 1.3. This thesis is motivated in section 1.4 and a few technical remarks are given in section 1.5.

¹<http://www.atnf.csiro.au/research/deep/index.html>

1.1 The Australia Telescope Large Area Survey

Tracing galaxy formation and evolution in the early universe is one of the main goals of ATLAS, using the Australia Telescope Compact Array (ATCA) in Narrabri, Australia. The survey area of around 6 deg^2 consists of two separate fields, the Chandra Deep Field-South (CDFS) at a declination between -27° and -29° , and the European Large Area Infrared space observatory Survey-South 1 (ELAIS-S1) at a declination between -43° and -44° . The survey aimed at a sensitivity between $10 \mu\text{Jy beam}^{-1}$ and $15 \mu\text{Jy beam}^{-1}$ at 1.4 GHz with an angular resolution of around 10 arcsec. With these characteristics, it was the widest deep radio survey ever accomplished. It also is an important test for the proposed next generation radio telescope, the SKA (Dewdney et al., 2009), and one of its pathfinders, ASKAP (Johnston et al., 2007, 2008; DeBoer et al., 2009). Many techniques and methods used for the EMU (Norris et al., 2011b) survey—the key science continuum project carried out with ASKAP—has been and will be tested on the data from the ATLAS survey.

Observations for ATLAS were started in April 2002 and finished in June 2010. A first data release (DR) has been presented by Norris et al. (2006) for CDFS and Middelberg et al. (2008a) for ELAIS-S1, reaching sensitivities of $36 \mu\text{Jy beam}^{-1}$ and $30 \mu\text{Jy beam}^{-1}$, respectively. Hales et al. (2014) presented the data from ATLAS DR2, and the work on DR3 has been finished (Franzen et al., 2015). Using the entire data taken between 2002 and 2010, DR3 reaches sensitivities of $14 \mu\text{Jy beam}^{-1}$ and $17 \mu\text{Jy beam}^{-1}$, respectively. In order to gather information about the spectral properties of the detected radio sources, both fields were observed at 2.3 GHz with the ATCA as part of ATLAS (Zinn et al., 2012).

The ATLAS fields were also covered by the *Spitzer* Wide-area Infrared Extragalactic survey (SWIRE; Lonsdale et al., 2003), providing near- and mid-infrared photometric data that were cross-matched to the ATLAS data. For this purpose, data from the Infrared Array Camera (IRAC; $3.6 \mu\text{m}$, $4.5 \mu\text{m}$, $5.8 \mu\text{m}$, and $8.0 \mu\text{m}$, with 5σ sensitivities of $5 \mu\text{Jy}$, $9 \mu\text{Jy}$, $43 \mu\text{Jy}$, and $40 \mu\text{Jy}$, respectively) and the Multiband Imaging Photometer for *Spitzer* (MIPS; $24 \mu\text{m}$ with a 5σ sensitivity of $192.5 \mu\text{Jy}$) instruments on board the *Spitzer* Space Telescope were used. The combination of radio and infrared (IR) data enables studying the mechanisms powering galaxies. Whereas galaxies mainly powered by star forming activity are known to follow the radio-far-IR correlation (e.g. Dickey and Salpeter, 1984; de Jong et al., 1985; Appleton et al., 2004), a departure from this correlation generally identifies a source as containing an AGN. Of particular interest are galaxies that show the optical and IR spectral

energy distribution (SED) of a typical star forming galaxy but also strong radio emission from an AGN in the galactic centre. These objects are promising candidates for studying a potential link between star forming activity and the central AGN, also known as “feedback” of the AGN on its host galaxy.

Although it was known that some radio sources are very faint in the optical and near-IR regime (Richards et al., 1999; Norris et al., 2005; Huynh et al., 2005), it was expected that each radio source in the ATLAS survey has a near- or mid-IR counterpart in the SWIRE survey, regardless of whether the radio emission is mainly powered by star forming or AGN activity. In particular, the dust of optically and near-IR faint galaxies—which might obscure the radio-emitting process—should be detected in the mid-IR SWIRE bands. However, unexpectedly, a number of sources were found in the ATLAS survey that did not provide near- or mid-IR counterparts. These sources—undetected at all *Spitzer* wavelengths—were named “infrared-faint radio sources” (IFRSs; Norris et al., 2006), further introduced in section 1.3.

1.2 Active galactic nuclei

A plausible candidate to explain the characteristics of IFRS are active galaxies. Active galaxies are a fascinating class of objects with a wide impact on our understanding of the structure of the universe, cosmology, and the evolution of galaxies. Although first discovered at the beginning of the 20th century (Fath, 1909), the study of active galaxies started in the 1940s (Seyfert, 1943) and was accelerated by the detection of the first quasars in the 1960s (Schmidt, 1963). Active galaxies were then found to be powered by AGNs with a massive black hole in their centre (Rees, 1984). Active galaxies are the most powerful and luminous objects in the universe, showing emission over the entire electromagnetic spectrum.

1.2.1 The standard unified AGN model

The class of AGNs contains a zoo of objects, differing e.g. in their luminosities, emission lines, emission line widths, and line ratios. The so called “standard unified model” of AGNs (Barthel, 1989; Antonucci, 1993; Urry and Padovani, 1995) links these objects and unifies them as one type of object, though intrinsic differences with respect to black hole mass, density, and luminosity are expected. In this unification scheme, the IR-optical-ultraviolet-X-ray emission (see Urry, 2004, Netzer, 2006, or Netzer, 2015 for reviews) on

the one hand and the radio emission (e.g. Tadhunter, 2008, and references therein) on the other hand are generally considered separately. Therefore, based on the two characteristics, an AGN can usually be labelled by more than one designation, implying potential confusion. For example, a Fanaroff-Riley (FR) type II galaxy can be classified as type I or type II AGN as described in detail below.

Further, names of different AGN subclasses are misleading and seem to be inappropriate from a current perspective, but were reasonable and well defined when introduced some decades ago. Historically, the term “quasar”—a short version of “quasi-stellar radio source”—was used for a radio-loud source, whereas “QSO” (quasi-stellar object) usually referred to a radio-quiet object. Specifically, QSO meant an object whose host galaxy was not visible, whereas advances in astronomical technology mean that almost all of the objects once called QSOs now have a visible host galaxy. Nowadays, the term quasar is used to refer to optically bright objects (e.g. $M_V < -23$ mag), whereas the term QSO is hardly used. Also, it should be kept in mind that dividing lines for different quantities were drawn in order to classify AGNs. However, usually, these quantities are continuous, so that the classification has no physical but only historical justification.

Despite these complicating conditions, the unification model (see e.g. Urry, 2004; Netzer, 2006, 2015 for reviews) successfully connects most of the different AGN subclasses discovered in the past decades. Main components of this unification model—from the centre to the outer parts as illustrated in Fig. 1.1—are as follows:

- a central supermassive black hole (SMBH) with a mass of $10^6 M_\odot$ to $10^{10} M_\odot$,
- a heated accretion disk,
- high- and low-velocity gas,
- an obscuring medium of gas and dust in some geometric form,
- and a relativistic jet².

The first four components are relevant for the IR-optical-ultraviolet-X-ray unification, whereas the last component is connected to the radio unification. In the following, the individual components are described in more detail.

The central SMBH is the engine of the entire AGN system and converts potential energy of the infalling material into kinetic and electromagnetic energy. Hard X-ray emission is

²In low-power AGNs, the jet is not necessarily relativistic.

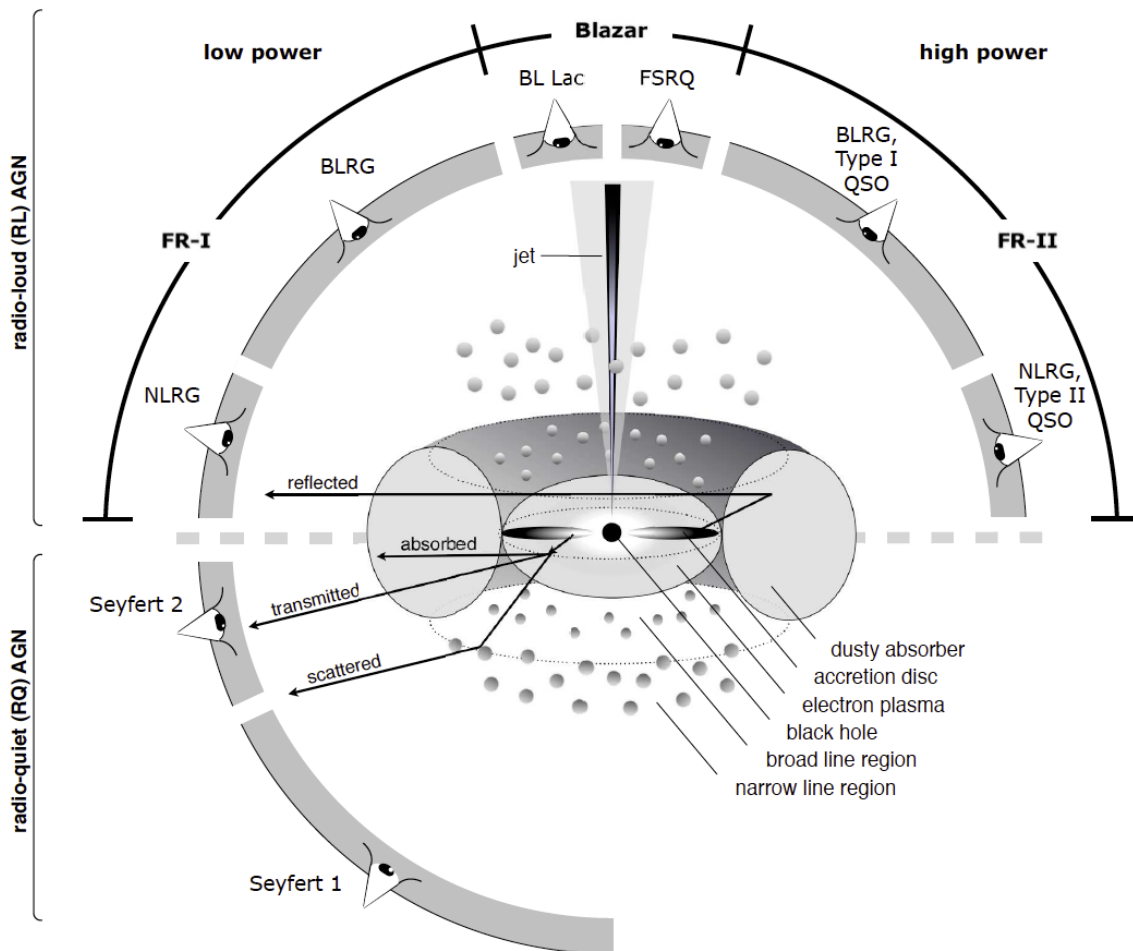


Figure 1.1: Illustration of the standard unified model of AGNs. The observed characteristics are thought to be given by three parameters as illustrated in the graphics: (1) the viewing angle with respect to the symmetry axis, (2) whether a significant jet is present (upper half of the graphics) or not (lower half), and (3) whether the central engine is powerful (right half of the graphics) or not (left half). Although not included in the illustration, Seyfert galaxies can also have jets. Radio-quiet quasars are omitted in the illustration. They are seen from the lower right, i.e. they are high-power, radio-quiet AGNs for which the BLR is seen. Acronyms are explained in the text. Graphic: Beckmann and Shrader (2012) © Wiley-VCH Verlag GmbH & Co. KGaA. Reproduced with permission.

produced in this most central part of the AGN.

The infalling material forms an accretion disk because of its non-zero angular momentum. This accretion disk is of sub-parsec scale and rotates around the SMBH, where the most central part of the disk ($\sim 10^{-5}$ pc) is known to be hottest ($\sim 10^5$ K) and to be an intense contributor of thermal emission between $1 \mu\text{m}$ and 1000 \AA . Generally, the accretion disk radiates in the optical through soft X-ray regime, where the X-ray emission comes from the inner parts of the disk because of the sufficiently high temperatures.

The high-velocity gas is referred to as broad-line region (BLR), characterised by emission

line widths of a few thousand km s^{-1} . It is of high density ($\sim 10^{10} \text{ cm}^{-3}$) and highly ionised by the energetic X-ray and ultraviolet (UV) radiation from the central part of the AGN and has temperatures of 15 000 K to 20 000 K. He III, O IV-VI, and C III-IV are amongst the most abundant ions. Thus, Ly α ($\lambda = 1216 \text{ \AA}$), C IV ($\lambda = 1549 \text{ \AA}$), and O VI ($\lambda = 1035 \text{ \AA}$) are typical strong emission lines. However, also some semi-forbidden emission lines like C III] ($\lambda = 1909 \text{ \AA}$) and O III] ($\lambda = 1663 \text{ \AA}$) are predicted and observed despite the high density. High-ionisation lines arise from regions closer to the centre compared to the emission regions of low-ionisation lines. Furthermore, the gas distribution is non-uniform, but consists of individual clouds or filaments as known from the ratio of emission lines and continuum emission (e.g. Peterson, 2006). The BLR is between 0.01 pc and 1 pc away from the SMBH and is too small to be resolved directly. The reverberation mapping technique is used to study its properties.

Around 100 pc to 1000 pc away from the central SMBH is the low-velocity gas, known as narrow-line region (NLR). The gas density is lower ($\sim 10^4 \text{ cm}^{-3}$) and the observed emission lines are of lower ionisation and narrower (widths of a few hundred km s^{-1}) than in the BLR. Because of the lower density, the spectrum of the NLR contains strong forbidden emission lines, whereas semi-forbidden and permitted emission lines are weak. Also, emission of fine-structure transitions in the inner part of the NLR can be observed in the IR regime. Strongest emission lines are O [III] ($\lambda = 5007 \text{ \AA}$), N [II] ($\lambda = 6584 \text{ \AA}$), O [II] ($\lambda = 3727 \text{ \AA}$), O [IV] ($\lambda = 25.9 \text{ \mu m}$), Ne [V] ($\lambda = 3426 \text{ \AA}$), C IV ($\lambda = 1549 \text{ \AA}$), and the hydrogen Balmer and Lyman lines. The NLR—which is much larger than the BLR—can be observed directly and is found to be composed of clouds (e.g. Kaiser et al., 2000).

A key component of the unified AGN model is the obscuring medium of dust and gas, located at 0.1 pc to 10 pc away from the SMBH. Originally, this obscuring medium was expected to be torus-shaped (e.g. Krolik and Begelman, 1988). However, observational findings indicate that a more complex structure and potentially clumpy distribution has to be taken into consideration (e.g. Nenkova et al., 2002; Elitzur and Ho, 2009; Miniutti et al., 2014; and references in Netzer, 2015). The density is around 10^4 cm^{-3} to 10^6 cm^{-3} with an enormous column density of up to 10^{25} cm^{-2} . The obscuring medium is located outside the BLR but inside the NLR (Antonucci and Miller, 1985). In nearby AGNs, the dusty torus is found to have a radius of up to a few hundred pc.

Radio-loud AGNs have relativistic jets. These jets consist of charged particles that are

accelerated away from the central core in opposite directions. It is unclear whether the jet material consists of electrons and ions or an electron-positron plasma. The jets are very narrow and straight, suggesting that they are collimated close to the central engine. They are formed around 100 AU outside the SMBH and can show lengths of tens or hundreds of kpc. Even jets with a size of more than one Mpc have been observed. The charged particles in the jet spiral in magnetic fields, radiating synchrotron emission as suggested by high brightness temperatures and high degrees of polarisation. However, the jets themselves are rather weak emission sites and usually contribute only a few percent to the total radio emission of a radio galaxy. Regions of high surface brightness are observed along the jets, referred to as knots or hot-spots. Their emission is explained either by in-situ particle acceleration because of shocks (e.g. Rees, 1978) or by the interaction between the jet and an overdense region (e.g. Blandford and Koenigl, 1979). When the jets run through higher-density regions of the intergalactic medium (IGM) or intracluster medium (ICM), the jet particles collide with the gas, form shock fronts, and are re-accelerated, emitting non-thermal synchrotron radiation (Rybicki and Lightman, 1979). This emission is observed as lobes.

Since the processes in the central region of the AGN are highly relativistic, related effects significantly affect how the source is observed (e.g. Kellermann and Owen, 1988). Assuming that the charged particles forming the jet are moving with speed $v \sim c$ at an angle θ towards the observer and the particles are emitting isotropic radiation $S_0(\nu)$, this emission is confined to the opening angle (“beaming angle”) $1/\gamma$, where the Lorentz factor $\gamma = 1/\sqrt{1 - \beta^2}$ is $\gg 1$ since $\beta = v/c \sim 1$. This phenomenon is called “beaming”. The apparent speed v_a is given by

$$v_a = v \sin \theta / (1 - \beta \cos \theta) \quad (1.1)$$

which has its maximum $v_m \approx \gamma c$ at an angle $\theta = 1/\gamma$, corresponding to apparently superluminal motion. Further, the observed emission $S(\nu)$ is given by

$$S(\nu) = S(\nu/\delta)\delta^3 = S_0(\nu)\delta^{3-\alpha}, \quad (1.2)$$

where α is the spectral index³ and δ the Doppler factor defined by

$$\alpha = \frac{\log\left(\frac{S(\nu_1)}{S(\nu_2)}\right)}{\log\left(\frac{\nu_1}{\nu_2}\right)} \quad \text{and} \quad \delta = \frac{1}{\gamma(1 - \beta \cos \theta)}, \quad (1.3)$$

respectively. This effect is known as Doppler boosting.

The radio emission referred to as “core emission” is just the emission of the jet close to the central engine. Because of the high speeds in the centre, core emission is significantly affected by the relativistic effects discussed above, whereas the jet and its particles generally decelerate with increasing distance. Therefore, synchrotron emission from these outer components of radio galaxies are less affected by relativistic effects.

The AGN components listed above are generally expected to be present in any AGN with the exception of the jets. The observed IR, optical, UV, and X-ray emission of most known types of active galaxies can be unified by this model based on different viewing angles with respect to the symmetry axis, resulting in changing observed emission because of (a) dust obscuration and (b) beaming. First evidence for the unified model was found by Antonucci and Miller (1985) who find broad polarised emission lines in Seyfert 2 galaxies which are interpreted to be scattered into the line of sight.

It is widely accepted that significant solid angles are obscured by the dusty absorber surrounding the accretion disk. If the AGN is seen edge-on—i.e. with a viewing angle of 90° to the symmetry axis in the most extreme case—, this obscuring medium blocks the emission from the BLR, resulting in observing an object that lacks broad emission lines. These objects, showing exclusively narrow emission lines (velocities of a few hundred km s^{-1}), are called type II AGNs and include NLR galaxies (NLRGs), type II quasars, and Seyfert 2 galaxies. In contrast, if the AGN is observed face-on—viewing angle of around 0° —, emission from the BLR is not blocked and the observed object shows both narrow and broad emission lines (velocities of a few thousand km s^{-1}). Classes of object with these characteristics are known as type I AGNs and include BLR galaxies (BLRGs), type I quasars, and Seyfert 1 galaxies.

Blazars are a special subclass of quasars characterised by high luminosities, high time variability, high polarisation, and lacking emission lines. All these characteristics are explained by a jet pointing directly towards the observer. Therefore, the emission from the highly relativistic processes in the centre of the AGN is beamed, explaining the high radio

³The spectral index is defined as $S \propto \nu^\alpha$.

and blue optical continuum luminosities, thought to be caused by synchrotron emission. In contrast, the emission lines arise from gas moving at significantly lower velocities and are not beamed, i.e. they are much fainter and can therefore not easily be observed against the highly beamed continuum emission. This class of AGN includes BL Lacs, optically violently variable (OVV) quasars, and highly polarized quasars (HPQs). If the observed radio emission is beamed, the core emission is dominating in the radio regime and the source is labelled as flat-spectrum radio quasars (FSRQs; also known as core-dominated quasars, CDQs). There is an overlap between FSRQs and blazars, but not all FSRQs are blazars.

Low-ionisation nuclear emission-line region galaxies (LINERs) are a subclass of Seyfert 2 galaxies, but with strong emission from low-ionisation lines and weak emission from high-ionisation lines. This type of AGN is very common in the local universe. Weak line radio galaxies (WLRGs) have the same emission line characteristics than LINERs. Narrow-line X-ray galaxies (NLXGs) are also similar to LINERs, but characterised by strong X-ray emission.

Further, AGNs are classified as radio-loud (RL; upper part in Fig. 1.1) and radio-quiet (RQ; lower part in Fig. 1.1) based on the ratio of radio to optical flux density. Usually, the dividing line is defined by $\log_{10}(S_{5\text{GHz}}/S_B) = 1$ (Kellermann et al., 1989), where the optical B band is centred at 4400 \AA . Around 10% of the AGN population is radio-loud, associated with the observational presence of one or two jets. There are different theories whether RL and RQ AGNs are generally similar—in this theory, differences in jet power and host galaxy density are thought to be responsible for the different appearance of RQ and RL AGNs—or whether these two types of AGNs are intrinsically different with respect to black hole mass or central magnetic field. In any case, the formation of relativistic jets requires a certain accretion and electromagnetic forces strong enough to collimate the jets.

For decades, there has been controversy whether a bimodality in the radio luminosity distribution of AGNs exists (e.g. Kellermann et al., 1989; Ivezić et al., 2002) or not (e.g. Lacy et al., 2001; Cirasuolo et al., 2003). This question, which is referred to as the “RL/RQ dichotomy”, is still unsolved. Kimball et al. (2011) favour a bimodality and suggest that the lower-luminosity end of the radio luminosity distribution is dominated by radio emission from starburst activity in the host galaxy, whereas high-luminosity objects are dominated by the AGN itself.

Similar to the IR-optical-UV-X-ray unification described above, the radio unification also

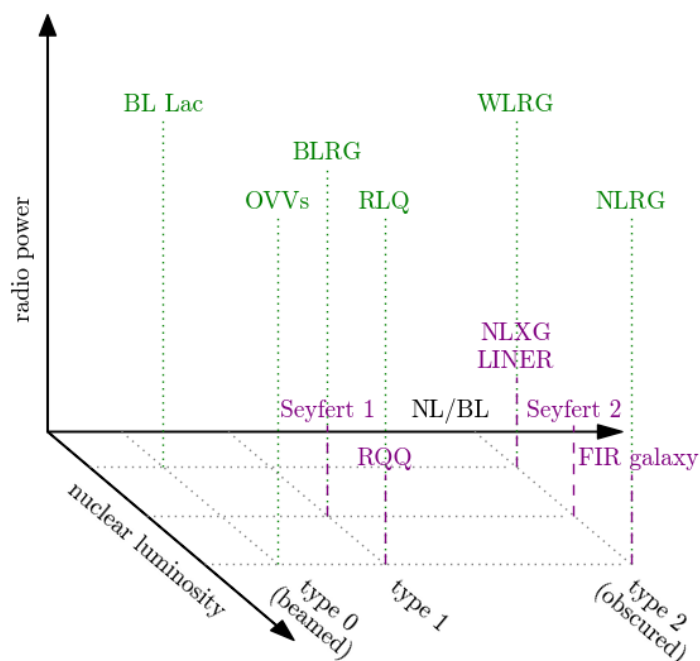


Figure 1.2: Qualitative representation of different AGN subclasses in the three-dimensional parameter space of emission line width, nuclear luminosity, and radio power. Radio-loud and radio-quiet subclasses are printed in green and magenta, respectively. RQQ means radio-quiet quasar and RLQ refers to radio-loud quasar. All other acronyms are explained in the text. Graphic adapted from Tadhunter (2008).

relates to the viewing angle, here with respect to the jet axis. This scheme divides RL AGNs into core- and lobe-dominated sources. Core-dominated sources are characterised by their flat radio spectra, interpreted in the way that the radio jet is pointing towards the observer. Processes in the core are expected to be highly relativistic, resulting in significant beaming effects and high Doppler factor(s). In contrast, if the observer does not look into the jet, the core is Doppler suppressed and the lobes—the processes causing the emission in the lobes are non-relativistic—dominate the observed radio emission, resulting in steep spectra. These sources are classified as lobe-dominated RL AGNs.

Often, the symmetry axes of the IR-optical-UV-X-ray and the radio unification scheme are the same. However, the dependency on the viewing angle is very different for the two schemes. Fig. 1.2 shows different AGN subclasses discussed in this section in the three-dimensional parameter space of emission line width, nuclear luminosity, and radio power.

Based on the power of the central engine, RL AGNs are again divided into two subclasses: FR type I and type II (Fanaroff and Riley, 1974). Observationally, FR I were found to have the radio-brightest part of the jet close to the core, whereas FR II are brightest further

away from the centre of the AGN. Also, FR II are known to be more radio-luminous than FR I, with a dividing luminosity $L_{178\text{MHz}} = 2 \times 10^{25} \text{ W Hz}^{-1} \text{ sr}^{-1}$. However, the dividing radio luminosity seems to slightly correlate with the optical luminosity (Owen and White, 1991; Ledlow and Owen, 1996).

Although this unification model connects many different AGN types based on very few parameters and is likely to be correct to first order, the model is simplifying and does not cover all observed characteristics of the various AGN classes. Further, crucial questions about different classes of AGN and their connection to each other are still open and highly debated. For example, there is observational evidence that Seyfert 2 lacking a hidden BLR exist (e.g. Veilleux et al., 1997). This can be explained by AGN variability (“flickering”; Schawinski et al., 2015) or by theories that systems with very weak AGNs—i.e. low accretion rates and luminosities—do not have a BLR (e.g. Nicastro, 2000; Elitzur and Ho, 2009). Also, AGNs are found without any evidence for an NLR, suggesting obscuration in all directions (Armus et al., 2007). The other extreme case—a type I AGN without any sign of hot and absorbing dust—is found at high and low redshifts (e.g. Jiang et al., 2010; Hao et al., 2011). These findings suggest a more diverse obscuring geometry than accounted for in the unified model. Another open question relates to the spins of the SMBH and the circumnuclear matter and whether these spins are necessarily aligned. Whilst an alignment seems to be reasonable because of angular momentum conservation, this might not be true in more complex systems that are the result of several independent merger events (Bianchi et al., 2012). Also highly debated is the finding that the covering factor of the obscuring medium decreases with AGN luminosity (e.g. Ueda et al., 2003; Hasinger, 2008; Lawrence and Elvis, 2010) and with redshift (e.g. La Franca et al., 2005; Hasinger, 2008; Gilli et al., 2007). It is also suggested that the covering factor is intrinsically different for type I and type II AGNs (Ricci et al., 2011). Other shortcomings of the standard unified AGN model include that it does not account for the dichotomy of RL and RQ AGNs or for the evolution of AGNs.

1.2.2 SMBHs and their host galaxies

For two decades it has been known that SMBHs are not only present in AGNs, but virtually in all galaxies with a bulge (Kormendy and Richstone, 1995; Magorrian et al., 1998). It was then found that those two components—SMBH and host galaxy—are not independent.

Instead, a strong link between SMBH and host galaxy exists, i.e. they jointly evolve. For example, the SMBH mass is found to be correlated to the luminosity, stellar mass, and velocity dispersion of the host galaxy (e.g. McLure and Dunlop, 2001; Magorrian et al., 1998; Kormendy and Bender, 2011).

Similarities are also found in the distribution of AGNs and star forming activity, directly linked to SMBHs and the host galaxies, respectively. The AGN volume density is luminosity-dependent, with that of low-luminosity AGNs peaking at lower redshifts (e.g. Hasinger et al., 2005). A similar behaviour—decreasing star forming activity to low redshifts, known as “cosmic down sizing”—is found for star forming galaxies (e.g. Cowie et al., 1996).

Over the past decade or two, observations and simulations pointed at a direct connection between AGN activity and processes in the host galaxy, referred to as “feedback”. Croton et al. (2006) simulated the growth of galaxies and SMBHs based on semi-analytic models using data from the Millenium Run (Springel et al., 2005) and assuming a favoured Λ CDM cosmology. Their results are inconsistent with the observed abundance of galaxies at the high-mass and -luminosity end of the distribution. The number of massive and luminous galaxies is overpredicted in the simulations by almost two orders of magnitude. Based on this discrepancy, Croton et al. suggest negative AGN feedback present in most massive galaxies, suppressing star formation and, by this, decreasing the number of extremely massive galaxies in their simulations. This suggested AGN feedback model involves two different phases—cold mode and hot mode—and is expected to be triggered by a galaxy merger. It is described by Hardcastle et al. (2007) and nicely illustrated by Hopkins et al. (2008b) as shown in Fig. 1.3. The springboard involves two separated, gas-rich late-type galaxies, that are approaching and finally start to merge. The interaction of these two galaxies triggers heavy star formation, whereas AGN activity starts delayed and finally stops the star forming activity. Left over is a red early-type galaxy.

The AGN is operating in the cold mode (e.g. Kauffmann et al., 2003; Croton et al., 2006; Hardcastle et al., 2007)—also referred to as quasar, standard, radiative, high-excitation, and wind mode—during the merger of the central SMBHs itself. Cold disk gas of the involved host galaxies is driven onto the SMBH and the accretion is radiatively efficient with high Eddington ratios of the order of a few per cent (Best and Heckman, 2012). This process is accompanied by high star formation activity in the host galaxy. Because of the strong emission from the accretion disk forming around the SMBH, X-ray emission is expected to

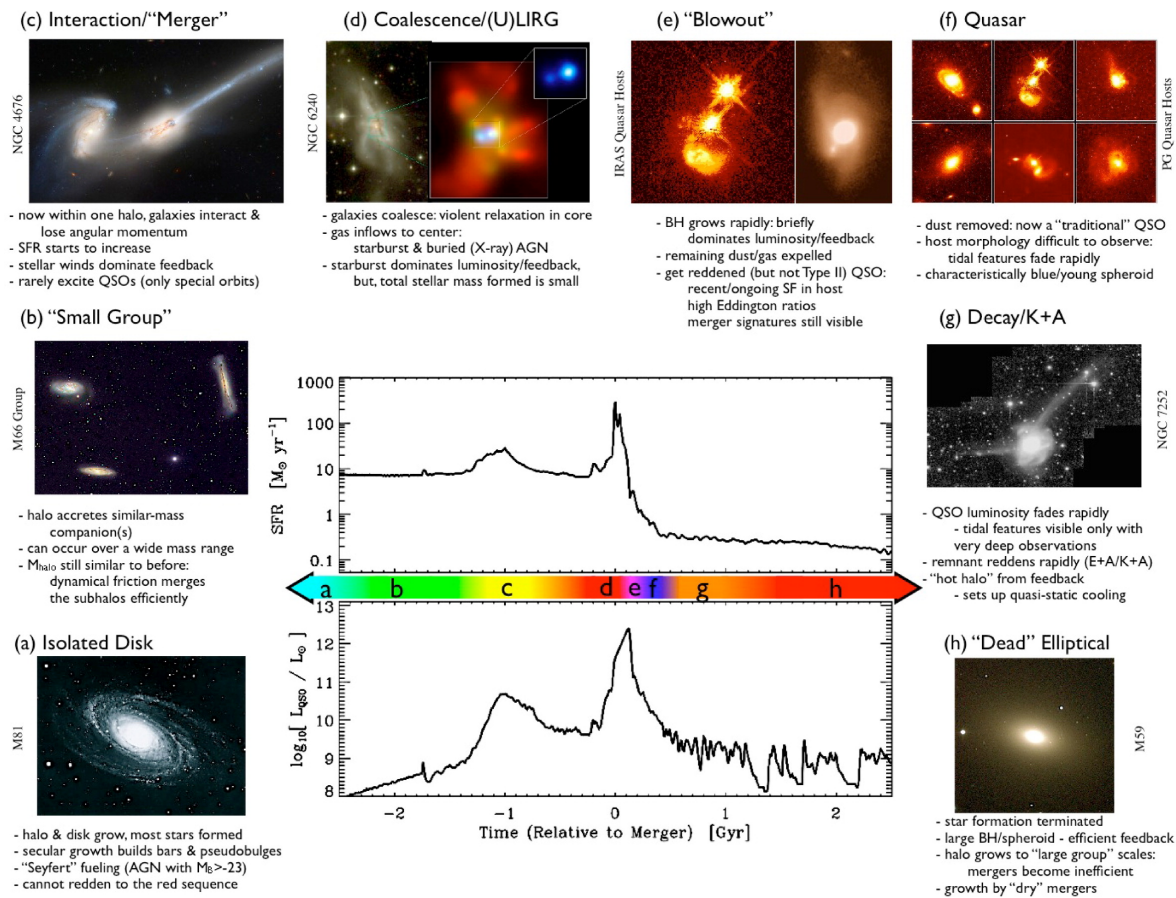


Figure 1.3: Illustration of the standard AGN feedback model. Two gas-rich late-type galaxies merge, accompanied by heavy star forming activity. Later, AGN activity starts, shutting down star formation and leaving a red early-type galaxy. Graphic: Hopkins et al. (2008b) © AAS. Reproduced with permission.

be a good tracer for AGNs in cold accretion mode. Observational evidence has been found in several objects that the most luminous RL AGNs show high star forming activity (Best and Heckman, 2012; Ivison et al., 2012; Norris et al., 2012). The observational finding that AGN activity and star formation density in the universe show the same behaviour—increasing from $z = 0$, peaking at $z = 2 - 3$, and steadily decreasing towards higher redshifts—is considered as evidence for this AGN mode.

Eventually, the AGN terminates star formation by heating or mechanically disrupting the surrounding gas. Thus, the host galaxy is red and of early-type, and the AGN is in radio mode (e.g. Narayan and Yi, 1995)—also referred to as hot, radiatively inefficient, low-excitation, and kinetic mode. This mode is characterised by lacking cold gas, leaving the SMBH with radiatively inefficient accretion of hot gas from the surrounding halo, well below the Eddington limit (below 1%). In this mode, the feedback on the host galaxy is kinetic and the mechanical power of the radio jets dominates the energy output, although radio jets are

not limited to SMBHs accreting in hot mode. In particular, sources in cold and hot mode have been found at all radio luminosities (Best and Heckman, 2012). The transition from cold to hot mode is expected to be of the order of $\sim 10^8$ yr (Hardcastle et al., 2007; Hopkins et al., 2008a,b).

Although this negative feedback scenario is widely accepted and observational evidence has been claimed (Page et al., 2012), it is not without controversy. Several examples are observationally known where AGN activity enhances star formation (Klamer et al., 2004; Gaibler et al., 2012; Zinn et al., 2013; Karouzos et al., 2014). In particular, powerful AGNs at high redshifts are found to be associated with heavy star formation (Seymour et al., 2007; Harrison et al., 2012). This positive AGN feedback is usually explained by gravitationally collapsing gas as a result of shocks caused by the jets of the AGN propagating through the surrounding gas (van Breugel et al., 2004).

1.3 Infrared-faint radio sources

When Norris et al. (2006) released the first ATLAS data for the CDFS, they presented a catalogue of 726 radio sources with 1.4 GHz flux densities between 0.1 mJy and 1.35 Jy. Out of these radio sources, 22 are found to lack IR counterparts in any of the four *Spitzer* wavebands used in the SWIRE survey and are labelled as IFRSs. These 22 IFRSs in CDFS have 1.4 GHz flux densities of a few hundred μ Jy up to 5 mJy, showing that at least the radio-brightest objects of this class are unambiguous detections and not just noise peaks. In particular, all these sources have $3.6 \mu\text{m}$ flux densities below $5 \mu\text{Jy}$. Two examples of IFRSs found by Norris et al. are shown in Fig. 1.4. Possible explanations for these extreme objects included at the time of discovery

- (I) luminous star forming galaxies obscured by enormous amounts of dust,
- (II) radio lobes of unidentified radio galaxies,
- (III) high-latitude pulsars,
- (IV) ultracool dwarf stars,
- (V) RL AGNs,
 - (a) dwarf galaxies hosting an RL AGN,
 - (b) heavily obscured, moderate-redshift ($z \sim 1$) RL AGNs,

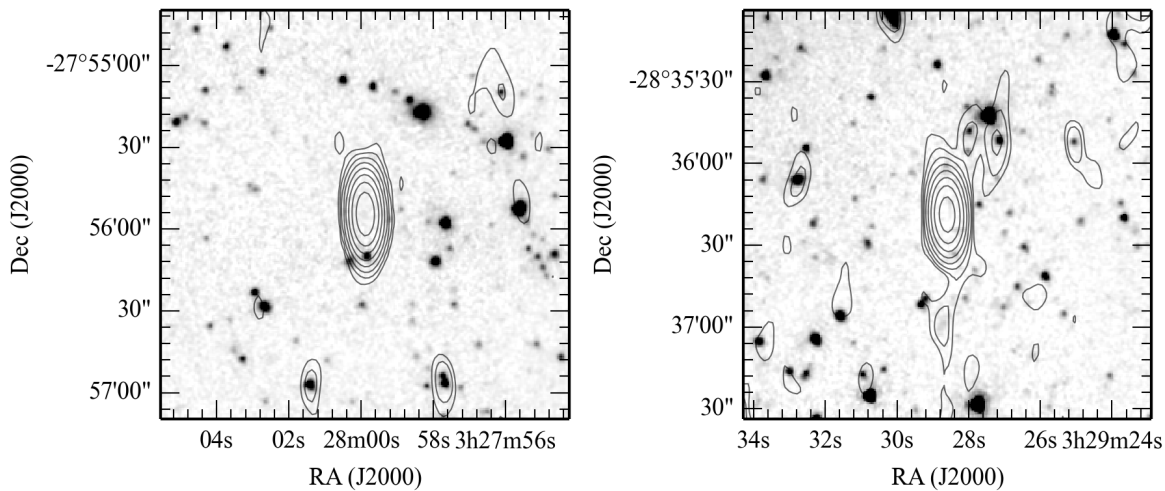


Figure 1.4: Two examples of the class of IFRSs: S114 (left) and S194 (right), found by Norris et al. (2006) in the CDFS. Shown is the $3.6 \mu\text{m}$ SWIRE map (Lonsdale et al., 2003) in greyscale, overplotted by the contours from the 1.4 GHz ATLAS DR3 data (Franzen et al., 2015), starting at 2σ and increasing by factors of 2, where σ is the noise in the image. Both sources are undetected in all *Spitzer* IR bands and their only information comes from the radio.

(c) high-redshift ($z \gtrsim 2$) RL AGNs,

(VI) misidentifications, or

(VII) unknown types of object, potentially of galactic origin.

It has also been argued that the class of IFRSs might be an inhomogeneous class of objects, containing different types of object (e.g. Garn and Alexander, 2008).

1.3.1 Samples of IFRSs in different survey fields

Norris et al. (2006) reported the first IFRS and presented a sample of 22 of these objects—defined as a radio source with signal-to-noise ratio (S/N) above five in the ATLAS DR1 data and without IR counterpart between $3.6 \mu\text{m}$ and $24 \mu\text{m}$ —in CDFS. Later, samples of IFRSs were found in other fields, continuously increasing their number and hence the possibility to study these objects.

When Middelberg et al. (2008a) presented the first ATLAS data of the ELAIS-S1 field, they also searched their catalogue—which had been cross-matched with the SWIRE catalogue—for IFRSs and find 31 examples of these objects. The first IFRSs outside the ATLAS fields are presented by Garn and Alexander (2008) who used radio data from the Very Large Array (VLA) and *Spitzer* IR data to detect 14 IFRSs in the *Spitzer* First Look Survey (xFLS)

field. Later, Banfield et al. (2011) found 18 radio sources in the European Large Area Infrared space observatory Survey-North 1 (ELAIS-N1) field without SWIRE counterparts.

Until then, the criteria to classify a source as IFRS was dependent on the sensitivity of the respective radio and IR data. A solid radio detection (5σ) at 1.4 GHz lacking an IR counterpart was classified as an IFRS. In order to obtain survey-independent criteria for the selection of IFRSs, Zinn et al. (2011) defined two criteria:

$$\begin{aligned} S_{1.4\text{ GHz}}/S_{3.6\text{ }\mu\text{m}} &> 500 \quad \text{and} \\ S_{3.6\text{ }\mu\text{m}} &< 30\text{ }\mu\text{Jy} . \end{aligned} \tag{1.4}$$

The first criterion represents the enormous ratios between 1.4 GHz radio flux densities and 3.6 μm IR flux densities of IFRSs, inevitably resulting from their solid radio detection and their IR faintness. However, Zinn et al. allowed radio sources with faint IR counterparts to be included in the sample of IFRSs. This is given by the second criterion, limiting the observed 3.6 μm flux density to a maximum of 30 μJy . Whilst the first criterion implies that the objects are clear outliers, the second criterion is connected to the distance. For example, nearby RL AGNs like Cygnus A fulfil the flux density ratio criterion, but are excluded from the sample of IFRSs based on their 3.6 μm flux density exceeding the limit of 30 μJy . If such objects are at higher redshifts, the observed near-IR flux density is decreased by cosmic dimming and the source fulfils both selection criteria of IFRSs as defined by Zinn et al.. However, the second criterion does not exclude the selection of heavily dust-obscured objects at low redshifts.

Although Norris et al. (2006) and Middelberg et al. (2008a) on the one hand and Zinn et al. (2011) on the other hand used slightly different selection criteria, they selected objects with the same characteristics and properties. Considering SWIRE data ($\sigma_{3.6\text{ }\mu\text{m}} \sim 1\text{ }\mu\text{Jy}$), an IR-undetected source has a 3.6 μm flux density of $\lesssim 5\text{ }\mu\text{Jy}$. In order to fulfil the first criterion from Zinn et al., the radio source needs to have a 1.4 GHz flux density above 2.5 mJy, corresponding to an S/N of at least 40 in the central parts of the ATLAS fields in DR1. In contrast, Norris et al. and Middelberg et al. selected their IFRSs to show a radio S/N of only five, resulting in a higher chance that spurious sources resulting from noise peaks in the radio maps were included in their IFRS catalogues. Thus, the criteria from Zinn et al. are more conservative with respect to the radio counterparts of IFRSs. Also, the radio-to-IR flux density criterion is more strict, considering that Norris et al. and Middelberg et al. selected

objects with a ratio $\gtrsim 100$. On the other hand, Zinn et al. are less strict with respect to the IR faintness of IFRSs and allow sources with a detected faint $3.6 \mu\text{m}$ counterpart to be included in the sample of IFRSs. Thus, the IR faintness of IFRSs is more extreme in the samples from Norris et al. and Middelberg et al. compared to the sample from Zinn et al. However, the overlap between the sources selected based on these different approaches is generally very high. All IFRS samples studied in this thesis are consistent with the selection criteria from Zinn et al.

Based on their selection criteria given in Eq. (1.4), Zinn et al. (2011) compiled the largest catalogue of IFRSs at that time. Covering the CDFS, ELAIS-S1, xFLS, and Cosmological Evolution Survey (COSMOS) fields, Zinn et al. present a sample of 55 IFRSs, using a total survey area of 11.5 deg^2 . Based on these numbers, Zinn et al. estimate the observed IFRS sky density to be $\sim 5 \text{ deg}^{-2}$.

Currently, work is ongoing to find more IFRSs based on deeper *Spitzer* Extragalactic Representative Volume Survey (SERVS; Mauduit et al., 2012) IR data with a 5σ sensitivity of $1.9 \mu\text{Jy}$ at $3.6 \mu\text{m}$ in already explored fields (CDFS, ELAIS-S1, ELAIS-N1) and in the so-far unexplored XMM-Newton Large Scale Structure Survey (XMM-LSS) and Lockman Hole (LH) fields (Maini et al., 2013). However, Maini et al. are aiming at studying the IR-faintest IFRSs, however with a lower radio-to-IR flux density ratio, required to be at least 200.

In the course of this PhD project, another catalogue of IFRSs became public. Whereas all previous attempts to find IFRSs were limited to deep survey fields of small area, Collier et al. (2014) used shallower data, however covering large parts of the sky. Based on the Unified Radio Catalogue (URC; Kimball and Ivezić, 2008, 2014)—combining radio data from the Green Bank 6 cm survey (GB6), the Faint Images of the Radio Sky at Twenty cm survey (FIRST), the NVSS, and the Westerbork Northern Sky Survey (WENSS)—and IR data from the WISE (Wright et al., 2010) all-sky survey, Collier et al. present a sample of 1317 IFRSs on the entire sky. All of their IFRSs have a detected near-IR counterpart, nevertheless fulfilling both IFRS selection criteria from Zinn et al. (2011). It should be noted that Collier et al. used the flux density at $3.4 \mu\text{m}$ instead of $3.6 \mu\text{m}$ because of the different wavelength coverage of WISE compared to *Spitzer*. On average, the IFRSs from Collier et al. are both IR- and radio-brighter than the sources in the sample from Zinn et al. (2011).

1.3.2 Deep infrared faintness of IFRSs

The unexpected finding of sources lacking an IR counterpart in ATLAS resulted in several studies aiming at finding faint IR counterparts below the detection limit based on stacking analyses. Norris et al. (2006) stacked the IR maps of their IFRSs sample in CDFS at all *Spitzer* IR bands and did not find a detection. Based on this result, they conclude that the IR emission of IFRSs is not just slightly below the detection threshold—which should result in a detection in the stacked map—but that it is well below the threshold, potentially indicating a bimodal distribution of the radio-to-IR flux density ratio of the radio-source population or a long tail of the radio-to-IR flux density ratio distribution to very high values.

Garn and Alexander (2008) find six potential near-IR counterparts below the detection limit ($\sigma_{3.6\mu\text{m}} = 2.9 \mu\text{Jy}$) for their sample of 14 IFRSs and show that the other eight sources are significantly IR-fainter by median-stacking the IR maps of these IFRSs. The most significant constraint on the IR emission of IFRSs was obtained by Norris et al. (2011a). They used $3.6 \mu\text{m}$ data from SERVS, a survey covering parts of the ATLAS field in the *Spitzer* warm mission and resulting in a lower noise than that of SWIRE. Norris et al. median-stacked the $3.6 \mu\text{m}$ maps of 39 IFRSs undetected in SERVS and set a conservative 3σ flux density upper limit of $0.63 \mu\text{Jy}$ at $3.6 \mu\text{m}$. They conclude that this IR faintness and the related enormously high radio-to-IR flux density ratios are uncommon in the local universe. Even stronger constraints are obtained by Maini et al. (2013) who median-stacked the $3.6 \mu\text{m}$ SERVS map of 33 IFRSs undetected at that wavelength and find a flux density upper limit of $0.41 \mu\text{Jy}$, however including sources that do not fulfil the first IFRS selection criterion from Zinn et al. (2011).

1.3.3 IFRSs in the optical and X-ray regime

The class of IFRSs is also faint at observed optical wavelengths and indeed the vast majority of IFRSs are lacking optical counterparts down to $R = 24.5 \text{ mag}$ (Vega; Norris et al., 2006; Middelberg et al., 2008a). Garn and Alexander (2008) find faint optical counterparts for eight out of their 14 IFRSs in xFLS. These sources have R band (Vega) magnitudes between 23.2 mag and 24.7 mag , whereas the undetected IFRSs are fainter than 24.5 mag . Huynh et al. (2010) studied two IFRSs in deep optical fields in the extended CDFS (eCDFS) and find one optical counterpart with a V band magnitude of 26.27 mag and one deep limit of

> 28.9 mag (V band). Based on the optical and near-IR faintness of IFRSs, it is suggested that these sources might suffer from heavy dust obscuration (e.g. Norris et al., 2011a; Zinn et al., 2011).

Zinn et al. (2011) checked their IFRS sample for counterparts in the X-ray regime and find that all IFRSs in the ELAIS-S1 field are undetected in the X-ray XMM Newton survey by Puccetti et al. (2006), setting an upper limit of $5.5 \times 10^{-19} \text{ W m}^{-2}$ in the $0.5 - 2.0$ keV band⁴. Similarly, no IFRS in the COSMOS field was detected with XMM Newton in the soft band down to $7.2 \times 10^{-19} \text{ W m}^{-2}$ (Cappelluti et al., 2007). One of the IFRSs in CDFS analysed by Huynh et al. (2010) was covered by the *Chandra* 2 Ms survey with an average sensitivity of $7.1 \times 10^{-20} \text{ W m}^{-2}$ by Luo et al. (2008) and remained undetected. Therefore, no X-ray counterpart has been found for an IFRS by the start of this PhD project. However, recently, Collier et al. (2014) found an X-ray counterpart for one IFRS from their all-sky sample in the *Chandra* XBoötes survey (El Boucheffry, 2009) with a flux of $0.44 [0.46, 0.99] \times 10^{-18} \text{ W m}^{-2}$ in the soft ($0.5 - 2$ keV) [hard ($2 - 7$) keV, full ($0.5 - 7$ keV)] band. Based on its hardness ratio of -0.60 , this source is classified as type I AGN. Zinn et al. show that the class of IFRSs might significantly contribute to the missing X-ray background reported by Moretti et al. (2003).

The class of IFRSs is defined based on the radio and IR flux densities, i.e. the IR faintness of IFRSs is given by the selection. In contrast, the selection is independent of the observed optical and X-ray faintness of IFRSs. Therefore, the faintness in these wavelength regimes provides additional insights into this class of objects.

1.3.4 Radio properties of IFRSs

Because of the faintness of IFRSs in all other wavelength regimes, the radio waveband often provides the most promising regime to study and constrain the origin of this extreme class of objects. Very long baseline interferometry (VLBI) observations are sensitive to objects with high brightness temperatures. Whereas thermal emission—dominating the energy output of e.g. star forming galaxies—is usually undetected in VLBI observations, such observations are generally sensitive to the compact radio emission of AGNs. Since the early hypotheses about the nature of IFRSs included both star forming galaxies and AGNs, VLBI studies of this class of objects were accomplished to narrow down the physical processes potentially

⁴Conversion between SI and cgs units: $1 \text{ W m}^{-2} = 10^3 \text{ erg s}^{-1} \text{ cm}^{-2}$

causing the relatively high radio flux densities of IFRSs.

Norris et al. (2007) targeted two IFRSs in CDFS with the Australian Long Baseline Array (LBA) at 1.65 GHz and detected one of them, providing strong evidence that this source contains an AGN. They find that most of the emission detected on arcsec-scales in the ATLAS data comes from compact emission, i.e. the radio emission of this IFRS is mainly produced by activity of the AGN core. Furthermore, Norris et al. find the compact emission to be unresolved, constraining the core size to less than 0.03 arcsec, corresponding to a physical length of less than 260 pc at any redshift.

Similarly, Middelberg et al. (2008b) observed four IFRSs in the ELAIS-S1 field with the LBA at 1.6 GHz or 1.4 GHz and detected compact emission in one source. This additional VLBI detection of an IFRS adds evidence that at least some IFRSs contain AGNs.

Middelberg et al. (2011), Banfield et al. (2011), and Collier et al. (2014) searched for polarised emission from IFRSs and find three, five, and 41 polarised IFRSs, respectively. The fractional polarisation was between 1% and 16%. However, all these studies were affected by incompleteness. Collier et al. conclude that these fractional numbers are consistent with typical polarised radio sources.

Further insights into the characteristics of IFRSs based on radio observations were obtained by Middelberg et al. (2011). They studied the radio properties of 17 IFRSs in the CDFS and ELAIS-S1 fields based on observations with the ATCA at 4.8 GHz and 8.6 GHz and archival data at 843 MHz, 1.4 GHz, and 2.4 GHz. They find a median spectral index between 1.4 GHz and 2.4 GHz of $\alpha = -1.40$. This is significantly steeper than the radio SED of the general radio source population and the AGN population in the ELAIS-S1 field and Middelberg et al. show that the spectral index distribution of IFRSs is intrinsically different from the spectral index distribution of these two broader populations. Furthermore, the steep radio spectral indices of IFRSs found by Middelberg et al. (2011) also suggest that these sources are at high redshifts since high-redshift galaxies tend to have steeper radio spectra (e.g. Tielens et al., 1979; Chambers et al., 1996), although exceptions are known (see Afonso et al., 2011, and references therein).

Based on their high-frequency data—resulting in high angular resolutions with a restoring beam of 4.6×1.7 arcsec²—, Middelberg et al. (2011) find that some IFRSs are unresolved and very compact. They conclude that the most compact IFRSs are smaller than $4.5 \text{ kpc} \times 2.1 \text{ kpc}$, ruling out radio lobes as an explanation for these IFRSs. Garn and Alexander (2008)

find most sources in their IFRS sample with angular sizes of less than 3 arcsec. They analysed the class of IFRSs in the context of sources from the Revised Revised Third Cambridge Catalogue (3CRR; Laing et al., 1983) in the parameter space of 1.4 GHz luminosity and linear size and find that most IFRSs are limited to sizes of 20 kpc at any redshift. In particular, Garn and Alexander conclude that most 3CRR sources are significantly larger than IFRSs and, therefore, cannot be considered as local versions of IFRSs.

If IFRSs are at lower redshifts, it has been suggested that some IFRSs might be pulsars since the observed radio flux densities and radio spectral indices of IFRSs are overlapping with corresponding numbers of the known pulsar population. Although the population of IFRSs has been found outside the galactic plane, Cameron et al. (2011) observed a sample of 16 IFRSs with the Parkes radio telescope at high time resolution and conclude that none of these sources are pulsars in our Galaxy.

1.3.5 Connection between IFRSs and other classes of objects

Modelling the SEDs of IFRSs was one of the first attempts to connect IFRSs to other classes of galaxies (Garn and Alexander, 2008; Huynh et al., 2010; Zinn et al., 2011). In these approaches, SED templates of known galaxies were modified—shifted to different redshifts and scaled in luminosity—and tested whether they are consistent with the available photometric data of the respective IFRSs. Huynh et al. also added templates of different stellar populations, and Zinn et al. implemented additional dust extinction in their modellings. All studies conclude that the radio emission of IFRSs cannot be explained by purely star forming galaxies, i.e. ultraluminous IR galaxies (ULIRGs) like Mrk 231 or Arp 220 are inappropriate to reproduce the characteristics of IFRSs. Instead, only RL galaxies at high redshifts ($z \gtrsim 1$), e.g. 3C 273 (an RL quasar with a one-sided jet at $z = 0.158$; Strauss et al., 1992; Bahcall et al., 1995) or galaxies from the 3CRR catalogue (Laing et al., 1983), are found to be in agreement with the photometric constraints of IFRSs. In particular, only galaxies of type FR II (Fanaroff and Riley, 1974) match the photometric characteristics of IFRSs, whereas FR I galaxies do not fulfil the requirements given by the IFRSs in any of the SED modelling studies.

The discrepancy between the SEDs of IFRSs and starburst galaxies (Garn and Alexander, 2008; Huynh et al., 2010; Zinn et al., 2011) can also be found based on the radio-IR-correlation (e.g. Yun et al., 2001). Starburst galaxies are known to follow this correlation,

whereas a deviation is a sign for an AGN. Galaxies with a radio excess are most likely RL AGNs, whereas sources with an IR excess suggest to be RQ AGNs. Directly linked to the radio-IR correlation is the q_{24} value defined by

$$q_{24} = \log_{10} \left(\frac{S_{24\ \mu\text{m}}}{S_{1.4\ \text{GHz}}} \right), \quad (1.5)$$

where $S_{24\ \mu\text{m}}$ and $S_{1.4\ \text{GHz}}$ are the flux densities at $24\ \mu\text{m}$ and $1.4\ \text{GHz}$, respectively. Starburst galaxies are found to be characterised by $q_{24} = 0.84 \pm 0.28$ at least up to $z = 2$ (Appleton et al., 2004). In contrast, RL AGNs show significantly lower q_{24} values because of their radio excess. For example, an IFRS with a $1.4\ \text{GHz}$ flux density of $1\ \text{mJy}$ and undetected in the SWIRE survey at $24\ \mu\text{m}$ ($3\sigma \approx 120\ \mu\text{Jy}$) is characterised by $q_{24} < -0.9$. Similarly, using the $1.4\ \text{GHz}$ luminosity as a tracer for star formation (e.g. Bell, 2003) results in unphysically high SFRs when assuming that IFRSs are at $z \gtrsim 1$ (Zinn et al., 2011).

Norris et al. (2006) and others point out that the class of optically invisible radio sources (OIRSs; Higdon et al., 2005, 2008) might be related to IFRSs. These compact radio sources are optically undetected down to R -band magnitudes of $25\ \text{mag}$ and lower. However, the majority of OIRSs is detected at $3.6\ \mu\text{m}$, in contrast to most IFRSs found in the ATLAS fields. Also, the radio flux densities of OIRSs are more than one order of magnitude lower than those of IFRSs. These characteristics made Norris et al. suggest that an overlap between OIRSs and IFRSs exists but that IFRSs are generally more extreme objects with respect to IR faintness and radio-to-IR flux density ratios. Based on the different IR characteristics, Higdon et al. (2008) conclude that OIRSs cannot be thought of a single source population, but contain starburst-powered systems, AGN- and starburst-powered systems, and radio galaxies.

Norris et al. (2011a) accomplished a comprehensive approach to compare IFRSs to other classes of objects frequently found at high redshifts. They started from the characteristic feature of IFRSs—the enormous radio-to-IR flux density ratios—and analysed this ratio as a function of redshift for different classes of objects. This is shown in Fig. 1.5 and emphasises that this ratio distinctly separates the class of IFRSs from other types of galaxies like starburst galaxies or ordinary AGNs. Further, Norris et al. find that IFRSs share their enormous radio excess exclusively with high-redshift radio galaxies (HzRGs). A potential similarity between IFRSs and HzRGs had already been pointed out by Huynh et al. (2010) and Middelberg et al. (2011).

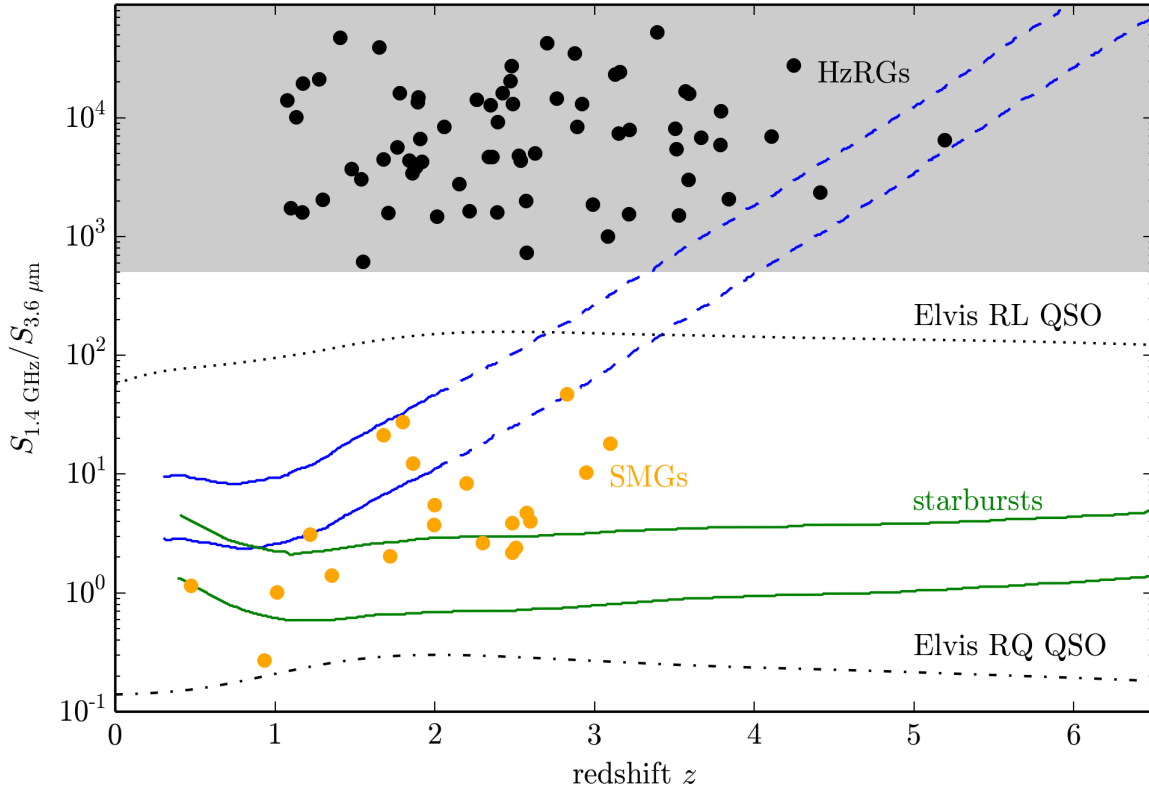


Figure 1.5: Radio-to-IR flux density ratio as a function of redshift for different classes of objects typically found at high redshifts $z \gtrsim 1$. Green lines represent the redshift tracks of luminous IR galaxies (LIRGs) and ULIRGs (Rieke et al., 2009), both classes of star forming galaxies. The tracks of RQ and RL QSOs (Elvis et al., 1994) are shown by a black dotted-dashed and dotted lines, respectively. Yellow dots represent sub-mm galaxies (SMGs). The sample of HzRGs from Seymour et al. (2007) is shown by black dots. The shaded area represents the potential position of IFRSs in this parameter space. Whereas their radio-to-IR flux density ratios exceed 500 as per definition from Zinn et al. (2011), their redshifts were unknown at that time, though high redshifts $z \gtrsim 1$ had been suggested. The blue lines show the effect of adding 10 mag of extinction to the LIRG and ULIRG templates. However, the radio emission of such objects at redshifts $z \gtrsim 2$ is below the sensitivity of current surveys and would not be detected as indicated by the dashed lines. Figure adapted from Norris et al. (2011a).

High-redshift radio galaxies are defined based on their redshift ($z > 1$) and their radio luminosity ($L_{3 \text{ GHz}} > 10^{26} \text{ W Hz}^{-1}$). These massive galaxies—the spiderweb galaxy is one example of this class of object—are the most massive galaxies in the early universe and they are expected to be the progenitors of massive elliptical galaxies in the local universe. HzRGs host AGNs and show SFRs of the order of hundreds or thousands of solar masses per year. However, HzRGs are very rare and less than 200 of these objects are known in the entire sky (Seymour et al., 2007; De Breuck et al., 2010; Drouart et al., 2014).

An additional similarity between IFRSs and HzRGs is their steep radio spectrum as

shown by Middelberg et al. (2011). Based on these findings, Norris et al. (2011a) suggest that IFRSs might follow the correlation between $3.6 \mu\text{m}$ flux density and redshift found for HzRGs (Seymour et al., 2007), similar to the $K - z$ relation known for other radio galaxies (Willott et al., 2003). Following this correlation, Norris et al. hypothesise that the IR-faintest IFRSs might be at redshifts $z \gtrsim 3$.

Huynh et al. (2010) discuss that the radio flux densities of IFRSs can be produced by ultracool dwarf stars. However, they conclude that such radio-detected objects should also be detected in optical observations, inconsistent with the optical faintness of IFRSs. Huynh et al. also compare the sky density of IFRSs to that of BzK galaxies—a color-selected class of star forming and passive galaxies at $z \sim 2$ (e.g. Daddi et al., 2004, 2007)—and dust-obscured galaxies (DOGs; Dey et al., 2008) and find that these types of object are much more abundant than IFRSs. Based on a comparison to optically faint RL AGNs, Huynh et al. suggest that IFRSs are RL AGNs that have not been studied in other samples before.

1.3.6 Remaining explanations for the characteristics of IFRSs

Based on the results outlined above, which were obtained during the first six years of research after the first detection of IFRSs in 2006, some of the originally proposed, potential explanations for the observed characteristics of IFRSs as listed at the beginning of Sect. 1.3 have been ruled out:

- (I) The low q_{24} values of IFRSs make it very unlikely that IFRSs are heavily obscured star forming galaxies. This conclusion has been supported by Norris et al. (2011a) based on the evolutionary tracks of star forming galaxies (see Fig. 1.5).
- (II) The VLBI detections of two IFRSs show that at least not all IFRSs can be lobes of unidentified radio galaxies. Furthermore, the compact morphology of IFRSs in high-resolution radio observations (Middelberg et al., 2011) argues against lobes as explanations for a significant fraction of IFRSs.
- (III) Radio observations provide direct evidence that the emission of IFRSs is not consistent with that of pulsars.
- (IV) Ultracool dwarf stars are excluded because of the optical faintness of IFRSs.

In contrast, the following explanations are consistent with all results obtained in the studies on IFRSs before this PhD project was started:

- (V) IFRSs might be a class of RL AGNs. The low q_{24} values point at RL AGNs and different SED modellings show that only RL AGNs can reproduce the characteristics of IFRSs. Finally, the VLBI detections of two IFRSs show that at least some IFRSs are AGNs. However, the more detailed characteristics remain unclear. Whereas dwarf galaxies hosting an RL AGN (Va) are observationally unknown and theoretically unlikely (Norris et al., 2011a) and RL AGNs at moderate redshifts (Vb) would need enormous amounts of obscuring dust, high-redshift RL AGNs (Vc) were considered to be the most likely explanation for the observed radio flux densities and IR faintness of IFRSs.
- (VI) It could not be ruled out that at least some IFRSs are misidentifications.
- (VII) It is impossible to disprove that a new, unknown class of objects explains the characteristics of IFRSs. However, since known objects were found to be consistent with the phenomenon of IFRSs as discussed above, the invention of new objects is the least favourable option, following Occam's razor⁵.

Although the studies summarised above narrowed down potential explanations for the observed characteristics of IFRSs, concluding that they are RL AGNs, the nature of this extreme class of objects is not fully understood yet. In particular, the lack of redshift information limits the interpretation of previous results and prevents a definite exclusion of some of the potential explanations for IFRSs.

1.4 Motivation and outline

Despite the observations and analyses summarised above, the nature of the class of IFRSs still remained unclear and vague. Several potential explanations for the phenomenon called IFRS have been ruled out and studies show that high-redshift RL AGNs are consistent with the observed characteristics of IFRSs. However, compact emission has been found in only two out of six targeted IFRSs, leaving doubts that the vast majority of IFRSs contain AGNs. Even more unclear is their redshift distribution, only indirectly constrained by SED modelling which has even higher uncertainties because of potential but undetermined dust obscuration.

⁵Occam's razor is a theorem by William Ockham (1287–1347), stating that the hypothesis with the fewest assumptions should be favoured in case of competing hypotheses performing equally well (e.g. Thorburn, 1915).

This thesis addresses these suggestions and aims at directly testing the hypothesis that IFRSs are high-redshift RL AGNs, presented in chapters 2 and 3. Chapter 2 is based on optical spectroscopic data of four optically detected IFRSs and reveals the first redshifts of IFRSs in the ATLAS fields. The presence of compact radio emission in IFRSs is tested based on VLBI observations of a large sample of sources as presented in chapter 3. A so far unexplored wavelength regime of IFRSs is unveiled in chapter 4, describing the first far-IR (FIR) observations of this class of objects. Finally, a detailed study of the broad radio-SEDs of IFRSs is presented in chapter 5, including the first observations of IFRSs in the mm regime. A summary and outlook is given in chapter 6.

The thesis presents a multi-frequency analysis of a relatively new and unexplored class of objects—the class of IFRSs—, combining results from photometric and spectroscopic observations and advanced observing strategies like VLBI. Based on these data, the contributions from the two main mechanisms of powering galaxies—nuclear and star forming activity—are explored. Further, the connections to the class of HzRGs and to young AGNs like GHz peaked-spectrum (GPS) and compact steep-spectrum (CSS) sources are analysed.

The multi-frequency approach to study the class of IFRSs presented in this thesis means that only partially overlapping sub-samples of IFRSs are used in the different analyses presented in chapters 2, 3, 4, and 5. Because of the faintness of IFRSs, only the most promising candidates at the respective frequency could be targeted in the different observations. For example, IFRSs with a detected optical counterpart are the best candidates to obtain spectroscopic redshifts (chapter 2). However, these sources are expected to be less affected by obscuring dust, making them less promising for FIR observations (chapter 4). Further, the detection of compact radio emission from these IFRSs is harder because they are radio-fainter than other IFRSs and a different sub-sample of IFRSs has been used for the VLBI observations (chapter 3). This is a typical shortcoming when multi-frequency datasets are required and these data are not available for an appropriately large area of the sky. Limitations arising from using non-overlapping subsamples are taken into account and summarised in the conclusion (chapter 6).

1.5 Technical remarks

Throughout this thesis, a Λ cold dark matter (Λ CDM) model is used to parameterise the Big Bang cosmological model. It is usually referred to as the standard model of cosmology and is characterised by the cosmological constant Λ —thought to be associated with dark energy—and cold dark matter (CDM). The Λ CDM model is based on general relativity and is consistent with cosmologically relevant observations like the accelerating expansion of the universe, the CMB, and the distribution of galaxies in the universe. The consistency of this model—described by six parameters—has recently been shown by the latest results of the Planck collaboration (Planck Collaboration et al., 2015). In this thesis, cosmological quantities are calculated based on the calculator by Wright (2006), using the parameters $\Omega_\Lambda = 0.7$, $\Omega_M = 0.3$, and $H_0 = 70 \text{ km s}^{-1} \text{ Mpc}^{-1}$. The spectral index α is defined as $S \propto \nu^\alpha$, where S denotes the flux density and ν is the frequency. SI units are used throughout this thesis.

Chapters 2, 3, 4, and 5 contain manuscripts that I wrote as first author in the course of this PhD project and that have been published or submitted for publication in peer-reviewed journals. At the beginning of these chapters, the respective manuscript is put in the context of this PhD thesis with respect to applied techniques and results. At a time, this is followed by bibliographic details and a short description of the respective manuscript, set in a grey-shaded box. These boxes also give details about the contribution of the individual authors. The remainder of the respective chapters contain the manuscripts.

2

Infrared-faint radio sources are at high redshifts

First suggestions about the nature of IFRSs included several, very different classes of objects: star forming galaxies, AGNs, pulsars, and dwarf stars. They were all thought to be able to reproduce the characteristics of IFRSs—IR faintness and enormous radio-to-IR flux density ratios—under certain conditions, although these suggested objects are characterised by very different emission mechanisms and linear sizes. In particular, the distance between these objects and the Earth is extremely different. While dwarf stars and pulsars are sources in our own Galaxy with distances in the order of parsecs or a few kiloparsecs, star forming galaxies and AGNs are extragalactic objects at cosmologically relevant redshifts.

Although local objects like pulsars and dwarf stars were most likely excluded based on pulsar radio observations and the optical faintness of IFRSs, respectively, most studies on IFRSs were aiming at constraining the redshifts of these objects. Garn and Alexander (2008), Huynh et al. (2010), and Zinn et al. (2011) used SED templates of AGNs and star forming

galaxies, shifted them to different redshifts, scaled them in luminosity and tested whether these modified SEDs reproduce the characteristics observed for IFRSs. Huynh et al. also added a stellar population to their templates, whereas Zinn et al. used additional extinction. Although differences between the samples exist, the results are all consistent that IFRSs can only be reproduced by RL AGNs at redshifts $z \gtrsim 1$. In particular, the IR-faintest IFRSs were expected to be at higher redshifts based on the modelling.

Norris et al. (2011a) put a particular emphasis on the redshifts of IFRSs based on the similarity of these objects with the class of HzRGs. Norris et al. show—based on the sample of 69 HzRGs presented by Seymour et al. (2007)—that HzRGs are the only objects sharing the enormous radio-to-IR flux density ratios of IFRSs of usually more than 1000. Since HzRGs are on average brighter than IFRSs in all wavelength regimes, Norris et al. suggest that IFRSs might be less luminous or higher-redshift siblings of HzRGs.

The sample of HzRGs presented by Seymour et al. (2007) is found to follow an anti-correlation between $3.6 \mu\text{m}$ flux density and redshift, similar to the very tight $K - z$ relation known for ordinary radio galaxies which is also known as “observed near-IR Hubble relation” (e.g. Lilly and Longair, 1984; Willott et al., 2003; Rocca-Volmerange et al., 2004.) The K band is a near-IR waveband—centred at $2.2 \mu\text{m}$ —and an important tool to study galaxy evolution since it is sensitive to the emission of galaxies in the wide redshift range $0 \leq z \leq 4$. At low redshifts, K band picks up the emission of the old low-mass red stellar population, whereas the band is dominated by the emission of young massive blue stars at higher redshifts. Because of these redshift-dependent characteristics, the cause of the nature and tightness of the $K - z$ correlation over this large redshift range remains unclear. The slight dispersion in the correlation is usually explained by different radio power since radio-luminous galaxies were found to be brighter in the K band (e.g. Willott et al., 2003).

Based on this $S_{3.6 \mu\text{m}} - z$ correlation known for HzRGs, Norris et al. (2011a) suggest that IFRSs might follow the same relation. If so, IFRSs would be located at redshifts $z \gtrsim 2$. Furthermore, Norris et al. show based on a stacking analysis that the IFRSs undetected at $3.6 \mu\text{m}$ in SERVS do not have a $3.6 \mu\text{m}$ counterpart slightly below the detection limit, but that they are significantly IR-fainter ($S_{3.6 \mu\text{m}} \lesssim 0.63 \mu\text{Jy}$). Based on this finding, Norris et al. suggest that these IR-faintest IFRSs might easily be located at $z \sim 5$ if this class of objects indeed follows the correlation between $3.6 \mu\text{m}$ flux density and redshift found for HzRGs.

Therefore, obtaining redshifts for the class of IFRSs is the crucial step to test the hypothesis that IFRSs are high-redshift RL AGNs. However, the optical faintness and confusion made this a challenging task. In the ATLAS survey, too many optical sources are located within the positional accuracy of the 1.4 GHz radio sources of ~ 2 arcsec. Therefore, a direct cross-matching between radio and optical sources was impossible. Instead, radio sources were first cross-matched to IR sources from SWIRE and then—based on the more precise positional information from the IR detection—to the optical sources. Later, follow-up observations at higher radio frequencies and higher resolution showed that this cross-matching was successful (R. P. Norris, private communication). However, the IFRSs found by Norris et al. (2006) and Middelberg et al. (2008a) do not provide a near- or mid-IR counterpart per definition—IFRSs were originally defined as radio sources without IR counterparts—, so that finding an optical counterpart for these sources was impossible because of confusion. The suggestion that most IFRSs were lacking an optical counterpart ($R \gtrsim 24.5$ mag) because of their intrinsic optical faintness and not because of confusion was later proven to be true based on follow-up observations at higher radio frequencies (R. P. Norris, private communication). For example, Huynh et al. (2010) studied two IFRSs in the deep optical fields of the eCDFs and found one with a V band magnitude of 26.27 mag and the other one > 28.9 mag.

When Zinn et al. (2011) defined their survey-independent criteria for the selection of IFRSs, radio sources with a faint counterpart at $3.6 \mu\text{m}$ below $30 \mu\text{Jy}$ were included in the class of IFRSs if these sources exceed a radio-to-IR flux density ratio of 500. Four of these sources—all located in the CDFS—have optical counterparts with R band (Vega) magnitudes between 22.0 mag and 24.1 mag. Thus, these sources are the most promising candidates to obtain spectroscopic redshifts for IFRSs, crucially needed to narrow down the nature of these objects. However, a powerful telescope—the Very Large Telescope (VLT)—and a significant on-source time of the order of an hour per source were required to observe even the most promising—i.e. optically brightest—candidates.

These IFRSs were spectroscopically observed and provided redshifts of 1.84, 2.13, and 2.76 as presented in the paper below. This finding is crucial for the understanding of IFRSs since it adds evidence that IFRSs are high-redshift objects as suggested before, e.g. based on SED modelling (Garn and Alexander, 2008; Huynh et al., 2010; Zinn et al., 2011). In particular, these redshifts rule out the hypothesis that the class of IFRSs contains a significant number of galactic objects like pulsars or dwarf stars.

At the same time when the paper below was submitted, Collier et al. (2014) presented a new catalogue of IFRSs that is based on all-sky data. They also cross-matched their catalogue of 1317 IFRSs with the SDSS data release 9 (Ahn et al., 2012) and obtained spectroscopic redshifts for 19 sources. One IFRS is found to have a redshift of 0.0196 and is classified as star forming galaxy. Collier et al. suggest that this source is either a misidentification or a star forming galaxy with an AGN in its centre. The other 18 redshifts are found in the range $2.0 \leq z \leq 3.0$.

Although the IFRSs sample from Collier et al. (2014) is generally both radio- and IR-brighter than the IFRSs sample in the deep fields like ATLAS—from which the four spectroscopically observed IFRSs presented here were taken—it was expected that the redshifts found by Collier et al. and in the paper below are overlapping. The median $3.6 \mu\text{m}$ flux density of the spectroscopic sample from Collier et al. is $26.7 \mu\text{Jy}$, compared to a median of $25.5 \mu\text{Jy}$ for the sample of IFRSs with spectroscopic redshifts in the ATLAS fields presented below. While the IFRSs with redshifts populate the overlapping region of $3.6 \mu\text{m}$ flux density ranges of the two samples, the entire samples cover different flux density ranges. The median IFRS in the sample from Collier et al. has a $3.6 \mu\text{m}$ flux density of $25.9 \mu\text{Jy}$, whereas the median IFRS in the ATLAS fields is undetected at $3.6 \mu\text{m}$ in the SWIRE survey or SERVS, corresponding to a flux density below $3 \mu\text{Jy}$.

All 22 IFRSs with spectroscopic redshifts—except for the one outlier discussed above—are consistent with the suggestion by Norris et al. (2011a) that IFRSs might follow a correlation between $3.6 \mu\text{m}$ flux density and redshift that was found for a sample of HzRGs (Seymour et al., 2007). However, it remains unclear whether the $S_{3.6 \mu\text{m}} - z$ correlation holds for IFRSs at redshifts $z \gtrsim 3$. To test the correlation in this redshift range, IR-fainter IFRSs would have to be spectroscopically observed. Because of the accompanying optical faintness of these objects, such observations are highly challenging and time-intensive at optical telescopes. In contrast, molecular lines like CO can be observed in the radio regime—e.g. with the Atacama Large Millimeter Array (ALMA)—and seem to provide a more efficient way to measure redshifts of IR-fainter IFRSs. The detection of an IR-fainter IFRS at $z \sim 5$ would also argue against the alternative hypothesis that all IFRSs have redshifts in the range $1.8 \lesssim z \lesssim 3.0$. Based on the available data, this hypothesis cannot be ruled out.

The redshifts found in the paper below and by Collier et al. (2014) also dispose of two potential explanations for the majority of IFRSs: lobes of unidentified radio galaxies and

misidentifications (see Sect. 1.3). If IFRSs are indeed lobes, there are two possibilities for the IR counterparts: (a) The IR sources are the real counterparts of the radio detections, or (b) the IR and radio sources are not associated. In case of (a), the redshift distribution of these objects would be expected to follow that of RL AGNs with lobes, i.e. FR II galaxies. This distribution peaks at $z \sim 1$ (e.g. Fig. 5 in Norris et al., 2011b). However, if (b) IR and radio counterparts are spurious associations, the redshift distribution should follow that of arbitrarily selected galaxies, peaking at $z \sim 0.1$ (e.g. Fig. 14 in Stoughton et al., 2002) and decreasing to higher redshifts. If IFRSs are misidentifications, case (b) would be expected. The observed redshift distribution of $1.8 \lesssim z \lesssim 3.0$ for IFRSs is in clear disagreement with both scenarios, ruling out that significant fractions of IFRSs are radio lobes or misidentifications. However, it cannot be ruled out that the class of IFRSs is contaminated by a few lobes or misidentifications, as suggested by the low-redshift star forming galaxy discussed by Collier et al.

Based on the available spectroscopic redshifts, even more conclusions can be drawn on the nature of IFRSs and their connection to other classes of object as presented in the paper below. In particular, all spectroscopically observed IFRSs are found to be powerful FR II radio galaxies with 1.4 GHz luminosities above $10^{26} \text{ W Hz}^{-1}$, a significant fraction even above $10^{27} \text{ W Hz}^{-1}$ which corresponds to the luminosity of the brightest RL AGNs (e.g. Urry and Padovani, 1995; Tadhunter, 2008). Also, the optical spectra presented in the paper below are typical broad line quasar spectra.

Moreover, the first redshift-based SED modelling—presented in the paper below—confirms the results from former modellings that only RL AGNs provide appropriate templates to model the SED of IFRSs. In particular, the templates of the RL quasar 3C 273 and the CSS source 3C 48 are found to properly reproduce the SEDs of the three IFRSs with spectroscopic redshifts in the ATLAS fields. These templates have already been successfully used by Garn and Alexander (2008), Huynh et al. (2010), and Zinn et al. (2011) in their modellings without known redshifts.

The remainder of this chapter has been published as

Infrared-faint radio sources are at high redshifts.
Spectroscopic redshift determination of infrared-faint radio sources
using the Very Large Telescope

A. Herzog, E. Middelberg, R. P. Norris, R. Sharp, L. R. Spitler, and Q. A. Parker
Astronomy & Astrophysics, 567, A104, 2014.

The paper presents data from optical spectroscopic observations with the VLT, resulting in the first spectroscopic redshifts of IFRSs—all fulfilling both selection criteria defined by Zinn et al. (2011)—in the ATLAS fields. It is shown that these sources have radio luminosities of FR II galaxies and that they are consistent with the suggested correlation between near-IR flux density and redshift. Further, the first redshift-based SED modelling of IFRSs finds these three sources to be in agreement with lower-luminosity siblings of the CSS source 3C 48 and the RL quasar 3C 273.

I was responsible for leading the work presented in the following manuscript. I calibrated the data using the Image Reduction and Analysis Facility (IRAF; Tody, 1986), measured the redshifts from the spectra, derived intrinsic properties of the observed IFRSs, modelled their SEDs, put them in the context of HzRGs, and wrote the manuscript. E. Middelberg, R. P. Norris, and L. R. Spitler supervised this work with respect to methodology and scientific interpretation and continuously provided feedback. E. Middelberg proposed and scheduled the observations, forming the basis of this work. R. Sharp measured the emission line widths from the spectra. All co-authors provided useful discussions towards the final manuscript. My contribution to the work presented in this manuscript is 90%.

Credit: Herzog et al., A&A, 567, A104, 2014, reproduced with permission © ESO.

Infrared-faint radio sources are at high redshifts

Spectroscopic redshift determination of infrared-faint radio sources using the Very Large Telescope

A. Herzog^{1,2,3}, E. Middelberg¹, R. P. Norris^{3,4}, R. Sharp⁵, L. R. Spitler^{2,6}, and Q. A. Parker^{2,6}

¹ Astronomisches Institut, Ruhr-Universität Bochum, Universitätsstr. 150, 44801 Bochum, Germany
e-mail: herzog@astro.rub.de

² Macquarie University, Sydney, NSW 2109 Sydney, Australia

³ CSIRO Astronomy and Space Science, Marsfield, PO Box 76, Epping, NSW 1710 Sydney, Australia

⁴ ARC Centre of Excellence for All-sky Astrophysics (CAASTRO), Australia

⁵ Research School of Astronomy & Astrophysics, Australian National University, Mount Stromlo Observatory, Cotter road, Weston Creek, ACT 2611 Canberra, Australia

⁶ Australian Astronomical Observatory, PO Box 915, NSW 1670 North Ryde, Australia

Received 30 November 2013 / Accepted 16 June 2014

ABSTRACT

Context. Infrared-faint radio sources (IFRS) are characterised by relatively high radio flux densities and associated faint or even absent infrared and optical counterparts. The resulting extremely high radio-to-infrared flux density ratios up to several thousands were previously known only for high-redshift radio galaxies (HzRGs), suggesting a link between the two classes of object. However, the optical and infrared faintness of IFRS makes their study difficult. Prior to this work, no redshift was known for any IFRS in the Australia Telescope Large Area Survey (ATLAS) fields which would help to put IFRS in the context of other classes of object, especially of HzRGs.

Aims. This work aims at measuring the first redshifts of IFRS in the ATLAS fields. Furthermore, we test the hypothesis that IFRS are similar to HzRGs, that they are higher-redshift or dust-obscured versions of these massive galaxies.

Methods. A sample of IFRS was spectroscopically observed using the Focal Reducer and Low Dispersion Spectrograph 2 (FORIS2) at the Very Large Telescope (VLT). The data were calibrated based on the Image Reduction and Analysis Facility (IRAF) and redshifts extracted from the final spectra, where possible. This information was then used to calculate rest-frame luminosities, and to perform the first spectral energy distribution modelling of IFRS based on redshifts.

Results. We found redshifts of 1.84, 2.13, and 2.76, for three IFRS, confirming the suggested high-redshift character of this class of object. These redshifts and the resulting luminosities show IFRS to be similar to HzRGs, supporting our hypothesis. We found further evidence that fainter IFRS are at even higher redshifts.

Conclusions. Considering the similarities between IFRS and HzRGs substantiated in this work, the detection of IFRS, which have a significantly higher sky density than HzRGs, increases the number of active galactic nuclei in the early universe and adds to the problems of explaining the formation of supermassive black holes shortly after the Big Bang.

Key words. techniques: spectroscopic – galaxies: active – galaxies: distances and redshifts – galaxies: high-redshift

1. Introduction

Active galactic nuclei (AGN) at high redshifts are an important field of current research since they play a crucial role in answering basic questions about the evolution of the Universe. For example, high-redshift AGN are used to study the evolution of the link between black hole mass and the properties of its host galaxy (e.g. Hopkins et al. 2005; Lamastra et al. 2010), their impact on the reionisation and the structure formation in the universe (e.g. Fan et al. 2006; Robertson et al. 2010; Boutsia et al. 2011), and the growth of supermassive black holes (SMBHs) with masses $>10^9 M_{\odot}$ in less than one billion years after the Big Bang (e.g. Volonteri & Rees 2005). Infrared-faint radio sources – a class of object whose detection was unexpected – could significantly contribute to the population of high-redshift AGN.

1.1. Definition and discovery of IFRS

Infrared-faint radio sources (IFRS) are peculiar objects, characterised by relatively high radio flux densities on the order

of 1 mJy at 1.4 GHz only associated with faint or even absent infrared (IR) counterparts. They are defined by Zinn et al. (2011) by two criteria:

- (i) radio-to-IR flux density ratio $S_{1.4 \text{ GHz}}/S_{3.6 \mu\text{m}} > 500$ and
- (ii) $3.6 \mu\text{m}$ flux density $S_{3.6 \mu\text{m}} < 30 \mu\text{Jy}$.

The first criterion selects objects that are clear outliers from the radio-IR correlation, while the second criterion prevents the selection of low-redshift objects with $z \lesssim 1.4$ (Zinn et al. 2011).

The discovery of IFRS was unexpected. When Norris et al. (2006) crossmatched the deep 1.4 GHz radio maps from the Australia Telescope Large Area Survey (ATLAS) with the data from the *Spitzer* Wide-area Infrared Extragalactic Survey (SWIRE; Lonsdale et al. 2003), it was expected that SWIRE would provide an IR counterpart for any extragalactic radio source detected in ATLAS. The spectral energy distribution (SED) of typical host galaxies at redshifts below 4, regardless of whether the radio emission is dominated by AGN or star forming activity, should place the IR flux above the

SWIRE detection limit (Norris et al. 2006). However, 22 sources were found in the Chandra Deep Field South (CDFS) without an IR counterpart in the crossmatching process. These sources – constrained at $3.6\mu\text{m}$ by a 5σ upper limit of $5\mu\text{Jy}$ – were labelled as IFRS. Using the same approach, Middelberg et al. (2008a) identified 31 IFRS using ATLAS radio observations of the European Large Area IR space observatory Survey South 1 (ELAIS-S1) field and SWIRE data. In total, 53 IFRS were detected in the overlapping region between SWIRE and ATLAS, with 1.4 GHz flux densities between tenths and tens of mJy. Zinn et al. (2011) noted that none of those IFRS has an X-ray counterpart in the XMM-Newton survey of the ELAIS-S1 field (Puccetti et al. 2006). One IFRS is located in the field of the CDFS *Chandra* 2 Ms survey (Giacconi et al. 2002; Luo et al. 2008; minimum full band sensitivity around $3.3 \times 10^{-16} \text{ erg s}^{-1} \text{ cm}^{-2}$ over the Great Observatories Origins Deep Survey-South field). However, this IFRS also remains undetected in the X-ray regime.

1.2. VLBI observations and SED modelling

The first attempts to further characterise the properties of IFRS used Very Long Baseline Interferometry (VLBI) observations. Norris et al. (2007) observed two IFRS and identified an AGN in one of them, showing a linear size of ≤ 260 pc at any redshift. Furthermore, Middelberg et al. (2008b) detected one of four targeted IFRS with VLBI and derived a brightness temperature of 3.6×10^6 K, implying non-thermal emission from an AGN since thermal emission processes cannot produce such high brightness temperatures. Therefore, Norris et al. and Middelberg et al. concluded that at least a fraction of all IFRS contain AGN.

Garn & Alexander (2008) found a sample of 14 IFRS in the *Spitzer* First Look Survey (FLS) field, using *Spitzer* Infrared Array Camera (IRAC; Fazio et al. 2004) and Multiband Imaging Photometer (MIPS; Rieke et al. 2004) data. They concluded from SED modelling that IFRS are probably 3C sources redshifted to $2 \leq z \leq 5$. Moreover, they excluded obscured star forming galaxies (SFGs) as an explanation for the objects in their sample because of the radio-to-IR flux density ratio upper limits, differing significantly from corresponding values of SFGs.

The first SED modelling of ATLAS-IFRS was presented by Huynh et al. (2010), using new ultra-deep imaging in the extended CDFS (eCDFs). From their detailed SED modelling of four IFRS, Huynh et al. concluded that a 3C 273-like object can reproduce the data when redshifted to $z > 2$. In agreement with Garn & Alexander (2008), Huynh et al. showed that all four analysed IFRS fall well beyond the radio-IR correlation, suggesting the radio emission is produced by the presence of an AGN, but not by star forming activity.

1.3. Similarities between IFRS and HzRGs

Middelberg et al. (2011) studied the radio properties of 17 out of all 31 IFRS from the ATLAS ELAIS-S1 sample between 2.3 GHz and 8.4 GHz. They found a median radio spectral index of $\alpha = -1.4^1$ and no index larger than -0.7 , which is significantly steeper than the radio spectra of the general source population (-0.86) and of the AGN source population (-0.82) in the ATLAS ELAIS-S1 field. Furthermore, Middelberg et al. noticed similarities between IFRS and the sample of high-redshift radio galaxies (HzRGs) from Seymour et al. (2007). These

HzRGs show steep radio spectra (median radio spectral index of -1.02) like IFRS. Moreover, the extremely high radio-to-IR flux density ratios of IFRS overlap with those of this HzRG sample. Recently, Singh et al. (2014) searched for HzRGs in faint ultra steep spectrum (USS) radio sources and found several sources overlapping with the selection criteria of IFRS.

The hypothesis of an AGN existing in at least a fraction of all IFRS was supported by Middelberg et al. who identified ten IFRS of their sample as AGN and the other seven as probable AGN, based on radio-to-IR flux density ratios, polarisation properties, radio spectral indices, VLBI detections, or radio morphology.

These similarities between IFRS and HzRGs were emphasised by Norris et al. (2011) who showed that no other type of object occupies the range of radio-to-IR flux density ratios of IFRS except for HzRGs. The sample of HzRGs of Seymour et al. (2007) shows a relation between the $3.6\mu\text{m}$ flux density and redshift similar to the $K - z$ relation for other radio galaxies (Willott et al. 2003). Norris et al. suggested that IFRS might follow the same correlation. They used deep data from the *Spitzer* Extragalactic Representative Volume Survey (SERVS; Mauduit et al. 2012) with a 3σ noise level of $\sim 1.5\mu\text{Jy}$ at $3.6\mu\text{m}$ in the fields of CDFS and ELAIS-S1 and stacked the $3.6\mu\text{m}$ images of 39 IFRS, which resulted in an upper flux density limit of $\sim 0.2\mu\text{Jy}$, but remained without a detection. This was interpreted as evidence for the significant IR faintness of IFRS.

1.4. IFRS catalogues

Zinn et al. (2011) compiled a catalogue of 55 IFRS in four deep radio fields, CDFS, ELAIS-S1, FLS, and Cosmological Evolution Survey (COSMOS, Schinnerer et al. 2007), based on their criteria mentioned in Sect. 1.1 and derived a survey-independent IFRS sky density of $(30.8 \pm 15.0) \text{ deg}^{-2}$.

Recently, Maini et al. (in prep.) found 21 IFRS in the Lockman Hole and looked for IR counterparts of IFRS located in the SERVS deep fields. Collier et al. (2014) used data from the all-sky survey Wide-Field Infrared Survey Explorer (WISE; Wright et al. 2010) and the Unified Radio Catalog (URC; Kimball & Ivezić 2008) and presented a catalogue of 1317 IFRS that fulfill the selection criteria from Zinn et al. (2011) given in Sect. 1.1 but are, on average, brighter than the IFRS found in the ATLAS fields. Collier et al. suggested that their IFRS are closer versions of the IFRS found by Norris et al. (2006) and Middelberg et al. (2008a).

We note that IFRS were originally selected as radio sources without any IR counterpart (i.e. Norris et al. 2006; Middelberg et al. 2008a; Garn & Alexander 2008). Since this definition was survey-specific, Zinn et al. (2011) generalised this criterion to the two survey-independent selection criteria given in Sect. 1.1. However, these two types of selection criteria are very similar in the sense that they select the same class of object. The definition by Norris et al. allows faint radio sources that are slightly above the noise level and show no counterpart at $3.6\mu\text{m}$ to be considered as an IFRS, whereas this is prevented by the Zinn et al. criteria. On the other hand, Zinn et al. consider objects with a faint near-IR counterpart as an IFRS, although only under the condition that the source is sufficiently radio-bright to fulfill the radio-to-IR flux density ratio criterion.

1.5. Current status of research

All observational findings so far are compatible with most, if not all, IFRS being high-redshift ($z > 2$) radio-loud AGN,

¹ The spectral index is defined as $S \propto \nu^\alpha$.

Table 1. Sample of spectroscopically observed IFRS.

IFRS ID	RA J2000.0	Dec	$S_{1.4\text{ GHz}}$ [mJy]	$S_{3.6\text{ }\mu\text{m}}$ [μJy]	$S_{1.4\text{ GHz}}/S_{3.6\text{ }\mu\text{m}}$	R (Vega) [mag]	t_{obs} [min]	z
S212	03:29:48.942	-27:31:48.98	18.9	17.5	1080	22.0	44	2.76 ± 0.05
S265	03:30:34.661	-28:27:06.51	18.6	29.3	635	22.3	88	1.84 ± 0.03
S539	03:33:30.542	-28:54:28.22	9.1	14.2	641	24.1	45	–
S713	03:35:37.525	-27:50:57.88	16.4	25.5	643	22.4	128	2.13 ± 0.03

Notes. Listed are the ID, the position in RA and Dec, the radio flux density at 1.4 GHz, the IR flux density at 3.6 μm , the radio-to-IR flux density ratio between 1.4 GHz and 3.6 μm , the optical R band (Vega) magnitude, the on-source time, and the redshift determined in this work. Positions, flux densities, and magnitudes were taken from Norris et al. (2006).

potentially suffering from heavy dust extinction. Considering their high sky density, IFRS could be a very numerous and so far overlooked population of high-redshift AGN that could have a significant impact on the evolution of the universe as suggested by Zinn et al. (2011). Furthermore, Zinn et al. concluded that the X-ray emission of AGN-driven IFRS is consistent with the unresolved components of the Cosmic X-ray background reported by Moretti et al. (2003).

The current knowledge about IFRS is wholly based on photometric detections or upper limits, apart from the VLBI observations. In this paper, we present the first spectroscopic data of IFRS in the ATLAS fields. Based on these observations made using the Focal Reducer and low dispersion Spectrograph 2 (FOR2; Appenzeller et al. 1998) on the Very Large Telescope (VLT), we present the first redshifts of ATLAS-IFRS. Using these results we test the hypothesis that IFRS are similar to HzRGs, derive their intrinsic properties, compare them to other objects and model the SEDs of IFRS. The sample of observed IFRS and the VLT FOR2 observations are described in Sect. 2. In Sect. 3, we summarise the data reduction and calibration and show the final spectra. In Sect. 4, redshifts are measured and intrinsic properties derived for our sample of IFRS. We test our hypotheses in Sect. 5 and present our conclusions in Sect. 6. The cosmological parameters used in this paper are $\Omega_{\Lambda} = 0.7$, $\Omega_{\text{M}} = 0.3$, $H_0 = 70\text{ km s}^{-1}\text{ Mpc}^{-1}$ in combination with the calculator by Wright (2006).

2. Sample and observations

The sample of IFRS consists of four objects, chosen by their detected optical counterparts between 22.0 and 24.1 (Vega) magnitudes in the R band. The condition of an optical counterpart ensures that the sources are bright enough for optical spectroscopy. All selected sources show a faint IR counterpart at 3.6 μm between 14.2 μJy and 29.3 μJy , fulfilling the selection criteria of IFRS by Zinn et al. (2011). The presence of an IR counterpart biases the observed sample towards less extreme IFRS, i.e. with lower radio-to-IR flux density ratios. In the case of the four observed IFRS, this ratio is between 600 and 1100, whilst for the majority of ATLAS-IFRS, which do not show a detected IR counterpart, lower limits of this ratio can be as high as 8000. These IR-undetected IFRS do not show an optical counterpart and, therefore, are not suitable for optical spectroscopy. Although the observed sample is not representative of all IFRS, it allows us to gather information about the intrinsic properties of less extreme IFRS and to test the hypotheses about their relation to other classes of object. Moreover, these findings will also allow conclusions on the more extreme IFRS which cannot be achieved by spectroscopy because of their deep optical

and IR faintness. We summarise the observed objects and their characteristic properties in Table 1.

The longslit spectroscopic observations of these four IFRS were carried out in project 087.B-0813(A) between July and September 2011 (ESO Period 87) in service mode, using FOR2 on UT1 at the VLT. Using the GRISM_150I grism, covering the wavelength range between 330 nm and 1100 nm, and a slit width of 2'', a high throughput is achieved at the cost of relatively low resolution, although sufficient to provide reliable redshifts. The dispersion was 3.45 $\text{\AA}/\text{pixel}$, resulting in a resolution of 54.76 \AA . The total on-source times were 44 min for S212, 88 min for S265, 45 min for S539, and 128 min for S713, where the exposure time for each object was split into several shorter exposures, enabling the correction of cosmic ray events. The seeing varied during and between the different observations from 0.86'' to 2.46''.

3. Data reduction and calibration

Data reduction was carried out using the standard Image Reduction and Analysis Facility (IRAF; Tody 1986) procedures. All exposures were bias-corrected and flatfielded, using normalised masterflats based on the individual dome flat exposures, whose faulty pixels were previously corrected using a bad pixel mask.

We rejected some single flat field exposures where an imperfect illumination was obvious before creating the masterflat. Cosmic rays were removed using the IRAF task `cosmicrays` and through manual inspection. Since the objects are not located in exactly one line in the two-dimensional spectra, i.e. the spatial position changes as a function of wavelength, we corrected the spatial axis for this distortion. Consequently, the wavelength calibration was carried out using lamp exposures taken in every observing night. Since all lamp exposures were saturated and the determination of the lines' peak positions was impossible, we applied a block average with width 3 on the spectral axis to all exposures used in the entire reduction procedure. At the end of the wavelength calibration, the data cover the wavelength range between 390 nm and 1100 nm. Consequently, we subtracted the sky background using the IRAF task `background`. Finally, all individual exposures of one object were averaged to increase the signal-to-noise ratio and one-dimensional spectra were extracted by applying a suitable aperture at the object's position using the IRAF task `apall`. For IFRS S265, which was observed on 2011 July 16 and 2011 July 30, we used only the data taken on 2011 July 30 for the final spectrum because of the poor quality of the data taken on 2011 July 16, arising from seeing in the range of 2.5'' compared to 0.9'' on the other day.

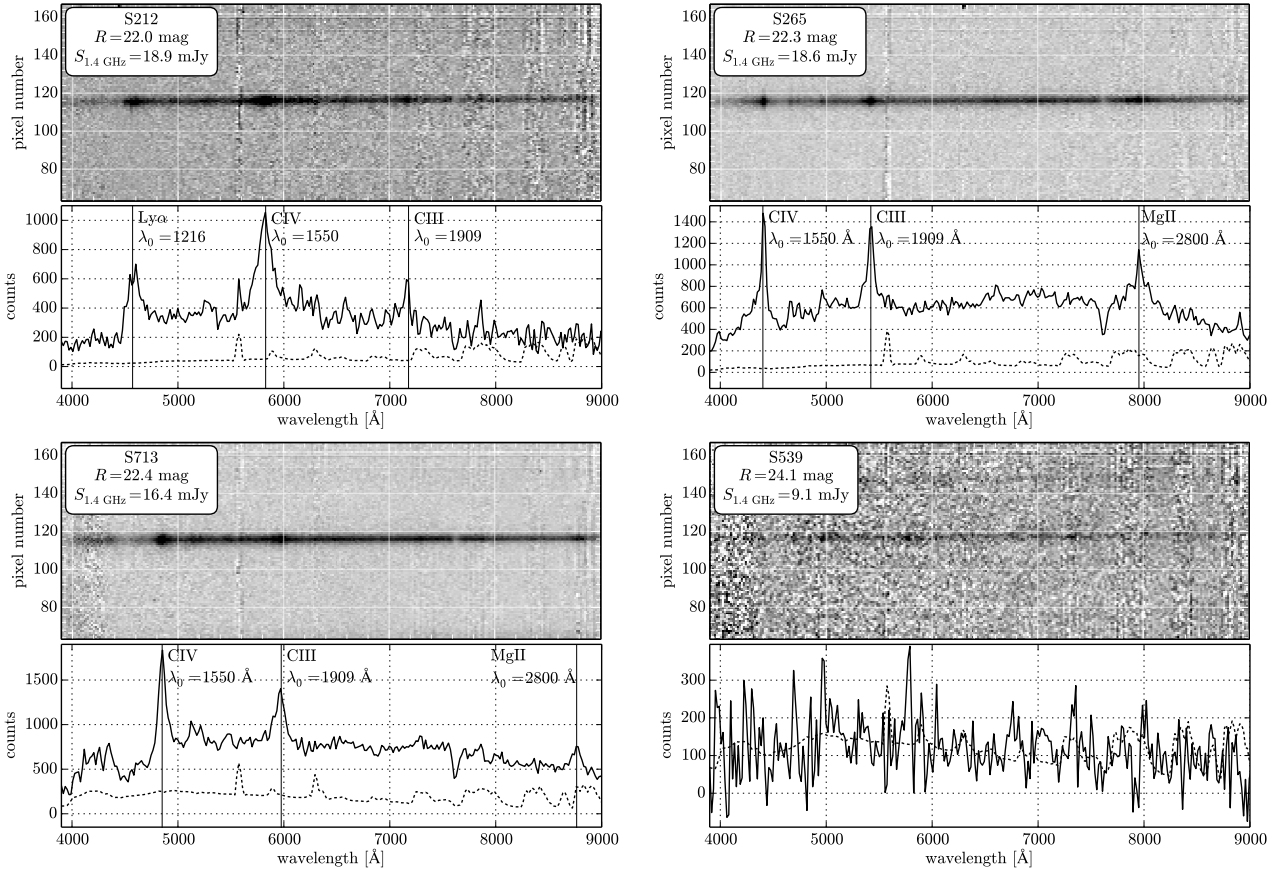


Fig. 1. Spectra of IFRS S212 (*upper left*), S265 (*upper right*), S713 (*lower left*), and S539 (*lower right*). For each IFRS we show the two-dimensional spectrum (*upper plot*) and the extracted one-dimensional spectrum (*lower plot*). We list the ID, the R band Vega magnitude, and the 1.4 GHz radio flux density of each IFRS. In the one-dimensional spectrum, the solid line represents the spectrum of the IFRS while the dotted line shows the sky background in arbitrary units. Additionally, the position of emission lines are marked by vertical lines for a redshift of $z = 2.76$ (S212), $z = 1.84$ (S265), and $z = 2.13$ (S713).

The resulting one- and two-dimensional spectra of IFRS S212, S265, S713, and S539 are shown in Fig. 1.

4. Redshifts and intrinsic properties of IFRS

Using the one-dimensional spectra, we measured redshifts – where applicable – from the Mg II line, which is generally considered to be the most reliable high ionisation line. Where Mg II was not available, we used C IV to derive the redshift, although C IV is known to be different from the galaxy’s redshift (Richards et al. 2011). However, the effect is below one percent and we therefore do not observe this effect in our low-resolution spectra. The Ly α emission line is again less suitable for redshift determinations because of uncertainties due to self-absorption.

Since the calibration uncertainties in the spectra are negligible compared to the uncertainties in the determination of the line position, we determined the redshift uncertainties only from the error in the line position which was obtained from a Gaussian fit to the emission line. We note that all redshifts measured from all available emission lines listed in Table 2 are within the uncertainty of our best redshift measured from Mg II or C IV.

Using the obtained redshifts, we calculated K-corrected radio luminosities, assuming a power law $S \sim \nu^\alpha$ with a radio spectral index of -1.4 which is the median spectral index found by Middelberg et al. (2011) for a sample of 17 IFRS from the ATLAS sample. We also used the flattest (-0.7) and steepest (-2.4) spectral index from Middelberg et al. to constrain the expected radio luminosity range of the observed IFRS.

Table 2. Spectroscopic information of the four IFRS observed with FORS2.

IFRS ID	z	Line	$FWHM$ [km s $^{-1}$]
S212	2.76 ± 0.05	C IV	8700 ± 600
	2.75 ± 0.02	C III]	3300 ± 700
S265	1.85 ± 0.02	C IV	3900 ± 500
	1.84 ± 0.02	C III]	4200 ± 300
S713	1.84 ± 0.03	Mg II	8400 ± 900
	2.13 ± 0.03	C IV	5400 ± 700
	2.12 ± 0.03	C III]	5900 ± 400
S539	2.13 ± 0.03	Mg II	4600 ± 1000
	–	–	–

Notes. Listed are the IFRS ID, the spectroscopic redshift, and the emission line identified in the spectrum with the associated line width. We obtain the final redshift of each IFRS from the Mg II emission line and from C IV where Mg II was not available.

Hereafter, we state these numbers in brackets. In the following, we describe the individual spectra of our four observed IFRS, S212, S265, S713, and S539, respectively.

4.1. S212

Three broad emission lines with full width at half maximum (FWHM) between 78 \AA and 169 \AA are visible in the spectrum of S212 which we identify as Ly α , C IV, and C III], at a

redshift $z = 2.76 \pm 0.05$ (see Fig. 1, upper left). Furthermore, a less distinct emission line can be associated with Si IV at around 5260 Å. The broad emission lines of a few thousand km s^{-1} suggest the presence of an AGN in S212. Using the determined redshift and the measured radio flux density listed in Table 1, S212 has a 1.4 GHz luminosity of $2.0 \times 10^{27} \text{ W Hz}^{-1}$ ($8.8 \times 10^{26} - 7.6 \times 10^{27} \text{ W Hz}^{-1}$).

4.2. S265

We found three broad emission lines with FWHM between 57 Å and 223 Å in the spectrum of S265 in Fig. 1 (upper right) which we identify as C IV, C III], and Mg II, at a redshift $z = 1.84 \pm 0.03$. These broad emission lines with line widths in the range of 4000 km s^{-1} to 8000 km s^{-1} clearly suggest the presence of an AGN in S265. We find a 1.4 GHz luminosity of $6.7 \times 10^{26} \text{ W Hz}^{-1}$ ($3.2 \times 10^{26} - 1.2 \times 10^{27} \text{ W Hz}^{-1}$).

4.3. S713

Three broad emission lines are visible in the spectrum of S713, with FWHMs between 884 Å and 134 Å, corresponding to line widths about 5000 km s^{-1} and suggesting the presence of an AGN. The lines are associated with C IV, C III], and Mg II at a redshift $z = 2.13 \pm 0.03$ (see Fig. 1, lower left). We find a 1.4 GHz luminosity of $8.7 \times 10^{26} \text{ W Hz}^{-1}$ ($3.9 \times 10^{26} - 2.7 \times 10^{27} \text{ W Hz}^{-1}$).

4.4. S539

The source S539 is the optically faintest IFRS in this observing programme. Unfortunately, it was only observed with 44 min on-source time, although 3 h had been requested. Therefore, the resulting spectrum does not provide the quality of the other spectra and we cannot use it to measure a redshift and line widths (see Fig. 1, lower right). Despite the short integration time, emission features are visible, although with poor signal-to-noise. We tentatively interpret the emission feature at around 4970 Å as Ly α , indicated by the related break towards lower wavelengths, and a second emission feature at redder wavelengths as Si IV. We suggest S539 to be at redshift $z \sim 3.1$, although the low signal-to-noise ratio prevents a reliable determination.

5. Discussion

We have obtained for the first time spectroscopic redshifts for three out of four IFRS in the ATLAS fields selected on the basis of their existing optical counterparts. All spectra provide solid determinations of redshifts between 1.8 and 2.8, providing strong evidence that these sources are located at high redshifts. The fourth IFRS has a low signal-to-noise ratio spectrum that indicates a redshift of 3.1 but needs additional confirmation. These redshifts are in agreement with the conclusions of Garn & Alexander (2008), Huynh et al. (2010), Norris et al. (2011), and Zinn et al. (2011) who suggested that IFRS are located at redshifts above 2, mainly from SED modelling. As mentioned in Sect. 2, we are aware that the selection of the optically brightest IFRS might bias our sample towards lower redshifts. This seems to be in agreement with the measured redshifts, which are in the lower part of the expected redshift range of IFRS. Recently, Collier et al. (2014) presented 19 IFRS with spectroscopic redshifts from archival data. Their sample was extracted from a shallow all-sky survey, in contrast to the IFRS analysed in this paper which were found in the deep ATLAS fields. Therefore,

the IFRS found by Collier et al. were radio brighter and slightly IR brighter than the ones presented in this work. Nevertheless, Collier et al. found redshifts in the range $2 < z < 3$, in agreement with those presented here.

All spectra shown in Fig. 1 are broad-line quasar spectra, characterised by high-ionisation emission lines with high equivalent widths. This finding agrees with former suggestions by Garn & Alexander (2008), Huynh et al. (2010), Norris et al. (2011), and Zinn et al. (2011) that IFRS contain AGN.

5.1. Similarity between IFRS and HzRGs

In Sect. 4, we derived 1.4 GHz radio luminosities between $6.7 \times 10^{26} \text{ W Hz}^{-1}$ and $2.0 \times 10^{27} \text{ W Hz}^{-1}$ ($3.2 \times 10^{26} - 7.6 \times 10^{27} \text{ W Hz}^{-1}$) for the IFRS investigated in this work. The classical separation between Fanaroff & Riley (1974) types 1 and 2 is $4.8 \times 10^{25} \text{ W Hz}^{-1}$ ($1.7 \times 10^{25} \text{ W Hz}^{-1}$) at 1.4 GHz, using a steep (ultrasteep) radio spectral index $\alpha = -0.8$ (-1.3) for the conversion from the 178 MHz luminosity given by Fanaroff & Riley. This clearly classifies IFRS as Fanaroff & Riley type 2.

Seymour et al. (2007) defined an HzRG as a radio galaxy with $z > 1$ and a 3 GHz luminosity above $10^{26} \text{ W Hz}^{-1}$, corresponding to $1.8 \times 10^{26} \text{ W Hz}^{-1}$ ($2.7 \times 10^{26} \text{ W Hz}^{-1}$) at 1.4 GHz. We find the IFRS in agreement with the radio luminosity range of HzRGs for the entire range of spectral indices of IFRS found by Middelberg et al. (2011), supporting the hypothesis of Norris et al. (2011) that IFRS might be siblings of HzRGs. We note that most IFRS are radio-brighter and possibly more radio-luminous than those analysed in this work.

Infrared-faint radio sources are characterised by their extremely high radio-to-IR flux density ratios typically in the range of several hundreds to a few thousands. The redshifts determined in Sect. 4 enable us to put these three IFRS in the plot showing the radio-to-IR flux density versus redshift (Fig. 2). This plot clearly separates IFRS from other classes of object which are typically found at high redshifts and indicates a potential connection between IFRS and HzRGs.

Based on this finding, Norris et al. (2011) suggested that IFRS might follow a relation between redshift and $3.6 \mu\text{m}$ flux density, similar to the correlation found for the sample of HzRGs by Seymour et al. (2007). We can now test this hypothesis.

Figure 3 shows the $3.6 \mu\text{m}$ IR flux density versus redshift for the three IFRS whose redshifts we determined in Sect. 4 and for the HzRGs from Seymour et al. (2007). Our IFRS clearly fall in the parameter space of HzRGs, supporting the hypothesis of Norris et al. in the tested redshift range between 1.8 and 2.8. This result provides evidence that the correlation works to redshifts of 2 or 3. It seems that IFRS define the lower bound of HzRGs in this plot.

5.2. Redshift-based SED modelling

The availability of redshifts for IFRS now allows us to perform a more accurate SED modelling. Garn & Alexander (2008), Huynh et al. (2010), and Zinn et al. (2011) modelled SEDs to constrain the redshift of IFRS.

Here, in contrast, we can use the redshift as an anchor and use it to test different SED templates against available photometric data. The method of our SED modelling is similar to the approaches by Huynh et al. (2010) and Zinn et al. (2011).

We built the SED templates using photometric data and redshifts from the NASA/IPAC Extragalactic Database (NED), connecting the datapoints by lines and smoothing the template. We used a variety of SED templates, including starburst, radio and

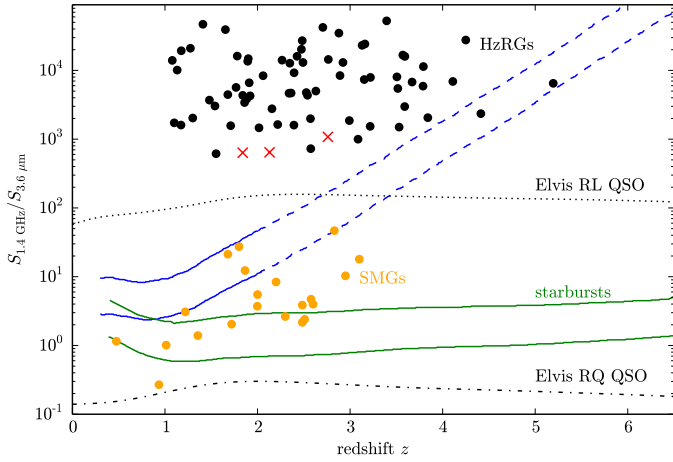


Fig. 2. Ratio of 1.4 GHz and $3.6 \mu\text{m}$ flux densities for IFRS and several other classes of object as a function of redshift, adapted from Norris et al. (2011). It shows that the IFRS analysed in this paper (red crosses) are more similar to HzRGs (black dots, Seymour et al. 2007) than to other types of galaxies frequently found at high redshifts. The solid lines indicate the expected loci of luminous and ultra-luminous infrared galaxies (ULIRGs), using the templates from Rieke et al. (2009). The dotted and dot-dashed lines indicate the loci of a classical radio-loud and radio-quiet QSO, respectively, from Elvis et al. (1994). The location of classical submillimetre galaxies is indicated by the orange dots. We note that dust extinction could cause any of the calculated tracks to rise steeply at high redshift, where the observed $3.6 \mu\text{m}$ emission is generated in visible wavelengths in the galaxy rest frame. This is illustrated by the dashed lines which show the effect of adding $A_v = 8^m$ of extinction to the two starburst tracks. However, the radio emission from these galaxies would then be undetectable at $z > 2$ with current sensitivity.

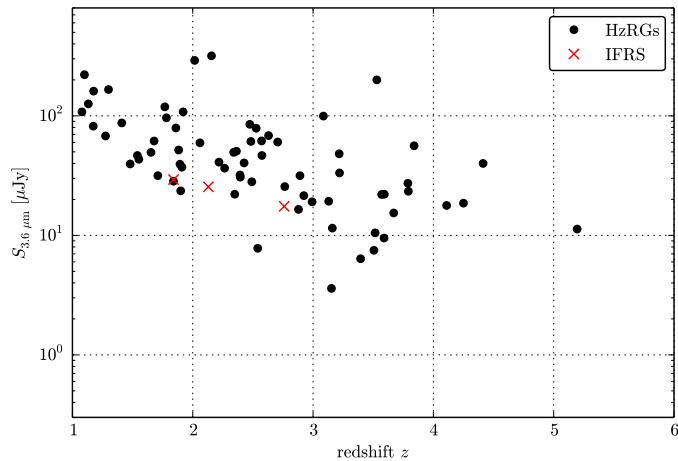


Fig. 3. $3.6 \mu\text{m}$ IR flux density versus redshift, adapted from Norris et al. (2011). Shown is the sample of HzRGs from Seymour et al. (2007) as black dots and the three IFRS whose redshifts are presented in this work as red crosses. The IFRS are located in the same parameter range as the HzRGs and seem to follow their $S_{3.6 \mu\text{m}} - z$ relation. It appears that IFRS define the lower bound of HzRGs.

dwarf galaxies, and quasars. Furthermore, we took all available photometric data of the IFRS from Norris et al. (2006). These data consist of optical (G and R bands), IR ($3.6 \mu\text{m}$ and $4.5 \mu\text{m}$), and radio (1.4 GHz) flux densities for all three IFRS, while S212 and S265 provide more data points in the optical and IR range.

To model the SEDs of IFRS, we shifted the template SEDs to the rest-frame and scaled them in luminosity to match the observed $3.6 \mu\text{m}$ flux density of the IFRS. Extinction was added

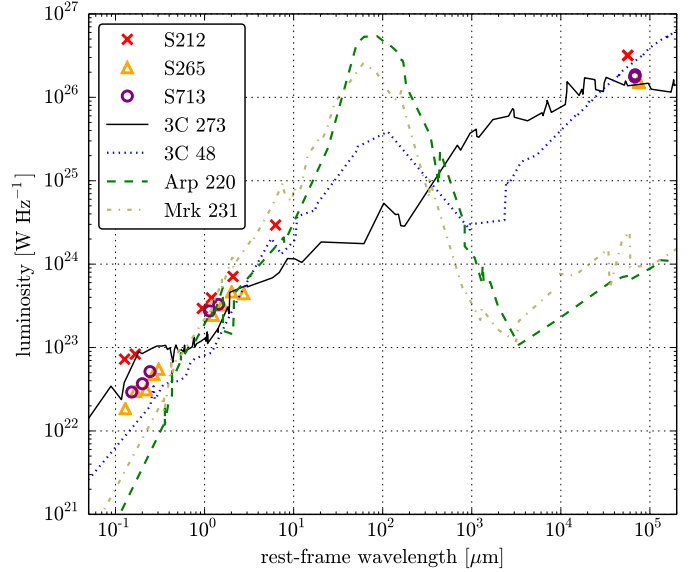


Fig. 4. Rest-frame SED modelling for the three IFRS whose redshifts were determined in this work. All templates are shifted to the rest-frame and scaled in luminosity to match the photometric data points shown by red crosses (S212), orange triangles (S265), and purple circles (S713). While the SED templates of star forming galaxy Arp 220 (green dashed line) and Seyfert galaxy Mrk 231 (olive dashed-dotted line) clearly disagree with the available photometric data, the templates of the radio-loud quasar 3C 273 (black solid line) and the compact steep spectrum (CSS) source 3C 48 (blue dotted line) fulfill the requirements.

in the rest-frame optical and near-IR, following a Calzetti et al. (2000) reddening law, where required by the photometric data. Furthermore, all available photometric datapoints of the IFRS from NED were also shifted to the IFRS rest-frames and used to test the template SEDs for compatibility with these available constraints.

Figure 4 shows the SED modelling for the three IFRS. We find that S265 and S713 have very similar SEDs; Infrared-faint radio source S212 is also similar, except that it is a factor of 2 or 3 brighter than the other two at all wavelengths. These SEDs are consistent with either the 3C 273 or the 3C 48 templates. In our modelling, we scaled down these two templates in luminosity by wavelength-independent factors of 17 and 10, respectively, to match the observed $3.6 \mu\text{m}$ flux densities. In the case of the templates of 3C 273 and 3C 48, no adding of extinction was needed to match the available flux densities.

Except for 3C 273 and 3C 48, none of the templates applied matches the SEDs of the IFRS, even with reddening applied. This result is in agreement with the finding that IFRS are high-redshift radio-loud AGN as confirmed by the spectra shown in Fig. 1. Our SED modelling is inconsistent with the alternative interpretation of IFRS mentioned by Norris et al. (2011), explaining IFRS as AGN that undergo heavy dust extinction.

5.3. Are IR-fainter IFRS at higher redshifts? Cosmological relevance of IFRS

In Sect. 5.1, we showed that our results provide evidence for the similarity between IFRS and HzRGs. In particular, we found our IFRS to be in agreement with the redshift– $3.6 \mu\text{m}$ flux density relation determined for HzRGs by Seymour et al. (2007) in the redshift range probed by our sample. However, our sample was essentially determined by observational constraints, since fainter sources would have required unreasonably long integration times on the largest facilities.

If we assume that IFRS follow the relation for at least somewhat higher redshifts, then most IFRS in the ATLAS fields would be at even higher redshifts, potentially reaching 5 or 6, since the IFRS analysed in this paper are the optically and IR-brightest IFRS in the ATLAS fields (see Sect. 2). Whilst measuring such redshifts in the optical regime requires prohibitive amounts of observing time, the detection of molecular lines such as CO at radio frequencies might be much more efficient. The Atacama Large Millimeter Array (ALMA) is therefore the instrument of choice with which to test this hypothesis of an extension of the redshift– $3.6\ \mu\text{m}$ flux density relation towards higher redshifts.

We have shown that IFRS have similar properties to HzRGs, but they have a significantly higher sky density of a few per square degree. If the IR-fainter IFRS are indeed at even higher redshifts, the number of AGN in the early universe would be larger, resulting in even greater problems with structure formation and the growth of SMBHs shortly after the Big Bang (see Haiman 2013 for a recent review). This had already been emphasised by Zimm et al. (2011) under the assumption that IFRS are AGN driven and are located at redshifts of 3. Since our evidence supports their premises, we conclude that IFRS are likely to be cosmologically relevant.

6. Conclusions

We present the first spectroscopic data of four IFRS in the ATLAS fields from the VLT FORS2 and determine the properties of IFRS.

- We determined the first redshifts of ATLAS-IFRS and find three IFRS at $z = 1.84, 2.13,$ and 2.76 , providing evidence of the suggested high redshifts of IFRS.
- Broad emission lines with line widths between $3300\ \text{km s}^{-1}$ and $8700\ \text{km s}^{-1}$ found in all spectra substantiate the claim that IFRS contain AGN.
- Using the redshifts measured in this work, we present the first SED modelling of IFRS based on redshifts and find the template SEDs of radio-loud quasars to agree with that of IFRS.
- IFRS have derived radio luminosities similar to those of HzRGs, providing further evidence of the similarity of IFRS and HzRGs.
- We test the hypothesis that IFRS follow the same correlation between $3.6\ \mu\text{m}$ flux density and redshift as HzRGs. Our findings support this hypothesis in the tested redshift range and increase the likelihood that IR-fainter IFRS are at even higher redshifts, potentially reaching 5 or 6. Considering their sky density of a few per square degree, IFRS would significantly increase the number of AGN in the early Universe, leading to even more problems with structure formation and the growth of SMBHs shortly after the Big Bang.

Acknowledgements. We thank Peter-Christian Zinn for providing the basics of the code for the SED modelling. AH acknowledges funding from *Bundesministerium für Wirtschaft und Technologie* under the label 50 OR 1202. The author is responsible for the content of this publication. Based on observations made with ESO Telescopes at the La Silla Paranal Observatory under programme ID 087.B-0813(A). IRAF is distributed by the National Optical Astronomy Observatory, which is operated by the Association of Universities for Research in Astronomy (AURA) under cooperative agreement with the National Science Foundation. This research has made use of the NASA/IPAC Extragalactic Database (NED) which is operated by the Jet Propulsion Laboratory, California Institute of Technology, under contract with the National Aeronautics and Space Administration.

References

- Appenzeller, I., Fricke, K., Fürtig, W., et al. 1998, *The Messenger*, 94, 1
- Boutsia, K., Grazian, A., Giallongo, E., et al. 2011, *ApJ*, 736, 41
- Calzetti, D., Armus, L., Bohlin, R. C., et al. 2000, *ApJ*, 533, 682
- Collier, J. D., Banfield, J. K., Norris, R. P., et al. 2014, *MNRAS*, 439, 545
- Elvis, M., Wilkes, B. J., McDowell, J. C., et al. 1994, *ApJS*, 95, 1
- Fan, X., Strauss, M. A., Becker, R. H., et al. 2006, *AJ*, 132, 117
- Fanaroff, B. L., & Riley, J. M. 1974, *MNRAS*, 167, 31
- Fazio, G. G., Hora, J. L., Allen, L. E., et al. 2004, *ApJS*, 154, 10
- Garn, T., & Alexander, P. 2008, *MNRAS*, 391, 1000
- Giacconi, R., Zirm, A., Wang, J., et al. 2002, *ApJS*, 139, 369
- Haiman, Z. 2013, *Astrophys. Space Sci. Lib.*, eds. T. Wiklund, B. Mobasher, & V. Bromm (Berlin Heidelberg: Springer-Verlag), 396, 293
- Hopkins, P. F., Hernquist, L., Martini, P., et al. 2005, *ApJ*, 625, L71
- Huynh, M. T., Norris, R. P., Siana, B., & Middelberg, E. 2010, *ApJ*, 710, 698
- Kimball, A. E., & Ivezić, Ž. 2008, *AJ*, 136, 684
- Lamastra, A., Menci, N., Maiolino, R., Fiore, F., & Merloni, A. 2010, *MNRAS*, 405, 29
- Lonsdale, C. J., Smith, H. E., Rowan-Robinson, M., et al. 2003, *PASP*, 115, 897
- Luo, B., Bauer, F. E., Brandt, W. N., et al. 2008, *ApJS*, 179, 19
- Mauduit, J.-C., Lacy, M., Farrah, D., et al. 2012, *PASP*, 124, 714
- Middelberg, E., Norris, R. P., Cornwell, T. J., et al. 2008a, *AJ*, 135, 1276
- Middelberg, E., Norris, R. P., Tingay, S., et al. 2008b, *A&A*, 491, 435
- Middelberg, E., Norris, R. P., Hales, C. A., et al. 2011, *A&A*, 526, A8
- Moretti, A., Campana, S., Lazzati, D., & Tagliaferri, G. 2003, *ApJ*, 588, 696
- Norris, R. P., Afonso, J., Appleton, P. N., et al. 2006, *AJ*, 132, 2409
- Norris, R. P., Tingay, S., Phillips, C., et al. 2007, *MNRAS*, 378, 1434
- Norris, R. P., Afonso, J., Cava, A., et al. 2011, *ApJ*, 736, 55
- Puccetti, S., Fiore, F., D’Elia, V., et al. 2006, *A&A*, 457, 501
- Richards, G. T., Kruczek, N. E., Gallagher, S. C., et al. 2011, *AJ*, 141, 167
- Rieke, G. H., Young, E. T., Engelbracht, C. W., et al. 2004, *ApJS*, 154, 25
- Rieke, G. H., Alonso-Herrero, A., Weiner, B. J., et al. 2009, *ApJ*, 692, 556
- Robertson, B. E., Ellis, R. S., Dunlop, J. S., McLure, R. J., & Stark, D. P. 2010, *Nature*, 468, 49
- Schinnerer, E., Smolčić, V., Carilli, C. L., et al. 2007, *ApJS*, 172, 46
- Seymour, N., Stern, D., De Breuck, C., et al. 2007, *ApJS*, 171, 353
- Singh, V., Beelen, A., Wadadekar, Y., et al. 2014, *A&A*, in press
DOI: 10.1051/0004-6361/201423644
- Tody, D. 1986, in *Instrumentation in astronomy VI*, ed. D. L. Crawford, *SPIE Conf. Ser.*, 627, 733
- Volonteri, M., & Rees, M. J. 2005, *ApJ*, 633, 624
- Willott, C. J., Rawlings, S., Jarvis, M. J., & Blundell, K. M. 2003, *MNRAS*, 339, 173
- Wright, E. L. 2006, *PASP*, 118, 1711
- Wright, E. L., Eisenhardt, P. R. M., Mainzer, A. K., et al. 2010, *AJ*, 140, 1868
- Zinn, P.-C., Middelberg, E., & Ibar, E. 2011, *A&A*, 531, A14

3

Active galactic nuclei cores in infrared-faint radio sources

The spectroscopic redshifts of IFRSs found by Collier et al. (2014) and in chapter 2 (Herzog et al., 2014) provide crucial information on the nature and intrinsic properties of this class of objects. In particular, the suggested, cosmologically relevant redshifts of IFRSs have been confirmed for all observed sources, neglecting one outlier. Based on these results, closeby or even galactic objects can be ruled out for the predominant fraction of IFRSs. Following the list of potential explanations for IFRSs presented in Sect. 1.3, these results narrow down the explanations to high-redshift RL AGNs. However, the evidence for IFRSs being AGNs is mainly indirect.

Modelling the SED of IFRSs shows that only RL AGNs provide suitable templates to reproduce the characteristics of IFRSs (Garn and Alexander, 2008; Huynh et al., 2010; Zinn et al., 2011; Herzog et al., 2014). Further, the low q_{24} values of IFRSs are interpreted as evidence for IFRSs being RL AGNs (e.g. Garn and Alexander, 2008; Huynh et al., 2010;

Middelberg et al., 2011). First direct evidence for an AGN in an IFRS was found by Norris et al. (2007) based on VLBI observations.

The VLBI technique makes use of long distances between the different antennas, resulting in high angular resolution down to a few milliarcseconds. Consequently, this technique is sensitive only to objects with strong radio emission on small scales. This means spatially extended radio emission—for example from lobes of radio galaxies—cannot be accessed with VLBI, thus the large-scale radio emission in a galaxy cannot be studied using this technique.

In radio astronomy, the brightness temperature T_B is defined as the temperature of a black body showing the observed flux density at the respective frequency. The temperature T_B of a black body—given by Planck’s law—can be approximated for low frequencies and high temperatures ($h\nu \ll k_B T_B$, where h is the Planck constant, ν the frequency, and k_B the Boltzmann constant) as

$$T_B = \frac{c^2}{2k_B \nu^2 \Omega} S_\nu, \quad (3.1)$$

following the Rayleigh-Jeans law. Here, c is the speed of light, and S_ν is the flux density at frequency ν . The beam solid angle Ω is given by

$$\Omega = \frac{\pi \Theta_{\text{maj}} \Theta_{\text{min}}}{4 \ln 2}, \quad (3.2)$$

where Θ_{maj} and Θ_{min} are the major and minor axes of the beam, respectively. This can be combined to

$$T_B = \frac{1225 S_\nu [\text{mJy beam}^{-1}]}{\nu^2 [\text{GHz}] \Theta_{\text{maj}} [\text{arcsec}] \Theta_{\text{min}} [\text{arcsec}]} \text{ K}. \quad (3.3)$$

For example, the Very Long Baseline Array (VLBA) has an angular resolution of around 10 milliarcseconds at 1.4 GHz. If a source shows a peak flux density of $200 \mu\text{Jy beam}^{-1}$ in these observations, this corresponds to a brightness temperature of around 10^6 K.

Brightness temperatures of the order of 10^6 K and higher are characteristic for the core emission of AGNs. The compact radio emission of star forming galaxies—usually dominated by thermal free-free emission—shows brightness temperatures of around 10^4 K (e.g. Condon et al., 1991). Therefore, the detection of a source in VLBI observations provides strong evidence that the emission comes from nuclear activity. It has been shown that very

luminous radio supernovae can also produce brightness temperatures of 10^6 K (Huang et al., 1994; Smith et al., 1998). However, the maximum 1.5 GHz luminosity of these objects on VLBI scales is around $10^{21.5}$ W Hz⁻¹ (Yin and Heeschen, 1991; Smith et al., 1998), i.e. they are only bright enough to be detected out to $z \sim 0.1$. Kewley et al. (2000) conclude that it is very unlikely to detect such a supernova in VLBI observations of a galaxy sample.

Norris et al. (2007) made use of this observational technique and targeted two IFRSs in CDFS with the LBA at 1.6 GHz. One source—with an arcsec-scale 1.4 GHz flux density of 5.7 mJy—was detected with a milliarcsecond-scale flux density of 5.0 mJy, whereas the other source (arcsec-scale 1.4 GHz flux density of 4.6 mJy beam⁻¹) remained undetected with a milliarcsecond-scale flux density < 1.0 mJy beam⁻¹.

The detection of one IFRS with the LBA suggests that at least some IFRSs are powered by nuclear activity. In particular, the radio emission of this detected source is dominated by the emission of the core since almost the entire arcsec-scale flux density was found to be emitted by the central core. On the other hand, the non-detection of the other IFRSs in these observations does not necessarily imply that this source does not have a compact core. Instead, the non-detection implies that the compact emission of the core is below the detection sensitivity, corresponding to an accordingly higher extended emission. Beaming effects might be relevant since the emission of the core can be highly beamed or Doppler-suppressed in contrast to the beaming-unaffected extended emission as discussed in section 1.2.1. This can result in different observed ratios between compact and extended emission. Also radio variability might prevent the detection of a source in VLBI observations if the compact emission is close to the detection sensitivity.

After the discovery of IFRSs in the ELAIS-S1 field (Middelberg et al., 2008a), Middelberg et al. (2008b) targeted four IFRSs in that field with the LBA, similar to the observations by Norris et al. (2007). The sample from Middelberg et al. (2008b) has a wider spread in arcsec-scale flux density, ranging between 0.2 mJy and 22.2 mJy at 1.4 GHz. The second-brightest source was detected with a milliarcsecond-scale flux density of 12.5 mJy, contributing more than half of the arcsec-scale flux density of 21.4 mJy. Middelberg et al. (2008b) derive a lower limit of the brightness temperature of 3.6×10^6 K for this source. The other three IFRSs remained undetected with compact flux densities below 0.27 mJy beam⁻¹.

These two observing projects provide evidence that at least a fraction of IFRSs contain AGNs. However, a larger sample of objects targeted in VLBI observations was needed to

find final evidence for the suggested AGN content in the majority of IFRSs. Because of the relatively radio-faint IFRSs in the ATLAS field and the comparatively insensitive LBA, such a project was hardly feasible for the IFRSs in the ATLAS fields.

When Collier et al. (2014) presented their catalogue of 1317 IFRSs located on the entire sky, conditions changed. This IFRS sample provides an enormous number of potential targets because (a) the total number of known IFRSs was increased by one order of magnitude, (b) the sources are located on the entire sky north of -10° declination, making them observable with different telescopes, and (c) the IFRSs presented by Collier et al. are radio-brighter than the IFRSs observed by Norris et al. (2007) and Middelberg et al. (2008b), resulting in shorter on-source times or—equivalently—higher sensitivity. All sources in the sample from Collier et al. fulfil both IFRS selection criteria from Zinn et al. (2011).

The VLBA with its ten antennas spread across North America provides long baselines and high sensitivity and was the instrument of choice to test the hypothesis that the majority of IFRSs contain AGNs. Since VLBI observations require high phase coherence between phase calibrator and target, all IFRSs from the sample presented by Collier et al. (2014) within 1 deg of a VLBA phase calibrator—which has a 2.3 GHz flux density of more than 0.2 Jy on a baseline of 5000 km—were selected, resulting in a subsample of 110 IFRSs. The main goal of these observations was the detection of compact emission, i.e. the quality of the resulting map and—equivalently—the uv coverage was not crucially important. Therefore, not all ten antennas were necessarily required to achieve the science goal. Using only six antennas, an on-source time of 45 min corresponds to a sensitivity of $66 \mu\text{Jy beam}^{-1}$. However, the applied phase referencing¹ technique results in a reduced sensitivity because of lower coherence though not changing the noise. Since (a) the targets were spread over the entire northern sky, (b) the observations were independent of the weather because of the observing frequency of 1.4 GHz, and (c) the individual observing sessions were of only one hour in duration, the project ideally suited the criteria for filler time projects and was proposed as such.

Out of the 110 IFRSs from the subsample, 57 were observed with the VLBA in semester 14A, resulting in 35 detections and increasing the number of VLBI-detected IFRSs from 2 to 37 as presented in the paper below. The detection fraction of 61% in the VLBA

¹Phase referencing means that target and phase calibrator are alternately observed. This technique is used when target and phase calibrator are not located within one primary beam. The closer these two sources are, the higher is the phase coherence.

observations provides strong evidence that most IFRSs contain AGNs, considering that non-detected sources might still have compact cores. Further, the data show an intrinsically higher VLBI detection fraction compared to the broader RL AGN population and suggest that IFRSs contain young AGNs in the earliest stages of their evolution from compact sources to extended radio galaxies (FR I/II).

The disk size of an average galaxy with fixed mass is known to scale as $R \propto 1/(1+z)$ (Bouwens et al., 2004, 2006; Oesch et al., 2010). VLBI observations, however, do not measure the size of the galaxy, but trace the nucleus itself or hot-spots in the jets, i.e. regions of radio emission with high brightness temperature. The size of these regions is presumably determined by fundamental physics of the jet. Therefore, the size of an AGN in VLBI observations is not expected to scale with $1/(1+z)$. In particular, the extended radio emission of a galaxy is not detected in VLBI observations because of its low brightness temperature. Thus, the putative correlation between compactness and redshift found for IFRSs in the paper below (Fig. 6) is not expected to be explained by the scaling of the galaxy disk size $R \propto 1/(1+z)$, but is pointing at intrinsic characteristics of the class of IFRSs. The finding is interpreted that IFRSs might contain young AGNs as discussed in more detail in the paper.

New spectroscopic redshifts of IFRSs

In the course of the project involving the VLBA observations, the sample of observed sources has been cross-matched with SDSS DR10 (Ahn et al., 2014) as described in the paper below. Collier et al. (2014) used DR9 for their catalogue. Therefore, I not only cross-matched the sample of VLBA-observed sources but the entire IFRS catalogue from Collier et al. with SDSS DR10 to obtain more photometric and spectroscopic information about the class of IFRSs in the optical regime and, in particular, to add redshift information. I used the same approach as presented by Collier et al., i.e. applying a cross-matching radius of 2 arcsec, resulting in 39 spectroscopic redshifts. 19 of these 39 redshifts were already reported by Collier et al. Out of the remaining 20 spectroscopic redshifts, I dropped two because they were flagged with a redshift warning. Therefore, I report 18 new spectroscopic redshifts for the class of IFRSs. They are listed in Table 3.1. One of these 18 spectroscopic SDSS counterparts has been classified as STAR in DR10 based on its optical spectrum with a redshift of $z = 0.0004 \pm 0.0003$. Most likely, this is a misidentification and the SDSS counterpart is not associated with the IFRS. In particular, the angular separation between SDSS object

Table 3.1: Spectroscopic redshift information for IFRSs from SDSS DR10. Listed are only those 18 IFRSs that did not have spectroscopic redshifts in the catalogue presented by Collier et al. (2014) based on SDSS DR9. The IDs follow the designation from Collier et al. The listed position is the SDSS position. Also listed is the angular separation between the SDSS and FIRST counterparts. The classification is taken from SDSS DR10.

IFRS ID	RA J2000	Dec J2000	z_{spec}	Separation [arcsec]	Classification
F0418	14:11:57.56	+44:28:03.71	2.2646 ± 0.0004	0.237	BROADLINE QSO
F0426	14:13:09.26	+24:07:00.65	2.3486 ± 0.0005	0.215	BROADLINE QSO
F0514	14:31:30.84	+23:34:22.22	3.5929 ± 0.0004	0.115	BROADLINE QSO
F0519	14:32:43.17	+23:20:09.42	2.8866 ± 0.0007	0.439	BROADLINE QSO
F0564	14:40:48.57	+36:35:35.51	3.1474 ± 0.0006	0.079	BROADLINE QSO
F0575	14:42:26.70	+13:29:56.28	3.0760 ± 0.0003	0.217	BROADLINE QSO
F0643	14:55:06.58	+13:59:27.61	2.4011 ± 0.0006	1.429	BROADLINE QSO
F0653	14:56:27.56	+43:55:00.03	2.9491 ± 0.0004	0.194	BROADLINE QSO
F0671	14:59:31.19	+14:56:50.37	2.6197 ± 0.0004	0.469	BROADLINE QSO
F0682	15:00:48.63	+45:28:05.82	2.7350 ± 0.0003	0.641	BROADLINE QSO
F0952	15:45:21.49	+41:30:25.17	2.8759 ± 0.0003	0.291	BROADLINE QSO
F0956	15:46:04.41	+44:49:10.50	2.7888 ± 0.0004	0.108	BROADLINE QSO
F0957	15:46:25.33	+36:53:13.23	1.9386 ± 0.0005	0.593	QSO
F1061	16:09:06.09	+42:53:23.41	2.4789 ± 0.0010	1.117	BROADLINE QSO
F1086	16:15:20.31	+43:47:25.29	2.8991 ± 0.0006	0.058	BROADLINE QSO
F1168	16:38:17.38	+41:27:29.91	2.2276 ± 0.0007	0.341	BROADLINE QSO
F1224	17:04:08.58	+44:08:39.78	3.2625 ± 0.0003	0.312	BROADLINE QSO
F1239	17:08:57.64	+38:13:07.78	0.0004 ± 0.0003	1.990	STAR

and the IFRS radio position is 1.99 arcsec, i.e. very close to the cross-matching radius of 2 arcsec. All other 17 IFRSs show redshifts in the range $1.94 \leq z \leq 3.59$. I find four IFRSs with $z \geq 3.0$, exceeding the redshift of the most distant IFRS at $z = 2.99$ as presented by Collier et al. Combining the data from Collier et al. based on SDSS DR9, the spectroscopic observations presented in chapter 2 (Herzog et al., 2014), and the additional data from SDSS DR10 reported here, spectroscopic redshifts for 40 IFRSs are known to date. They cover the redshift range $1.84 \leq z \leq 3.59$, excluding two potential misidentifications.

I suggest that the observed redshift distribution of IFRSs towards low redshifts—showing no IFRS at $z < 1.8$ —is not just a cosmological selection effect. The comoving volume corresponding to the redshift range $z \leq 1.8$ ($1.8 \leq z \leq 3.6$) is 486 Gpc^3 (875 Gpc^3), i.e. the fact that IFRSs are not found at $z < 1.8$ cannot be explained by a small probed volume for that redshift regime.

Another potential reason for the observed break in the redshift distribution of IFRSs at

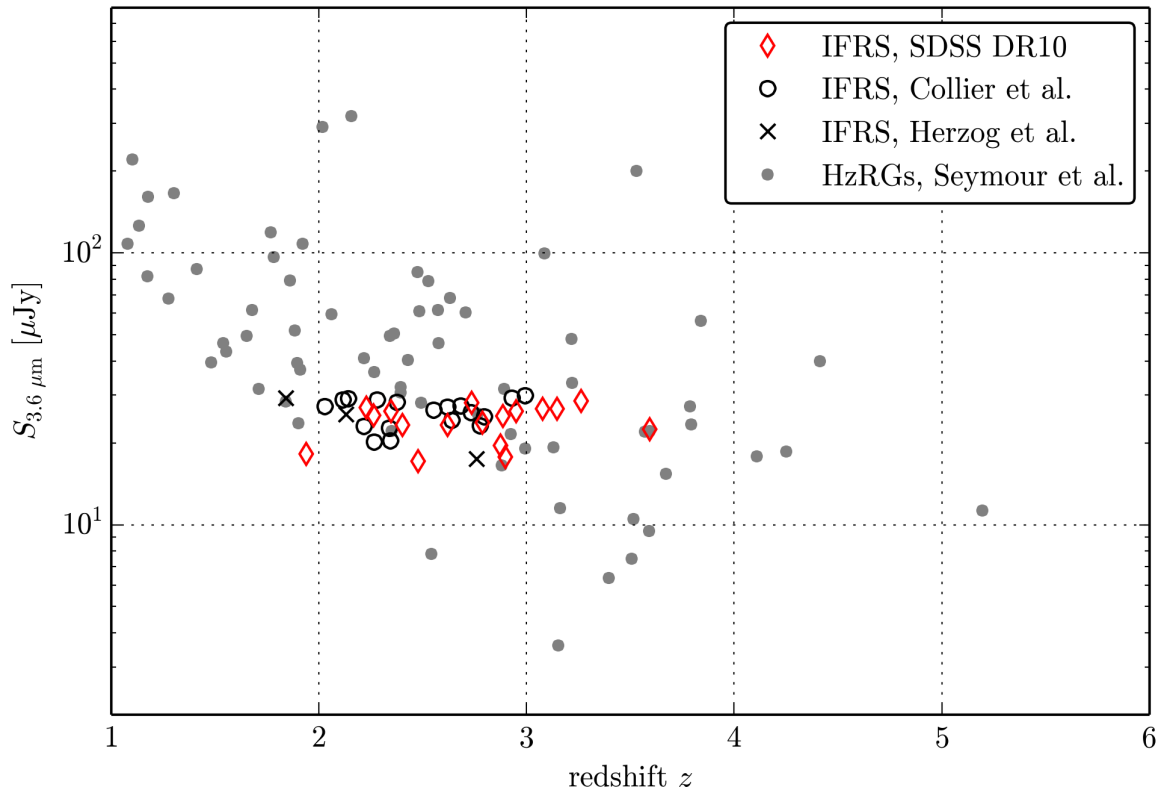


Figure 3.1: Observed near-IR $3.6 \mu\text{m}$ flux density as a function of redshift for all IFRSs with known spectroscopic redshifts. Red open diamonds represent IFRSs with new redshift information from SDSS DR10 presented here. Data from Collier et al. (2014) and Herzog et al. (2014) are shown by black open circles and black crosses, respectively. The sample of HzRGs from Seymour et al. (2007) is represented by grey dots. Two IFRSs were found to be at very low redshifts—potentially misidentifications as discussed in the main text—and are not visible in this plot.

$z < 1.8$ is the redshift desert². For the IFRS sample from Collier et al. (2014), the observed redshift distribution—compiled in this thesis and by Collier et al.—might indeed be affected by the redshift desert. For this sample, it is unknown how many sources are lacking spectroscopic redshift information because they are just located in the redshift desert. In contrast, all four spectra presented in chapter 2 (Herzog et al., 2014) show distinct spectral features, i.e. these objects are not in the redshift desert. However, the low number of objects in this study prevents a general statement on the class of IFRSs. Further, the redshift desert cannot explain why no IFRS has been found at $z \lesssim 1.4$.

Figure 3.1 shows the observed $3.6 \mu\text{m}$ near-IR flux density as a function of redshift for

²The so-called redshift desert refers to the redshift range $1.4 \lesssim z \lesssim 1.8$ in which many optical spectroscopic features are moved into the near-IR regime, preventing measuring redshifts from optical spectra. At $z \gtrsim 1.4$, the lowest-wavelength strong emission line—O [II] at $\lambda = 3727 \text{ \AA}$ —is moved out of the optical window, defining the beginning of the redshift desert. At $z \gtrsim 1.8$, the Ly α line at $\lambda = 1216 \text{ \AA}$ is shifted into the optical window, closing the redshift desert.

the 40 IFRSs with spectroscopically confirmed redshifts, similar to the plot presented by Norris et al. (2011a). The additional 17 IFRSs with reliable spectroscopic redshifts presented above all fall in the region covered by HzRGs in this parameter space, adding evidence to the suggestion by Norris et al., Collier et al. (2014), and Herzog et al. (2014) that IFRSs might follow the correlation between $3.6 \mu\text{m}$ flux density and redshift that has been found for HzRGs.

Broad optical emission lines in the spectra of IFRSs

Out of the 37 IFRSs with spectroscopic redshifts from SDSS DR10 discussed above, 35 have been classified in SDSS as QSO, one as GALAXY—the star forming galaxy discussed by Collier et al. (2014)—, and one as STAR as mentioned above. 31 out of the 35 IFRSs classified as QSO have been assigned the subclass BROADLINE, whereas the remaining four spectra do not have a subclass. However, studying the spectra of these four sources shows that they also have broad emission lines. Adding the spectra presented in chapter 2 (Herzog et al., 2014), all 38 reliable optical spectra of IFRSs show broad emission lines, revealing that these objects are type I AGNs. This conclusion can be confidently drawn for the IR and optically brightest IFRSs, i.e. those sources that have been targeted by spectroscopic observations. However, it still has to be tested whether these characteristics are also given for the optically fainter IFRSs. This most extreme subclass of IFRSs has not yet been spectroscopically observed because of its faintness.

Black hole mass estimates for IFRSs

The $H\beta$ emission line ($\lambda = 4861 \text{ \AA}$) can be used as a tracer of the black hole mass M_{BH} (Kaspi et al., 2000, 2005). However, this only works at low redshifts since this line is shifted out of the optical window at redshifts $z \gtrsim 0.75$. Instead, the Mg II emission line ($\lambda = 2798 \text{ \AA}$) can be used as a tracer for higher-redshift objects as shown by McLure and Jarvis (2002) and Trakhtenbrot and Netzer (2012) if the line width is below 6000 km s^{-1} . The black hole mass is then given by

$$M_{\text{BH}} = 6.79 \times 10^6 \left(\frac{L(\text{Mg II})}{10^{35} \text{ W}} \right)^{0.5} \cdot \left(\frac{\text{FWHM}(\text{Mg II})}{10^3 \text{ km s}^{-1}} \right)^2 M_{\odot}, \quad (3.4)$$

where $L(\text{Mg II})$ denotes the luminosity and $\text{FWHM}(\text{Mg II})$ the full width at half maximum (FWHM) of the Mg II emission line, tracing the size of the BLR and the velocity dispersion, respectively (Trakhtenbrot and Netzer, 2012). The proportionality between these quantities is then given by the virial theorem (described e.g. in Fine et al., 2006). Out of the 37 optical spectra for IFRSs from SDSS DR10 with QSO classification, 17 reveal the Mg II emission line, showing Mg II line widths between 800 km s^{-1} and 3200 km s^{-1} . I used the relation from Trakhtenbrot and Netzer and find BH masses between $1.2 \times 10^7 M_{\odot}$ and $4.3 \times 10^8 M_{\odot}$ for these 17 IFRSs. The mean is $(1.7 \pm 1.0) \times 10^8 M_{\odot}$ and the median is $(1.6 \pm 0.3) \times 10^8 M_{\odot}$. These black hole masses have been calculated for IFRSs in the redshift regime $1.9 \lesssim z \lesssim 2.7$. At higher redshifts, the Mg II line is shifted out of the optical window.

Franceschini et al. (1998), Laor (2000), and Lacy et al. (2001) show that the radio luminosity can also be used as a tracer for the black hole mass of quasars. I derived black hole masses for all 37 IFRSs with an SDSS spectrum classified as QSO using the 5 GHz luminosity, approximated based on the 1.4 GHz flux density and the spectral index between 6 cm and 20 cm presented by Collier et al. (2014). If no spectral index was available for an individual source, I used the median spectral index of the entire IFRS sample from Collier et al. In the approach presented by Lacy et al., the black hole mass depends on the Eddington ratio, defined as the ratio between bolometric luminosity and Eddington luminosity. Independent on this ratio, the black hole masses of IFRSs derived from the radio luminosities are $> 10^9 M_{\odot}$, i.e. at least one order of magnitude higher than estimated from the Mg II emission line. However, the Mg II emission line and the radio luminosity are indirect tracers of the black hole mass, and a significant scatter in the respective correlations is known (Lacy et al., 2001; Trakhtenbrot and Netzer, 2012). Therefore, this discrepancy between the black hole masses derived from different tracers should not be overinterpreted.

The class of HzRGs is found to have black hole masses of up to a few $10^{10} M_{\odot}$, accreting at Eddington ratios between 0.1 and 1 (Nesvadba et al., 2011; Drouart et al., 2014). Assuming this ratio for the subsample of IFRSs, I obtained black hole masses between $10^9 M_{\odot}$ and $10^{10} M_{\odot}$ based on the radio luminosity. These numbers suggest that the black holes of IFRSs are slightly less massive than those of HzRGs.

Stellar mass estimates for IFRSs

In the following paper, the software EAZY (Brammer et al., 2008) was used to measure photometric redshifts for those eleven IFRSs which have optical counterparts in SDSS DR9. Based on these photometric redshifts and using the SED templates of the best fit, stellar masses can be obtained. To gain new insights into the class of IFRSs, I used this EAZY feature and estimated stellar masses for nine of these eleven IFRSs. The photometric redshift fit failed for one IFRS as discussed in the paper below, and the redshift uncertainty for one other IFRS was very large, preventing a reliable stellar mass estimate for these two sources. Stellar masses estimated with EAZY for the remaining nine IFRSs are in the range between $10^{10.0} M_{\odot}$ and $10^{10.9} M_{\odot}$ with a median $10^{10.7 \pm 0.1} M_{\odot}$. These numbers provide a rough idea about the masses of this class of objects. However, the optical faintness of these objects introduces significant uncertainties to the EAZY fitting and thus to the stellar masses.

The stellar masses estimated in this thesis suggest that IFRSs are massive galaxies. However, IFRSs are less massive than HzRGs which are known to be the most massive galaxies in the early universe. Seymour et al. (2007) studied their HzRG sample based on *Spitzer* data and find stellar masses of the order of $10^{11-11.5} M_{\odot}$, even at the highest redshifts $z \sim 5$. De Breuck et al. (2010) present similar results with median stellar masses of $10^{11.4} M_{\odot}$ at $z < 3$ and $10^{11.2} M_{\odot}$ at $z > 3$. Comparing the stellar masses derived for IFRSs, these sources are around half an order of magnitude less massive than HzRGs. However, this is not necessarily true for the entire population of IFRSs since stellar masses could only be estimated for those IFRSs with SDSS counterparts, i.e. for the optically brightest IFRSs.

Continuing VLBA observations of IFRSs

The paper below presents VLBA data of 57 IFRSs and suggests that IFRSs might be young AGNs, for example based on a putative correlation between redshift and compactness³. However, the analysis suffers from low-number statistics since spectroscopic or photometric redshifts could be derived for only ten IFRSs. To address this shortcoming, I proposed further VLBA observations of 74 additional IFRSs which are currently carried out in semester 15A. These observations are similar to the first VLBA project of IFRSs, but the targets were selected in a different way. In order to benefit from ancillary data, I considered only IFRSs

³Compactness is defined as ratio between milliarcsecond-scale and arcsec-scale radio flux density.

with photometric SDSS counterparts from the catalogue by Collier et al. (2014). In particular, these optical data enable to measure photometric redshifts as shown in the paper below. 74 IFRSs with a VLBA phase calibrator ($S_{2.3\text{ GHz}} > 0.2\text{ Jy}$ on a baseline of 5000 km) within 2 deg and not observed in the first VLBA project were found and constitute the target list of the VLBA project BH207. Naturally, this second sample is affected by a selection bias since the sources were required to be detected in SDSS. However, a sample unaffected by selection bias has already been studied and presented: the sample of 57 IFRSs observed in the first VLBA project, resulting in the paper presented below.

The remainder of this chapter has been published as

**Active galactic nuclei cores in infrared-faint radio sources:
Very long baseline interferometry observations
using the Very Long Baseline Array**

A. Herzog, E. Middelberg, R. P. Norris, L. R. Spitler, A. T. Deller, J. D. Collier,
and Q. A. Parker

Astronomy & Astrophysics, 578, A67 (2015).

The paper presents the most comprehensive project to test the hypothesis that IFRSs contain AGNs. Based on VLBI observations of 57 IFRSs using the VLBA, compact emission has been detected for the majority of IFRSs, adding evidence that most—if not all—IFRSs have active compact cores. Further, IFRSs seem to be slightly more compact than ordinary AGNs of the same flux density and their ratio of milliarcsecond- to arcsec-scale flux density is correlated with redshift and anti-correlated with arcsec-scale flux density. Based on these results, it is suggested that IFRSs are young AGNs in the earliest stages of their evolution to extended radio galaxies. The paper also discusses two peculiar IFRSs that were found to be composed of two compact components.

I was responsible for leading the work presented in the following manuscript. I proposed the observations with the VLBA and was awarded the proposed 110 hours of filler time. I then scheduled the observations based on `sched`⁴, a program to schedule VLBI observations. 57 of the 110 awarded hours were carried out, forming the basis for the paper below. Further, I calibrated and imaged the data. For this purpose, I wrote scripts in `ParselTongue` (Kettenis et al., 2006)—the python implementation of the Astronomical Image and Processing System⁵ (AIPS)—to automatise these steps. I used components from template scripts provided by E. Middelberg and A. T. Deller, but built my own script. I then measured flux densities from the maps, cross-matched the observed sample of IFRSs with SDSS DR10, and measured photometric redshifts using `EAZY` (Brammer et al., 2008) for those IFRSs with photometric detections. I carried out the entire analysis presented in the paper below and wrote the manuscript. E. Middelberg, R. P. Norris, and L. R. Spitler supervised the work and provided continuous feedback and discussion. E. Middelberg and A. T. Deller provided helpful discussions with respect to the data calibration and imaging. J. D. Collier provided unpublished ancillary data for the IFRSs sample. All co-authors contributed by commenting on the manuscript. My contribution to the work presented in this manuscript is 95%.

Credit: Herzog et al., *A&A*, 578, A67, 2015, reproduced with permission © ESO.

⁴<http://www.aoc.nrao.edu/software/sched/>

⁵<http://www.aips.nrao.edu/>

Active galactic nuclei cores in infrared-faint radio sources

Very long baseline interferometry observations using the Very Long Baseline Array

A. Herzog^{1,2,3}, E. Middelberg¹, R. P. Norris³, L. R. Spitler^{2,4}, A. T. Deller⁵, J. D. Collier^{6,3}, and Q. A. Parker^{2,4}

¹ Astronomisches Institut, Ruhr-Universität Bochum, Universitätsstr. 150, 44801 Bochum, Germany
e-mail: herzog@astro.rub.de

² Macquarie University, Sydney, NSW 2109, Australia

³ CSIRO Astronomy and Space Science, Marsfield, PO Box 76, Epping, NSW 1710, Australia

⁴ Australian Astronomical Observatory, PO Box 915, North Ryde, NSW 1670, Australia

⁵ The Netherlands Institute for Radio Astronomy (ASTRON), Postbus 2, 7990 AA Dwingeloo, The Netherlands

⁶ University of Western Sydney, Locked Bag 1797, Penrith, NSW 2751, Australia

Received 2 March 2015 / Accepted 31 March 2015

ABSTRACT

Context. Infrared-faint radio sources (IFRS) form a new class of galaxies characterised by radio flux densities between tenths and tens of mJy and faint or absent infrared counterparts. It has been suggested that these objects are radio-loud active galactic nuclei (AGNs) at significant redshifts ($z \gtrsim 2$).

Aims. Whereas the high redshifts of IFRS have been recently confirmed based on spectroscopic data, the evidence for the presence of AGNs in IFRS is mainly indirect. So far, only two AGNs have been unquestionably confirmed in IFRS based on very long baseline interferometry (VLBI) observations. In this work, we test the hypothesis that IFRS contain AGNs in a large sample of sources using VLBI.

Methods. We observed 57 IFRS with the Very Long Baseline Array (VLBA) down to a detection sensitivity in the sub-mJy regime and detected compact cores in 35 sources.

Results. Our VLBA detections increase the number of VLBI-detected IFRS from 2 to 37 and provide strong evidence that most – if not all – IFRS contain AGNs. We find that IFRS have a marginally higher VLBI detection fraction than randomly selected sources with mJy flux densities at arcsec-scales. Moreover, our data provide a positive correlation between compactness – defined as the ratio of milliarcsec- to arcsec-scale flux density – and redshift for IFRS, but suggest a decreasing mean compactness with increasing arcsec-scale radio flux density. Based on these findings, we suggest that IFRS tend to contain young AGNs whose jets have not formed yet or have not expanded, equivalent to very compact objects. We found two IFRS that are resolved into two components. The two components are spatially separated by a few hundred milliarcseconds in both cases. They might be components of one AGN, a binary black hole, or the result of gravitational lensing.

Key words. techniques: interferometric – galaxies: active – galaxies: high-redshift – galaxies: nuclei – radio continuum: galaxies

1. Introduction

One of the most controversially discussed topics in current astrophysics is the question of how active galactic nuclei (AGNs) influence star forming activity in their host galaxies. This interaction is known as feedback, and both negative and positive feedback of the AGN have been proposed.

Negative AGN feedback is thought to be caused by the AGN heating or disrupting the surrounding gas and, by this, quenching star formation. This scenario consists of two consecutive phases and may be caused by a merger of two galaxies. In the first phase, which is called cold mode (or quasar mode; e.g. Kauffmann et al. 2003; Croton et al. 2006; Hardcastle et al. 2007), cold gas from the galaxies involved in the merger fuels the accretion accompanied by high star forming activity. Finally, the AGN heats or blows away the remaining gas and star formation ends. This represents the transition to the second phase, the so-called hot mode accretion (also known as radio mode; e.g. Narayan & Yi 1995). In this phase, the supermassive black hole (SMBH) can only accrete hot gas from the halo in so-called advection dominated accretion flows.

The accretion in the cold mode phase is radiatively efficient and observational evidence is difficult because of the highly obscured nucleus. In contrast, accretion in the hot mode phase is typically well below the Eddington limit and the accretion flow radiatively inefficient. In hot mode, AGN feedback is kinetic and the total energy output usually dominated by the mechanical power of the radio jets. Radio jets are associated with both accretion modes and the radio emission can be used to trace the mechanical jet power (e.g. Alexander & Hickox 2012 and references therein).

This scenario of negative AGN feedback is an important ingredient for the current preferred cosmological Λ cold dark matter (Λ CDM) model. In this model, negative AGN feedback is needed to make the number of massive and luminous galaxies in simulations consistent with the observed number (Springel et al. 2005; Croton et al. 2006).

Contrary to this widely accepted negative AGN feedback, examples have been found where AGN activity enhances star formation, i.e. showing a positive feedback (e.g. Klammer et al. 2004; Gaibler et al. 2012; Zinn et al. 2013; Karouzos et al. 2014). These observations are explained by the AGN jets propagating

through the gas of the host galaxy, generating shocks that trigger the gravitational collapse of the gas and, by this, boost star formation.

One important class of object in studying AGN feedback processes is the class of high-redshift radio galaxies (HzRGs) since these galaxies can be observed out to high redshifts. HzRGs are very powerful radio-galaxies that contain significant emission both from a starburst activity and AGN activity. They are expected to be the progenitors of the most massive galaxies in the local universe (e.g. Seymour et al. 2007; De Breuck et al. 2010). Only around 200 of these objects – which are defined by $z > 1$ and $L_{3\text{GHz}} > 10^{26} \text{ W Hz}^{-1}$ – are known in the entire sky. However, a new class of object has recently been found that suggests a link to HzRGs: the class of infrared-faint radio sources.

1.1. Discovery and definition of infrared-faint radio sources

Infrared-faint radio sources (IFRS) are characterised by radio emission of the order of tenths to tens of mJy and associated deep near-infrared faintness. Norris et al. (2006) and Middelberg et al. (2008a) discovered these objects in the deep radio maps of the Australia Telescope Large Area Survey (ATLAS) in the *Chandra* Deep Field South (CDFs) and the European Large Area IR space observatory Survey South 1 (ELAIS-S1) as lacking infrared (IR) counterparts in the co-located *Spitzer* Wide-area Infrared Extragalactic Survey (SWIRE; Lonsdale et al. 2003). Zinn et al. (2011) defined two survey-independent criteria for the selection of IFRS:

- (i) $S_{1.4\text{GHz}}/S_{3.6\mu\text{m}} > 500$ and
- (ii) $S_{3.6\mu\text{m}} < 30 \mu\text{Jy}$.

The high radio-to-IR flux density ratios, ensured by the first criterion, show that IFRS are clear outliers from the radio-to-IR correlation. The second criterion is equivalent to a distance selection and prevents ordinary objects at $z \lesssim 1.4$ from being included in this class of object.

Based on the two selection criteria, Zinn et al. (2011) compiled a catalogue of 55 IFRS in the deep fields of the CDFs, ELAIS-S1, *Spitzer* extragalactic First Look Survey (xFLS), and the Cosmological Evolution Survey (COSMOS), based on the work by Norris et al. (2006), Middelberg et al. (2008a), and Garn & Alexander (2008). Later, IFRS were also found in the European Large Area IR space observatory Survey North 1 (ELAIS-N1) field by Banfield et al. (2011) and in the Lockman Hole field by Maini et al. (2013). Around 100 IFRS have been found in these deep fields, covering a total area of around 35 deg^2 .

Recently, Collier et al. (2014), for the first time, used a different approach and looked for IFRS in much shallower radio and IR data, which covered a much larger area compared to the deep fields mentioned above. Collier et al. used data from the Unified Radio Catalogue (URC; Kimball & Ivezić 2008; Kimball & Ivezić 2014) and from the all-sky Wide-Field IR Survey Explorer (WISE; Wright et al. 2010). Based on these data, Collier et al. compiled a catalogue of 1317 IFRS, all of them fulfilling both selection criteria from Zinn et al. (2011).

1.2. The properties of IFRS

Since the first detection of IFRS by Norris et al. (2006) it has been suggested that IFRS are radio-loud AGNs at significant redshifts ($z \gtrsim 2$). Different studies found evidence for this suggestion. Norris et al. (2007) and Middelberg et al. (2008b) presented very long baseline interferometry (VLBI) observations

of IFRS and detected compact cores in two IFRS. Norris et al. used the Australian Long Baseline Array (LBA) and targeted two IFRS from the CDFs, out of which one was detected, showing a total VLBI flux density of 5.0 mJy at 1.6 GHz. The source was unresolved on VLBI scales and its size measured to be less than $0.03''$, corresponding to less than 260 pc at any redshift. Middelberg et al. also used the LBA and observed four IFRS from the ELAIS-S1 field at 1.6 GHz or 1.4 GHz. One out of these four IFRS was detected with a VLBI flux density of 12.5 mJy at 1.6 GHz. Based on a flux density of 7 mJy on the longest baselines, Middelberg et al. measured a lower limit on the brightness temperature of $3.6 \times 10^6 \text{ K}$. Three IFRS were included in the sample observed with the Very Long Baseline Array (VLBA) in the CDFs by Middelberg et al. (2011a); however, they remained undetected. The two VLBI detections of IFRS showed that at least a fraction of IFRS contain AGNs.

Garn & Alexander (2008) and Huynh et al. (2010) found that obscured star forming galaxies cannot reproduce the characteristics of IFRS because IFRS clearly deviate from the radio-IR correlation, providing another hint for the AGN content in IFRS. Furthermore, Garn & Alexander and Huynh et al. presented the first spectral energy distribution (SED) modelling of IFRS and showed that 3C sources like 3C 273 are in agreement with the characteristics of IFRS if these sources are at redshifts $z \gtrsim 2$. Herzog et al. (2014) showed that the SED of their sample of IFRS can only be explained by radio-loud AGN templates.

A potential link between IFRS and HzRGs was first suggested by Huynh et al. (2010) based on the similarly high radio-to-IR flux density ratios. Middelberg et al. (2011b) showed that IFRS have steeper radio spectra¹ (median spectral index $\alpha = -1.4$) than the general radio source population ($\alpha = -0.86$) and the AGN source population ($\alpha = -0.82$), using data in the ELAIS-S1 field between 2.3 GHz and 8.4 GHz. Moreover, Middelberg et al. found that the radio spectrum of IFRS is even steeper than that of HzRGs ($\alpha = -1.02$). Norris et al. (2011) pointed out that HzRGs are the only objects known at high redshifts that share the extreme radio-to-IR flux density ratios with IFRS. Based on this similarity and the deep IR faintness of IFRS, Norris et al. suggested that IFRS might follow the correlation between $3.6 \mu\text{m}$ flux density and redshift found for HzRGs (Seymour et al. 2007), similar to the $K - z$ relation (Willott et al. 2003). Herzog et al. (2015) showed that the non-detection of IFRS in deep far-IR *Herschel* observations can only be explained by SED templates of HzRGs.

Collier et al. (2014) and Herzog et al. (2014) presented the first spectroscopic redshifts of IFRS and found all of 22 but one – which is most likely a misidentification or a star forming galaxy with an AGN – redshifts in the range $1.7 \leq z \leq 3.0$, confirming the suggested high-redshift nature of IFRS. Furthermore, both studies found their data in agreement with the suggested correlation between near-IR flux density and redshift, indicating that most IFRS in deep fields – which were summarised by Zinn et al. (2011) and Maini et al. (2013) – might be at even higher redshifts.

1.3. Populations of IFRS found in deep and shallow surveys

Here, we consider the relationship between IFRS found in deep surveys of small area and those found in shallow all-sky surveys. First, all IFRS found in the various works mentioned above fulfil the – in some cases slightly changed – selection criteria by Zinn et al. (2011) and therefore qualify as IFRS. Maini et al. (2013)

¹ The spectral index is defined as $S \propto \nu^\alpha$.

lowered the radio-to-IR flux density criterion and replaced the IR flux density criterion by an extension criterion. Others – like Norris et al. (2007) and Middelberg et al. (2008a) – required IFRS to be undetected at $3.6\ \mu\text{m}$ without applying a radio-to-IR flux density criterion. Nevertheless, these IFRS, which were selected based on slightly different criteria, are close to fulfil the criteria by Zinn et al.

While the IFRS in deep fields usually have 1.4 GHz flux densities of tenths of mJy to a few mJy, the IFRS in the all-sky survey have median radio flux densities of several tens of mJy, some reaching even several hundred mJy. Similarly, each IFRS in the sample from Collier et al. (2014) provides an IR counterpart at $3.4\ \mu\text{m}$ with a mean flux density of around $25\ \mu\text{Jy}$, while a significant fraction of IFRS in deep fields has no IR counterpart in the even deeper $3.6\ \mu\text{m}$ data. Thus, the median IFRS in deep fields is both radio and IR-fainter than the median IFRS in the shallower all-sky sample from Collier et al.

All spectroscopic redshifts of IFRS from both the deep fields and the shallow survey were found to be in the same redshift range $1.7 \lesssim z \lesssim 3.0$. However, a selection effect putatively biases the observed spectroscopic redshift distribution of IFRS in the deep fields since the IFRS with known spectroscopic redshifts in these fields are the optically and IR brightest IFRS in that sample. Since their optical, IR, and radio properties are similar to those of the all-sky IFRS, it is expected that these IFRS represent the overlap between the fainter IFRS population in deep fields and the brighter all-sky IFRS population (Herzog et al. 2014).

It has been suggested by Collier et al. (2014) that their IFRS sample consists of the lowest-redshift IFRS while the IFRS found in deep fields are on average at higher redshifts. This suggestion is in agreement with the correlation between $3.6\ \mu\text{m}$ flux density and redshift discussed by Norris et al. (2011), Collier et al., and Herzog et al. (2014). The overlapping spectroscopic redshifts found for both subsets are in agreement with this suggested unification, too.

Collier et al. (2014) could only set a lower limit of $\sim 0.1\ \text{deg}^{-2}$ for the sky density of IFRS with $S_{1.4\text{GHz}} \geq 7.5\ \text{mJy}$ because of the non-uniform sensitivity of the WISE survey. In contrast, the sky density of IFRS in deep fields is of the order of a few per square degree and might reach $30\ \text{deg}^{-2}$ (Zinn et al. 2011).

In this paper, we test the AGN content in IFRS based on VLBI observations with the VLBA of a large number of sources taken from the all-sky catalogue of IFRS (Collier et al. 2014). In Sect. 2, we describe our sample and the observing strategy. We discuss data calibration, imaging, flux measuring, and redshifts in Sect. 3. We analyse our data in Sect. 4 with respect to detection fraction (Sect. 4.1), compactness (Sect. 4.2), and individual sources (Sect. 4.3). We discuss the implications of our analysis in Sect. 5, and present our conclusions in Sect. 6. Throughout this paper, we use flat ΛCDM cosmological parameters $\Omega_\Lambda = 0.7$, $\Omega_M = 0.3$, $H_0 = 70\ \text{km s}^{-1}\ \text{Mpc}^{-1}$ and the calculator by Wright (2006). We quote 1σ confidence intervals of binomial population proportions based on the Bayesian approach, following Cameron (2011).

2. Sample and observations

We selected all IFRS from the catalogue from Collier et al. (2014) which were located within 1 deg of a VLBA calibrator. This low angular separation between source and calibrator ensured the phase coherence required for VLBI observations. Since 1.4 GHz VLBI observations of the calibrators were not available, we required the calibrators to have a 2.3 GHz flux density of at

least 0.2 Jy on a baseline of 5000 km. Out of the 1317 IFRS presented by Collier et al., 110 were found to provide a calibrator which fulfills the given conditions.

A VLBI detection provides unambiguous evidence for an AGN because compact radio emission in AGNs is a non-thermal process and results in brightness temperatures of more than $10^6\ \text{K}$ to which our observations are sensitive. In contrast, compact radio emission in starburst galaxies, which is usually dominated by thermal free-free emission, is represented by brightness temperatures of around $10^4\ \text{K}$ (e.g. Condon et al. 1991). Although brightness temperatures of $10^6\ \text{K}$ can also be produced by very luminous radio supernovae (SNe; Huang et al. 1994; Smith et al. 1998), Kewley et al. (2000) showed that the probability for a VLBI-detected radio SN in a galaxy sample is very low. Therefore, a VLBI detection provides strong evidence for an AGN. However, it should be noted that the reverse is not true, i.e. the non-detection of a source in a VLBI observation does not imply the non-existence of an AGN. Instead, a VLBI non-detection implies significant extended emission compared to the compact core. The ratio of extended emission to core emission depends on beaming which can boost or suppress the compact core emission, AGN age, and the surrounding medium, affecting the brightness and extent of the diffuse radio lobes.

Since this is a detection experiment, the uv coverage is not critically important and a minimum number of six out of ten VLBA antennas was requested. Since the individual observations were short and independent of the weather conditions because of the observing frequency of 1.4 GHz, the observations were scheduled in filler time. Although the maps resulting from the data will be of rather poor quality, they will unambiguously resolve potential compact components.

Out of 110 proposed objects, 57 IFRS were observed in semester 14A in project BH197. The 57 observed IFRS were randomly selected based on the IFRS positions and available filler time at the VLBA. These observed sources have 1.4 GHz integrated flux densities between 11 mJy and 183 mJy in the NRAO VLA Sky Survey (NVSS; Condon et al. 1998). The VLBA observations were set to a bandwidth of 32 MHz in each of the eight basebands which were observed in dual polarisation at 1.4 GHz, resulting in a total data rate of 2048 Mbps.

Each of the 57 epochs had a total observing time of one hour. We decided to use two different approaches for the scan settings, depending on the distance between source and calibrator. If the separation between source and calibrator was less than $25'$, we continuously pointed at the position in between IFRS and calibrator to prevent unnecessary nodding between the two sources. If the separation was more than $25'$, we alternately observed the calibrator for 60 s and the source for 225 s, starting and ending with a scan on the calibrator. The resulting observing time on the IFRS was around 45 min. The data were correlated using the VLBA Distributed FX (DiFX) software correlator (Deller et al. 2007, 2011).

3. VLBA data calibration, optical properties, and redshifts

3.1. Data calibration, imaging, and flux measurement of the VLBA data

Calibration and imaging of the individual epochs was carried out based on a ParseITongue script. ParseITongue (Kettenis et al. 2006) is a Python-based interface to the Astronomical Image

and Processing System² (AIPS). The calibration and imaging strategy used here is very similar to the procedure described by Deller & Middelberg (2014). However, we calibrated the amplitudes using the technique suggested by VLBA Scientific Memo #37 (R. Craig Walker; Dec. 15, 2014).

In the pipeline, we loaded the data into AIPS and applied a priori flags and manual flags. We then corrected for ionospheric effects using the task TECOR, applied the latest earth orientation parameters, and corrected for parallactic angles, in the latter cases using the task CLCOR. Amplitudes were calibrated based on autocorrelation data using the task ACCOR. We corrected for primary beam effects using the task CLVLB, following the procedure outlined by Middelberg et al. (2013). Delay correction was carried out based on the calibrator, using the task FRING and a solution interval of 2 min. We applied a bandpass correction using the task BPASS. The new task ACSCL, implemented in AIPS in consequence of the flux density calibration errors described in the VLBA Scientific Memo #37, kept the calibrated autocorrelation values at unity. The flux density calibration was completed by using APCAL, calibrating the amplitudes based on system temperatures and gains. We used the AIPS/ParseITongue implementation of Pieflag (Middelberg 2006), *dynspec-flagger*, to automatically flag data affected by interference. Using the task CALIB, we performed one iteration of phase and amplitude self-calibration on the calibrator and applied the solution on the target. Finally, we imaged the UV data based on the task IMAGR into a map of 2048×2048 pixels with a pixel size of 1 milliarcsecond (mas) – matching the angular resolution of ~5 mas – using uniform weighting. In this step, we cleaned the dirty image in a given box, down to a flux of three times the root mean square (rms) or up to 500 iterations.

The mean synthesised beam size in our observations is $14.3 \times 4.7 \text{ mas}^2$. Because the linear scale is limited in a Λ CDM cosmology at redshifts $0.5 \leq z \leq 12$ between $4 \text{ kpc}''$ and $8.5 \text{ kpc}''$, we were able to convert this beam size over this redshift range to an area of between $57 \text{ pc} \times 19 \text{ pc}$ and $122 \text{ pc} \times 40 \text{ pc}$. The rms in the final maps is around $60 \mu\text{Jy beam}^{-1}$, depending on the number of antennas. Of the 57 observations, 31, 21, 4, and 1 were carried out with 10, 9, 8, and 7 antennas, respectively. Since the longest VLBA baseline of 8611 km – between the stations Mauna Kea and St. Croix – was available in all observations, the east-west angular resolution of around 5 mas is similar for all 57 observations, whereas the north-south angular resolution varies slightly because of changing antenna availability. As an example, Fig. 1 shows the final map of IFRS F0398.

We measured the flux density of each component using the AIPS task JMFIT, setting a box of size of 40 pixels around the components. For a few sources, image artefacts resulted in unreasonable fluxes. In these cases, we manually measured flux densities using the task TVSTAT. Checks on control sources resulted in consistent flux measurements based on TVSTAT and JMFIT. For the brighter component in IFRS F0030, we measured the flux density using the *blobcat* package (Hales et al. 2012) because of the complex structure of this source. Following Deller & Middelberg (2014), we set a 6.75σ detection limit for all sources, corresponding to a mean detection sensitivity of around $450 \mu\text{Jy beam}^{-1}$. Most of our sources are slightly resolved, but insufficiently resolved to determine the morphology. The resulting flux densities and flux density upper limits are summarised in Table 1. Since observations and data calibration are very similar to the approach taken by Deller & Middelberg who targeted more than 20 000 sources in their mJy Imaging VLBA

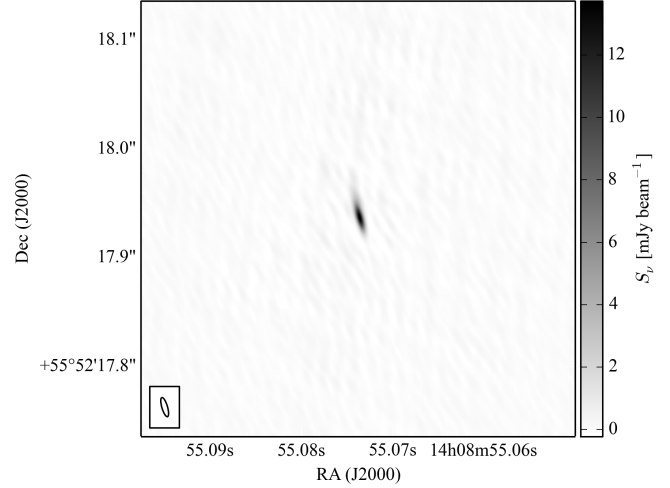


Fig. 1. VLBA map of IFRS F0398. The source is slightly resolved with a peak flux density of $13.7 \text{ mJy beam}^{-1}$ and an integrated flux density of 17.2 mJy .

Exploration (mJIVE) survey, we expect our flux densities to be of similar accuracy of 20%.

3.2. Optical properties and redshifts

Our sample was taken from the all-sky IFRS catalogue from Collier et al. (2014) who cross-matched their sources with the Sloan Digital Sky Survey (SDSS) DR9 (Ahn et al. 2012). For the purpose of this work, we cross-matched our sample of VLBA-observed IFRS to the recent SDSS DR10 (Ahn et al. 2014). $53 (93^{+2}_{-5}\%)$ out of our IFRS are covered by SDSS DR10. Eleven ($21^{+7}_{-4}\%$) out of these 53 IFRS provide photometric counterparts which are all close to the sensitivity limit of SDSS.

We used the software *EAZY* (Brammer et al. 2008) with the standard template set to derive photometric redshifts for our sources. Since most IFRS in the catalogue from Collier et al. (2014) are only detected in the WISE bands W1 ($3.4 \mu\text{m}$) and W2 ($4.6 \mu\text{m}$) – apart from the radio detections which are not used in the redshift fitting – measuring photometric redshifts is impossible for most of the IFRS in our sample. However, measuring photometric redshifts is possible for those IFRS with SDSS counterparts. For these eleven IFRS in our sample with SDSS counterparts, we obtained ten photometric redshifts using *EAZY*. As examples, we show the resulting fits for IFRS F0197 and F0273 in Fig. 2. The fitting of IFRS F0277 failed. Table 2 summarises the photometric redshifts and – where applicable – spectroscopic redshifts for our subsample of IFRS with SDSS DR10 counterparts. Figure 3 shows the photometric redshifts as a function of the spectroscopic redshifts for the three IFRS in our sample for which SDSS DR10 provides spectroscopic redshifts.

Based on the SEDs resulting from the fitting of photometric redshifts, we find that most of our fitted IFRS are very blue. These characteristics can be explained by a Type I AGN in the optical. However, we stress that we might be significantly affected by selection bias since these IFRS are very close to the detection sensitivity of SDSS and SDSS is more sensitive to blue objects. Nevertheless, this study shows that at least some IFRS are very blue, non-dusty galaxies.

² <http://www.aips.nrao.edu/>

Table 1. Component catalogue of 57 IFRS observed with the VLBA.

Identifier	NVSS ID	RA _{FIRST} J2000.0	Dec _{FIRST} J2000.0	$S_{\text{NVSS,peak}}$ [mJy beam ⁻¹]	$S_{\text{NVSS,int}}$ [mJy]	$S_{\text{VLBA,peak}}$ [mJy beam ⁻¹]	$S_{\text{VLBA,int}}$ [mJy]	S/N	$\Theta_{\text{maj}} \times \Theta_{\text{min}}$ [mas × mas]
F0013	NVSS J014418-092158	01:44:18.196	-09:21:54.77	13.3	13.3	<0.3	–	–	–
F0030_1	NVSS J021557-082517	02:15:57.080	-08:25:17.55	70.7	75.6	4.1	21.8	54.9	14.0 × 4.4
F0030_2	NVSS J021557-082517	02:15:57.080	-08:25:17.55	70.7	75.6	3.5	6.0	45.7	14.0 × 4.4
F0037	NVSS J022022-011017	02:20:22.049	-01:10:16.49	30.0	30.6	1.3	4.8	27.9	13.4 × 4.6
F0052	NVSS J023033-030909	02:30:33.435	-03:09:08.37	49.7	50.5	<0.6	–	–	–
F0072	NVSS J024150-032011	02:41:50.196	-03:20:12.17	19.2	19.2	6.5	11.1	64.4	13.7 × 4.7
F0076	NVSS J024346-050737	02:43:46.908	-05:07:36.51	42.1	43.3	5.5	21.2	74.8	20.7 × 4.7
F0081	NVSS J024700+062831	02:47:00.457	+06:28:34.34	28.7	29.3	<0.3	–	–	–
F0100	NVSS J090337+515142	09:03:37.302	+51:51:42.90	19.7	19.7	10.3	11.2	263.8	14.0 × 4.2
F0106	NVSS J093243+521400	09:32:43.626	+52:13:59.53	13.0	13.3	0.7	1.1	17.4	13.7 × 4.8
F0127	NVSS J104946+531947	10:49:46.291	+53:19:50.81	10.9	15.5	<0.4	–	–	–
F0146	NVSS J112624+375323	11:26:23.726	+37:53:34.75	8.4	16.1	3.6	3.9	74.8	12.4 × 6.0
F0149	NVSS J113330+585506	11:33:29.982	+58:55:05.01	39.4	39.6	24.0	29.3	93.3	16.8 × 4.6
F0154	NVSS J114333+582209	11:43:33.395	+58:22:07.59	15.7	16.5	3.7	7.1	83.6	13.2 × 4.5
F0167	NVSS J115544+495437	11:55:44.856	+49:54:36.55	53.8	54.2	<0.4	–	–	–
F0169	NVSS J115900+474005	11:59:00.500	+47:40:05.26	17.5	17.7	<0.2	–	–	–
F0173	NVSS J120221+482514	12:02:21.184	+48:25:13.80	58.4	59.9	26.4	40.4	248.7	19.8 × 4.7
F0187	NVSS J121731+485954	12:17:31.830	+48:59:53.73	43.9	44.1	<0.4	–	–	–
F0189	NVSS J121814+590516	12:18:14.097	+59:05:16.16	26.9	27.1	0.7	1.0	15.2	15.8 × 4.1
F0194	NVSS J122524+433439	12:25:24.786	+43:34:38.92	25.7	25.7	<0.3	–	–	–
F0197	NVSS J122743+364252	12:27:43.502	+36:42:55.83	23.8	24.1	<0.3	–	–	–
F0209	NVSS J123952+604958	12:39:52.632	+60:49:55.77	18.9	19.5	3.0	7.1	71.2	14.3 × 6.1
F0222	NVSS J125148-064218	12:51:48.680	-06:42:17.01	11.6	23.9	<0.3	–	–	–
F0241	NVSS J130316+481558	13:03:16.442	+48:15:57.70	13.8	13.9	6.9	8.1	137.8	12.8 × 5.7
F0244	NVSS J130748+555452	13:07:48.324	+55:54:50.53	14.2	14.5	1.0	1.3	22.4	13.8 × 5.0
F0251	NVSS J131322+322105	13:13:22.589	+32:21:10.13	36.1	37.6	<0.4	–	–	–
F0257_1	NVSS J131551+512710	13:15:51.150	+51:27:10.01	36.0	36.7	2.5	5.7	77.3	14.2 × 4.4
F0257_2	NVSS J131551+512710	13:15:51.150	+51:27:10.01	36.0	36.7	1.2	2.1	35.9	14.2 × 4.4
F0273	NVSS J132804+431418	13:28:04.382	+43:14:17.27	18.1	18.5	2.2	2.3	39.3	12.7 × 4.2
F0277	NVSS J133024+221800	13:30:24.695	+22:18:00.36	177.0	179.6	7.8	20.3	104.4	12.3 × 4.8
F0283	NVSS J133431+543930	13:34:31.807	+54:39:32.23	13.5	14.4	<0.3	–	–	–
F0293	NVSS J133733+591837	13:37:33.098	+59:18:37.68	44.7	45.4	13.6	21.2	214.3	18.3 × 4.1

Notes. Listed is the identifier, the NVSS ID, the FIRST position, the NVSS peak and integrated flux densities, the VLBA peak flux density and integrated flux density, the VLBA S/N, and the VLBA beam size. If a source is found to be composed of several components in the VLBA observations, we list the components individually. In case of a non-detection, we quote a 6.75σ peak flux density upper limit. The identifier follows the numbering by [Collier et al. \(2014\)](#). NVSS and FIRST data are taken from [Collier et al.](#)

Table 1. continued.

Identifier	NVSS ID	RA _{FIRST} J2000.0	Dec _{FIRST} J2000.0	$S_{\text{NVSS, peak}}$ [mJy beam ⁻¹]	$S_{\text{NVSS, int}}$ [mJy]	$S_{\text{VLBA, peak}}$ [mJy beam ⁻¹]	$S_{\text{VLBA, int}}$ [mJy]	S/N	$\Theta_{\text{maj}} \times \Theta_{\text{min}}$ [mas × mas]
F0319	NVSS J134921+081217	13:49:21.396	+08:12:15.75	27.2	27.9	<0.4	—	—	—
F0334	NVSS J135248+093020	13:52:48.328	+09:30:16.60	16.9	17.4	<0.4	—	—	—
F0351	NVSS J135601-012539	13:56:01.445	-01:25:38.70	34.9	35.3	3.0	4.2	51.0	13.0 × 4.7
F0382	NVSS J140707+285558	14:07:07.241	+28:55:56.39	66.7	68.8	<0.3	—	—	—
F0385	NVSS J140730+040234	14:07:30.593	+04:02:34.61	16.3	16.5	3.1	4.8	55.8	18.1 × 4.2
F0398	NVSS J140855+555218	14:08:54.995	+55:52:17.62	62.4	62.9	13.7	17.2	184.1	18.1 × 5.2
F0406	NVSS J141004+024051	14:10:04.764	+02:40:49.82	30.0	32.9	19.3	21.9	219.2	13.6 × 4.7
F0471	NVSS J142228+264716	14:22:28.909	+26:47:16.63	19.8	19.8	5.1	5.0	136.9	12.5 × 4.8
F0472	NVSS J142241+363956	14:22:41.669	+36:39:57.74	17.1	18.2	0.7	0.6	14.2	13.4 × 4.5
F0509	NVSS J143110+360317	14:31:10.868	+36:03:17.05	16.3	18.3	<0.2	—	—	—
F0588	NVSS J144500+624605	14:45:00.769	+62:46:05.55	16.7	17.2	<0.4	—	—	—
F0611	NVSS J144924+085628	14:49:24.799	+08:56:32.59	36.1	36.8	<0.4	—	—	—
F0633	NVSS J145334-014513	14:53:34.184	-01:45:13.48	18.0	18.1	0.4	2.6	9.5	13.0 × 4.9
F0726	NVSS J150623+103048	15:06:23.301	+10:30:47.54	49.0	50.0	20.8	32.0	317.8	12.4 × 4.3
F0732	NVSS J150649+422059	15:06:49.247	+42:20:59.02	101.8	103.6	9.1	25.5	167.3	13.8 × 5.1
F0787	NVSS J151557+201248	15:15:57.840	+20:12:47.13	17.5	18.0	2.6	3.2	56.6	12.8 × 4.3
F0807	NVSS J151817+042327	15:18:17.648	+04:23:26.84	77.5	78.8	6.5	13.5	58.8	15.8 × 4.2
F0838	NVSS J152348+321541	15:23:48.347	+32:15:43.79	96.5	98.8	<0.3	—	—	—
F0912	NVSS J153826+145505	15:38:26.812	+14:55:05.91	14.7	15.1	<0.6	—	—	—
F1037	NVSS J160235+310832	16:02:35.685	+31:08:33.12	13.9	14.2	1.3	1.4	25.6	16.0 × 4.1
F1111	NVSS J161910+483709	16:19:10.025	+48:37:13.21	12.2	12.6	8.5	10.9	199.4	14.0 × 4.3
F1268	NVSS J172102+333445	17:21:02.788	+33:34:47.29	25.7	26.7	<0.3	—	—	—
F1286	NVSS J172923+390532	17:29:24.122	+39:05:31.52	11.6	11.6	<0.3	—	—	—
F1287	NVSS J173019+460128	17:30:19.022	+46:01:28.48	43.4	43.9	18.4	28.5	309.9	14.5 × 3.9
F1301	NVSS J173517+474300	17:35:17.371	+47:42:59.30	180.0	183.8	0.9	2.6	14.2	12.0 × 6.6
F1305	NVSS J173703+494446	17:37:02.943	+49:44:46.26	23.0	23.4	5.7	7.9	71.3	14.9 × 3.9
F1313	NVSS J174243+621908	17:42:43.642	+62:19:08.65	79.6	82.5	9.2	29.9	176.2	15.2 × 3.7

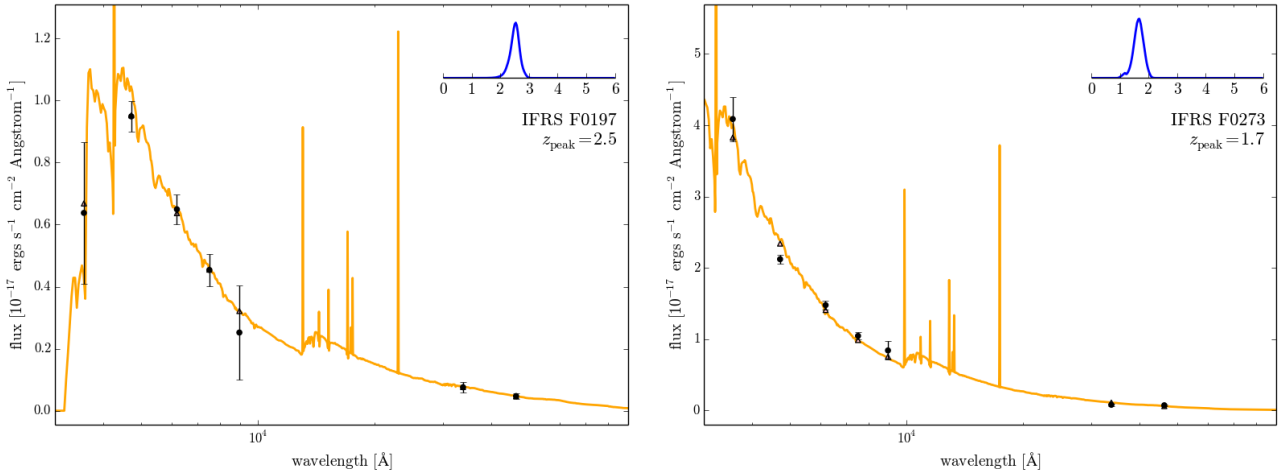


Fig. 2. Resulting photometric redshift fit from *EAZY* for IFRS F0197 (*left*) and F0273 (*right*). The SED (orange line) shows the best fit template based on the peak redshift in the observer’s frame. Black dots with error bars represent photometric data points of the IFRS, whereas black triangles show the flux density of the fitted SED at the same wavelengths. The subplots in the upper right of both plots show the redshift-probability distribution. The redshift of the peak in the probability distribution is quoted below each subplot.

Table 2. Redshift information for those IFRS with SDSS DR10 detections.

IFRS ID	u [mag]	z_{phot}	z_{spec}
F0146	20.21 ± 0.05	$1.26^{+0.29}_{-0.25}$	–
F0194	23.82 ± 0.95	$0.78^{+0.42}_{-0.34}$	–
F0197	22.83 ± 0.32	$2.54^{+0.14}_{-0.22}$	2.1150 ± 0.0014
F0273	20.84 ± 0.08	$1.65^{+0.20}_{-0.18}$	–
F0277	24.16 ± 0.86	–	–
F0293	22.94 ± 0.33	$3.02^{+0.09}_{-0.08}$	–
F0398	20.49 ± 0.06	$2.24^{+0.07}_{-0.08}$	2.55265 ± 0.00021
F0726	23.21 ± 0.52	$3.07^{+0.26}_{-0.24}$	–
F0732	22.88 ± 0.27	$2.26^{+0.27}_{-0.28}$	–
F0912	21.55 ± 0.10	$2.47^{+0.06}_{-0.06}$	2.61873 ± 0.00023
F1037	25.14 ± 0.79	$0.39^{+3.77}_{-0.08}$	–

Notes. Listed is the IFRS ID, the u -band model magnitude from SDSS DR10, the photometric redshift measured in this work using *EAZY*, and the spectroscopic redshift from SDSS DR10. The SED fitting for F0277 failed.

4. Analysis

4.1. VLBI detection fraction

In our VLBA observations, we detected 35 ($61^{+6}_{-7}\%$) out of 57 observed IFRS, showing peak flux densities between $0.4 \text{ mJy beam}^{-1}$ and $26.4 \text{ mJy beam}^{-1}$ and integrated flux densities between 0.6 mJy and 40.4 mJy as listed in Table 1.

The detection of a source in VLBI observations with brightness temperatures above 10^6 K – which is reached for our VLBA observations – is an unambiguous sign for an AGN as discussed in Sect. 2. However, we note that the reverse is not true, i.e. the non-detection of a source in VLBI observations does not exclude the existence of an AGN. The detection of 35 out of 57 IFRS in our VLBA observations provides strong evidence that most – if not all – IFRS contain AGNs.

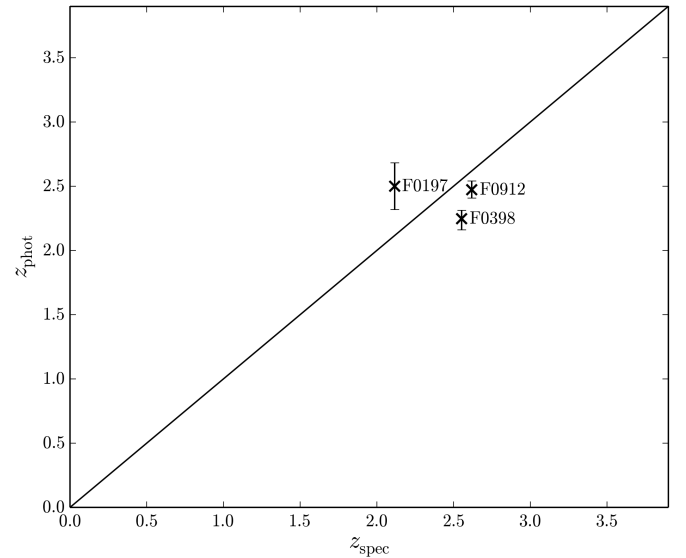


Fig. 3. Comparison of the photometric redshifts obtained from *EAZY* and the spectroscopic redshifts from SDSS DR10. The error bars show the 1σ uncertainties in the photometric redshifts as determined by *EAZY*. The solid line represents the positions of exact agreement between photometric and spectroscopic redshifts.

4.1.1. VLBI detection fraction compared to other samples

The detection fraction in our VLBA observations of $61^{+6}_{-7}\%$ down to a 6.75σ detection limit of $\sim 0.45 \text{ mJy beam}^{-1}$ is significantly higher than the detection fractions found by Garrington et al. (1999) or Deller & Middelberg (2014) who targeted large samples of sources from the Faint Images of the Radio Sky at Twenty centimetres (FIRST; Becker et al. 1995) survey in VLBI observations and detected 35% and 20%, respectively. However, the sensitivity of the respective VLBI observations and the sample selection criteria were different. Garrington et al. had a detection sensitivity between 1 mJy and 2 mJy and targeted FIRST sources with 1.4 GHz peak flux densities above 10 mJy , whereas Deller & Middelberg targeted all kinds of FIRST sources without any preselection at a varying detection sensitivity. In order

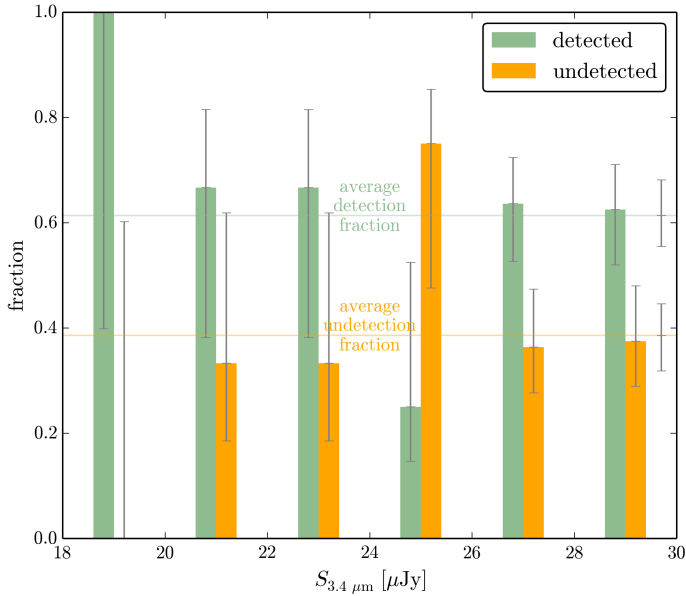


Fig. 4. Histogram of the VLBA detection and non-detection fraction, binned by the flux density at $3.4 \mu\text{m}$. The horizontal lines show the overall detection and non-detection fraction of the observations presented in this work. 1σ confidence intervals are shown in grey.

to compare their detection fraction with that of Garrington et al., Deller & Middelberg cut their catalogue to FIRST sources with $S_{1.4\text{GHz}} > 10 \text{ mJy beam}^{-1}$ and to the VLBI detection sensitivity from Garrington et al. Deller & Middelberg found a detection fraction of 36% in that subsample, in agreement with the number from Garrington et al.

We followed the approach from Deller & Middelberg (2014) and compiled a subsample of our IFRS sample by including only those sources with an arcsec-scale 1.4 GHz flux density above 10 mJy beam^{-1} , ending up with 56 IFRS. Setting our detection sensitivity to 1.5 mJy , we would have detected 25 ($45_{-6}^{+7}\%$) out of these 56 IFRS, i.e. a slightly higher fraction than those from Garrington et al. (1999) and Deller & Middelberg. Using a Fisher’s exact test (e.g. Wall & Jenkins 2012), we found a probability of 0.88 that our sample has a higher VLBI detection fraction than the sample from Deller & Middelberg.

It is known that the radio source population at 1.4 GHz with flux densities above 1 mJy consists almost exclusively of AGNs (e.g. Condon et al. 2012, Fig. 11). This implies that the VLBI-observed subsamples from Garrington et al. (1999) and Deller & Middelberg (2014) and the sample presented in this work – all cut to 10 mJy and matched to the same sensitivity as discussed above – contain virtually only AGNs. Thus, based on the numbers given above, we find a tendency of a higher VLBI detection fraction for IFRS compared to the general AGN population.

Collier et al. (2014) discarded all objects from their IFRS catalogue which provided a spurious WISE counterpart to one of the radio lobes. It is unclear whether this selection criterion can explain the higher VLBI detection fraction of IFRS compared to the general AGN population. Apart from that, the only difference in selecting the objects of the general AGN sample and the IFRS sample is the application of the IFRS selection criteria from Zinn et al. (2011) mentioned in Sect. 1.1.

Figure 4 shows the VLBA detection fraction binned in the $3.4 \mu\text{m}$ flux density for our sample of IFRS. We do not find any evidence for a dependence of the VLBI detection fraction on the

$3.4 \mu\text{m}$ flux density. We also tested the detection fraction against the arcsec-scale 1.4 GHz flux density, the radio-to-IR flux density ratio, and the WISE colour [W1-W2] and found no significant correlation.

Compact radio cores are detected in eight ($73_{-16}^{+9}\%$) of the eleven IFRS with SDSS counterpart and in 24 ($57_{-8}^{+7}\%$) of the 42 IFRS covered by SDSS without SDSS counterpart. However, we do not consider this a significant difference (a) because these two subsamples are not flux-complete; (b) because of the non-uniform sensitivity of SDSS; and (c) because SDSS is biased towards detecting blue objects as discussed above.

Three out of the eleven IFRS with SDSS counterpart are classified as “galaxy” in SDSS. We detected two ($67_{-28}^{+14}\%$) of these three galaxy-type IFRS in our VLBA observations. The other eight IFRS with SDSS counterpart are classified as “star” in SDSS. We note that this photometry-based classification is based on the extension of the object, i.e. objects classified as star are point-like, whereas extended objects are classified as galaxy. Out of these eight IFRS classified as star, we detected six ($75_{-19}^{+9}\%$) in our VLBA observations. Deller & Middelberg (2014) found a higher VLBI detection fraction for sources classified as star-like in SDSS. Our results are in agreement with this finding.

4.1.2. Dependence of the VLBI detection fraction on radio properties

Gigahertz peaked spectrum (GPS) and compact steep spectrum (CSS) sources are very compact AGNs and expected to be the earliest phases in the evolution of AGNs. GPS sources have a turnover frequency of around 1 GHz and are usually less than 1 kpc in size, whereas CSS sources are more extended with a size of a few kpc or a few tens of kpc. CSS sources are named for their steep radio spectra ($\alpha \leq -0.5$; e.g. Randall et al. 2011).

Based on data at 6 cm , 20 cm , and 92 cm , Collier et al. (2014) classified 124 of their IFRS as CSS sources and 32 as GPS sources. Out of the 57 IFRS observed with the VLBA, five IFRS were classified as CSS sources and two as GPS sources. In our VLBA observations, we detected four out of five IFRS which were classified as CSS sources and both IFRS which were classified as GPS sources so that CSS/GPS sources have a higher detection rate ($85_{-21}^{+5}\%$) than the non-classified sources ($58_{-7}^{+6}\%$).

Collier et al. (2014) used the lower-resolution data of NVSS for the flux densities in their IFRS catalogue. They also listed the number of sources in the higher-resolution FIRST survey associated with the NVSS source. IFRS detected with more than one FIRST component are clearly extended radio galaxies and not GPS or CSS sources. Out of the 57 IFRS observed with the VLBA, 47 are associated with exactly one FIRST source, while ten IFRS are associated with two or three FIRST sources. Out of these ten IFRS with two or three FIRST counterparts, we detected one ($10_{-3}^{+17}\%$) in our VLBA observations, whereas 34 ($72_{-7}^{+5}\%$) out of 47 IFRS with exactly one FIRST counterpart were detected with the VLBA. We found a statistically significantly higher VLBA detection fraction for IFRS with exactly one FIRST counterpart compared to the detection fraction of IFRS with more than one FIRST counterpart.

We also compared our VLBA detection fraction of IFRS with exactly one FIRST counterpart to the detection fraction found by Deller & Middelberg (2014) for the general radio source population. As described above, we matched the arcsec-scale radio flux density and the VLBA detection sensitivity to 10 mJy beam^{-1} and $1.5 \text{ mJy beam}^{-1}$, respectively. We found a

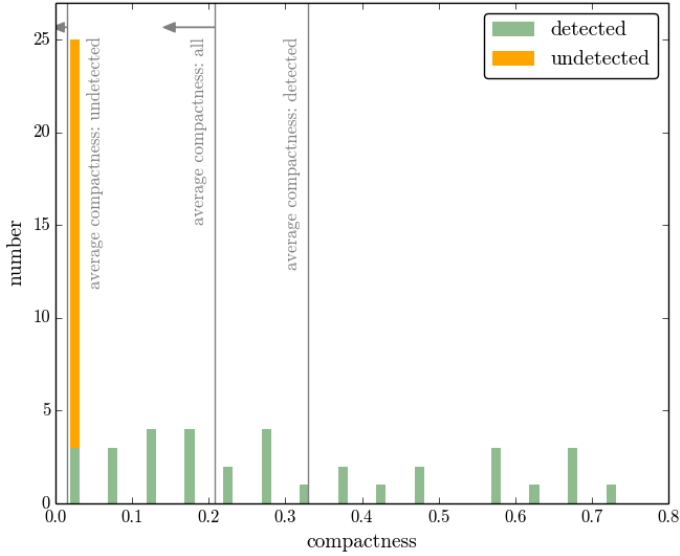


Fig. 5. Histogram of the VLBA detections and non-detections, binned in the compactness at 1.4 GHz. Compactness is defined as the ratio of mas-scale flux density to arcsec-scale flux density. The vertical lines show the mean compactness – from left to right – of all VLBA-undetected IFRS, of all VLBA-observed IFRS, and of all VLBA-detected IFRS, respectively. The former two lines represent upper limits as indicated by the horizontal arrows.

detection fraction of $54^{+7}_{-7}\%$ for those IFRS with exactly one FIRST counterpart, compared to a detection fraction of 36% for the general radio source population above 10 mJy beam^{-1} measured by Deller & Middelberg. Thus, our sample of IFRS with exactly one FIRST counterpart is statistically different to the general radio source population, based on a probability of 0.01 in a *Fisher's exact test* (e.g. Wall & Jenkins 2012) that the two samples are taken from the same parent population.

4.2. Compactness

We determined ratios of the integrated mas-scale flux density in the VLBA observations at 1.4 GHz to the integrated arcsec-scale flux density in NVSS at 1.4 GHz to fall between 0.86 and 0.014 for the IFRS detected in our VLBA observations. On average, this ratio, which we refer to as compactness, was 0.33 ± 0.23 . Figure 5 shows the number of detections binned by the compactness.

The mean compactness of our detected IFRS of 0.33 ± 0.23 is lower than that of the two former VLBI detections of IFRS where Norris et al. (2007) and Middelberg et al. (2008b) detected 88% and 58%, respectively, of the arcsec-scale flux density. This discrepancy may be due to small-number statistics or because our fluxes are measured on smaller scales than those from Norris et al. and Middelberg et al. The restoring beam of the LBA observations presented by Middelberg et al. was $51.7 \text{ mas} \times 23.6 \text{ mas}$, i.e. 17 times larger compared to the median beam of $14.3 \text{ mas} \times 4.7 \text{ mas}$ in our VLBA observations. Norris et al. did not image their *uv* data because of the poor *uv* coverage, but their angular resolution was similar to that of Middelberg et al. Therefore, a lower fraction of detected flux in our VLBA observations could be expected.

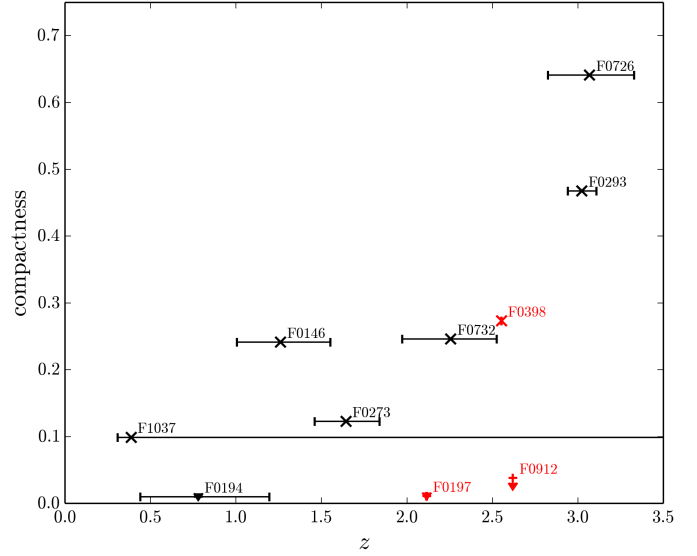


Fig. 6. Compactness as a function of redshift for those IFRS with redshift information. VLBA-detected IFRS are shown by crosses and the 6.75σ upper limits on the compactness of VLBA-undetected IFRS are shown by arrows. Three spectroscopic (red markers) and seven photometric (black markers) redshifts were used in this analysis. Note that the errors on the compactness are around 20%.

4.2.1. Dependence of the compactness on the redshift

In the following, we tested our data against a potential correlation between redshift and compactness. SDSS DR10 provides spectroscopic redshifts for three out of our 57 IFRS. Two ($z = 2.11$ and $z = 2.62$) of those are undetected and one ($z = 2.55$) is detected in the VLBA observations. However, IFRS F0912 at $z = 2.62$ was observed for only ~ 25 min with the VLBA, resulting in a sensitivity only half that of the other sources. Since the number of objects in this subsample is too low to test our data, we extended our subsample by including those IFRS with photometric redshifts presented in Sect. 3.2.

Figure 6 shows the compactness as a function of the redshift for all ten VLBA-observed IFRS with redshift information. The data do not provide compact objects at low redshifts, whereas compact objects were found at higher redshifts. The data suggest a possible correlation between compactness and redshift for IFRS. We tested the data using a *Spearman rank correlation test* (e.g. Wall & Jenkins 2012) and found a correlation coefficient between 0.66 and 0.52, indicating a positive correlation between redshift and compactness. A correlation coefficient of +1 and -1 represents an ideal correlation and anticorrelation, respectively, whereas an uncorrelated data set is represented by a coefficient of 0. In our case, the probability that the two parameters are uncorrelated is between 0.019 and 0.063. The margin arises from the unknown compactnesses of the VLBA-undetected sources for which only upper limits are known. We determined this margin using a permutation test. Based on the strong positive correlation coefficients, we suggest a correlation between compactness and redshift for our sample of IFRS. When considering only the VLBA-detected sources, we found a correlation coefficient of 0.96 and a probability of 4.5×10^{-4} that the parameters are uncorrelated. We cautiously note that the putative positive correlation seems to be mainly based on the two highest-redshift IFRS in Fig. 6 which might be outliers. Therefore, we emphasise that this suggested correlation needs further testing.

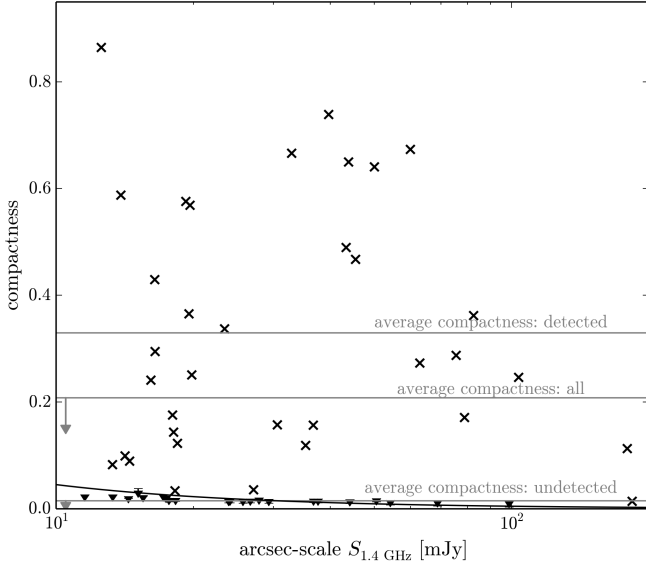


Fig. 7. Compactness as a function of the arcsec-scale 1.4 GHz flux density. VLBA-detected IFRS are shown by crosses and the 6.75σ upper limits on the compactness of VLBA-undetected IFRS are shown by black arrows. The grey horizontal lines represent – from top to bottom – the mean compactness of all VLBA-detected IFRS, of all VLBA-observed IFRS, and all VLBA-undetected IFRS, respectively. The latter ones represent upper limits as indicated by grey arrows. The black line shows the minimal detectable compactness depending on the arcsec-scale flux density, based on a mean detection sensitivity of $450 \mu\text{Jy}$ in our VLBA observations.

4.2.2. Dependence of the compactness on the 1.4 GHz flux density

Figure 7 shows the compactness as a function of the arcsec-scale 1.4 GHz flux density and includes detections and upper limits for the non-detections. We did not find compact radio-bright IFRS, whereas compact radio-faint IFRS are common in our sample. If we divide our sample at an arcsec-scale flux density of 60 mJy, we find twelve ($25_{-5}^{+7}\%$) sources with compactnesses above 0.4 and 36 ($75_{-5}^{+5}\%$) sources with compactnesses below 0.4 in the fainter subsample. At arcsec-scale flux densities above 60 mJy, we find nine ($100_{-17}\%$) sources with compactnesses below 0.4 and no ($0_{-17}\%$) source with a compactness above 0.4. This is in agreement with results from Deller & Middelberg (2014), who found a statistically significant anti-correlation between compactness and arcsec-scale 1.4 GHz flux density in their sample of randomly selected radio sources. We used a *Spearman rank correlation test* (e.g. Wall & Jenkins 2012) to test for putative correlations. However, because of the significant fraction of upper limits in this plot, we can only narrow down the correlation coefficient to a rather broad range. We found that the correlation coefficient is between 0.39 and -0.15 . Based on this test, we cannot exclude either a positive or a negative correlation or a decorrelation.

4.3. Individual sources

In the following, we discuss three individual sources which are of particular interest.

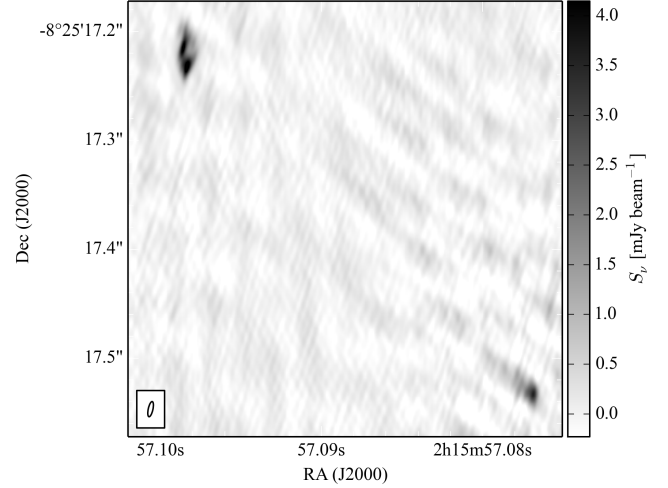


Fig. 8. VLBA map of IFRS F0030. The brighter component (upper left) has a complex morphology and a flux density of 21.8 mJy. The second component (lower right) has a flux density of 6.0 mJy and is separated by $442.1_{-0.3}^{+0.3}$ mas, corresponding to a distance between 1.7 kpc and 3.8 kpc at any reasonable redshift.

4.3.1. F0398

The only VLBA-detected IFRS with spectroscopic redshift is F0398 at $z = 2.55$, showing an arcsec-scale 1.4 GHz integrated flux density of 62.9 mJy. This corresponds to a K -corrected 1.4 GHz rest-frame luminosity of $2.3 \times 10^{27} \text{ W Hz}^{-1}$, using the radio spectral index $\alpha = -0.72$ between 20 cm and 92 cm from Collier et al. (2014). In our VLBA observations, the source – shown in Fig. 1 – is slightly resolved with a peak flux density of $13.7 \text{ mJy beam}^{-1}$ and an integrated flux density of 17.2 mJy, corresponding to a luminosity of $6.3 \times 10^{26} \text{ W Hz}^{-1}$ on scales smaller than $146 \text{ pc} \times 43 \text{ pc}$. Based on this luminosity, F0398 can be classified as Fanaroff-Riley (FR; Fanaroff & Riley 1974) Type II. The source has a compactness of 0.283.

4.3.2. F0030

A particularly interesting source is F0030 which has two spatially separated components in the VLBA map shown in Fig. 8. The first, brighter component shows a mas-scale flux density of 21.8 mJy ($S/N = 55$) and is spatially resolved with a complex morphology which is unique in our observations. The second component shows a flux density of 6.0 mJy ($S/N = 46$) and is separated by $442.1_{-0.3}^{+0.3}$ mas. The linear distance between both components is between 1.7 kpc and 3.8 kpc at any redshift in the range $0.5 \leq z \leq 12$.

In order to obtain a rough spectral index of the components, we separately imaged the four lower-frequency basebands and the four higher-frequency basebands centered at 1.380 GHz and 1.508 GHz, respectively. Fluxes were measured as described in Sect. 3.1. We obtained spectral indices of -1.2 ± 1.2 and -1.2 ± 0.6 for component 1 and 2, respectively.

4.3.3. F0257

Source F0257 – shown in Fig. 9 – consists of two individual components. While the brighter component shows a flux density of 5.7 mJy ($S/N = 77$), the weaker component is $155.5_{-0.2}^{+0.2}$ mas distant and shows less than half of the other component's flux density ($2.1 \text{ mJy beam}^{-1}$, $S/N = 36$). This angular distance

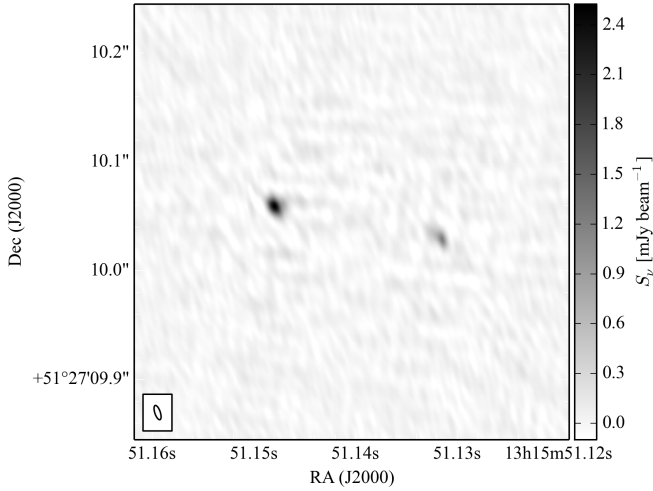


Fig. 9. VLBA map of IFRS F0257. The brighter component (left) has a flux density of 5.7 mJy. The second component (right) has a flux density of 2.1 mJy and is separated by $155.5^{+0.2}_{-0.2}$ mas, corresponding to a distance between 0.6 kpc and 1.3 kpc at any reasonable redshift.

corresponds to a linear distance between 0.6 kpc and 1.3 kpc. We measured mas-scale radio spectral indices between 1.380 GHz and 1.508 GHz of -0.3 ± 0.4 and 0.2 ± 0.9 , respectively, for component 1 and 2. Collier et al. (2014) measured an arcsec-scale radio spectral index of -0.6 between 6 cm, 20 cm, and 92 cm.

4.3.4. Could double component sources be a coincidence?

Sources F0030 and F0257 have both two compact components separated by 445 mas and 155 mas, respectively. In the following, we estimate the probability that two close by components are unrelated background sources. NVSS found 1.8 million radio sources in an area of $3 \times 10^4 \text{ deg}^2$, out of which less than 50% have compact cores detectable in VLBI observations (Deller & Middelberg 2014). This corresponds to a sky density of $1.8 \times 10^{-6} \text{ arcsec}^{-2}$. The probability of finding an additional unrelated source at a given position in an area of $0.5'' \times 0.5''$ is therefore of the order of 5×10^{-7} . Thus, we can effectively rule out any chance that the two components found both in F0030 and F0257 are physically unrelated.

5. Discussion

Our observations increase the number of VLBI-detected IFRS from 2 to 37. Based on our detection fraction of $61^{+6}_{-7}\%$ and a reasonably large sample size, we find strong evidence that most – if not all – IFRS contain AGNs. This result confirms earlier studies by e.g. Garn & Alexander (2008), Middelberg et al. (2011b), and Herzog et al. (2014), who suggested compact cores in IFRS based on SED modelling, radio-to-IR flux density ratios, and emission lines in optical spectra. With higher sensitivity, we would have most likely detected more sources in our VLBA observations.

We also tested our data for different potential correlations in Sect. 4. Although not all of them are statistically significant, in the following, we explore the astrophysical consequences if these results are confirmed by subsequent observations and describe how these hypotheses can be tested.

In Sect. 4.2.2, we found a tendency that radio-brighter IFRS are less compact. Deller & Middelberg (2014) found the same

behaviour when testing the general AGN population and argued that this anti-correlation might be explained by Doppler boosting effects as presented by Mullin et al. (2008). Mullin et al. studied a complete sample of narrow-line and broad-line radio galaxies and found an anti-correlation between radio luminosity and core prominence. They argued that higher-luminosity sources have higher boosting factors, associated with narrower boosting solid angles and a higher fraction of sources for which a Doppler suppressed core is seen. In contrast, lower-luminosity sources have lower boosting factors and wider solid angles, corresponding to a lower core suppression fraction and a higher compactness.

We argue that another factor might contribute to the observed behaviour in our sample. It is known that AGNs evolve from very compact to extended objects by forming and expanding jets, associated with an increasing total luminosity. Namely, GPS sources are most compact and evolve into CSS sources and finally into the largest radio galaxies, FR Type I or II (e.g. O’Dea 1998; Snellen et al. 1999; Fanti 2009). Following this sequence, we would expect younger AGNs to be more compact than old AGNs.

We note that both effects might overlap since they both predict a lower compactness at higher luminosities. Based on the slightly higher VLBI detection fraction of IFRS – which is expected to be a result of higher compactnesses – compared to the general AGN population as found in Sects. 4.1.1 and 4.1.2, we suggest that IFRS are on average younger than the general AGN population. This would be in agreement with results by Middelberg et al. (2011b) and Collier et al. (2014) who found some IFRS to be GPS and CSS sources. The higher VLBI detection fraction for IFRS classified as GPS and CSS sources compared to non-classified IFRS reported in Sect. 4.1.2 also agrees with this reasoning.

We suggest that – at least some – IFRS are young AGNs. However, the sample presented by Collier et al. (2014) contains IFRS with different characteristics. IFRS, which are associated with more than one FIRST source, are clearly no GPS or CSS sources but extended radio galaxies. Those sources would be expected to be older and less compact than IFRS with exactly one FIRST counterpart. We found evidence for this expected behaviour in Sect. 4.1.2 based on a lower detection fraction for IFRS that are extended in arcsec-resolution images. We therefore suggest that these extended IFRS are on average older and more evolved than the VLBA-detected IFRS.

We found lower mean compactnesses of our VLBA-detected IFRS compared to the other two VLBI-detections of IFRS by Norris et al. (2007) and Middelberg et al. (2008b). In addition to the technical explanations given in Sect. 4.2, this discrepancy can also be explained by boosting effects. The IFRS from Norris et al. and Middelberg et al. are radio-fainter than the IFRS analysed in our work. Following the reasoning by Deller & Middelberg (2014) that brighter objects are more likely to be Doppler suppressed, lower compactnesses for our IFRS compared to the fainter IFRS from Norris et al. and Middelberg et al. could be expected.

In Sect. 4.2.1, we found a statistically significant correlation between redshift and compactness, with higher-redshift IFRS being more compact. Two arguments can explain this correlation. (a) Higher-redshift objects have a tendency to be younger than low-redshift versions of the same class of object. Combining the increasing luminosity of GPS and CSS sources with time and the boosting-related argument of decreasing compactness with luminosity, higher-redshift – and thus younger and fainter – IFRS would be expected to be more compact. (b) At higher redshifts, IFRS are more likely to be located in gas-rich

environments as shown for high-redshift galaxies (Klamer et al. 2006). The higher gas density confines these objects and keeps them more compact.

These results are all in agreement with the scenario that IFRS are younger and therefore less luminous compared to the general AGN population, resulting in higher compactnesses and higher detection fractions. However, we stress that this putative connection between the age of IFRS and their VLBI properties is not statistically significant and needs further testing.

Alternatively, the slightly higher VLBI detection fraction of IFRS compared to the general AGN population could also be explained by a higher dust content of IFRS, making it harder for the jets to expand and resulting in a more compact object. However, no evidence has been found that IFRS are obscured by dust. On the contrary, Collier et al. (2014) and Herzog et al. (2014) argued that the IR faintness of IFRS is not caused by dust extinction. The SEDs resulting from our photometric redshift fitting presented in Sect. 3.2 also indicate that at least some IFRS are very blue and do not support the hypothesis that a significant fraction of IFRS is associated with dusty galaxies.

Future observations will help to test the hypotheses made in this work. In particular, additional VLBA observations – similar to the observations presented in this work – scheduled for semester 15A will increase the sample size of VLBI-observed IFRS, providing the basis for more robust tests.

We plan to match arcsec-resolution radio data at higher and lower frequencies, enabling the measurement of spectral indices and turnover frequencies of IFRS. This information will bring out a putative overlap between IFRS and GPS/CSS sources and provide further insights into the evolutionary status of IFRS (Herzog et al., in prep.).

Radio observations – exposing the intermediate-resolution morphologies of IFRS – could discriminate between the two mechanisms which may be responsible for the lower compactness of brighter objects: beaming and age. If beaming is the predominant cause for this effect, the radio-fainter IFRS should mainly be one-sided objects (core-jet) since a beaming effect is more likely to be seen for fainter objects as discussed above. In contrast, radio-brighter IFRS would be expected to show a more symmetric structure. However, if the anti-correlation between compactness and arcsec-scale radio flux density is mainly driven by the age of the objects, no difference in the morphology would be expected, although radio-brighter objects should be larger.

Two IFRS stand out from our sample since they were found to be composed of two mas-scale components, separated by a few hundred mas. There are four different explanations for those sources which we now discuss.

- (i) GPS/CSS double lobe sources: it is known that GPS and CSS double lobe sources can appear as separate components in VLBI observations (Snellen et al. 2003). In that case, the two components would be hot-spots in the two jets and steep spectral indices would be expected (e.g. Hovatta et al. 2014), while the VLBI-undetected core of the source would be between both components. GPS sources are usually smaller than 1 kpc (O’Dea 1998), whereas CSS sources show extensions of a few to a few tens of kpc (Fanti 2009; Randall et al. 2011).
- (ii) Compact core and jet of a GPS or CSS source: related to the first scenario, the two components could be the compact core of the AGN and a hot-spot in one jet. In that case, the spectral indices of both components can be different. While the hot-spot should provide a steep spectrum

as discussed above, the core component would most likely provide a flat spectrum. However, the core spectrum could also be steep (Hovatta et al. 2014).

- (iii) Gravitational lensing: the appearance of two components can also be explained by gravitational lensing (e.g. Porcas 1998). In that case, the emission seen as two components would originate from one distant source whose emission is deflected by the gravitation of a nearby object. Therefore, similar spectral indices for the two components are expected. In F0030 and F0257, the two components are too close to find a potential gravitational lensing effect in optical images.
- (iv) Binary black hole: the two components could also be a binary black hole (e.g. Burke-Spolaor 2011). In that case, the spectral indices of the components could be flat or steep or mixed as discussed in (ii) for the compact core.

Based on the available data, we are not able to exclude any of those four different explanations because of the large error bars on the spectral indices. F0030 is unlikely to be a GPS source because of the linear size of more than 1.7 kpc. Following the correlation between intrinsic peak frequency and linear size of compact AGNs presented by O’Dea & Baum (1997), F0030 would be expected to show a rest-frame turn-over frequency of less than a few hundred MHz. Particularly, F0030 has different characteristics than the high-redshift ($z = 5.774$) steep spectrum source J0836+0054 (Petric et al. 2003; Frey et al. 2005). This RL quasar shows arcsec-scale properties ($S_{1.4\text{GHz}} = 1.75$ mJy, $\alpha = -0.8$) similar to those of IFRS. However, in contrast to F0030, J0836+0054 has a second arcsec-scale radio component which was undetected in VLBI observations and is most likely associated with a lower-redshift galaxy.

6. Conclusion

We observed 57 IFRS with the VLBA and detected compact emission in 35 of them. Based on these observations, we draw the following conclusions.

- We tested the hypothesis that IFRS contain AGNs. Our observations finally confirm the suggested compact cores in the majority of – if not all – IFRS, establishing IFRS as a new class of AGN. Our data increase the number of VLBI-detected IFRS from 2 to 37.
- Our data suggest that radio-brighter IFRS are on average less compact. This finding agrees with the evolutionary scenario that young AGNs evolve by expanding jets, becoming radio brighter and less compact with time. However, boosting effects may play a role, too.
- We found a marginal tendency for IFRS to show a higher VLBI detection fraction compared to randomly selected sources with mJy arcsec-scale flux densities, i.e. mainly AGNs. In our sample, the detection fraction is higher for IFRS with exactly one FIRST counterpart and for IFRS classified as GPS and CSS sources.
- A statistically significant correlation between redshift and compactness was found in our data for IFRS with higher-redshift sources to be more compact. This is in agreement with higher-redshift sources being located in denser environments and having a tendency to be younger.
- Two sources show two components each, separated by between 0.4 kpc and 3 kpc at any reasonable redshift. These components might be jet/jet or core/jet components of an AGN, a binary black hole, or arising from gravitational lensing.

All our findings are in agreement with the scenario that IFRS contain young AGNs which are in an early stage of their evolution. Their jets are not yet formed or expanded significantly, resulting in a very compact source. When evolving, the jets expand and the total radio fluxes of the sources increase, while the compactnesses decrease at the same time. We note that some IFRS already formed jets as known from arcsec-resolution maps.

Our analyses in this work were limited because of the low number of objects in relevant subsamples. Based on new data from VLBA observations of IFRS in semester 15A and planned lower-resolution observations, we are aiming at extending our study and further testing the hypotheses presented in this work.

Acknowledgements. A.T.D. acknowledges support from an NWO Veni Fellowship. The National Radio Astronomy Observatory is a facility of the National Science Foundation operated under cooperative agreement by Associated Universities, Inc. This work made use of the Swinburne University of Technology software correlator, developed as part of the Australian Major National Research Facilities Programme and operated under licence. Funding for SDSS-III has been provided by the Alfred P. Sloan Foundation, the Participating Institutions, the National Science Foundation, and the US Department of Energy Office of Science. The SDSS-III web site is <http://www.sdss3.org/>. SDSS-III is managed by the Astrophysical Research Consortium for the Participating Institutions of the SDSS-III Collaboration including the University of Arizona, the Brazilian Participation Group, Brookhaven National Laboratory, Carnegie Mellon University, University of Florida, the French Participation Group, the German Participation Group, Harvard University, the Instituto de Astrofísica de Canarias, the Michigan State/Notre Dame/JINA Participation Group, Johns Hopkins University, Lawrence Berkeley National Laboratory, Max Planck Institute for Astrophysics, Max Planck Institute for Extraterrestrial Physics, New Mexico State University, New York University, Ohio State University, Pennsylvania State University, University of Portsmouth, Princeton University, the Spanish Participation Group, University of Tokyo, University of Utah, Vanderbilt University, University of Virginia, University of Washington, and Yale University.

References

- Ahn, C. P., Alexandroff, R., Allende Prieto, C., et al. 2012, *ApJS*, 203, 21
- Ahn, C. P., Alexandroff, R., Allende Prieto, C., et al. 2014, *ApJS*, 211, 17
- Alexander, D. M., & Hickox, R. C. 2012, *New Astron. Rev.*, 56, 93
- Banfield, J. K., George, S. J., Taylor, A. R., et al. 2011, *ApJ*, 733, 69
- Becker, R. H., White, R. L., & Helfand, D. J. 1995, *ApJ*, 450, 559
- Brammer, G. B., van Dokkum, P. G., & Coppi, P. 2008, *ApJ*, 686, 1503
- Burke-Spolaor, S. 2011, *MNRAS*, 410, 2113
- Cameron, E. 2011, *PASA*, 28, 128
- Collier, J. D., Banfield, J. K., Norris, R. P., et al. 2014, *MNRAS*, 439, 545
- Condon, J. J., Huang, Z.-P., Yin, Q. F., & Thuan, T. X. 1991, *ApJ*, 378, 65
- Condon, J. J., Cotton, W. D., Greisen, E. W., et al. 1998, *AJ*, 115, 1693
- Condon, J. J., Cotton, W. D., Fomalont, E. B., et al. 2012, *ApJ*, 758, 23
- Croton, D. J., Springel, V., White, S. D. M., et al. 2006, *MNRAS*, 365, 11
- De Breuck, C., Seymour, N., Stern, D., et al. 2010, *ApJ*, 725, 36
- Deller, A. T., & Middelberg, E. 2014, *AJ*, 147, 14
- Deller, A. T., Tingay, S. J., Bailes, M., & West, C. 2007, *PASP*, 119, 318
- Deller, A. T., Brisken, W. F., Phillips, C. J., et al. 2011, *PASP*, 123, 275
- Fanaroff, B. L., & Riley, J. M. 1974, *MNRAS*, 167, 31
- Fanti, C. 2009, *Astron. Nachr.*, 330, 120
- Frey, S., Paragi, Z., Mosoni, L., & Gurvits, L. I. 2005, *A&A*, 436, L13
- Gaibler, V., Khochfar, S., Krause, M., & Silk, J. 2012, *MNRAS*, 425, 438
- Garn, T., & Alexander, P. 2008, *MNRAS*, 391, 1000
- Garrington, S. T., Garrett, M. A., & Polatidis, A. 1999, *New Astron. Rev.*, 43, 629
- Hales, C. A., Murphy, T., Curran, J. R., et al. 2012, *MNRAS*, 425, 979
- Hardcastle, M. J., Evans, D. A., & Croston, J. H. 2007, *MNRAS*, 376, 1849
- Herzog, A., Middelberg, E., Norris, R. P., et al. 2014, *A&A*, 567, A104
- Herzog, A., Norris, R. P., Middelberg, E., et al. 2015, *A&A*, accepted
- Hovatta, T., Aller, M. F., Aller, H. D., et al. 2014, *AJ*, 147, 143
- Huang, Z. P., Thuan, T. X., Chevalier, R. A., Condon, J. J., & Yin, Q. F. 1994, *ApJ*, 424, 114
- Huynh, M. T., Norris, R. P., Siana, B., & Middelberg, E. 2010, *ApJ*, 710, 698
- Karouzos, M., Im, M., Trichas, M., et al. 2014, *ApJ*, 784, 137
- Kauffmann, G., Heckman, T. M., Tremonti, C., et al. 2003, *MNRAS*, 346, 1055
- Kettenis, M., van Langevelde, H. J., Reynolds, C., & Cotton, B. 2006, in *Astronomical Data Analysis Software and Systems XV*, eds. C. Gabriel, C. Arviset, D. Ponz, & S. Enrique, *ASP Conf. Ser.*, 351, 497
- Kewley, L. J., Heisler, C. A., Dopita, M. A., et al. 2000, *ApJ*, 530, 704
- Kimball, A., & Ivezić, Z. 2014, ArXiv e-prints [arXiv:1401.1535]
- Kimball, A. E., & Ivezić, Ž. 2008, *AJ*, 136, 684
- Klamer, I. J., Ekers, R. D., Sadler, E. M., & Hunstead, R. W. 2004, *ApJ*, 612, L97
- Klamer, I. J., Ekers, R. D., Bryant, J. J., et al. 2006, *MNRAS*, 371, 852
- Lonsdale, C. J., Smith, H. E., Rowan-Robinson, M., et al. 2003, *PASP*, 115, 897
- Maini, A., Prandoni, I., Norris, R. P., et al. 2013, *A&A*, submitted
- Middelberg, E. 2006, *PASA*, 23, 64
- Middelberg, E., Norris, R. P., Cornwell, T. J., et al. 2008a, *AJ*, 135, 1276
- Middelberg, E., Norris, R. P., Tingay, S., et al. 2008b, *A&A*, 491, 435
- Middelberg, E., Deller, A., Morgan, J., et al. 2011a, *A&A*, 526, A74
- Middelberg, E., Norris, R. P., Hales, C. A., et al. 2011b, *A&A*, 526, A8
- Middelberg, E., Deller, A. T., Norris, R. P., et al. 2013, *A&A*, 551, A97
- Mullin, L. M., Riley, J. M., & Hardcastle, M. J. 2008, *MNRAS*, 390, 595
- Narayan, R., & Yi, I. 1995, *ApJ*, 452, 710
- Norris, R. P., Afonso, J., Appleton, P. N., et al. 2006, *AJ*, 132, 2409
- Norris, R. P., Tingay, S., Phillips, C., et al. 2007, *MNRAS*, 378, 1434
- Norris, R. P., Afonso, J., Cava, A., et al. 2011, *ApJ*, 736, 55
- O’Dea, C. P. 1998, *PASP*, 110, 493
- O’Dea, C. P., & Baum, S. A. 1997, *AJ*, 113, 148
- Petric, A. O., Carilli, C. L., Bertoldi, F., et al. 2003, *AJ*, 126, 15
- Porcas, R. W. 1998, in *IAU Colloq. 164: Radio Emission from Galactic and Extragalactic Compact Sources*, eds. J. A. Zensus, G. B. Taylor, & J. M. Wrobel, *ASP Conf. Ser.*, 144, 303
- Randall, K. E., Hopkins, A. M., Norris, R. P., & Edwards, P. G. 2011, *MNRAS*, 416, 1135
- Seymour, N., Stern, D., De Breuck, C., et al. 2007, *ApJS*, 171, 353
- Smith, H. E., Lonsdale, C. J., Lonsdale, C. J., & Diamond, P. J. 1998, *ApJ*, 493, L17
- Snellen, I. A. G., Schilizzi, R. T., Miley, G. K., et al. 1999, *New Astron. Rev.*, 43, 675
- Snellen, I. A. G., Mack, K.-H., Schilizzi, R. T., & Tschager, W. 2003, *PASA*, 20, 38
- Springel, V., White, S. D. M., Jenkins, A., et al. 2005, *Nature*, 435, 629
- Wall, J. V., & Jenkins, C. R. 2012, *Practical statistics for astronomers*, Cambridge Observing Handbooks for Research Astronomers (Leiden: Cambridge Univ. Press)
- Willott, C. J., Rawlings, S., Jarvis, M. J., & Blundell, K. M. 2003, *MNRAS*, 339, 173
- Wright, E. L. 2006, *PASP*, 118, 1711
- Wright, E. L., Eisenhardt, P. R. M., Mainzer, A. K., et al. 2010, *AJ*, 140, 1868
- Zinn, P.-C., Middelberg, E., & Ibar, E. 2011, *A&A*, 531, A14
- Zinn, P.-C., Middelberg, E., Norris, R. P., & Detmar, R.-J. 2013, *ApJ*, 774, 66

4

Infrared-faint radio sources remain undetected at far-infrared wavelengths

The extreme character of IFRSs has been quantified by their enormous radio-to-IR flux density ratios (e.g. Huynh et al., 2010; Middelberg et al., 2011; Norris et al., 2011a). Whereas starburst galaxies are known to have ratios of the order of one, RQ and RL quasars are characterised by ratios below one and a few tens, respectively (Norris et al., 2011a). In contrast, IFRSs have radio-to-IR flux density ratios exceeding 500, following the selection criterion from Zinn et al. (2011). However, most IFRSs show significantly higher ratios. Since most IFRSs are undetected at $3.6\ \mu\text{m}$, only lower limits on the ratio are known, where these limits easily exceed a few thousand. Zinn et al. find IFRS CS703 to have the highest radio-to-IR flux density ratio of an IFRS, given by a lower limit of 8700. Maini et al. (2013) update this limit to $> 12\,784$.

Norris et al. (2011a) show that this ratio of IFRSs is significantly different from that of most classes of galaxy frequently found at high redshifts. However, a class of very rare

objects has been found to show similar radio-to-IR flux density ratios to those of IFRSs: the class of HzRGs, with ratios of a few hundred up to tens of thousand.

High-redshift radio galaxies are very powerful radio galaxies at high redshifts, defined by two selection criteria (Seymour et al., 2007; De Breuck et al., 2010):

$$z \geq 1 \quad \text{and} \quad (4.1)$$

$$L_{3\text{GHz}} \geq 10^{26} \text{ W Hz}^{-1} ,$$

where the highest-redshift HzRG has been found at $z = 5.2$ (Seymour et al., 2007). These galaxies are very massive with stellar masses of $10^{11} - 10^{11.5} M_{\odot}$ even at highest redshifts. They are expected to be the progenitors of the most massive elliptical galaxies in the local universe and to be located in dark matter overdensities (Miley and De Breuck, 2008).

Evidence for this hypothesis has been added based on the $K - z$ correlation which HzRGs were found to follow. The $K - z$ correlation has been known for radio galaxies for three decades (Lilly and Longair, 1984; Jarvis et al., 2001; Willott et al., 2003; Rocca-Volmerange et al., 2004). It connects the near-IR K band—centred at $2.2 \mu\text{m}$ —magnitude with the redshift (“Hubble K band diagram”) and reveals a tight correlation holding to $z \sim 1$. Towards higher redshifts, the observed K band starts to sample rest-frame optical emission, resulting in moderate scatter in the continuing correlation. Therefore, the existence of this correlation to $z \sim 4$ is still puzzling. In any case, the $K - z$ correlation has been used as a successful tool to find radio galaxies at high-redshift.

The class of HzRGs has IR luminosities $L_{8-1000 \mu\text{m}}$ above $10^{11} L_{\odot}$, $10^{12} L_{\odot}$, or $10^{13} L_{\odot}$ which would classify these objects as LIRGs, ULIRGs, and hyper-luminous IR galaxies (HyLIRGs), respectively, if their enormous radio power was unknown (Seymour et al., 2007; Drouart et al., 2014). Similar IR luminosities are found for some quasars and radio galaxies in the 3CRR catalogue, suggesting that HzRGs have a hidden quasar in their centre, i.e. a SMBH accreting at rates ($1 M_{\odot} \text{ yr}^{-1}$ to $100 M_{\odot} \text{ yr}^{-1}$) close to the Eddington limit (Ogle et al., 2006; Fernandes et al., 2011; Drouart et al., 2014). The SMBHs of HzRGs are known to be very massive ($3 \times 10^9 - 2 \times 10^{10} M_{\odot}$; Nesvadba et al., 2011). Instead, star forming activity cannot explain the IR luminosities (Seymour et al., 2007), although SFRs between $100 M_{\odot} \text{ yr}^{-1}$ and $5000 M_{\odot} \text{ yr}^{-1}$ are suggested (Archibald et al., 2001; Reuland et al., 2004; Drouart et al., 2014). Since HzRGs are known to harbour active SMBHs and vigorous star

formation, these galaxies are important objects to study the highly debated connection between AGN and star forming activity, referred to as feedback (see section 1.2.2).

Crucial for understanding the evolution of star forming activity is knowledge about the content of molecular gas—the key ingredient for star formation activity—in the galaxy. Observational studies and simulations find evidence that galaxies at high redshifts have a much larger ratio of molecular gas to total mass than nearby spirals (Obreschkow and Rawlings, 2009; Daddi et al., 2010; Tacconi et al., 2010). Carbon monoxide ^{12}CO is a tracer of H_2 and is used to estimate the molecular hydrogen content in some HzRGs, suggesting a few $10^{10} M_{\odot}$ (Emonts et al., 2011a,b). In particular, ^{12}CO is found to be aligned with the radio jets in some of the sources, potentially pointing at jet-induced star formation (Emonts et al., 2014).

The object MRC 1138-26, also referred to as spiderweb galaxy, is a prominent example of the class of HzRGs at $z = 2.156$. Its name was inspired by several satellite galaxies, interpreted as “flies”, with the radio galaxy as centre of this proto-cluster. It is expected that the central galaxy will further on interact with these companion galaxies, e.g. by merging. The spiderweb galaxy is very radio-luminous ($L_{500\text{MHz}} = 1.2 \times 10^{29} \text{ W Hz}^{-1}$; De Breuck et al., 2010) with a massive black hole ($2 \times 10^{10} M_{\odot}$; Nesvadba et al., 2011), accreting at 20% of the Eddington rate (Seymour et al., 2012). It is expected to harbour one of the most powerful AGNs, providing no evidence for significant extinction (Seymour et al., 2012). The spiderweb galaxy also shows high star forming activity ($\text{SFR} \sim 1200 M_{\odot} \text{ yr}^{-1}$; Ogle et al., 2012). Seymour et al. (2012) suggest that the spiderweb galaxy is undergoing a transition from merger-induced starburst phase to an AGN phase.

Since HzRGs are the only known high-redshift objects sharing the enormous radio-to-IR flux density ratios of IFRSs, a connection between those two classes of objects has been suggested (Norris et al., 2011a). All IFRSs with spectroscopic redshifts fulfil the selection criteria of HzRGs as shown in chapters 2 (Herzog et al., 2014) and 3 and were found to be consistent with the $S_{3.6\mu\text{m}} - z$ correlation of HzRGs. However, HzRGs are generally radio-brighter than IFRSs with flux densities of a few hundred mJy compared to a few or a few tens of mJy for the IFRSs in the deep fields. Also the brighter IFRSs, presented by Collier et al. (2014), are radio-fainter than HzRGs. For those IFRSs with spectroscopic redshifts, the radio luminosities were found to be around one order of magnitude lower than those of HzRGs (see chapter 2; Herzog et al., 2014). Similarly, IFRSs are IR-fainter than

HzRGs. Whereas most IFRSs in the deep fields are undetected at $3.6\ \mu\text{m}$ down to $3\ \mu\text{Jy}$, the vast majority of HzRGs have detected $3.6\ \mu\text{m}$ counterparts of a few tens of μJy , some even above $100\ \mu\text{Jy}$ (Seymour et al., 2007). However, there is an overlap with the class of IFRSs since one third of the sample of HzRGs presented by Seymour et al. have $3.6\ \mu\text{m}$ flux densities below $30\ \mu\text{Jy}$, fulfilling the IFRS selection criteria from Zinn et al. (2011).

Further, the sky density of IFRSs—a few per square degree—is three orders of magnitude higher than that of HzRGs of which less than 200 are known on the entire sky (Miley and De Breuck, 2008). Based on the suggested link between IFRSs and HzRGs and the fainter appearance of the former class, Norris et al. (2011a) hypothesise that IFRSs might be (a) higher-redshift versions of HzRGs, or (b) fainter siblings of HzRGs at similar redshifts.

Based on the spectroscopic redshift presented in chapter 2 (Herzog et al., 2014), IFRS S265 has been observed with the ATCA in a pilot project to search for CO in this source and to test whether IFRSs have similar CO properties than HzRGs (M. Y. Mao, A. Herzog, et al., in prep.). The data provide a tentative detection, though additional observations are needed for confirmation. However, this preliminary result adds evidence to the suggested link between IFRSs and HzRGs. In particular, the CO in S265 is not detected in the centre of that galaxy, but aligned with a radio extension, similar to the finding by Emonts et al. (2014) for HzRGs. If IFRSs have high masses of cold molecular gas as indicated by the tentative detection, blind CO observations with radio telescopes covering a wide bandwidth and high sensitivity—e.g. ATCA, VLA, or ALMA—would be very promising to measure redshifts using the CO emission lines. Redshift information for the median IFRS in deep fields is crucial. However, since these IFRSs are undetected in the optical and IR regime, it is hardly feasible to obtain this information from optical spectroscopic observations.

The presence of active SMBHs in the majority of IFRSs has been confirmed based on VLBI observations as presented in chapter 3 (Herzog et al., 2015a). This finding implies that nuclear activity is a significant contributor to the bolometric luminosity of these objects. Generally, the bolometric luminosity of high-redshift galaxies is dominated by emission from the AGN or by starburst activity. Therefore, it is crucial to study the star forming properties of IFRSs and to determine how this process contributes to their energy output. In particular, the question arises whether IFRSs show similar starburst activity than HzRGs with SFRs of the order of hundreds or thousands of solar masses per year. In the following paper, these questions were asked. Basis for this study are FIR observations of six IFRSs,

fulfilling the selection criteria from Zinn et al. (2011), carried out with the *Herschel* Space Observatory (Pilbratt et al., 2010) between 100 μm and 500 μm , covering a so-far unexplored wavelength regime of IFRSs.

Observations using the two photometric instruments on board the *Herschel* Space Observatory¹—the Photodetecting Array Camera and Spectrometer (PACS; Griffin et al., 2010) and the Spectral and Photometric Imaging Receiver (SPIRE; Poglitsch et al., 2010)—enable studies of IR emission produced by both star forming and AGN activity. SPIRE observed simultaneously in three wavebands centred at 250 μm , 350 μm , and 500 μm , picking up the starburst emission in high-redshift ($z \gtrsim 2$) AGNs (Hatziminaoglou et al., 2010). In contrast, the three wavebands of PACS—centred at 70 μm , 100 μm , and 160 μm , whereof two could be used simultaneously—mainly trace the rest-frame mid-IR emission of the high-redshift AGN itself.

These *Herschel* FIR observations of the six most extreme IFRSs—characterised by radio-to-IR flux density ratios exceeding 2300, two even above 12 000—are presented in the paper below. All targeted sources remain undetected at all five wavelengths, putting valuable constraints on the SEDs of these sources. In the paper, these constraints are used to model the broadband SEDs of IFRSs in the redshift range $1 \leq z \leq 12$. SED templates of different galaxies—including starburst galaxies and AGNs—were shifted to different redshifts. Figure 4.1 presents the results of this modelling in a different way than in the paper below. Whereas Fig. 5 in the paper shows the cumulative fractional deviation of the respective templates from the photometric data of IFRSs as a function of redshift, the plots here visualise whether the templates are consistent with the individual characteristics of IFRSs. These are (a) the 1.4 GHz flux density, (b) the 3.6 μm flux density upper limit, (c) the radio-to-IR flux density ratio, and (d) the FIR non-detections, represented by the 100 μm flux density. The 1.4 GHz flux densities of these IFRSs are between 7 mJy and 28 mJy, their median 3.6 μm flux density is below 1.2 μJy , their radio-to-IR flux density ratio above 2000, and their median 100 μm flux density below 2.3 mJy. These allowed ranges in the respective parameter spaces are indicated by the green shaded areas.

All galaxies exclusively powered by star forming activity—M 82 and Arp 220—cannot reproduce the radio flux densities of IFRSs at any redshift in the range $1 \leq z \leq 12$. Only RL

¹The operation of *Herschel* stopped on 29 April 2013 when the telescope ran out of liquid helium which was needed to cool the instruments.

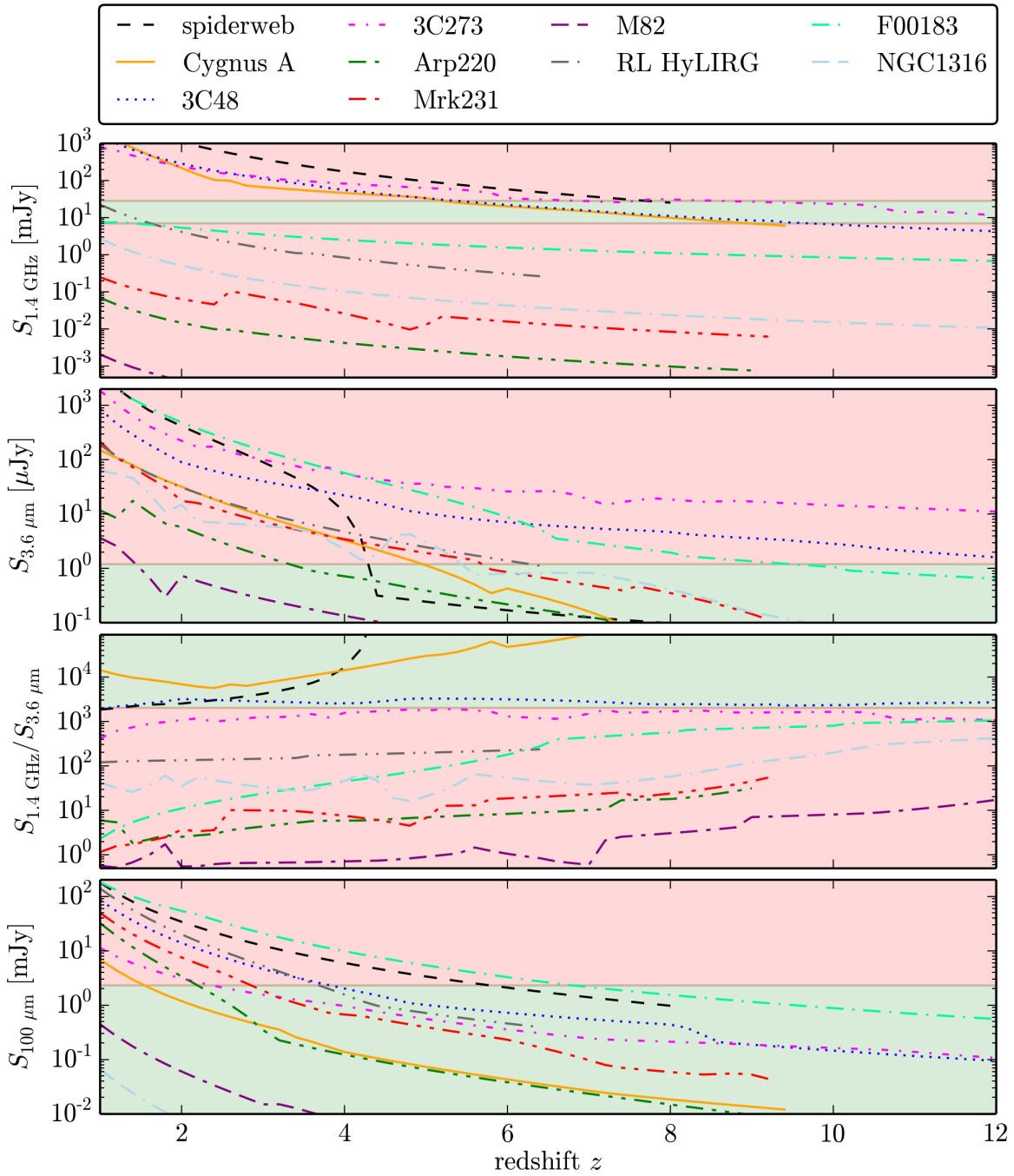


Figure 4.1: Broadband SED modelling for the IFRSs observed with *Herschel*. Presented are (from top to bottom) the 1.4 GHz flux density, the 3.6 μm flux density, the 1.4 GHz to 3.6 μm flux density ratio, and the 100 μm flux density, as a function of redshift for different galaxies. No scaling has been applied and no extinction added to the templates, corresponding to Fig. 4 and the upper left subplot in Fig. 5 in the paper below. Green shaded areas show the allowed regions of IFRSs in the respective parameter space; objects in red shaded areas are inconsistent with the photometric constraints of the IFRSs observed with *Herschel*.

objects—3C 273, 3C 48, Cygnus A, F00183, the RL HyLIRG, and the spiderweb galaxy—are able to meet the radio criterion. However, F00183 and the RL HyLIRG are inconsistent with the IR flux densities and the flux density ratio. 3C 273 and 3C 48 have radio-to-IR flux density ratios of around 2000—consistent with the ratio of IFRSs—but these sources are too bright at $3.6 \mu\text{m}$ even if shifted to $z \gtrsim 5$. In contrast, the spiderweb galaxy and Cygnus A in the redshift ranges $z \gtrsim 8$ and $5 \lesssim z \lesssim 8.5$, respectively, are consistent with the observed radio and near-IR flux densities of IFRS as presented in the paper below. These redshifts obtained from the SED modelling are higher than any spectroscopic redshift found for IFRSs as discussed in chapters 2 (Herzog et al., 2014) and 3. However, these six IFRSs observed with *Herschel* are fainter at $3.6 \mu\text{m}$ than all IFRSs with spectroscopic redshifts. Assuming the suggested correlation between $3.6 \mu\text{m}$ flux density and redshift (see chapters 2 and 3) applies to these IR-faintest IFRSs, it is speculated that this sub-class of IFRSs may exist at $z \gtrsim 5$. This is consistent with the findings in the SED modelling presented in the paper below.

Near-IR flux densities of a few tens of μJy prevented the templates of 3C 48 and 3C 273 at $z \gtrsim 5$ to meet the photometric characteristics of IFRSs. Additional dust obscuration—suggested e.g. by Norris et al. (2011a) to cause the IR faintness of IFRSs—could dim the observed near-IR flux. At the expected redshifts of IFRSs, the observed $3.6 \mu\text{m}$ emission corresponds to the optical rest-frame regime. To test whether dust obscuration can make these SED templates consistent with the IR faintness of IFRSs, the Calzetti et al. (2000) reddening law was used to modify the templates by additional amounts of extinction. The wavelength-dependent observed flux density $S_{\text{obs}}(\lambda)$ is given by $S_{\text{obs}}(\lambda) = S_{\text{int}}(\lambda)10^{-0.4A_\lambda}$, where S_{int} is the intrinsic flux density. The extinction A_λ at wavelength λ is related to the colour excess $E(B - V)$ by $A_\lambda = k(\lambda)E(B - V) = \frac{k(\lambda)A_V}{R_V}$ with $R_V = 4.05$ and the extinction A_V . Calzetti et al. parameterised the reddening curve $k(\lambda)$ by

$$k(\lambda) = \begin{cases} 2.659 \left(-2.156 + \frac{1.509}{\lambda} - \frac{0.198}{\lambda^2} + \frac{0.011}{\lambda^3} \right) + R_V & 0.12 \mu\text{m} \leq \lambda \leq 0.63 \mu\text{m} \\ 2.659 \left(-1.857 + \frac{1.040}{\lambda} \right) + R_V & 0.63 \mu\text{m} \leq \lambda \leq 2.20 \mu\text{m} . \end{cases} \quad (4.2)$$

The energy absorbed by dust at optical and near-IR wavelengths is then reprocessed and re-emitted at rest-frame mid- and far-IR wavelengths. In the SED modelling presented in the paper below, energy conservation was applied to test whether the FIR non-detections are

consistent with additional dust needed to squeeze the SED templates below the near-IR flux density upper limits of IFRSs. The thermal dust emission S_ν was assumed to be given by a modified black-body spectrum,

$$S_\nu \propto B_\nu(T)\epsilon_\nu, \quad (4.3)$$

where $\epsilon_\nu \propto \nu^\beta$ is the emissivity function at frequency ν (e.g. Franceschini, 2000). The spectral index β depends on dust grain size and composition and is expected to be between 1 and 2 (Draine and Lee, 1984). $B_\nu(T)$ is the black-body spectrum given by

$$B_\nu(T) = \frac{2h\nu^3}{c^2} \frac{1}{\exp\left(\frac{h\nu}{k_B T}\right) - 1}, \quad (4.4)$$

where h is the Planck constant, c the speed of light in the medium, k_B the Boltzmann constant, and T the temperature. The model was simplified by assuming that the thermal emission is given by only one dust temperature.

To test whether the SED templates of 3C 273 or 3C 48 can be modified to be consistent with the characteristics of IFRSs, extinction was added to these—and all other—templates if the observed $3.6 \mu\text{m}$ flux densities were inconsistent with the flux density upper limit of IFRSs. This is presented in the paper below (lower left subplot in Fig. 5). Here, additional diagnostic plots of the resulting modelling are shown in Fig. 4.2, providing more information about the consistency between the different templates,—obscured by additional dust if required—and the characteristics of IFRSs. The analysis shows that the templates of 3C 273 and 3C 48 can indeed be modified to match the $3.6 \mu\text{m}$ non-detections of IFRSs. Additional dust extinction of the order of 1 mag needed to be added to the 3C 48 SED template in the redshift range $5 \lesssim z \lesssim 9$. For 3C 273, around 2 mag of extinction were needed at $z \gtrsim 8$. However, at $z \lesssim 7$, both templates exceed the $24 \mu\text{m}$ flux density upper limits of IFRSs. This is not visible from Fig. 4.2 and shows the complexity of the parameter space that has to be controlled to model the broadband SEDs of IFRSs. Summarising, some RL AGN templates can be modified by additional dust extinction to be consistent with the characteristics of IFRSs if placed at redshifts $z \gtrsim 5$.

A detailed description of the different approaches carried out to compare modified SEDs of known galaxies to the characteristics of IFRSs is given in the paper below. These approaches include shifting the SED templates to different redshifts, scaling them in luminosity, and adding dust extinction. The paper concludes that all modified templates found to be

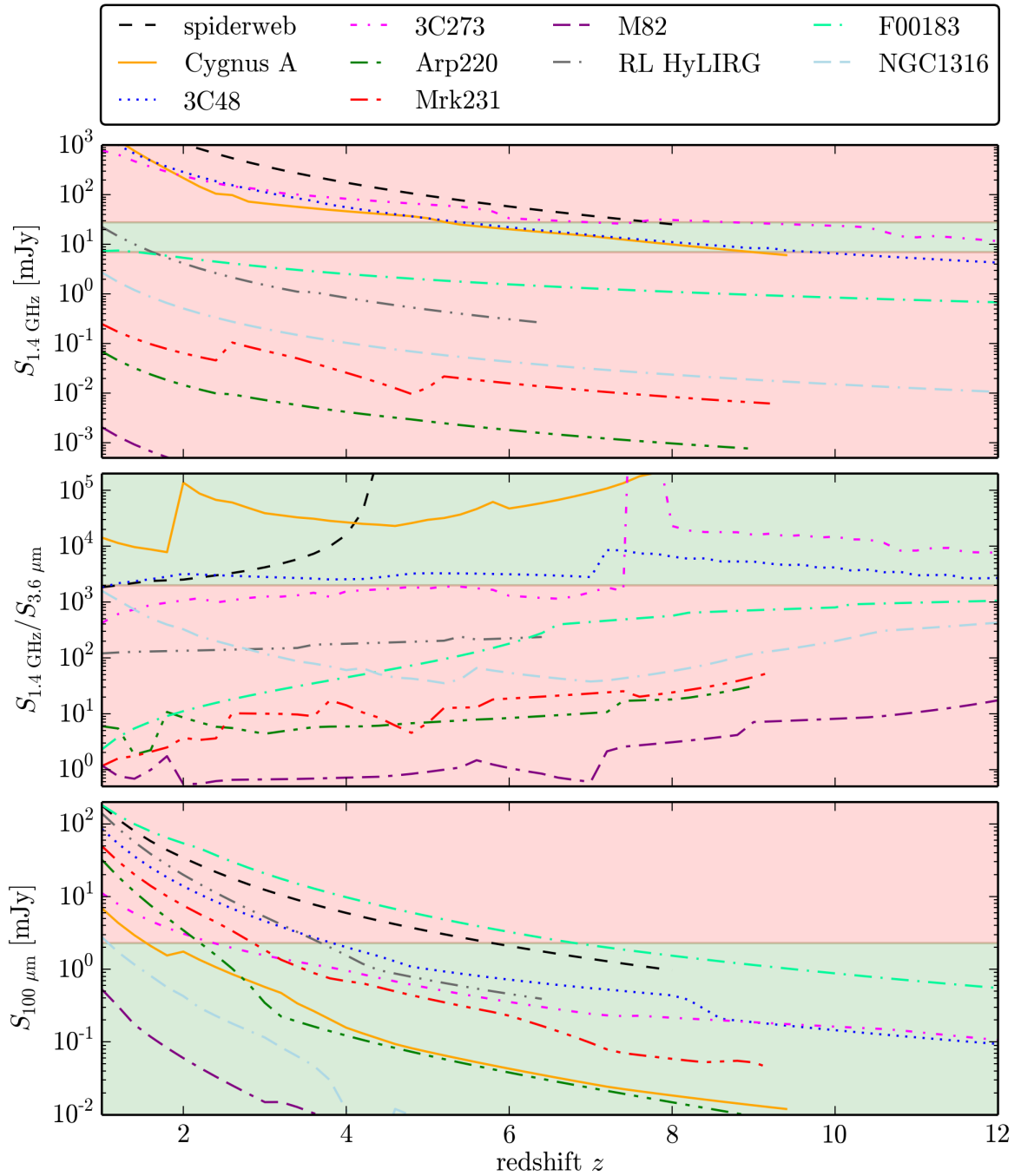


Figure 4.2: Broadband SED modelling for the IFRSs observed with *Herschel*, similar to Fig. 4.1. However, here, extinction has been added to the templates where required, corresponding to the lower left subplot in Fig. 5 in the paper below.

consistent with the data of IFRSs would be classified as HzRGs. In particular, the modelling is consistent with IFRSs being (a) siblings of HzRGs with similar luminosities at higher redshifts ($z \gtrsim 5$), and (b) fainter versions of HzRGs at similar redshifts ($2 \lesssim z \lesssim 5$). Also, upper limits of IR luminosity, SFR, and black hole accretion rate of IFRSs—obtained from modelling the radio-IR SED of IFRSs based on the FIR flux density upper limits—are found to be consistent with numbers of HzRGs.

The remainder of this chapter has been accepted for publication as

**Infrared-faint radio sources remain undetected at far-infrared wavelengths:
Deep photometric observations using the *Herschel* Space Observatory**

A. Herzog, R. P. Norris, E. Middelberg, L. R. Spitler, C. Leipski, and Q. A. Parker
Astronomy & Astrophysics, 580, A7 (2015).

This paper presents photometric *Herschel* observations of six IFRSs, leaving all sources undetected in any of the five FIR wavebands. Also a stacking analysis did not provide a detection. Based on these results and ancillary data in the radio and near- and mid-IR regime, a comprehensive broad-band SED modelling was accomplished. In this approach, SED templates of known galaxies were tested against the photometric data of IFRSs. First, the templates were only shifted in redshift; in later attempts, they were modified in luminosity and additional dust extinction was added. The analysis shows that all consistent SED templates fulfil the selection criteria of HzRGs. Finally, the IR SED of IFRSs was modelled to constrain the maximum luminosity based on the FIR flux density upper limits. Luminosities and estimates on star formation and accretion rates were found to be consistent with corresponding numbers of HzRGs.

I was responsible for leading the work presented in the following manuscript. I calibrated the *Herschel* data and measured flux densities using the *Herschel* Interactive Processing Environment (HIPE; Ott, 2010) based on template pipeline scripts provided in HIPE and by C. Leipski that I used to build an appropriate pipeline script for our observations. I then stacked the near-, mid-, and far-IR maps using my own python script. Further, I used the available photometric data to model the broad-band SEDs of IFRSs based on an automatised python script that I wrote for this purpose. I also modelled the IR SEDs of IFRSs, again using python. Finally, I wrote the manuscript. R. P. Norris, E. Middelberg, and L. R. Spitler supervised the work and provided continuous discussions on the methodology and astrophysical interpretation. E. Middelberg proposed and scheduled the *Herschel* observations providing the basis of this work. C. Leipski contributed with helpful discussions about the data calibration and photometry. He also provided template scripts for the calibration and photometry. All co-authors contributed with discussions to the final manuscript. My contribution to the work presented in this manuscript is 90%.

Credit: Herzog et al., A&A, 580, A7, 2015, reproduced with permission © ESO.

Infrared-faint radio sources remain undetected at far-infrared wavelengths

Deep photometric observations using the *Herschel* Space Observatory^{*}

A. Herzog^{1,2,3}, R. P. Norris³, E. Middelberg¹, L. R. Spitler^{2,4}, C. Leipski⁵, and Q. A. Parker^{2,4,6}

¹ Astronomisches Institut, Ruhr-Universität Bochum, Universitätsstr. 150, 44801 Bochum, Germany
e-mail: herzog@astro.rub.de

² Macquarie University, Sydney, NSW 2109, Australia

³ CSIRO Astronomy and Space Science, Marsfield, PO Box 76, Epping, NSW 1710, Australia

⁴ Australian Astronomical Observatory, PO Box 915, North Ryde, NSW 1670, Australia

⁵ Max-Planck-Institut für Astronomie, Königsstuhl 17, 69117 Heidelberg, Germany

⁶ Department of Physics, Chong Yeut Ming Physics Building, The University of Hong Kong, Pokfulam Road, Hong Kong

Received 26 November 2014 / Accepted 27 May 2015

ABSTRACT

Context. Showing 1.4 GHz flux densities in the range of a few to a few tens of mJy, infrared-faint radio sources (IFRS) are a type of galaxy characterised by faint or absent near-infrared counterparts and consequently extreme radio-to-infrared flux density ratios up to several thousand. Recent studies showed that IFRS are radio-loud active galactic nuclei (AGNs) at redshifts $\gtrsim 2$, potentially linked to high-redshift radio galaxies (HzRGs).

Aims. This work explores the far-infrared emission of IFRS, providing crucial information on the star forming and AGN activity of IFRS. Furthermore, the data enable examining the putative relationship between IFRS and HzRGs and testing whether IFRS are more distant or fainter siblings of these massive galaxies.

Methods. A sample of six IFRS was observed with the *Herschel* Space Observatory between 100 μm and 500 μm . Using these results, we constrained the nature of IFRS by modelling their broad-band spectral energy distribution (SED). Furthermore, we set an upper limit on their infrared SED and decomposed their emission into contributions from an AGN and from star forming activity.

Results. All six observed IFRS were undetected in all five *Herschel* far-infrared channels (stacking limits: $\sigma = 0.74$ mJy at 100 μm , $\sigma = 3.45$ mJy at 500 μm). Based on our SED modelling, we ruled out the following objects to explain the photometric characteristics of IFRS: (a) known radio-loud quasars and compact steep-spectrum sources at any redshift; (b) starburst galaxies with and without an AGN and Seyfert galaxies at any redshift, even if the templates were modified; and (c) known HzRGs at $z \lesssim 10.5$. We find that the IFRS analysed in this work can only be explained by objects that fulfil the selection criteria of HzRGs. More precisely, IFRS could be (a) known HzRGs at very high redshifts ($z \gtrsim 10.5$); (b) low-luminosity siblings of HzRGs with additional dust obscuration at lower redshifts; (c) scaled or unscaled versions of Cygnus A at any redshift; and (d) scaled and dust-obscured radio-loud quasars or compact steep spectrum sources. We estimated upper limits on the infrared luminosity, the black hole accretion rate, and the star formation rate of IFRS, which all agreed with corresponding numbers of HzRGs.

Key words. techniques: photometric – galaxies: active – galaxies: high-redshift – galaxies: star formation – infrared: galaxies

1. Introduction

A new class of extreme radio galaxies, which are characterised by their infrared (IR) faintness and their enormous radio-to-IR flux density ratios, has recently been found in deep surveys: the class of infrared-faint radio sources (IFRS; Norris et al. 2006). While various suggestions had been presented to explain the extreme characteristics of these objects, recent observations clearly indicate that IFRS are radio-loud (RL) active galactic nuclei (AGNs) at high redshifts.

Infrared-faint radio sources were first discovered in the *Chandra* Deep Field South (CDFs) and the European Large Area Infrared space observatory Survey South 1 (ELAIS-S1) field of the Australia Telescope Large Area Survey (ATLAS) by Norris et al. (2006) and Middelberg et al. (2008a), respectively.

^{*} *Herschel* is an ESA space observatory with science instruments provided by European-led Principal Investigator consortia and with important participation from NASA.

The radio maps at 1.4 GHz provided detections with flux densities in the order of tenths to tens of mJy, whilst the co-located *Spitzer* Wide-area Infrared Extragalactic Survey (SWIRE; Lonsdale et al. 2003) showed only a faint or, in most cases, no IR counterpart at 3.6 μm with a noise $\sigma = 1$ μJy . Later, Zinn et al. (2011) defined the class of IFRS by two selection criteria:

- (i) radio-to-IR flux density ratio $S_{1.4 \text{ GHz}}/S_{3.6 \mu\text{m}} > 500$; and
- (ii) 3.6 μm flux density $S_{3.6 \mu\text{m}} < 30$ μJy .

The enormous radio-to-IR flux density ratios imply that IFRS are clear outliers from the radio-IR correlation. The second criterion implicates a distance selection, preventing ordinary objects of redshift $\lesssim 1.4$ from being included in the class of IFRS. In addition to the detections by Norris et al. (2006) and Middelberg et al. (2008a), IFRS were later found in the *Spitzer* extragalactic First Look Survey (xFLS) field by Garn & Alexander (2008), in the Cosmological Evolution Survey (COSMOS) by Zinn et al. (2011), in the European Large Area IR space observatory

Survey North 1 (ELAIS-N1) by [Banfield et al. \(2011\)](#), and in the Lockman Hole field by [Maini et al. \(2015\)](#). In total, around 100 IFRS have been found in these deep fields at a sky density of a few per square degree.

Recently, [Collier et al. \(2014\)](#) found 1317 IFRS in shallow all-sky catalogues, that satisfied both selection criteria given above. They used the Unified Radio Catalog (URC; [Kimball & Ivezić 2008](#)) based on the NRAO VLA Sky Survey (NVSS; [Condon et al. 1998](#)) and data from the all-sky Wide-Field Infrared Survey Explorer (WISE; [Wright et al. 2010](#)). [Collier et al.](#) replaced $S_{3.6\ \mu\text{m}}$ by $S_{3.4\ \mu\text{m}}$. All IFRS in that sample provide an IR counterpart at $3.4\ \mu\text{m}$ and have radio flux densities above 7.5 mJy at 1.4 GHz, some of them exceeding 100 mJy. By this, the IFRS in this sample are on average radio-brighter than the IFRS found in the deep fields by around one order of magnitude. Since the WISE sensitivity is non-uniform, [Collier et al.](#) could only set a lower limit on the sky density of IFRS with a radio flux density above 7.5 mJy of $\sim 0.1\ \text{deg}^{-2}$.

First attempts to explain the existence of IFRS included lobes or hotspots of radio galaxies, obscured star forming galaxies (SFGs), pulsars or high-redshift RL galaxies. Later results (for an overview, see [Collier et al. 2014](#) and references therein) provided evidence that IFRS are indeed RL AGN at high redshifts.

[Norris et al. \(2007\)](#) and [Middelberg et al. \(2008b\)](#) used very long baseline interferometry (VLBI) to confirm the presence of active nuclei in two IFRS. Recently, [Herzog et al. \(2015\)](#) detected 35 out of 57 IFRS in VLBI observations, unquestionably confirming that at least a significant fraction of all IFRS contains AGN.

[Garn & Alexander \(2008\)](#) and [Huynh et al. \(2010\)](#) present the first spectral energy distribution (SED) modelling of IFRS and find that 3C sources (for example 3C 273) can reproduce the observational data when redshifted to $z \gtrsim 2$. Furthermore, [Garn & Alexander](#) and [Huynh et al.](#) conclude that obscured SFGs cannot explain the characteristics of IFRS since the radio-to-IR flux density ratios of IFRS significantly exceed those of SFGs. This finding suggests the presence of an AGN in IFRS, too.

Recently, the first spectroscopic redshifts of IFRS were found, confirming the suggested high-redshift character of this class of objects. [Collier et al. \(2014\)](#) find 19 redshifts for their all-sky sample of IFRS, all but one in the range $2 < z < 3$. The outlier is expected to be a misidentification or an SFG with an AGN in its centre. [Herzog et al. \(2014\)](#) measured redshifts of three IFRS in the deep ATLAS fields based on optical spectroscopy from the Very Large Telescope (VLT) and found them to be in the range $1.8 < z < 2.8$. The IFRS with spectroscopic redshifts, both from [Collier et al.](#) and [Herzog et al.](#), lie at the IR-bright boundary of this class of objects with IR flux densities between $14\ \mu\text{Jy}$ and $30\ \mu\text{Jy}$ at $3.6\ \mu\text{m}$ or $3.4\ \mu\text{m}$. Both [Collier et al.](#) and [Herzog et al.](#) suggest that the IFRS with measured spectroscopic redshifts are the closest ones and that IR-fainter IFRS are at even higher redshifts.

Additionally, the results by [Collier et al. \(2014\)](#) and [Herzog et al. \(2014\)](#) finally disposed of the alternative hypothesis that IFRS are hotspots of spatially separated radio galaxies. If the IR detections were real counterparts of the radio detections, the redshift distribution of these objects would be expected to follow that of Fanaroff Riley type 2 (FR II) galaxies which peaks at $z \sim 1$. In contrast, if the IR detections were spurious associations to the radio emission, their redshift distribution would be expected to follow that of star forming galaxies, peaking at $z \sim 0$. Both cases are in clear disagreement with the observed

redshift distribution of IFRS, providing redshifts only in the regime $1.8 \lesssim z \lesssim 3.0$.

Based on the redshifts measured in their work, [Herzog et al. \(2014\)](#) present the first redshift-based SED modelling of IFRS. They find the templates of an RL AGN (3C 273) and a compact-steep spectrum (CSS) source (3C 48) in agreement with all available photometric data, while an ultraluminous IR galaxy (ULIRG, Arp 220) or a Seyfert galaxy (Mrk 231) are clearly ruled out.

[Huynh et al. \(2010\)](#) and [Middelberg et al. \(2011\)](#) first pointed out a potential similarity between IFRS and high-redshift radio galaxies (HzRGs). HzRGs are a class of powerful radio galaxies ($L_{3\ \text{GHz}} > 10^{26}\ \text{W Hz}^{-1}$) at high redshifts ($z \geq 1$). They are amongst the most massive and most luminous galaxies in the early universe and are expected to be the progenitors of the most massive galaxies in the local universe (e.g. [Seymour et al. 2007](#); [De Breuck et al. 2010](#)). Moreover, HzRGs are known to host powerful AGNs and to show high star formation rates (SFRs). Therefore, they are an important tool to study galaxy evolution and the interplay between AGNs and star forming activity. However, HzRGs are rare objects; only around 100 of these objects are known in the entire sky, located at redshifts $1 \leq z \lesssim 5$.

[Huynh et al.](#) note that IFRS have similar mid-IR to radio flux density ratios to those of HzRGs. [Middelberg et al.](#) studied the radio properties of IFRS in the ELAIS-S1 field and find steep radio spectra between 2.3 GHz and 8.4 GHz with a median of $\alpha = -1.4^1$ and no index larger than -0.7 . This is steeper than the general radio source population ($\alpha = -0.86$) and the AGN source population ($\alpha = -0.82$) in that field. [Middelberg et al.](#) find that the radio spectra are even steeper than those of the sample of HzRGs by [Seymour et al. \(2007\)](#), showing a median radio spectral index $\alpha = -1.02$. HzRGs are the only objects known at significant redshifts sharing the extreme radio-to-IR flux densities of IFRS in the order of thousands as shown by [Norris et al. \(2011\)](#). Furthermore, [Norris et al.](#) suggest that IFRS might follow the correlation between $3.6\ \mu\text{m}$ flux density and redshift found for the sample of HzRGs by [Seymour et al.](#), similar to the $K - z$ relation for other radio galaxies ([Willott et al. 2003](#)).

[Collier et al. \(2014\)](#) and [Herzog et al. \(2014\)](#) tested this hypothesis in the reachable redshift range between 2 and 3 and find IFRS follow this correlation. This adds evidence to the suggestion that IR-fainter IFRS are located at even higher redshift, potentially reaching $z \approx 5$ or 6. Furthermore, [Herzog et al.](#) show that the radio luminosities of IFRS are in the same range as for HzRGs, although IFRS lie at the lower bound of the radio luminosity distribution of HzRGs.

Besides these similarities between IFRS and HzRGs, there is one significant difference. While HzRGs are rare objects of which only around 100 are known in the entire sky, IFRS are much more abundant. The observed sky density of IFRS in the ATLAS fields is around $5\ \text{deg}^{-2}$; [Zinn et al. \(2011\)](#) estimate a survey-independent sky density of $(30.8 \pm 15.0)\ \text{deg}^{-2}$.

Summarising, there is growing evidence that IFRS are related to HzRGs in the sense that IFRS are fainter, but much more abundant siblings of HzRGs, potentially at even higher redshifts. HzRGs are known to be vigorously forming stars while harbouring AGNs in their centres. Both components dominate the emission of galaxies in the IR regime. Observations at far-infrared (FIR) wavelengths are a key test for the hypothesis that IFRS are related to HzRGs.

Here, we analyse the IR and particularly the FIR regime of IFRS based on *Herschel* observations. Results in this wavelength

¹ The spectral index is defined as $S \propto \nu^\alpha$.

range will enable us to further study the suggested link between IFRS and HzRGs.

This paper is organised as follows. In Sect. 2, we describe the sample selection of the observed IFRS and the observations with *Herschel*. The calibration of the resulting data and the mapping is presented in Sect. 3. In Sect. 4, we describe the photometry and the consequent stacking analysis. We use the resulting flux density upper limits in Sect. 5 for two different modelling approaches. First, we model the broad-band SED of IFRS based on SED templates of known galaxies (Sect. 5.1). In a second approach, we set an upper limit on the IR SED of IFRS in order to constrain their IR emission (Sect. 5.2). Based on the latter fitting, we estimate the black hole accretion rate and upper limits for the star formation rate. Finally, in Sect. 6, we present our conclusion. In this paper, we use flat Λ CDM cosmological parameters $\Omega_\Lambda = 0.7$, $\Omega_M = 0.3$, $H_0 = 70 \text{ km s}^{-1} \text{ Mpc}^{-1}$ and the calculator by [Wright \(2006\)](#).

2. Sample and observations

Six IFRS from the sample compiled by [Zinn et al. \(2011\)](#) were photometrically observed with the ESA *Herschel* Space Observatory ([Pilbratt et al. 2010](#)), using the instruments PACS (Photodetecting Array Camera and Spectrometer; [Griffin et al. 2010](#)) and SPIRE (Spectral and Photometric Imaging Receiver; [Poglitsch et al. 2010](#)). The sources were selected to be comparatively bright in the radio regime, showing 1.4 GHz flux densities between 7 mJy and 26 mJy, and to provide high radio-to-IR flux density ratios (see Table 1 also in the following). Since all observed sources are undetected in the SWIRE data between $3.6 \mu\text{m}$ and $24 \mu\text{m}$, their $S_{1.4 \text{ GHz}}/S_{3.6 \mu\text{m}}$ lower limits based on SWIRE range between 2300 and 8700. Five observed IFRS are located in the field of ELAIS-S1 and one in the CDFS. No IFRS located in the ELAIS-S1 field has been detected in the X-ray *XMM-Newton* survey (flux limit of $\sim 5.5 \times 10^{-16} \text{ erg cm}^{-2} \text{ s}^{-1}$ in the 0.5–2 keV band; [Puccetti et al. 2006](#)) as mentioned by [Zinn et al. \(2011\)](#). IFRS S703, located in the CDFS field, has not been covered by the CDFS *Chandra* 4 Ms survey ([Xue et al. 2011](#)). No optical counterpart is known for the six observed IFRS ([Norris et al. 2006](#); [Middelberg et al. 2008a](#)). By these characteristics, the six observed sources are prototypical for the class of IFRS. We note that [Maini et al. \(2015\)](#) find a 3σ counterpart at $3.6 \mu\text{m}$ based in the *Spitzer* Extragalactic Representative Volume Survey (SERVS; [Mauduit et al. 2012](#)) for IFRS S427 after the observations with *Herschel* were carried out.

Figure 1 shows the SWIRE $3.6 \mu\text{m}$ maps of all IFRS observed with *Herschel*, overlaid by the 1.4 GHz radio contours. IFRS S427, S509, and S798 are point-like sources and show almost no extended structure. For S703, in contrast, it might be suggested because of the additional radio component at around RA 03h35m33.5s Dec $-27^\circ 26' 40''$ and the bridge to the IFRS itself that the IFRS is part of a double lobe radio source with the IFRS and the additional component as radio lobes and the host galaxy in between those two components. However, the additional radio component shows a weak $3.6 \mu\text{m}$ counterpart, excluding this component as a radio lobe. Therefore, S703 can be considered as a proper IFRS.

Infrared-faint radio source S973 shows an extended structure and has been listed as two components (RA 00h38m44.723m Dec $-43^\circ 19' 14.58''$ and RA 00h38m43.489s Dec $-43^\circ 19' 26.94''$) by [Middelberg et al. \(2008a\)](#), with the source position in between the two components. Here, however, we considered the position of the

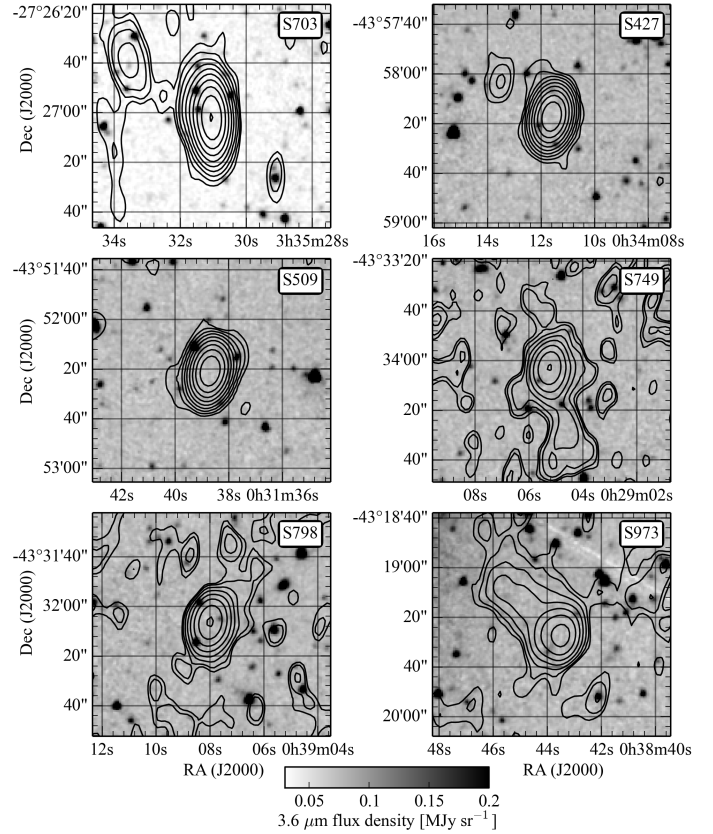


Fig. 1. SWIRE $3.6 \mu\text{m}$ maps (greyscale; [Lonsdale et al. 2003](#)) of all six IFRS observed with *Herschel* overlaid by the 1.4 GHz radio contours (ATLAS data release 3; $\sigma \approx 20 \text{ mJy beam}^{-1}$; [Franzen et al. 2015](#)). Shown are the contours at 2σ , 4σ , 8σ , 16σ , etc. *Top down and from left to right:* S703, S427, S509, S749, S798, and S973.

second, radio-brighter component to be the centre of the host with the weaker component more likely to be a jet. However, the choice of host position does not affect our overall conclusion. The position of the brighter component is listed in Table 1.

Infrared-faint radio source S749 shows an extended structure in the radio map, too. However, this source is located close to the edge of the ATLAS ELAIS-S1 field and, therefore, the noise is higher than for the other IFRS discussed in this work. In the scheduling of the *Herschel* observations, a slightly wrong position of IFRS S749 had been used. Thus, this source is not located in the centre of the *Herschel* maps but closer to the edge, resulting in a higher noise compared to the other sources, particularly at shorter wavelengths. Therefore, we exclude this source from our stacking analysis in Sect. 4.

The PACS observations of these six objects were carried out in July and December 2011 (observation IDs 1342224373, 1342224374, 1342233615, 1342233616, 1342233617, 1342233618, 1342233619, 1342233620, 1342233621, 1342233622, 1342233623, 1342233624). Using the mode mini-scan map, each observation was divided into two parts, arising from two different scan angles. Both scanning parts were centred on the source, observing simultaneously at $100 \mu\text{m}$ and $160 \mu\text{m}$ with a total on-source time of 22.5 min for each source.

The SPIRE observations were carried out in December 2011 and January 2012 (observation IDs 1342234729, 1342234730, 1342234731, 1342234732, 1342234733, 1342238290). Using the observing mode SpirePhotoSmallScan, the sources were

Table 1. Sample of IFRS observed with *Herschel*.

IFRS ID	RA J2000.0	σ_{RA} [arcsec]	Dec J2000.0	σ_{Dec} [arcsec]	$S_{1.4 \text{ GHz}}$ [mJy]	$S_{3.6 \mu\text{m}}$ [μJy]	$S_{24 \mu\text{m}}$ [μJy]	$S_{1.4 \text{ GHz}}/S_{3.6 \mu\text{m}}$	References
S703	03:35:31.025	0.11	-27:27:02.20	0.12	26.1	<2.04	<115	>12 784	(1), (4)
S427	00:34:11.592	0.01	-43:58:17.04	0.00	21.4	1.77 ± 0.54	<150	12 000	(2), (4)
S509	00:31:38.633	0.01	-43:52:20.80	0.01	22.2	<3	<150	>7400	(2), (3)
S749	00:29:05.229	0.04	-43:34:03.94	0.04	7.0	<3	<150	>2337	(2), (3)
S798	00:39:07.934	0.04	-43:32:05.83	0.03	7.8	<3	<150	>2597	(2), (3)
S973	00:38:43.489	0.04	-43:19:26.94	0.04	9.1	<2.70	<150	>3385	(2), (4)

Notes. Infrared-faint radio source S703 is located in CDFS while the other five sources are located in the ELAIS-S1 field. All six IFRS are undetected at $3.6 \mu\text{m}$ in the SWIRE survey ($3\sigma \sim 3 \mu\text{Jy}$) as presented by Zimm et al. (2011). Maini et al. (2015) analysed the deeper SERVS data for three IFRS observed with *Herschel* and find one week counterpart. All upper limits represent 3σ . S973 consists of two radio components. Here, we used the position of the strongest component as the position of the source, in contrast to Middelberg et al. who used the centre between both components. Positions, position uncertainties, radio and $24 \mu\text{m}$ flux densities were taken from the first reference listed in each row, $S_{3.6 \mu\text{m}}$ and $S_{1.4 \text{ GHz}}/S_{3.6 \mu\text{m}}$ from the second reference.

References. (1) Norris et al. (2006); (2) Middelberg et al. (2008a); (3) Zimm et al. (2011); (4) Maini et al. (2015).

observed simultaneously at $250 \mu\text{m}$, $350 \mu\text{m}$ and $500 \mu\text{m}$ for 12 min each.

We recognise that, since these observations were made and this analysis was performed, additional *Herschel* data on IFRS have been released into the public domain by the *Herschel* Multi-Tiered Extragalactic Survey (HerMES; Oliver et al. 2012), the PACS Evolutionary Probe (PEP; Lutz et al. 2011), and the Cosmic Assembly Near-infrared Deep Extragalactic Legacy Survey (CANDELS; Grogin et al. 2011). These data have not been used for the study presented in this work, but will be discussed in a future paper.

3. Data calibration and mapping

The data sets were calibrated using the *Herschel* Interactive Processing Environment (HIPE; Ott 2010, version 12.1.0). We followed the steps presented in the PACS photometer pipeline for deep survey maps provided within HIPE to process the PACS data sets from level 0 to level 2. During the processing to level 1, a mask was created and applied in the task `highpass filter` to prevent artefacts in this median-subtraction process arising from nearby bright sources. The position of the IFRS has also been masked. We obtained the best results using a high-pass filter radius of $15''$. The final maps were built using the task `photProject`, setting the parameter `pixfrac` to 0.5, both for $100 \mu\text{m}$ and $160 \mu\text{m}$. Output pixel sizes of $1.5''$ (for $100 \mu\text{m}$) and $2.1''$ (for $160 \mu\text{m}$), respectively, were found to provide the best maps. Both quantities are parameters of the task `photProject` which is based on the Drizzle method (Fruchter & Hook 2002). Finally, we matched the two maps of each object, obtained from the two different scan angles, using the task `mosaic`. The final PACS maps have a size of around $3.5' \times 6.5'$. The central region with a diameter of around $50''$ provides the highest and an almost uniform sensitivity. Figure 2 (upper subplots) shows the final PACS maps of IFRS S509.

Correspondingly, for the SPIRE data sets, we followed the steps in the appropriate HIPE standard pipeline – the ‘‘Photometer Small Map user pipeline’’ – to calibrate the data. The maps were built using the task `Destriper`, an iterative algorithm to remove the baseline signal in the timeline data. In this task, the implemented `deglitcher` was used. We used the algorithm `naive mapping` implemented in HIPE to build the final maps, projecting the full power seen by each bolometer timeline step to the closest sky map pixel with the pixel sizes given in Table 2. The usable area of the final SPIRE maps is

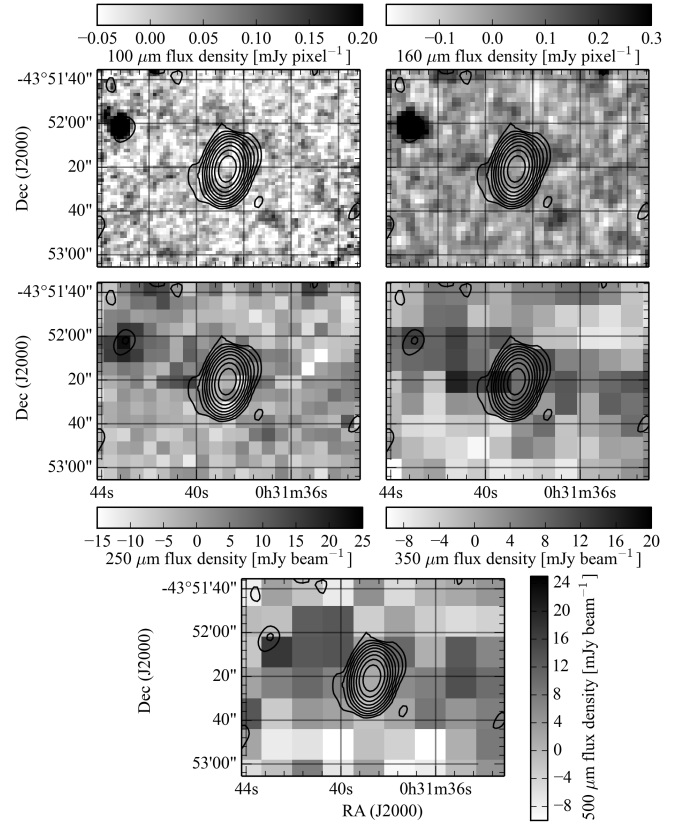


Fig. 2. Final *Herschel* maps (greyscale) of IFRS S509 overlaid by the 1.4 GHz radio contours (ATLAS data release 3; $\sigma \approx 20 \mu\text{Jy beam}^{-1}$; Franzen et al. 2015). Shown are the contours at 2σ , 4σ , 8σ , 16σ , etc. Top down and from left to right: $100 \mu\text{m}$, $160 \mu\text{m}$ (both PACS), $250 \mu\text{m}$, $350 \mu\text{m}$, and $500 \mu\text{m}$ (SPIRE) maps. None of the five maps provides a detection of S509.

around $8' \times 10'$. Figure 2 (lower three subplots) shows the resulting SPIRE maps of IFRS S509.

4. Photometry and stacking

4.1. Photometry

We used the HIPE task `AnnularSkyAperturePhotometry` for photometry on the PACS maps, performing aperture photometry

Table 2. Characteristics of the instruments and parameters of the data reduction and photometry, used in HIPE for the different channels.

Band	<i>FWHM</i> [arcsec ²]	Pixel size [arcsec pixel ⁻¹]	Exposure time [s]
PACS 100 μm	6.69×6.89	1.5	1354
PACS 160 μm	10.65×12.13	2.1	1354
SPIRE 250 μm	17.6×17.6	6	721
SPIRE 350 μm	23.9×23.9	10	721
SPIRE 500 μm	35.2×35.2	14	721

Notes. The numbers of the FWHM are taken from “PACS Observer’s Manual” version 2.5.1 and from “The SPIRE Handbook” version 2.5, respectively.

on a chosen target based on a circular aperture. The related task `PhotApertureCorrectionPointSource` corrected the measured flux density for the finite size of the applied aperture, yielding the requested flux density of the nominal source. We used aperture radii of 5.6'' and 10.5'' for the PACS maps at 100 μm and 160 μm , respectively. The background was estimated and subtracted based on a ring between 20'' and 25'', and 24'' and 28'', respectively. The flux density uncertainties were obtained from 100 similar apertures randomly placed on the map where the coverage was at least 75% of the maximum coverage. We fit a Gaussian to the histogram of these background flux densities, providing the Gaussian width σ . We repeated this procedure ten times and took the median of these Gaussian widths as the uncertainty of the measured flux density. For S749, where the IFRS was not in the centre of the *Herschel* maps as discussed in Sect. 2, we placed 100 similar apertures in a field with a maximum distance to the source of five times the full width at half maximum (FWHM) of a point source to estimate the flux uncertainty.

Our six nominal objects were not detected at 100 μm or at 160 μm . Table 3 summarises the resulting point source flux density uncertainties σ for the six observed IFRS.

Photometry on the SPIRE maps was carried out using the HIPE task `sourceExtractorSussexextractor` based on the SUSSEXtractor algorithm (Savage & Oliver 2007). Adapting this task to the maps, sources were extracted, providing data about brightnesses, positions, and related errors of the sources as well as a cleaned map. The extracted sources were checked for their angular distance to the known position of IFRS (<0.5 FWHM). We repeated this procedure as a second level source extraction on the cleaned map. Again, we checked the extracted sources for their distance to the IFRS’ positions. By this, we were able to extract sources which had been overseen in the first extraction step because of bright and close by sources in the map. These sources had been eliminated in the cleaned map.

For five out of the six IFRS, the source extraction did not provide any FIR component in any SPIRE channel, neither by the source extraction performed on the map itself nor on the cleaned map. For S973, we found 3σ detections in the cleaned maps at 350 μm and 500 μm . The positions of these two FIR counterparts were in agreement with each other and were 12'' distant from the IFRS radio position, which is only slightly below our distance criterion. However, we found that these FIR detections were very close to one source which was detected with a flux density of 6.1 μJy at 3.6 μm in the SERVS survey. Because of those three reasons – weak flux, relatively large distance to the IFRS position, and overlap with a SERVS source – we suggest that these FIR counterparts are associated with the SERVS source and not with our SERVS-undetected IFRS.

We summarise that none of the six observed IFRS was detected in any SPIRE channel. The flux density uncertainties were obtained from the cleaned map by fitting a Gaussian to the pixel values within a square of the size of eight times the FWHM of a point source (see numbers in Table 2). The SPIRE flux density uncertainties at the positions of the IFRS are summarised in Table 3. Our mean noise is lower than the overall confusion noise of 5.8 mJy, 6.3 mJy, and 6.8 mJy at 250 μm , 350 μm , and 500 μm , respectively (Nguyen et al. 2010). However, Nguyen et al. also showed that the residual confusion noise after removing bright sources is lower. Our noises are in agreement with these numbers.

4.2. Stacking of *Herschel* maps

Since no counterpart of an IFRS was detected in the *Herschel* maps, we performed a stacking analysis to search for a potentially weak counterpart slightly below the detection limit. The positional uncertainties for our sources are at least one order of magnitude lower than the pixel size of the *Herschel* maps (see Tables 1 and 2). For each observed wavelength, we stacked the maps centred on the known position of the IFRS. However, we excluded IFRS S749 from the stacking analysis because of the higher noise in the FIR maps (see discussion in Sect. 2). The stacking maps are the results of median stacking the *Herschel* maps for all the five sources with proper centring and signal-to-noise ratio at each wavelength. In case of SPIRE maps, we stacked the cleaned maps, resulting from the first iteration of source extraction described above. The stacking map at 100 μm is shown in Fig. 3 and did not provide a detection. Corresponding stacking maps at 160 μm , 250 μm , 350 μm , and 500 μm , respectively, were similar and did not provide a detection either. We performed photometry on the stacked maps in the same way as described in Sect. 4.1 for the individual maps. The resulting flux density uncertainties are summarised in the last column in Table 3.

4.3. Stacking in the near- and mid-infrared regime

Since the six observed IFRS were also undetected in the SWIRE maps at 3.6 μm and 24 μm , we performed a stacking analysis at these wavelengths to obtain mean properties of our IFRS population in the following analysis.

At 3.6 μm , all six IFRS were covered by SWIRE, but only four by the deeper SERVS survey. We median stacked the 3.6 μm maps at the positions of the six sources. We carried out aperture photometry using an annulus of 1.9'' in radius and a background ring between 3.8'' and 7.6'' and applied aperture corrections. No source was found in the stacked map. The uncertainty was obtained based on 225 randomly placed apertures and background rings of same size and iteratively removing those apertures resulting in flux densities exceeding 3σ . We found an uncertainty of $\sigma_{3.6 \mu\text{m}} = 0.397 \mu\text{Jy}$ in the stacked map.

At 24 μm , all six IFRS were covered by SWIRE. We median stacked the six individual maps and carried out aperture photometry using an annulus of 3.5'' in radius and a background ring between 6.0'' and 8.0'' and applying aperture corrections. No source was found in the stacked map either. We obtained the uncertainty in the same way as described for the stacked map at 3.6 μm and found it to be $\sigma_{24 \mu\text{m}} = 31.3 \mu\text{Jy}$.

Table 3. Resulting point source flux density uncertainties for the six IFRS at the five observed wavelengths.

Band	σ_{S703} [mJy]	σ_{S427} [mJy]	σ_{S509} [mJy]	σ_{S749} [mJy]	σ_{S798} [mJy]	σ_{S973} [mJy]	σ_{stacked} [mJy]
PACS 100 μm	1.78	1.40	1.83	2.17	1.51	1.43	0.76
PACS 160 μm	4.02	3.56	2.43	6.09	2.84	2.77	1.66
SPIRE 250 μm	5.03	4.20	4.51	4.43	4.94	4.99	2.68
SPIRE 350 μm	4.61	3.81	4.42	4.59	3.87	5.71	2.52
SPIRE 500 μm	5.50	4.80	4.85	6.24	5.36	7.23	3.53

Notes. The last column shows the respective uncertainties in the stacked maps, resulting from a median stack of five individual maps at each wavelength.

5. Modelling and analysis

The *Herschel* observations between 100 μm and 500 μm of the six IFRS presented in this work did not provide a detection. A stacking analysis did not show an FIR counterpart below the detection limit either. However, the flux density upper limits measured in Sect. 4 put constraints on the SED of IFRS.

The six IFRS observed with *Herschel* were selected to show high radio-to-IR flux density ratios (>2000 ; see Sect. 2). Five of these IFRS are undetected in the near-IR regime while SERVS provides a 3.2σ counterpart at 3.6 μm for one IFRS as reported by Maini et al. (2015). This counterpart was unknown at the time when the observations with *Herschel* were carried out. Except for this single near-IR detection, these six IFRS are solely detected in the radio regime. Thus, no redshift is known for these sources. By these characteristics, the six IFRS observed with *Herschel* are among the most extreme objects in the class of IFRS.

All IFRS with known spectroscopic redshifts, presented by Collier et al. (2014) and Herzog et al. (2014), are faintly detected in the near-IR regime. Their redshifts, $1.8 \lesssim z \lesssim 3$, are in agreement with the suggestion by Norris et al. (2011) that IFRS follow the correlation between 3.6 μm flux density and redshift found for HzRGs by Seymour et al. (2007). Assuming that this correlation holds at lower IR flux densities, as it does for HzRGs, the IFRS observed with *Herschel* would be placed at redshifts of $z \gtrsim 4$ or higher because of their 3.6 μm faintness.

We emphasise that no redshift above $z \gtrsim 3$ has been measured for an IFRS, presumably because those are too faint for spectroscopic observations. Although we speculate that the IFRS discussed here are at $z \gtrsim 4$, we consider the broad redshift range $1 \leq z \leq 12$.

In the following, we tried to limit possible explanations for the phenomenon of IFRS, performing a broad-band SED modelling based on SED templates of known galaxies (Sect. 5.1). We started with the simplest approach and shifted these templates in a broad redshift range, testing them against the photometric data of IFRS (Sect. 5.1.1). Subsequently, we broadened the parameter space by modifying our broad-band SED templates. We scaled the templates in luminosity (Sect. 5.1.2), added extinction (Sect. 5.1.3), and finally modified them simultaneously in luminosity and extinction (Sect. 5.1.4). In each approach, we tested their compatibility with the photometric constraints of IFRS. Finally, we constrained the IR SED of IFRS based on decomposing their IR SED into an AGN and a starburst (SB) component (Sect. 5.2), both putatively contributing to the total emission of this peculiar class of objects.

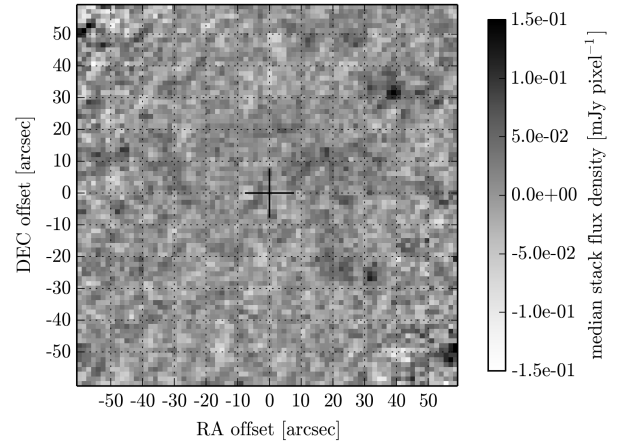


Fig. 3. Resulting stacking map obtained from a median stack of the five IFRS at 100 μm . IFRS S749 was excluded because of the higher noise as discussed in Sect. 2. The individual maps were centred on the position of the IFRS which is marked by a cross in the centre of the map. No detection has been found in the stacking map.

5.1. Broad-band SED modelling

In order to model the broad-band SED of IFRS, we used photometric data of our objects in all available wavelength regimes. The IFRS observed with *Herschel* provided 1.4 GHz flux densities between 7 mJy and 26 mJy. In the modelling, we used a median 1.4 GHz flux density of 15 mJy, but also discuss the outcome for higher and lower radio flux densities. Furthermore, we used available constraints at 3.6 μm and 24 μm . At 3.6 μm , we used a median 3σ flux density upper limit of 1.19 μJy as discussed in Sect. 4.3. In the mid-IR at 24 μm , we used a 3σ flux density upper limit of 94 μJy based on the stacking described in Sect. 4.3. Furthermore, we made use of the FIR flux density upper limits at five wavelengths between 100 μm and 500 μm measured in this work. More precisely, we used 3σ flux density upper limits based on the uncertainties in the median stacked maps presented in Sect. 4.2 and summarised in the last column in Table 3.

Based on photometric data and redshifts from the NASA/IPAC Extragalactic Database (NED), we built SED templates for different objects by connecting the data points and smoothing the template where appropriate. We used templates of the spiderweb galaxy (an HzRG, also known as MRC 1138-262), the local radio galaxy Cygnus A (also known as 3C 405), the CSS source 3C 48, the RL quasar 3C 273, the local ULIRG Arp 220, the Seyfert galaxy Mrk 231, the local SB galaxy M82, an RL hyper-luminous infrared galaxy (HyLIRG; IRAS F15307+3252), IRAS F00183-7111 (referred to as F00183; this object is a ULIRG, showing contribution of an

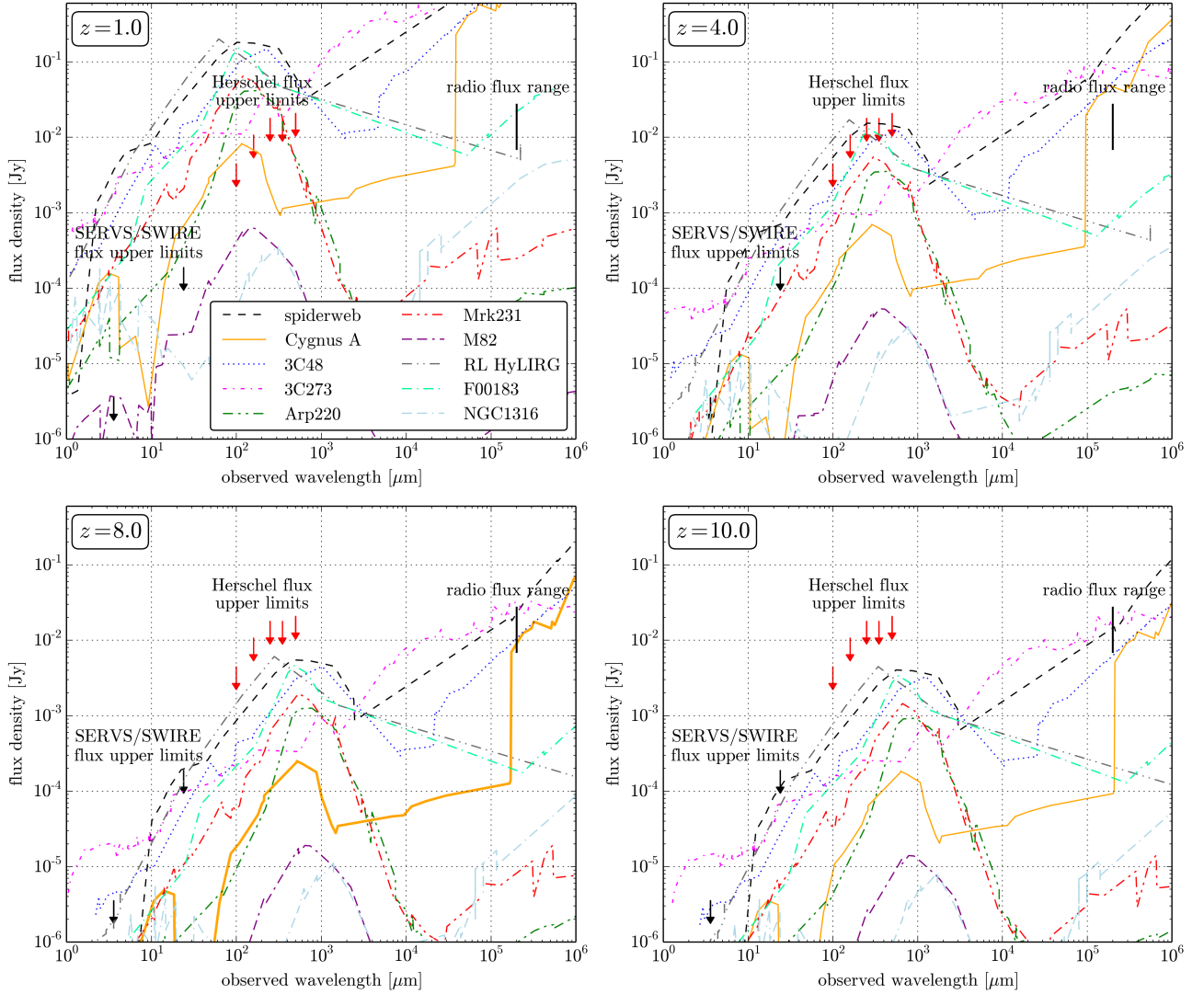


Fig. 4. Broad-band SED modelling for IFRS, using the FIR flux density upper limits measured in this work (red arrows), SERVS/SWIRE near- and mid-IR flux density upper limits (black arrows), and the detections at 1.4 GHz (black bar). The template SEDs were shifted to redshifts between $z = 1$ and $z = 12$. Shown are the results at $z = 1$ (upper left subplot), $z = 4$ (upper right), $z = 8$ (lower left), and $z = 10$ (lower right), respectively. The legend shown in the upper left subplot is valid for all four subplots. At redshifts $z \lesssim 5$, no template is in agreement with the photometric constraints of IFRS. However, if shifted to the redshift regime $5 \lesssim z \lesssim 8.5$, Cygnus A (orange solid line) is in agreement with all constraints. The spiderweb galaxy (black dashed line) provides an appropriate template if shifted to very high redshifts $z \gtrsim 10.5$. The CSS source 3C 48 (blue dotted line) and the RL quasar 3C 273 (magenta dashed-dotted line) fulfil the constraint in the radio regime at redshifts $6 \lesssim z \lesssim 9$ and $8 \lesssim z \lesssim 12$, respectively, but disagree with the $3.6 \mu\text{m}$ flux density upper limits at these redshifts.

RL AGN combined with significant SB activity), and the quiescent elliptical brightest cluster galaxy NGC 1316. We added photometric IR data between $100 \mu\text{m}$ and $870 \mu\text{m}$ from Seymour et al. (2012) to the template of the spiderweb galaxy since the IR coverage of this template is poor in NED and this wavelength regime is crucial for our analysis. All photometric data points from Seymour et al. are at least 4σ detections.

5.1.1. Shifting broad-band SED templates to various redshifts

As a simplest approach, we tested whether any SED template of a known galaxy is in agreement with the available photometric data of IFRS when these templates were shifted to different redshifts, keeping constant rest-frame luminosity and scaling flux densities using a flat Λ CDM cosmology ($\Omega_\Lambda = 0.7$, $\Omega_M = 0.3$,

$H_0 = 70 \text{ km s}^{-1} \text{ Mpc}^{-1}$). The resulting plots for redshifts of 1, 4, 8, and 10, respectively, are shown in Fig. 4.

In the redshift regime $1 \lesssim z \lesssim 5$, no template fulfils all available photometric constraints, i.e. none of these objects would produce the observational characteristics of IFRS if placed at redshifts $z \lesssim 5$. However, for redshifts in the range $5 \lesssim z \lesssim 8.5$, Cygnus A provided an appropriate template to fulfil the photometric constraints of IFRS. The spiderweb galaxy SED was in agreement with all available photometric data of IFRS when shifted to $z \gtrsim 10.5$. At lower redshifts, the radio and the near-, mid-, and FIR flux densities of the spiderweb galaxy exceeded the measured fluxes of IFRS. We also tried templates of other HzRGs (e.g. 3C 470, 4C 23.56) and found the same qualitative result.

The CSS source 3C 48 and the RL quasar 3C 273 matched the measured radio flux density of IFRS if shifted to the redshift regimes $6 \lesssim z \lesssim 9$ and $8 \lesssim z \lesssim 12$, respectively. However, at

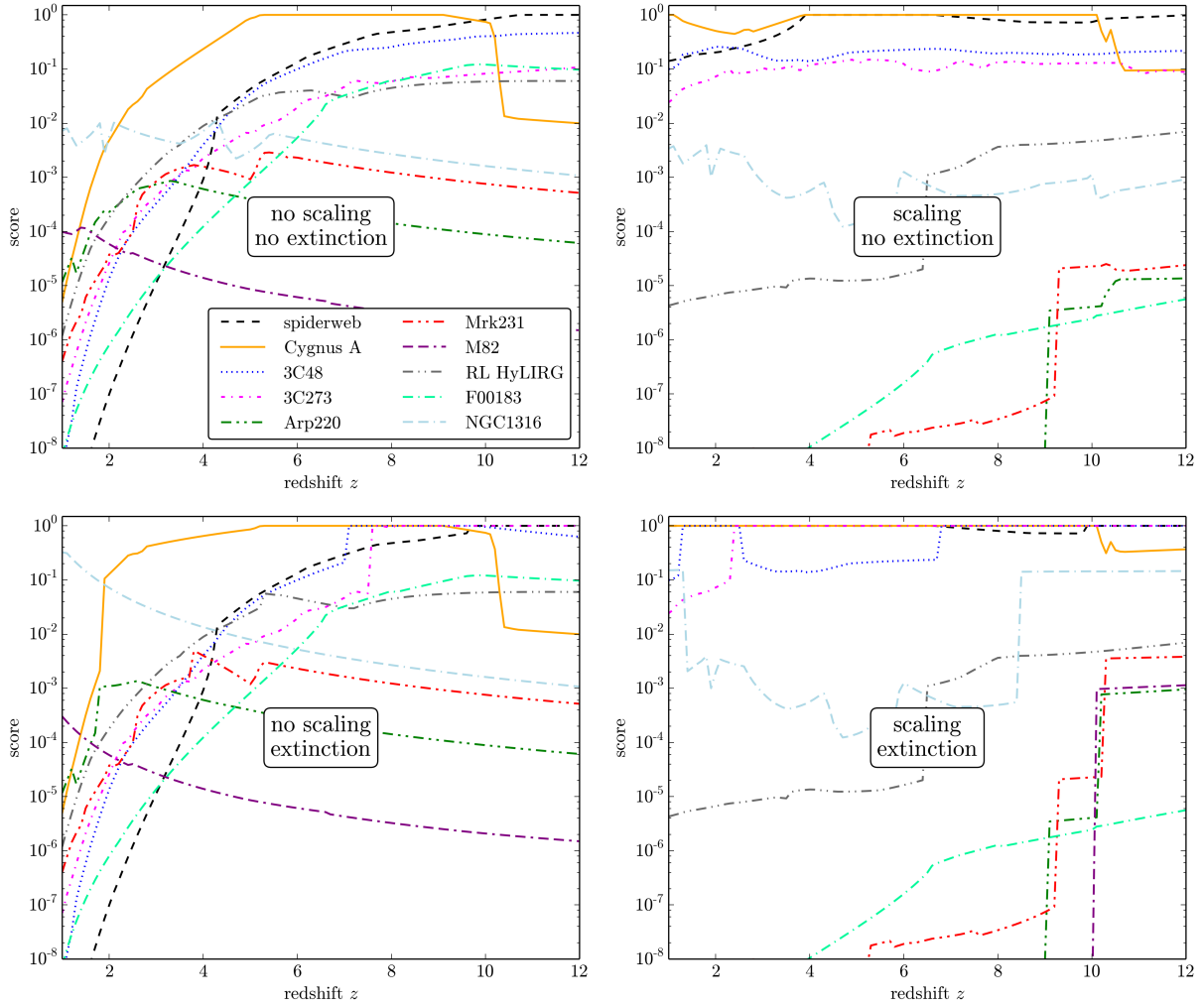


Fig. 5. Score for different SED templates as a function of redshift, measured in our broad-band SED modelling. A score of 1 implies that the SED is in agreement with all photometric constraints of the IFRS discussed in this work. Shown is the score resulting from modelling without scaling and without additional extinction (*upper left*), with scaling and without additional extinction (*upper right*), without scaling and with additional extinction (*lower left*), and with scaling and with additional extinction (*lower right subplot*), respectively. In both plots on the right hand side, the templates were scaled to a 1.4 GHz flux density of 15 mJy. The legend shown in the *upper left subplot* is valid for all four subplots.

these redshifts, their $3.6 \mu\text{m}$ flux densities exceeded the related measured flux density upper limits of IFRS up to a factor of ten, ruling out these templates. All other templates were found to be in strong disagreement with the IFRS data at all redshifts between 1 and 12. Either the radio flux densities of the templates exceeded the measured flux density of IFRS or the templates disagreed with the near-, mid-, and FIR flux density upper limits of IFRS by several orders of magnitude.

We also estimated a score for each SED template at each redshift. For this purpose, we derived the score s based on a modified L_1 norm (e.g. [Horn & Johnson 1985](#)) given by

$$s = 10^{-\sum_i \left| \log_{10} \frac{y_i}{m_i} \right| - \sum_j H[m_j - 3\sigma_j] \left| \log_{10} \frac{3\sigma_j}{m_j} \right|} \quad (1)$$

The first sum in the exponent runs over the wavelengths i at which our sample of IFRS is detected, where y denotes the flux density of IFRS and m the flux density of the respective SED model. The second sum accounts for deviations of the SED model from the flux density upper limits of IFRS and sums over the wavelengths j at which the IFRS are undetected with an rms σ , using a Heaviside step function H . In order to avoid an

overweighting of the FIR regime when deriving a score due to the five independent flux density measurements in this regime, we only used one out of the five *Herschel* wavelengths. Thus, the wavelength resulting in the highest addend $|\log_{10}(3\sigma_j/m_j)|$ was used for this purpose.

This implies that a score of 1 is obtained by an SED which is in agreement with all eight photometric constraints of the IFRS considered in this work. We emphasise that a score of 1 does not imply that the SED of IFRS necessarily follows the respective template. However, the score provides useful insights how well a template agrees with the data of IFRS at a respective redshift. The upper left subplot in Fig. 5 shows the score as a function of redshift for different templates.

We found only the spiderweb galaxy and Cygnus A are consistent with the photometric data of IFRS when shifted to appropriate redshifts. If IFRS have the SED of a known galaxy, IFRS have to be at redshifts $z \gtrsim 5$. This is consistent with the suggestion by [Norris et al. \(2011\)](#), [Collier et al. \(2014\)](#), and [Herzog et al. \(2014\)](#) that the IFRS observed with *Herschel* are at redshifts $z \gtrsim 4$ because of their faintness at $3.6 \mu\text{m}$ as discussed above.

5.1.2. Modifying broad-band SED templates in redshift and luminosity

In the broad-band SED modelling presented in Sect. 5.1.1, redshift was the only free parameter. We found that only HzRGs (e.g. the spiderweb galaxy) and Cygnus A provide appropriate templates to explain the emission characteristics of IFRS, and only if shifted to redshifts $z \gtrsim 5$. In the following, however, we aimed at testing whether the SED characteristics of IFRS can be reproduced by objects at lower redshifts. For this purpose, we broadened the parameter space and used templates modified by varying their luminosity.

In this approach, we included a wavelength-independent luminosity scaling factor as an additional parameter. This allowed the templates to be scaled to match the mean radio flux density of the IFRS observed with *Herschel* ($S_{1.4\text{ GHz}} \approx 15\text{ mJy}$), since these sources are solely detected in the radio regime apart from the weak $3.6\text{ }\mu\text{m}$ counterpart of S427.

The upper right subplot in Fig. 5 shows the score versus redshift for the different templates when they were scaled in luminosity to match the median radio flux density of the IFRS discussed in this work. In this approach, we found the spiderweb galaxy is in agreement with the available photometric constraints at redshifts in the range $4 \lesssim z \lesssim 6.5$ when scaled in luminosity by factors between 0.08 and 0.4. At higher redshifts, the scaled template SED exceeded the $24\text{ }\mu\text{m}$ flux density upper limits and therefore resulted in a score below 1. The SED template of Cygnus A was also found to be in agreement with the data at $z \sim 1$ and in the redshift range $4 \lesssim z \lesssim 10$ when scaled in luminosity by factors between 0.007 and 2. In the redshift range $1.5 \lesssim z \lesssim 4$, the scaled template disagreed with the $3.6\text{ }\mu\text{m}$ flux density upper limit. All other templates were in disagreement with at least one upper limit at any redshift.

When scaling the templates to match the faint end of the observed radio flux density range of IFRS of 7 mJy, the spiderweb galaxy template was in agreement with all constraints when shifted to the redshift range $z \gtrsim 3.5$, and Cygnus A if shifted to the range $z \lesssim 2$ or $3 \lesssim z \lesssim 10.5$. None of the other templates agreed with all photometric constraints. In contrast, if the templates were scaled to the radio flux density of the radio-brightest IFRS in our sample (26 mJy), only the template of Cygnus A was in agreement with the IR flux density upper limits ($4.5 \lesssim z \lesssim 10$). However, at $z \sim 4$, the template of the spiderweb galaxy only slightly violated the $24\text{ }\mu\text{m}$ flux density upper limit.

5.1.3. Modifying broad-band SED templates in redshift and extinction

We found in Sect. 5.1.1 that the redshifted SED templates of 3C 48, and 3C 273 were in agreement with the radio flux density range and the FIR flux density upper limits of IFRS, however exceeding the near- or mid-IR flux density upper limits. Therefore, here, we tested whether some of our templates could be squeezed below these IR flux density upper limits when additional extinction was added to the templates.

For this purpose, we added extinction in the rest-frame optical and near-IR regime of the template SEDs if required. We used the Calzetti et al. (2000) reddening law which reduces emission at rest-frame wavelengths between $0.12\text{ }\mu\text{m}$ and $2.2\text{ }\mu\text{m}$. We limited the additional extinction to an arbitrary number of 500 mag. In our modelling, we applied energy conservation by calculating the power hidden by the additional amount of dust in the rest-frame optical and near-IR regime and re-radiating this power at mid- and FIR wavelengths. We implemented this power

conservation in our modelling by adding a dust emission component of the same power as hidden by the additional extinction in the optical and near-IR regime.

The emission of dust is usually described by a modified black-body spectrum, i.e. $S_\nu \propto B_\nu(T)\epsilon_\nu$, where $B_\nu(T)$ is the black-body emission given by the temperature T and ϵ_ν is the emissivity function at a frequency ν . We followed simple approaches, using only one dust temperature $T = 70\text{ K}$ and assuming $\epsilon \propto \nu^\beta$ with $\beta = 1.5$. The emissivity spectral index β depends on dust grain properties as size and composition and usually ranges between 1 and 2. We note that the choice of this spectral index in the given range did not qualitatively change our results; neither did changing the dust peak temperature between 30 K and 100 K.

The plot of the scores resulting from this modelling approach – adding extinction to the redshifted SED templates – is shown in the lower left subplot in Fig. 5. It should be noted that no scaling in luminosity as presented in Sect. 5.1.2 had been applied in this approach. We found the spiderweb galaxy template in agreement with the data at redshifts $z \gtrsim 9.5$. At $z \sim 10$, 5.6 mag of additional extinction brought this SED template in agreement with the data. At higher redshifts, no additional extinction was required. Cygnus A was in agreement with all flux density upper limits in the redshift range $5 \lesssim z \lesssim 9$ without adding extinction as shown in Sect. 5.1.1. 3C 273 matched the data at redshifts $z \gtrsim 7.5$ if between 8.6 mag and 1.4 mag of extinction were added. 3C 48 was in agreement with all IR flux density upper limits at $z \gtrsim 7$ if between 1.4 mag and 0.2 mag of extinction were added. However, the radio flux density of 3C 48 exceeded the minimum flux density of 7 mJy at high redshifts $z \gtrsim 9.5$. All other SED templates were found to be in disagreement with the data at any redshift.

Even enormous and unphysically high amounts of extinction of 500 mag were insufficient to squeeze the near-IR emission of some templates below the flux density upper limit at the observed wavelength of $3.6\text{ }\mu\text{m}$. In that case, we did not add extinction to the templates, resulting in the appropriately low score at the respective redshift. This happened for all radio-quiet templates like Arp220, Mrk231, or M82 at redshifts $z \lesssim 5$. However, at higher redshifts, when additional extinction was able to squeeze the templates below the IR flux density upper limits, the templates were by far too faint in the radio regime to explain the emission features of IFRS.

5.1.4. Modifying broad-band SED templates in redshift, luminosity, and extinction

Finally, in the last step of our broad-band SED modelling, we combined the approaches presented in Sects. 5.1.2 and 5.1.3. Here, we modified the SED templates by shifting them in the redshift range $1 \leq z \leq 12$, scaling them in luminosity to match the observed radio flux density, and adding extinction – if required – to squeeze the SED templates below the near- and mid-IR flux density upper limits. IR re-radiation was implemented as described in Sect. 5.1.3.

The resulting plot of the score as a function of redshift is shown in the lower right subplot in Fig. 5. We note that each template at each redshift had been modified by an individual scaling factor and – if necessary – an individual amount of extinction had been added.

Similar to the approaches presented before, we only found the spiderweb galaxy, Cygnus A, the CSS source 3C 48, and the RL quasar 3C 273 to provide suitable templates to explain the observational data of IFRS. The spiderweb galaxy was in

agreement with the data at all redshifts except for the range $6.5 \lesssim z \lesssim 9.5$. In this redshift range, the template exceeded the $24 \mu\text{m}$ flux density upper limit despite adding additional extinction. The template of Cygnus A matched all constraints at $z \lesssim 10$ and 3C 273 at redshifts $z \gtrsim 2.5$. 3C 48 was in agreement with the data at any redshift except for very low redshifts $z \lesssim 1.5$ and except for the range $2.5 \lesssim z \lesssim 7$.

In the respective redshift ranges, an appropriate scaling factor and an appropriate amount of extinction was found for the spiderweb galaxy, Cygnus A, 3C 48, and 3C 273 to match all photometric constraints known for these IFRS. For example at $z = 4$, the spiderweb galaxy and Cygnus A needed to be scaled down in luminosity by a factor of 10 and 3, respectively, to match the radio flux density of 15 mJy. No extinction was needed in these cases. In contrast, 3C 273 required 3.2 mag of extinction when scaled down by a factor of 5 to match the radio data point, while 3C 48 could not be modified at this redshift to match all constraints.

Matching the radio flux densities of the radio-brightest IFRS in our sample (26 mJy at 1.4 GHz), again in case of a shift to $z = 4$, an additional extinction of 1.3 mag was required in case of Cygnus A, whereas no reasonable amount of extinction could be added to the templates of the spiderweb galaxy, 3C 48, and 3C 273, to match the near- and mid-IR flux density upper limits. Considering the radio-brightest IFRS in our sample, at $z \lesssim 4.5$, only the Cygnus A SED template could be brought in agreement with the constraints of these most extreme – i.e. with the highest radio-to-IR flux density ratios – IFRS, if up to 4.1 mag of extinction were added. At higher redshifts $z \gtrsim 10$, 3C 48 and the spiderweb galaxy provided appropriate templates, too. 3C 273 was in agreement with the data at $4.5 \lesssim z \lesssim 5.5$ and $7.5 \lesssim z \lesssim 12$. In contrast, if the templates were scaled to a 1.4 GHz flux density of 7 mJy, the spiderweb galaxy, Cygnus A, 3C 273, and 3C 48 could be modified to be in agreement with all photometric constraints at any redshift, except for Cygnus A at very high redshifts $z \gtrsim 10$.

All other templates used in this broad-band SED modelling disagreed with the observational data when shifted to the redshift range $1 \leq z \leq 12$, scaled in luminosity, and extinction was added. These templates were clearly ruled out by their disagreement with the flux density upper limits of IFRS in the FIR regime measured in this work. Particularly, the templates of an RL HyLIRG or F00183, representing common classes of luminous objects at $z \gtrsim 2$, were found to be inappropriate to reproduce the SED constraints of IFRS at any redshift.

5.1.5. Summary of broad-band SED modelling

We summarise our findings from the broad-band SED modelling as follows. When using templates of existing galaxies (Sect. 5.1.1), the SED characteristics of IFRS can only be explained by the SEDs of Cygnus A and HzRGs, however only at high redshifts $5 \lesssim z \lesssim 8.5$ and $z \gtrsim 10.5$, respectively. If IFRS are at lower redshifts ($z \lesssim 5$), their SED constraints can be fulfilled by fainter versions of an HzRG or Cygnus A (Sects. 5.1.2 and 5.1.4), by a dust-obscured CSS source, or by a dust-obscured RL quasar (Sects. 5.1.3 and 5.1.4).

If IFRS are linked to HzRGs as suggested by Middelberg et al. (2011), Norris et al. (2011), Collier et al. (2014), and Herzog et al. (2014), there are two different suggested options: (a) IFRS are very similar to HzRGs – i.e. with similar luminosities – however at higher redshifts ($z \gtrsim 5$); or (b) IFRS are fainter siblings of HzRGs at similar redshifts ($1 \leq z \lesssim 5$). Based on the template of the spiderweb galaxy, we found that

both options are consistent with the FIR flux density upper limits of IFRS measured in this work and the related broad-band SED modelling. If IFRS have the same intrinsic properties as HzRGs, represented by no scaling and no adding of extinction in our modelling, they have to be located at very high redshifts $z \gtrsim 10.5$ (Fig. 5, upper left subplot). Alternatively, if IFRS are fainter siblings of HzRGs, i.e. they are scaled down in luminosity and potentially more dusty, they could be located at lower redshifts $z \geq 1$ (Fig. 5, lower right subplot). It should be noted that extinctions between 14 mag and 5 mag had to be added to the scaled spiderweb galaxy SED template at redshifts $z \leq 2$ to match the IR flux density upper limits.

Two of the templates, 3C 48 and 3C 273, were found to be in agreement with the data of IFRS only if additional extinction in the order of up to several magnitudes was added to the templates as discussed in Sect. 5.1.4. Particularly, these modified templates did not exceed the FIR flux density upper limits of IFRS measured in this work. This implies that a significant dust obscuration in IFRS, explaining the optical and near-IR faintness of these objects, cannot be ruled out. In fact, if the IFRS observed here are similar to 3C 48 or 3C 273, these sources have to be dust obscured to produce the photometric constraints of IFRS.

The results of this broad-band SED modelling are generally in agreement with the findings by Herzog et al. (2014). Herzog et al. measured spectroscopic redshifts of three IFRS detected in the optical and near- and mid-IR regime and did the first redshift-based SED modelling for the class of IFRS. They find the modified templates of 3C 48 and 3C 273 in agreement with all available photometric data of these three IFRS, whereas the templates of star forming galaxies and Seyfert galaxies were clearly ruled out. We also agree with the finding that only RL objects can explain the photometric constraints of IFRS. However, Herzog et al. find that no additional extinction is required for 3C 48 and 3C 273 in their SED modelling. Here, in contrast, we found that IFRS might be dust obscured RL quasars with spectra similar to 3C 48 or 3C 273. However, Herzog et al. studied the IR-brightest IFRS, whereas the IR-faintest IFRS are studied in the current work, providing a valid reason for the discrepancy. Huynh et al. (2010) modelled the SED of individual IFRS and find that the scaled SED template of 3C 273 is in agreement with their data if around one magnitude of extinction was added. This is in agreement with our modelling, considering that the IFRS from Huynh et al. are more than ten times fainter in the radio compared to the IFRS discussed in the present work. We found that IFRS have to be dust obscured, too, if IFRS are similar to HzRGs at $z \lesssim 3.5$. However, if the spectral shape of IFRS is related to that of HzRGs, no extinction is required to explain the SED characteristics of IFRS if these templates are shifted to higher redshifts.

Our broad-band SED modelling showed that the SED templates of the spiderweb galaxy and of Cygnus A can be shifted to $1 \leq z \leq 2$ and modified to agree with the photometric observations of IFRS. However, in contrast, all 21 spectroscopic redshifts of IFRS are in the range $1.8 < z < 3$, i.e. no IFRS has been found at lower redshifts $z \sim 1$. There are two potential reasons for this discrepancy. (a) Our modelling – by shifting the templates in redshift, scaling them in luminosity, and adding extinction – is not physically realistic for galaxies at $z \sim 1$. At these low redshifts, all appropriate templates needed to be scaled down in luminosity up to factors of 500. Presumably, the black hole mass needs to be scaled down by a similar factor. However, RL AGN with lower-mass black holes are very rare (Rees et al. 2015). If the galaxy loses its radio excess by scaling down the black hole mass, the characteristically high radio-to-IR flux density ratio of

IFRS would not be reached and the galaxy would not be considered as an IFRS. Furthermore, in case of the spiderweb galaxy template, the required high amounts of additional extinction of around 10 mag at low redshifts are very rare and decrease the possibility to observe such extreme objects. (b) The IFRS discussed in this work are intrinsically different to the IFRS with known spectroscopic redshifts. Cygnus A provided the only template which can reproduce the characteristics of IFRS at $z \sim 1$ without additional dust obscuration. However, it is known that Cygnus A contains a hidden quasar (Antonucci et al. 1994), resulting in narrow emission lines, whereas IFRS were found to show broad emission lines in their optical spectra (Collier et al. 2014; Herzog et al. 2014). If the IFRS discussed in this work are indeed fainter versions of Cygnus A at redshifts $z \sim 1$, these IFRS would have different properties than the IR-detected IFRS presented by Collier et al. and Herzog et al.. They would form a separate subclass with different redshift and emission line properties. However, so far, no evidence has been found that the population of IFRS might be divided into two sub-classes.

We note that the modified templates of Cygnus A, 3C 48, and 3C 273 – found to match all photometric constraints of IFRS – can be considered as HzRGs in our modelling at $z \geq 1$. At these redshifts, they fulfil both selection criteria of HzRGs: $z > 1$ and $L_{3\text{ GHz}} > 10^{26} \text{ W Hz}^{-1}$. Although we scaled down the templates in luminosity at lower redshifts, they were radio-luminous enough to be considered as HzRGs. We can therefore conclude that only HzRGs can explain the photometric characteristics of IFRS.

Our broad-band SED modelling showed several templates that contain a significant SB contribution in disagreement with the available photometric data (Arp220, M82, RL HyLIRG, F00183). In contrast, the highly star forming spiderweb galaxy fulfilled the photometric data constraints of IFRS. Therefore, in the following, we analysed a potential star forming contribution to the SED of IFRS, instead or in addition to an RL AGN.

5.2. IR SED modelling

One of the crucial questions in revealing the nature of IFRS consists in unmasking the star forming activity and its contribution to the energy output in contrast to the activity of the galactic nucleus. In the IR regime, the emission of galaxies is mainly given by these two components, i.e. AGN and SB. The AGN emission comes from dust, reprocessing far-UV through optical light, and peaks at around $10 \mu\text{m}$, corresponding to a dust temperature of 300 K. In contrast, the stellar component is strongest in the FIR and arises from stellar emission reprocessed to the FIR regime by dust grains with a maximum at a wavelength around $100 \mu\text{m}$, corresponding to 30 K.

5.2.1. IR SED fitting based on IR flux density upper limits

In order to decompose the IR emission of HzRGs, Drouart et al. (2014) fit the IR SED of HzRGs constrained by *Herschel* and ancillary IR data. They used an IR SED model based on the assumption that the IR emission comes from dust heated by star forming activity and an AGN. They built template SEDs, adding an empirical AGN template and one SB template out of a set of empirical SB templates.

Here, we followed this approach, aiming at setting upper limits on the IR SED of IFRS based on the available FIR flux density upper limits measured in Sect. 4. We used templates derived by Mullaney et al. (2011), covering the rest-frame wavelength

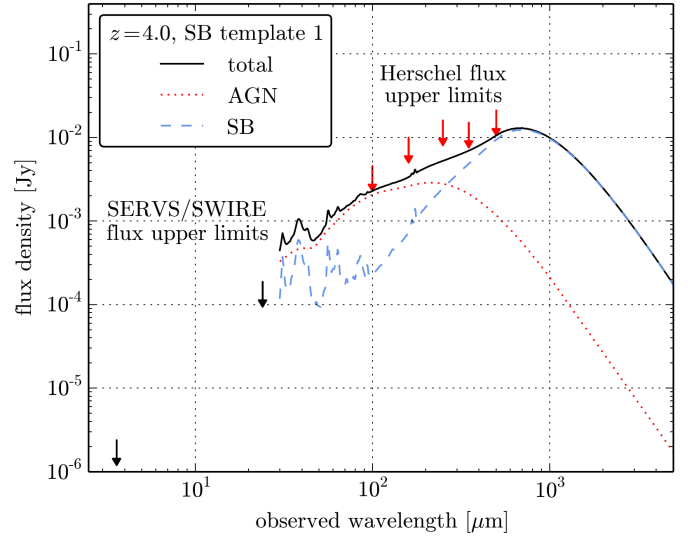


Fig. 6. IR SED modelling for IFRS at redshift $z = 4$, using the FIR flux density upper limits (red arrows) measured in this work. The total (black solid line) IR emission is composed of an AGN component (red dotted line) and a SB component (blue dashed line). The maximum model represents an upper limit on the IR emission of IFRS and is defined by the highest IR flux which is in agreement with all available flux density upper limits.

range between $6 \mu\text{m}$ and $1090 \mu\text{m}$. Mullaney et al. empirically built five different SB templates, differing in their peaking temperature as well as in the strength of the emission of the polycyclic aromatic hydrocarbon (PAH) molecules. These templates cover the entire range of host galaxies (see Mullaney et al. 2011 for a detailed description of the SEDs). Based on these SB templates, they derived one AGN template as the residual SED after removing the SB contribution.

We used these templates and built the total IR SED by multiplying the AGN template by a wavelength-independent luminosity scaling factor and adding one SB template which was also multiplied by a wavelength-independent luminosity scaling factor. We set an upper limit on the IR emission by modelling the SED in order to minimise the deviation between the total SED, i.e. the sum of SB and AGN template, and the available observed 3σ FIR flux density upper limits from the stacked maps (see last column in Table 3). It was required that the available flux density upper limits were fulfilled in the modelling. In this procedure, the most appropriate SB template out of the five available templates was determined based on the lowest deviation. At redshifts $z \leq 3$, the observed $24 \mu\text{m}$ emission fell into the templates' wavelength coverage. At these redshifts, we used the 3σ flux density upper limit at $24 \mu\text{m}$ – measured in Sect. 4.3 from the stacked map – in addition to the FIR flux density upper limits measured in the present work.

By this approach, we determined exactly that total IR SED – consisting of the AGN template and one SB template – which has maximum IR flux but is still in agreement with all available flux density upper limits. Figure 6 shows the resulting IR SED modelling for $z = 4$. We emphasise that our modelling represents an upper limit on the total IR emission of IFRS.

This approach implies that the true AGN contribution to the emission of the IFRS could be higher than the contribution calculated from the maximum total model described above, though accompanied by a lower SB contribution, and the other way

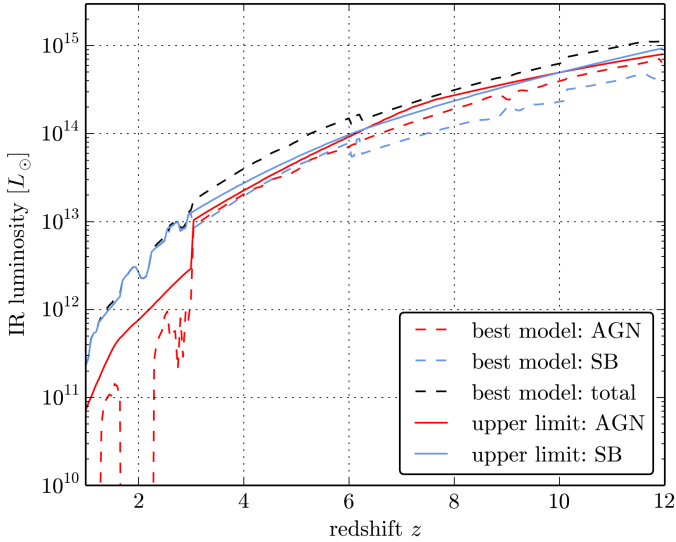


Fig. 7. Infrared luminosity versus redshift for the SB (blue) and AGN (red) component as well as for the total IR luminosity (black). The dashed lines show the data of the maximum IR SED model, combining the AGN and the most appropriate SB template. The solid lines show the IR luminosity upper limits for both components, assuming that the other component does not contribute to the IR emission at each time.

around. However, the difference to the highest possible contribution of each component is generally rather low.

By this modelling, aiming at setting upper limits on the IR emission and referred to as “maximum model”, we decomposed the maximum IR SED into an AGN component and an SB component. Based on this decomposition, we were able to derive IR luminosities of both components by integrating the flux density in the rest-frame wavelength range between $8 \mu\text{m}$ and $1000 \mu\text{m}$. Figure 7 shows the IR luminosities versus redshift for both components and the total IR luminosity of the maximum model. Furthermore, the figure shows the absolute upper limit for both the SB and the AGN IR luminosity, assuming that the other IR emitting process does not contribute at each time. For both components, the luminosities of the maximum model are generally only slightly lower than the absolute upper limit luminosities, except for the SB component at very high redshifts. We note that the jump in the maximum IR luminosity of the AGN and of the SB component at $z = 3$ is related to the flux density upper limit at $24 \mu\text{m}$ which only coincides with the template’s wavelength range at redshifts $z \lesssim 3$.

We emphasise that almost any decomposition of the IR SED into SB and AGN component is possible for IFRS since this wavelength regime is only constrained by upper limits. Therefore, we are only able to set upper limits on the luminosity. Particularly, we note that the maximum model shown in Figs. 6 and 7 is not more likely than any other combination of SB and AGN components which is in agreement with the flux density upper limits. However, the maximum model represents exactly that combination of SB and AGN components which results in the highest total flux but is still in agreement with all flux density upper limits. Therefore, this maximum model sets the upper limit on the total IR luminosity.

We found that the FIR flux density upper limits measured in this work constrain IFRS to have total IR luminosities of $<10^{12} L_{\odot}$ at redshifts $z \lesssim 1.5$. At $z \lesssim 2.5$, IFRS can have a maximum IR luminosity between $10^{12} L_{\odot}$ and $10^{13} L_{\odot}$. Such sources

are labelled as ULIRGs. At redshifts $z \lesssim 6$, the IR luminosity of IFRS can be at most $10^{14} L_{\odot}$ which allows IFRS to be HyLIRGs.

Drouart et al. (2014) find absolute numbers and upper limits for the total IR luminosity of HzRGs in the range of a few to a few tens of $10^{12} L_{\odot}$. Our redshift-dependent IR luminosity upper limits of IFRS are in agreement with these numbers of HzRGs.

We note that the maximum model shown in Fig. 7 (dashed lines) is unphysical for redshifts $z \lesssim 2.5$. For these redshifts, the AGN contribution to the maximum model is very low, corresponding to a very low AGN activity or even an absent AGN. Instead, according to that model, the IR emission is mainly or even completely produced by SB activity. In case of a purely star forming galaxy, a direct connection between the radio and the IR emission was found (i.e. Yun et al. 2001), known as radio-IR correlation. Using the outcome of the maximum model that the emission of IFRS is dominated by the SB component for redshifts $z \lesssim 2.5$, we could estimate the radio luminosity from the IR luminosity. Using our FIR luminosity upper limits, we found that this radio luminosity is at least two orders of magnitude lower than the radio luminosity calculated from the measured 1.4 GHz flux density of IFRS. This discrepancy clearly showed that the existence of an AGN in the IFRS is essential to explain their radio flux densities. Modelling their IR SED by only an SB template is inappropriate. The existence of an AGN in IFRS is also in agreement with VLBI observations by Norris et al. (2007), Middelberg et al. (2008b), and Herzog et al. (2015).

5.2.2. Including the radio data point into the IR SED modelling

The IR SED modelling presented above, aiming at setting upper limits on the total IR flux of IFRS, led to unphysical results because it neglected the measured radio flux density of IFRS. In this section, we attempted to address this issue by expanding our modelling to the radio regime based on an RL AGN template.

In Sect. 5.1, we showed that all SEDs in agreement with the photometric characteristics of IFRS were HzRGs and that the spiderweb galaxy provided an appropriate SED template in the broad-band SED modelling. It is known that both star forming activity and an AGN contribute to the emission of this powerful galaxy. Therefore, in the following, we used the broad-band SED of the spiderweb galaxy, built from NED and the additional IR data from Seymour et al. (2012) as described in Sect. 5.1, as a basic template, modified by a wavelength-independent luminosity scaling factor. Beyond that, to account for an SB component independent of the component already present in the spiderweb galaxy template, we added the most appropriate SB template from the sample by Mullaney et al. (2011). Similar to our approach in Sect. 5.2.1, we modified this SB template by a wavelength-independent luminosity scaling factor. However, here, we also used the radio-IR correlation (Yun et al. 2001) to estimate the radio luminosity of the star formation component, in addition to that from the RL AGN.

Recapitulating, similar to the approach presented in Sect. 5.2.1, we composed our total SED of two different components. The spiderweb galaxy contributed SB and AGN emission, while the additional SB component contributed additional SB emission. Based on the two independent scaling factors, both the AGN contribution and the SB contribution could be varied independently. We note that the scaling factor of the additional SB component could also be negative, i.e. representing a lower star forming activity than that in the spiderweb galaxy.

Similar to our approach in Sect. 5.2.1, we modelled the maximum IR SED by maximising the flux of the total template

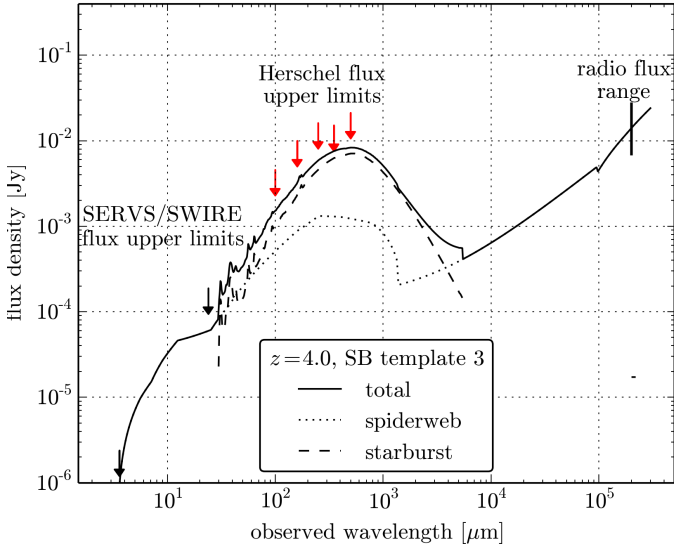


Fig. 8. IR SED modelling for IFRS at redshift $z = 4$, using the FIR flux density upper limits (red arrows) measured in this work, the SERVS/SWIRE flux density upper limits (black arrows), and the measured radio flux density of 15 mJy at 1.4 GHz. The total (solid line) emission is composed of the scaled spiderweb galaxy template (dotted line) and one scaled SB component (dashed line). Note that the limited wavelength coverage of the SB template caused the leaps at $30 \mu\text{m}$ and $5450 \mu\text{m}$. The fit represents an upper limit on the IR emission of IFRS and is defined by matching the radio flux density of 15 mJy at 1.4 GHz and providing the lowest deviation between all available flux density upper limits and the total SED. Note that the dash at 21 cm (flux density of $\approx 20 \mu\text{Jy}$) is the contribution of the additional SB component to the 1.4 GHz flux density.

– i.e. composite from the spiderweb galaxy template and one additional SB template – however, requesting the template to be in agreement with all available flux density upper limits. Furthermore, here, we required the total template to match the median measured 1.4 GHz flux density of the observed IFRS of 15 mJy. Figure 8 shows the resulting maximum model for $z = 4$.

We found that the contribution of the additional SB component to the radio emission, calculated based on the radio-IR correlation, is negligible compared to the radio emission of the spiderweb galaxy template. In case of $z = 4$, this SB contribution is around $20 \mu\text{Jy}$ at 1.4 GHz which is more than two orders of magnitude lower than the contribution of the spiderweb galaxy template at this frequency.

Based on the results of this modelling, we calculated the maximum total IR luminosity by integrating the flux density of the total SED template between $8 \mu\text{m}$ and $1000 \mu\text{m}$ in the rest frame. Furthermore, we decomposed the maximum IR luminosity in the SB contribution and the AGN contribution. Seymour et al. (2012) studied the IR properties of the spiderweb galaxy and find that 59% of its IR luminosity is contributed from the AGN and 41% from the star forming activity. We used these fractional numbers and decomposed the contribution of the spiderweb galaxy template correspondingly. The maximum total IR luminosity and its decomposition in AGN and SB contribution as a function of redshift are shown in Fig. 9. We found that, based on this modelling, IFRS are constrained to IR luminosities below $10^{12} L_{\odot}$ at redshifts $z \lesssim 2$. At $z \lesssim 5$, IFRS can have a maximum luminosity of $10^{13} L_{\odot}$. At higher redshifts, we cannot exclude IFRS to be HyLIRGs which are defined by IR luminosities above $10^{13} L_{\odot}$.

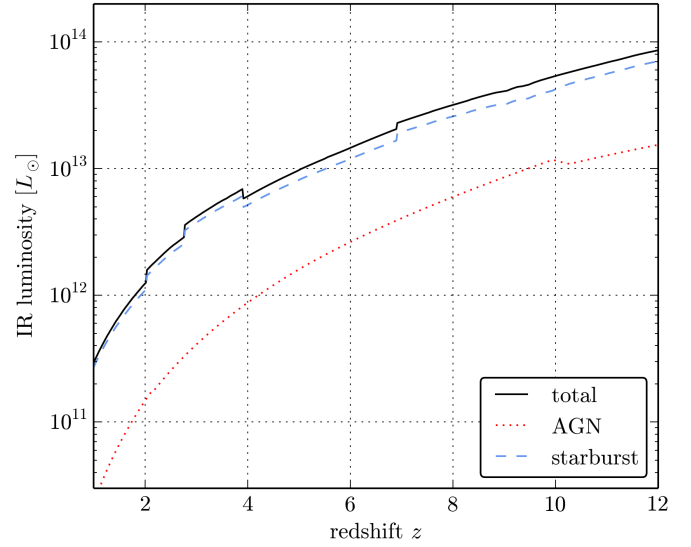


Fig. 9. Maximum infrared luminosity versus redshift for the AGN (red dotted line) component, the SB (blue dashed line) component, and for the total IR luminosity (black solid line). The underlying model (see Fig. 8 for an example) matched the measured radio flux density of 15 mJy at 1.4 GHz. We note that the total IR luminosity and the SB IR luminosity are upper limits.

We note that the luminosity upper limits obtained in this approach are up to one order of magnitude lower than those inferred in Sect. 5.2.1 and presented in Fig. 7. This shows that it is crucial to include the measured radio flux density in the IR SED modelling. A modelling just based on the IR flux density upper limits is physically inappropriate and results in excessive IR luminosities.

The numbers of the maximum total IR luminosity and the SB contribution are upper limits since they were obtained by a model aiming at the lowest deviation to the available IR flux density upper limits. In contrast, the IR luminosities of the AGN component can be considered to be rough estimates because of their direct link to the measured radio flux density. However, we point out that the IR emission of AGNs at high redshifts is known to spread by more than one order of magnitude (Drouart et al. 2014). It should be emphasised that we assumed IFRS to be similar to HzRGs in this approach. Although several indications for this similarity have been found so far, it is not proven yet. While the luminosities shown in Fig. 9 can be considered to be more realistic numbers, the IR luminosity upper limits presented in Fig. 7 are absolute upper limits which should not be exceeded, independent of the nature of IFRS.

In our broad-band SED modelling described in Sect. 5.1, we found that the local radio galaxy Cygnus A, the local CSS source 3C 48 and the RL quasar 3C 273 provide appropriate templates to explain the SED characteristics of IFRS, too. As mentioned above, these modified templates shifted to $z \geq 1$ fulfil the selection criteria of HzRGs. Therefore, we also used the SEDs of these galaxies as basic templates, i.e. containing an AGN and potentially a certain contribution from star forming activity, instead of the spiderweb galaxy. We performed the modelling in the same way as described above, i.e. using the scaled SED of Cygnus A, 3C 48 and 3C 273, respectively, as basic template and adding the most appropriate and scaled SB template, matching all available flux density upper limits and the measured 1.4 GHz flux density. However, in case of Cygnus A, 3C 48 and 3C 273, we did not find appropriate numbers in the literature to convert

the IR emission of these objects into an AGN and an SB contribution as we did for the spiderweb galaxy based on the results from Seymour et al. (2012). Therefore, we could only compare the total IR luminosity upper limits. We found that these numbers derived based on Cygnus A, 3C 48 and 3C 273 as basic templates are very similar to the numbers based on the spiderweb galaxy template shown in Fig. 9, differing by not more than a factor of two. This finding provides evidence that the total IR luminosity upper limits presented in Fig. 9 are indeed general upper limits, independent on the assumed nature of IFRS.

5.2.3. Estimates of star formation and black hole accretion rate upper limits

Based on the maximum IR luminosities measured in Sect. 5.2.2, we derived upper limit estimates of the star formation rate (SFR), causing the IR emission given by the SB component, and estimates of the black hole accretion rate, generating the AGN contribution to the IR flux. Since these numbers can only be considered as rough estimates, we used very general and simple approaches. We calculated the SFR based on the IR luminosity $L_{\text{SB}}^{\text{IR}}$ integrated between $8 \mu\text{m}$ and $1000 \mu\text{m}$,

$$\text{SFR} [M_{\odot} \text{yr}^{-1}] = 1.72 \times 10^{-10} \times L_{\text{SB}}^{\text{IR}} [L_{\odot}], \quad (2)$$

following the relation for local galaxies from Kennicutt (1998).

We estimated the black hole accretion rate ($\dot{M}_{\text{BH}}^{\text{acc}}$) from the equation

$$\kappa_{\text{AGN}}^{\text{Bol}} L_{\text{AGN}}^{\text{IR}} = \epsilon \dot{M}_{\text{BH}}^{\text{acc}} c^2, \quad (3)$$

based on the IR luminosity $L_{\text{AGN}}^{\text{IR}}$ of the AGN. This relation assumes that a fraction of the rest-frame energy of the matter accreting onto the black hole is converted into radiation over the whole electromagnetic spectrum. The conversion is given by the efficiency factor ϵ , only slightly constrained by empirical studies. While for example Shankar et al. (2010) suggest $\epsilon > 0.2$ based on quasar clustering, others like Davis & Laor (2011) find $0.06 < \epsilon < 0.4$, depending on the mass. Here, we used a conservative number $\epsilon = 0.1$ since we were interested in upper limits for the black hole accretion rate. Furthermore, we needed to make an assumption for the factor κ , converting the IR AGN luminosity to the bolometric luminosity. This factor is uncertain and can vary between 1.4 and 15. We adopted the number from Drouart et al. (2014), $\kappa = 6$, assuming an RL AGN template.

Figure 10 shows the estimated upper limit of the SFR and an estimate of the black hole accretion rate versus redshift based on the maximum IR luminosities derived in Sect. 5.2.2. For the accretion rate, we also showed the related uncertainty, arising from the assumptions made for the efficiency factor ϵ and the conversion factor κ as discussed above. Varying ϵ between 0.06 and 0.4, and κ between 1.4 and 15, representing the range of reasonable numbers, results in the uncertainties shown by the red shaded area in Fig. 10.

We found that IFRS at $z \lesssim 4.5$ are constrained by SFRs of a few hundred solar masses per year. The SFR upper limit increases with redshift and exceeds $10^4 M_{\odot} \text{yr}^{-1}$ at $z \approx 11$. Drouart et al. (2014) find SFRs for their HzRGs in the range of $100 M_{\odot} \text{yr}^{-1}$ to $5000 M_{\odot} \text{yr}^{-1}$. These numbers are in agreement with our results, considering that the SFRs calculated here are meant to be upper limits.

The estimates of the black hole accretion rate are below $1 M_{\odot} \text{yr}^{-1}$ at $z \lesssim 3$ and below $10 M_{\odot} \text{yr}^{-1}$ at $z \approx 6$. At redshifts $z \geq 10$, the accretion rate is below a few tens of solar

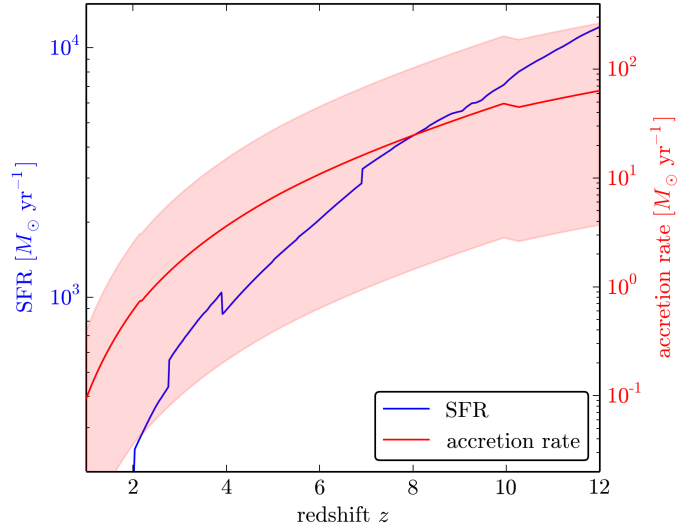


Fig. 10. Star formation rate (blue line) and accretion rate (red line) versus redshift. The calculation of both rates is based on the modelling described in Sect. 5.2.2, matching the measured 1.4 GHz flux density of 15 mJy and providing the lowest deviation to all available flux density upper limits. The red shaded area represents the uncertainty in the determination of the BH accretion rate, based on varied numbers for the efficiency factor ϵ and the conversion factor κ . We note that the SFR is meant to be an upper limit since the SB contribution is only constrained by upper limits.

masses per year. Drouart et al. (2014) find accretion rates between $1 M_{\odot} \text{yr}^{-1}$ and $100 M_{\odot} \text{yr}^{-1}$ for their sample of HzRGs. Again, our results are in agreement with the numbers presented by Drouart et al.. Considering that the HzRGs in the sample of Drouart et al. are at $z \lesssim 5$, IFRS seem to show lower accretion rates if they are located at similar redshifts. In contrast to the SFR estimated in this work, which are meant to be upper limits as discussed above, the black hole accretion rates are considered to be rough estimates under the assumption that the SEDs of IFRS are similar to those of HzRGs. However, the assumption for the conversion factor κ and the efficiency factor ϵ and the scattering of the IR luminosity of AGNs (Drouart et al. 2014) add significant uncertainties.

All our findings in this IR SED modelling are in agreement with the results by Drouart et al. (2014) for HzRGs. The redshift-dependent IR luminosity upper limits and the directly related SFRs and black hole accretion rates derived in this work agree with the numbers calculated by Drouart et al. for their sources which, in contrast to IFRS, partially provide FIR detections. In our IR SED modelling, we did not find any evidence disproving the hypothesis that IFRS are similar to HzRGs.

6. Conclusion

In this work, we presented the first FIR data of IFRS. Six IFRS have been observed between $100 \mu\text{m}$ and $500 \mu\text{m}$ with the instruments PACS and SPIRE on board the *Herschel* Space Observatory. None of the observed IFRS has been detected at any of the five FIR wavelengths down to median 3σ levels between 4.4 mJy at $100 \mu\text{m}$ and 17.6 mJy at $500 \mu\text{m}$. Even the stacking of the five maps of five IFRS at each wavelength did not provide a detection.

We used the FIR flux density upper limits combined with the radio detections and the SERVS/SWIRE flux density upper

limits to model the broad-band SED of IFRS. The characteristics of IFRS can only be explained by known SEDs of HzRGs (e.g. the spiderweb galaxy) if these templates are shifted to $z \gtrsim 10.5$ or by the SED of Cygnus A at $5 \lesssim z \lesssim 8.5$. All other templates, for example RL HyLIRGs, ULIRGs with an AGN in their centre, or RL quasars fail to reproduce the SED constraints of IFRS. We also tested whether modified templates of known galaxies can explain the characteristics of IFRS at lower redshifts $z \lesssim 5$. In this approach, we scaled the templates in luminosity to match the measured flux densities at 1.4 GHz or added extinction in the rest-frame optical and near-IR regime if required. We found that the templates of the spiderweb galaxy, Cygnus A, the CSS source 3C 48, and the RL quasar 3C 273 can be modified to match all photometric constraints of IFRS. However, at low redshifts, additional obscuration by dust was needed for most SED templates to match the near-IR faintness of IFRS.

Although no IFRS has been found at low redshifts $z \sim 1$, our modelling provided appropriate modified templates for this scenario. This implies that our modelling is physically unrealistic at low redshifts, potentially because of scaling down the luminosity and – by this – the supermassive black hole (SMBH) mass which might prevent the object to be an RL AGN. On the other hand, if the IFRS analysed in this work are indeed at $z \sim 1$, they would form a new subclass of IFRS with different characteristics than the IFRS with known spectroscopic redshifts. Particularly, we showed that SED templates of star forming galaxies, Seyfert galaxies, ULIRGs, and HyLIRGs are inappropriate to reproduce the photometric constraints of IFRS.

We modelled the maximum IR SED of IFRS based on a set of SB templates and an AGN contribution and using all available flux density upper limits, aiming at measuring the maximum IR flux of IFRS. We found that this model is unphysical at lower redshifts because of its disagreement with the radio-IR correlation. We found that the IFRS could also be modelled by the spiderweb galaxy template, together with an additional SB component. The related IR luminosity upper limits are in agreement with those of HzRGs. Using these maximum IR luminosities, we estimated black hole accretion rates and upper limits for the SFR. These numbers agree with the numbers of HzRGs, too.

In summary, the IFRS discussed here might be (a) objects identical to known HzRGs, but at high redshifts ($z \gtrsim 10.5$); (b) objects similar to Cygnus A, but at high redshifts $5 \lesssim z \lesssim 8.5$; (c) objects similar to known HzRGs or Cygnus A, but scaled down in luminosity; or (d) objects similar to CSS sources or RL quasars, but modified by significant additional extinction and scaled in luminosity which makes these templates to HzRGs, too. In any case, objects which reproduce the characteristics of IFRS fulfil the selection criteria of HzRGs. We estimated that IFRS contain SMBHs accreting at the rate of $1 M_{\odot} \text{ yr}^{-1}$ to $50 M_{\odot} \text{ yr}^{-1}$, together with star formation at a rate of up to several thousand solar masses per year in case of an additional SB component.

Acknowledgements. We thank the anonymous referee who has helped to improve this paper significantly. We also thank Nick Seymour for valuable discussions about the IR SED modelling and Elaine Sadler for suggestions about SED templates. A.H. acknowledges funding from *Bundesministerium für Wirtschaft und Technologie* under the label 50OR 1202. The author is responsible for the content of this publication. PACS has been developed by a consortium of institutes led by MPE (Germany) and including UVIE (Austria);

KU Leuven, CSL, IMEC (Belgium); CEA, LAM (France); MPIA (Germany); INAF-IFSI/OAA/OAP/OAT, LENS, SISSA (Italy); IAC (Spain). This development has been supported by the funding agencies BMVIT (Austria), ESA-PRODEX (Belgium), CEA/CNES (France), DLR (Germany), ASI/INAF (Italy), and CICYT/MCYT (Spain). SPIRE has been developed by a consortium of institutes led by Cardiff University (UK) and including Univ. Lethbridge (Canada); NAOC (China); CEA, LAM (France); IFSI, Univ. Padua (Italy); IAC (Spain); Stockholm Observatory (Sweden); Imperial College London, RAL, UCL-MSSL, UKATC, Univ. Sussex (UK); and Caltech, JPL, NHSC, Univ. Colorado (USA). This development has been supported by national funding agencies: CSA (Canada); NAOC (China); CEA, CNES, CNRS (France); ASI (Italy); MCINN (Spain); SNSB (Sweden); STFC, UKSA (UK); and NASA (USA). HIPE is a joint development by the *Herschel* Science Ground Segment Consortium, consisting of ESA, the NASA *Herschel* Science Center, and the HIFI, PACS and SPIRE consortia. This research has made use of the NASA/IPAC Extragalactic Database (NED) which is operated by the Jet Propulsion Laboratory, California Institute of Technology, under contract with the National Aeronautics and Space Administration.

References

- Antonucci, R., Hurt, T., & Kinney, A. 1994, *Nature*, 371, 313
 Banfield, J. K., George, S. J., Taylor, A. R., et al. 2011, *ApJ*, 733, 69
 Calzetti, D., Armus, L., Bohlin, R. C., et al. 2000, *ApJ*, 533, 682
 Collier, J. D., Banfield, J. K., Norris, R. P., et al. 2014, *MNRAS*, 439, 545
 Condon, J. J., Cotton, W. D., Greisen, E. W., et al. 1998, *AJ*, 115, 1693
 Davis, S. W., & Laor, A. 2011, *ApJ*, 728, 98
 De Breuck, C., Seymour, N., Stern, D., et al. 2010, *ApJ*, 725, 36
 Drouart, G., De Breuck, C., Vernet, J., et al. 2014, *A&A*, 566, A53
 Franzen, T. M. O., Banfield, J. K., Hales, C. A., et al. 2015, *MNRAS*, submitted
 Fruchter, A. S., & Hook, R. N. 2002, *PASP*, 114, 144
 Garn, T., & Alexander, P. 2008, *MNRAS*, 391, 1000
 Griffin, M. J., Abergel, A., Abreu, A., et al. 2010, *A&A*, 518, L3
 Grogin, N. A., Kocevski, D. D., Faber, S. M., et al. 2011, *ApJS*, 197, 35
 Herzog, A., Middelberg, E., Norris, R. P., et al. 2014, *A&A*, 567, A104
 Herzog, A., Middelberg, E., Norris, R. P., et al. 2015, *A&A*, 578, A67
 Horn, R. A., & Johnson, C. R. 1985, *Matrix Analysis* (New York, NY, USA: Cambridge University Press)
 Huynh, M. T., Norris, R. P., Siana, B., & Middelberg, E. 2010, *ApJ*, 710, 698
 Kennicutt, Jr., R. C. 1998, *ARA&A*, 36, 189
 Kimball, A. E., & Ivezić, Ž. 2008, *AJ*, 136, 684
 Lonsdale, C. J., Smith, H. E., Rowan-Robinson, M., et al. 2003, *PASP*, 115, 897
 Lutz, D., Poglitsch, A., Altieri, B., et al. 2011, *A&A*, 532, A90
 Maini, A., Prandoni, I., Norris, R. P., et al. 2015, *A&A*, 578, A67
 Mauduit, J.-C., Lacy, M., Farrah, D., et al. 2012, *PASP*, 124, 714
 Middelberg, E., Norris, R. P., Cornwell, T. J., et al. 2008a, *AJ*, 135, 1276
 Middelberg, E., Norris, R. P., Tingay, S., et al. 2008b, *A&A*, 491, 435
 Middelberg, E., Norris, R. P., Hales, C. A., et al. 2011, *A&A*, 526, A8
 Mullaney, J. R., Alexander, D. M., Goulding, A. D., & Hickox, R. C. 2011, *MNRAS*, 414, 1082
 Nguyen, H. T., Schulz, B., Levenson, L., et al. 2010, *A&A*, 518, L5
 Norris, R. P., Afonso, J., Appleton, P. N., et al. 2006, *AJ*, 132, 2409
 Norris, R. P., Tingay, S., Phillips, C., et al. 2007, *MNRAS*, 378, 1434
 Norris, R. P., Afonso, J., Cava, A., et al. 2011, *ApJ*, 736, 55
 Oliver, S. J., Bock, J., Altieri, B., et al. 2012, *MNRAS*, 424, 1614
 Ott, S. 2010, in *Astronomical Data Analysis Software and Systems XIX*, eds. Y. Mizumoto, K.-I. Morita, & M. Ohishi, *ASP Conf. Ser.*, 434, 139
 Pilbratt, G. L., Riedinger, J. R., Passvogel, T., et al. 2010, *A&A*, 518, L1
 Poglitsch, A., Waelkens, C., Geis, N., et al. 2010, *A&A*, 518, L2
 Puccetti, S., Fiore, F., D’Elia, V., et al. 2006, *A&A*, 457, 501
 Rees, G. A., Spitler, L. R., Norris, R. P., et al. 2015, *MNRAS*, submitted
 Savage, R. S., & Oliver, S. 2007, *ApJ*, 661, 1339
 Seymour, N., Stern, D., De Breuck, C., et al. 2007, *ApJS*, 171, 353
 Seymour, N., Altieri, B., De Breuck, C., et al. 2012, *ApJ*, 755, 146
 Shankar, F., Weinberg, D. H., & Shen, Y. 2010, *MNRAS*, 406, 1959
 Willott, C. J., Rawlings, S., Jarvis, M. J., & Blundell, K. M. 2003, *MNRAS*, 339, 173
 Wright, E. L. 2006, *PASP*, 118, 1711
 Wright, E. L., Eisenhardt, P. R. M., Mainzer, A. K., et al. 2010, *AJ*, 140, 1868
 Xue, Y. Q., Luo, B., Brandt, W. N., et al. 2011, *ApJS*, 195, 10
 Yun, M. S., Reddy, N. A., & Condon, J. J. 2001, *ApJ*, 554, 803
 Zinn, P.-C., Middelberg, E., & Ibar, E. 2011, *A&A*, 531, A14

5

The radio spectral energy distribution of infrared-faint radio sources

The class of IFRSs is characterised by their relatively bright radio and faint observed near-IR faintness emission, separating these objects from other galaxies. The observed $3.6 \mu\text{m}$ flux density of IFRSs in the deep fields like the ATLAS and xFLS fields are usually below $3 \mu\text{Jy}$. IFRSs are also very faint in the observed optical regime and usually remain undetected down to ~ 24.5 mag. The few optically detected IFRSs have R band magnitudes between 22.0 and 24.6; one IFRS has been detected with 26.3 mag in V band. In chapter 4 (Herzog et al., 2015b), the first FIR observations of IFRSs were presented and yield no detection down to a limit of 4.5 mJy at $100 \mu\text{m}$. Even stacking analyses in the near- and mid-IR (Norris et al., 2006; Garn and Alexander, 2008; Norris et al., 2011a) and FIR (chapter 4 of this thesis, Herzog et al., 2015b) regimes did not reveal detections, showing that the respective counterparts are not only slightly below the detection sensitivity, but emphasising the deep faintness of IFRSs in the entire IR regime.

Though observations at observed optical wavelengths revealed crucial information about the nature of IFRSs as presented in chapter 2 (Herzog et al., 2014) and FIR flux density upper limits provided useful constraints on the SEDs of this class of object (chapter 4; Herzog et al., 2015b), studying IFRSs in the optical and IR regimes is challenging and expensive in observing time. In contrast, IFRSs are relatively radio-bright with 1.4 GHz flux densities of the order of mJy or tens of mJy and can therefore be studied rather easily at radio-wavelengths. For example, observations in the radio regime unveiled the presence of AGNs in a large number of IFRSs as described in chapter 3 (Herzog et al., 2015a).

The first targeted radio observations of IFRSs were carried out by Norris et al. (2007) and Middelberg et al. (2008b) and resulted in the detection of compact emission in two out of six observed sources. Middelberg et al. analysed IFRS S427—one of these two detected sources—and conclude that it is most likely not a typical FR I/II radio galaxy based on its putative luminosity and the ratio of compact to total radio emission. Further, Middelberg et al. suggest that this source is physically smaller than typical FR I/II galaxies, following from its angular size.

The angular size θ of an object is defined as

$$\tan \theta = \frac{x}{d} \quad (5.1)$$

in Euclidean geometry, where x is the linear size of the object and d the distance between that object and the observer. When θ is small, Eq. (5.1) can be approximated by $\theta \approx \frac{x}{d}$. In a non-Euclidean space, the relation is more complex and the so-called angular diameter distance d_A needs to be defined to hold the approximated equation (see e.g. Weinberg, 2008 for details). Remarkable is the fact that objects appear larger with increasing redshift at $z \gtrsim 1.6$. This can be seen from Fig. 5.1, showing the scale in kpc/arcsec as a function of redshift for a standard Λ CDM cosmology. Increasing with redshift, the scale reaches a maximum of around 8.5 kpc/arcsec at $z \approx 1.6$. Towards higher redshifts, the scale decreases as a weak function of redshift. In particular, the scale is between 4.5 kpc/arcsec and 8.5 kpc/arcsec in the redshift range $0.5 \leq z \leq 8.0$.

Middelberg et al. (2008b) used this relation in combination with the deconvolved angular size of IFRS S427 of $3.30 \times 2.74 \text{ arcsec}^2$ in the 1.4 GHz ATLAS DR1 map and suggest that the linear size of this source is of the order of 24 kpc. This is significantly smaller

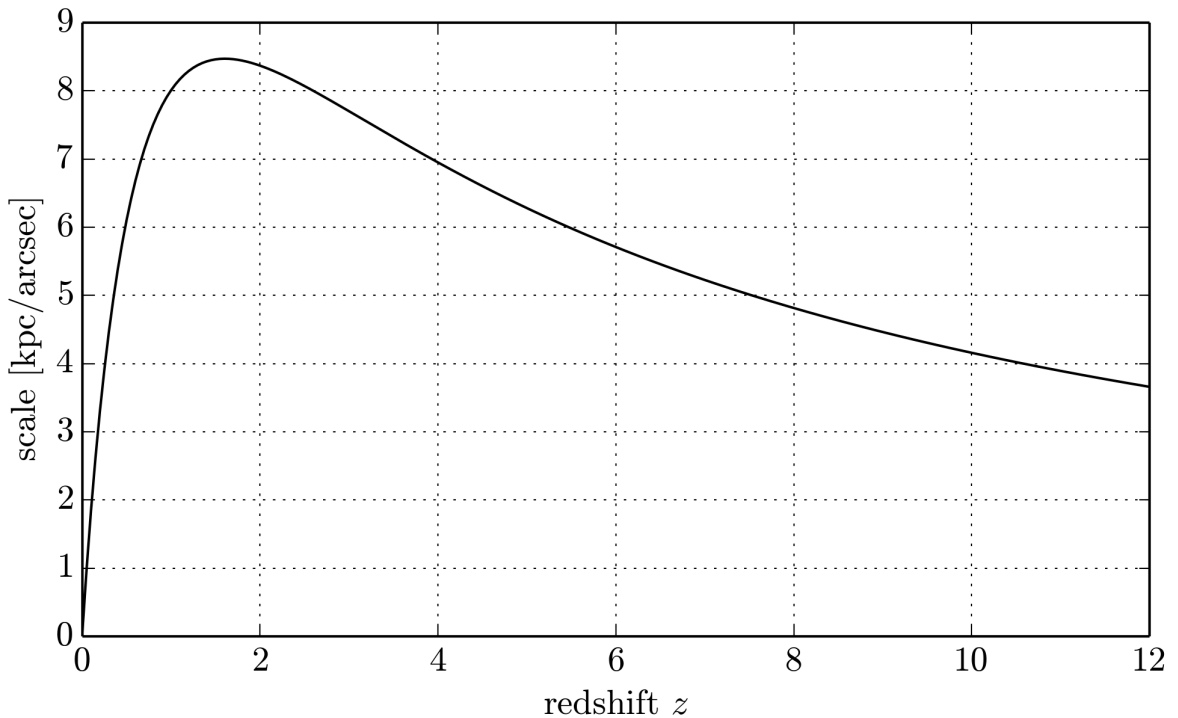


Figure 5.1: Scale as a function of redshift in standard Λ CDM cosmology, assuming $\Omega_{\Lambda} = 0.7$, $\Omega_{\text{M}} = 0.3$, and $H_0 = 70 \text{ km s}^{-1} \text{ Mpc}^{-1}$. At $z \gtrsim 0.5$, the scale only weakly depends on the redshift. The formula to calculate the scale has been taken from Wright (2006).

than ordinary FR I/II galaxies with sizes of the order of 100 kpc and adds evidence to the hypothesis that IFRSs are indeed different than extended radio galaxies. Garn and Alexander (2008) present the same conclusion based on their sample of 14 IFRSs in the xFLS field, suggesting a typical linear size of less than 20 kpc. Further, Middelberg et al. measured a spectral index $\alpha = -1.31$ for S427 between 843 MHz and 8.6 GHz. Combining this steep radio SED with the compact morphology and low linear size of this source, Middelberg et al. suggest that S427 might be a compact steep-spectrum (CSS) source.

The class of CSS sources contains compact radio galaxies with linear sizes of a few or a few tens of kpc and steep radio SEDs ($\alpha \lesssim -0.6$). Further, CSS sources show a turnover in their radio SED at frequencies below 500 MHz (see O’Dea, 1998 for a review, and references in Randall et al., 2011). Related to the class of CSS sources are GPS sources. With linear sizes of less than 1 kpc, they are more compact than CSS sources and even smaller than the NLR. As indicated by their name, GPS sources peak at frequencies above 500 MHz, usually at a few GHz (O’Dea, 1998; Randall et al., 2011). Finally, the class of high-frequency peakers (HFPs) is most compact (sizes of a few pc) and shows turnovers at frequencies above 5 GHz (Dallacasa et al., 2000; Stanghellini et al., 2009; Orienti and Dallacasa, 2014).

In the generally accepted picture, these three classes of objects are put in an evolutionary scenario where linear size correlates with age (Dallacasa et al., 2000). Thus, HFPs are expected to be the youngest AGNs. These objects are very rare since they evolve quickly—within a few tens of years (Dallacasa, 2003)—to GPS sources, by shifting their peak in the radio SED to lower frequencies. The relativistic jets expand into the interstellar medium (ISM) of the host galaxy. They first penetrate the NLR—during the GPS phase—, followed by more homogeneous regions of the ISM—corresponding to the CSS phase—, and finally extend into the IGM and forming an extended radio galaxy (Dallacasa, 2003). During this evolution, the radio luminosity increases in the GPS phase and then decreases in the CSS phase because of expansion losses (Fanti et al., 1995; Readhead et al., 1996; Snellen et al., 2000).

Alternative scenarios suggest that these compact AGNs are “frustrated” sources that are confined by dense gas, preventing the jets from expanding (O’Dea et al., 1991), or dying AGNs without further energy supply (Fanti, 2009).

The radio emission of these sources—and generally all AGNs—is dominated by synchrotron emission. The observed turnover in the radio SED of HFPs, GPS sources, and CSS sources is generally thought to be caused by absorption of synchrotron emission. However, different physical processes causing the absorption have been suggested and this issue is still highly debated. Free-free absorption (FFA) between the synchrotron electrons and ionised gas in the host galaxy can cause the turnover. On the other hand, synchrotron self absorption (SSA) in the synchrotron-emitting region itself might also explain the observed decreasing flux densities towards low frequencies (see the introduction in Marr et al., 2014 for a comprehensive overview).

For these classes of AGN, O’Dea and Baum (1997) present a correlation that describes how the radio peak frequency ν_p relates to the linear size l , quantified by

$$\log\left(\frac{\nu_p}{\text{GHz}}\right) = -(0.21 \pm 0.05) - (0.65 \pm 0.05) \log\left(\frac{l}{\text{kpc}}\right). \quad (5.2)$$

This correlation holds for the entire data set of GPS and CSS sources, characterised by peak frequencies in the range $0.05 \text{ GHz} \leq \nu_p \leq 20 \text{ GHz}$ and linear sizes in the range $0.01 \text{ kpc} \leq l \leq 20 \text{ kpc}$.

The steep radio SED of S427 presented by Middelberg et al. (2008b) as discussed above is not an outlier in the class of IFRSs but rather common. Middelberg et al. (2011) analysed

the radio spectral indices of 17 IFRSs and find a median index of -1.4 between 1.4 GHz and 2.4 GHz and no index flatter than -0.7 . Considering the compact morphology of the majority of IFRSs and the related low linear sizes (Middelberg et al., 2008b; Garn and Alexander, 2008; Middelberg et al., 2011), the class of IFRSs seems to be prototypical for CSS and potentially GPS sources as pointed out by Middelberg et al. (2008b) for the individual IFRS S427.

Generally, different emission regions contribute to the total radio luminosity of radio galaxies (see e.g. Miley, 1980; Bridle et al., 1981; Begelman et al., 1984). If the jets are still fed, the core of a radio galaxy—i.e. the innermost parts of the jets, at the centre of the host galaxy—is characterised by the continuous injection of jet material, emitting synchrotron emission. This region typically shows a flat or inverted radio SED with a spectral index in the range $-0.5 \lesssim \alpha \lesssim 1.0$. Inverted SEDs are expected to arise from optically thick regions where low-frequency photons are suppressed by FFA or SSA. Flat SEDs are thought to be the result of superpositions of SEDs from different emission regions along the jet with progressively lower turnover frequency. In evolved radio galaxies, the radio core emission hardly contributes to the total radio emission of the galaxy. The contribution of the jets themselves and knots¹ in the jets is similarly low. These components usually have spectral indices in the range $-0.8 \lesssim \alpha \lesssim -0.5$. Hot-spots² have similar spectral indices. The total radio emission of evolved radio galaxies—i.e. FR I/II—is dominated by the lobes. Spectral indices depend on the size—or equivalently, the age—of the radio galaxy, but are typically in the range $-1.0 \lesssim \alpha \lesssim -0.7$.

The following paper studies the radio SED of IFRSs and addresses the question whether the majority of IFRSs are young AGNs, i.e. GPS or CSS sources, as suggested based on the results from studying the compact radio emission of IFRSs presented in chapter 3 (Herzog et al., 2015a). Radio SEDs of 34 IFRSs were built using data in up to 15 wavebands, covering the frequency range between 150 MHz and 34 GHz. Indeed, the data pick up the suggested turnover in the radio regime for some IFRSs. However, the abundance of young AGNs is not higher than for the ordinary RL AGN population, potentially because of higher redshifts of IFRSs which would shift the turnover into the lower, unexplored frequency regime. The SEDs show that IFRSs have steeper radio SEDs than the general RL source population. In

¹Knots are high surface brightness regions in the jet, interpreted as resulting from interactions between the jet particles and overdense regions or from particle re-acceleration.

²Hot spots are regions of particle shock-acceleration at the edges of the lobes.

particular, the steep SEDs and the absence of flat or inverted SEDs shows that the radio emission of IFRSs is not affected by beaming effects and that IFRSs are very unlikely to be blazars.

In the paper below, several IFRSs are found to have ultra-steep radio SEDs, characterised by spectral indices $\alpha < -1.3$. Following the correlation that higher-redshift sources show steeper radio SEDs (e.g. Klammer et al., 2006), these ultra-steep IFRSs are suggested to be at high redshifts. Since observational confirmation of the putatively very high redshifts of the IR-faintest IFRSs—suggested to be at $z \sim 5$ by Norris et al. (2011a), Collier et al. (2014), and Herzog et al. (2014)—is challenging and requires time at the most advanced telescopes as discussed in chapters 2 and 3, it is important to select the most promising sources for such future observations. Knowledge of the radio SED steepness as presented in the following paper might provide crucial information to select the targets, and these ultra-steep spectrum sources are good candidates to find IFRSs at very high redshifts.

The remainder of this chapter has been submitted for publication as

The radio spectral energy distribution of infrared-faint radio sources

A. Herzog, R. P. Norris, E. Middelberg, N. Seymour, L. R. Spitler, B. H. C. Emonts, T. M. O. Franzen, R. Hunstead, H. T. Intema, J. Marvil, Q. A. Parker, S. K. Sirothia, N. Hurley-Walker, M. Bell, G. Bernardi, J. D. Bowman, F. Briggs, R. J. Cappallo, J. R. Callingham, A. A. Deshpande, K. S. Dwarakanath, B.-Q. For, L. J. Greenhill, P. Hancock, B. J. Hazelton, L. Hindson, M. Johnston-Hollitt, A. D. Kapińska, D. L. Kaplan, E. Lenc, C. J. Lonsdale, B. McKinley, S. R. McWhirter, D. A. Mitchell, M. F. Morales, E. Morgan, J. Morgan, D. Oberoi, A. Offringa, S. M. Ord, T. Prabu, P. Procopio, N. Udaya Shankar, K. S. Srivani, L. Staveley-Smith, R. Subrahmanyam, S. J. Tingay, R. B. Wayth, R. L. Webster, A. Williams, C. L. Williams, C. Wu, Q. Zheng, K. W. Bannister, A. P. Chippendale, L. Harvey-Smith, I. Heywood, B. Indermuehle, A. Popping, R. J. Sault, M. T. Whiting
in *Astronomy & Astrophysics* on 20 July 2015.

Based on published and unpublished radio data in up to 15 radio wavebands between 150 MHz and 34 GHz, radio SEDs of 34 IFRSs—selected based on the criteria from Zinn et al. (2011)—in the ATLAS fields were built. Sources with a turnover, an upturn, and a steepening in their SEDs were found. However, most IFRSs seem to follow a single power law. Comparison to a control sample shows that IFRSs have statistically significantly steeper radio SEDs than the population of ordinary RL AGNs. The abundances of GPS and CSS sources in the population of IFRSs are consistent with numbers in the broader RL AGN population. Further, the paper presents the highest-frequency radio observation of an IFRS—obtained with the Plateau de Bure Interferometer (PdBI) at 105 GHz—and discusses this source based on a detailed broad-band SED modelling.

I was responsible for leading the work presented in the following manuscript. I measured flux densities from the radio maps and cross-matched published catalogues as described in the manuscript below. I then built and classified the radio SEDs, fitted the SEDs using `python`, and analysed the results. Further, I proposed and scheduled the mm observations with the PdBI, carried out the data calibration and analysis using the Grenoble Image and Line Data Analysis Software³ (GILDAS). Based on the results, I modelled the broad-band SED of this IFRS. I also produced the radio-FIR SED template and modelled that part of the SED. Finally, I wrote the manuscript. R. P. Norris, E. Middelberg, and L. R. Spitler supervised the work and provided continuous discussions about technical issues and the interpretation of the data. T. M. O. Franzen provided additional ATLAS DR3 data and R. Hunstead made the 843 MHz map of the CDFS available. B. H. C. Emonts, H. T. Intema, J. Marvil, S. K. Sirothia, provided unpublished data used in this project as referenced in the manuscript below. Beyond that, unpublished data from the MWA and ASKAP-BETA were used. Following the publication policies of these two survey telescopes, all scientists involved in the development of the telescopes or in the observations themselves are entitled to co-author related publications data, explaining the long author list of this manuscript. Several co-authors contributed with feedback to the manuscript. My contribution to the work summarised in the manuscript below is 95%.

³<http://www.iram.fr/IRAMFR/GILDAS>

The radio spectral energy distribution of infrared-faint radio sources[★]

A. Herzog^{1,2,3}, R. P. Norris³, E. Middelberg¹, N. Seymour⁴, L. R. Spitler^{2,5}, B. H. C. Emonts⁶, T. M. O. Franzen⁴, R. Hunstead⁷, H. T. Intema⁸, J. Marvil³, Q. A. Parker^{2,5,9}, S. K. Sirothia¹⁰, N. Hurley-Walker⁴, M. Bell³, G. Bernardi^{11,12,13}, J. D. Bowman¹⁴, F. Briggs¹⁵, R. J. Cappallo¹⁶, J. R. Callingham^{7,17,3}, A. A. Deshpande¹⁸, K. S. Dwarakanath¹⁸, B.-Q. For¹⁹, L. J. Greenhill¹³, P. Hancock^{4,17}, B. J. Hazelton²⁰, L. Hindson²¹, M. Johnston-Hollitt²¹, A. D. Kapińska^{19,17}, D. L. Kaplan²², E. Lenc^{7,17}, C. J. Lonsdale¹⁶, B. McKinley^{23,17}, S. R. McWhirter¹⁶, D. A. Mitchell^{3,17}, M. F. Morales²⁰, E. Morgan²⁴, J. Morgan⁴, D. Oberoi²⁵, A. Offringa²⁶, S. M. Ord^{4,17}, T. Prabu¹⁸, P. Procopio²³, N. Udaya Shankar¹⁸, K. S. Srivani¹⁸, L. Staveley-Smith^{19,17}, R. Subrahmanyan^{18,17}, S. J. Tingay^{4,17}, R. B. Wayth^{4,17}, R. L. Webster^{23,17}, A. Williams⁴, C. L. Williams²⁴, C. Wu¹⁹, Q. Zheng²¹, K. W. Bannister³, A. P. Chippendale³, L. Harvey-Smith³, I. Heywood³, B. Indermuehle³, A. Popping^{19,17,3}, R. J. Sault^{3,23}, and M. T. Whiting³

(Affiliations can be found after the references)

Received xx Month 2015 / Accepted xx Month 2015

ABSTRACT

Context. Infrared-faint radio sources (IFRS) are a class of radio-loud (RL) active galactic nuclei (AGNs) at high redshifts ($z \geq 1.7$) that are characterised by their relative infrared faintness, resulting in enormous radio-to-infrared flux density ratios of up to several thousand.

Aims. Because of their optical and infrared faintness, it is very challenging to study IFRS at these wavelengths. However, IFRS are relatively bright in the radio regime with 1.4 GHz flux densities of a few to a few tens of mJy. Therefore, the radio regime is the most promising wavelength regime in which to constrain their nature. We aim to test the hypothesis that IFRS are young AGNs, particularly GHz peaked-spectrum (GPS) and compact steep-spectrum (CSS) sources.

Methods. We use the rich radio data set available for the Australia Telescope Large Area Survey fields, covering the frequency range between 150 MHz and 34 GHz with up to 15 wavebands from different telescopes, and build radio spectral energy distributions (SEDs) for 34 IFRS. We then study the radio properties of this class of object with respect to turnover, spectral index, and behaviour towards higher frequencies. We also present the highest-frequency radio observations of an IFRS, observed with the Plateau de Bure Interferometer at 105 GHz, and model the multi-wavelength and radio-far-infrared SED of this source.

Results. We find IFRS usually follow a single power law down to observed frequencies of around 200 MHz. Mostly, the radio SEDs are steep ($\alpha < -0.8$; $85^{+4}_{-8}\%$), but we also find ultra-steep SEDs ($\alpha < -1.3$; $12^{+8}_{-4}\%$). In particular, IFRS show statistically significantly steeper radio SEDs than the broader RL AGN population. Our analysis reveals that the fractions of GPS and CSS sources in the population of IFRS are consistent with the fractions in the broader RL AGN population. We find that at least $15^{+8}_{-4}\%$ of IFRS contain young AGNs, although the fraction might be significantly higher as suggested by the steep SEDs and the compact morphology of IFRS. Furthermore, IFRS with a turnover in their radio SED are found to be radio- and infrared-fainter than IFRS without observed turnover. The detailed multi-wavelength SED modelling of one IFRS shows that it is different from ordinary AGNs, although it is consistent with a composite starburst-AGN model with a star formation rate of $170 M_{\odot} \text{ yr}^{-1}$.

Key words. Galaxies: active – Galaxies: high-redshift – Radio continuum: galaxies

1. Introduction

Infrared-faint radio sources (IFRS) are comparatively bright radio sources with a faint or absent near-infrared counterpart. They were serendipitously discovered in the Chandra Deep Field-South (CDFs) by Norris et al. (2006) in the Australia Telescope Large Area Survey (ATLAS) 1.4 GHz map and the co-located *Spitzer* Wide-area Infrared Extragalactic Survey (SWIRE; Lonsdale et al. 2003) infrared (IR) map. Based on the SEDs of ordinary galaxies, it was expected that every object in the deep radio survey (rms of $36 \mu\text{Jy beam}^{-1}$ at 1.4 GHz in CDFS) would

have a counterpart in the SWIRE survey (rms of $\sim 1 \mu\text{Jy}$ at $3.6 \mu\text{m}$). However, Norris et al. found 22 radio sources with 1.4 GHz flux densities of a few or a few tens of mJy without $3.6 \mu\text{m}$ counterpart and labelled them as IFRS. Later, IFRS were also found in the European Large Area IR space observatory Survey South 1 (ELAIS-S1) field, the *Spitzer* extragalactic First Look Survey (xFLS) field, the Cosmological Evolution Survey (COSMOS) field, the European Large Area IR space observatory Survey North 1 (ELAIS-N1) field, and the Lockman Hole field (Middelberg et al. 2008a; Garn & Alexander 2008; Zinn et al. 2011; Banfield et al. 2011; Maini et al. 2013), resulting in around 100 IFRS known in deep fields.

[★] Based on observations carried out with the IRAM Plateau de Bure Interferometer. IRAM is supported by INSU/CNRS (France), MPG (Germany) and IGN (Spain).

While IFRS were originally defined as radio sources without IR counterpart in the first works, Zinn et al. (2011) set two criteria for the survey-independent selection of IFRS:

- (i) radio-to-IR flux density ratio $S_{1.4\text{GHz}}/S_{3.6\mu\text{m}} > 500$, and
- (ii) $3.6\mu\text{m}$ flux density $S_{3.6\mu\text{m}} < 30\mu\text{Jy}$.

The first criterion accounts for the enormous radio-to-IR flux density ratios resulting from the solid radio detection and the IR faintness. These ratios identify IFRS as clear outliers. The second criterion selects objects at cosmologically significant redshifts because of cosmic dimming or heavily obscured objects.

Collier et al. (2014) followed a different approach than used in the previous studies and searched for IFRS based on shallower data, but in a much larger area. Using the Unified Radio Catalog (URC; Kimball & Ivezić 2008) based on the NRAO VLA Sky Survey (NVSS; Condon et al. 1998) and IR data from the all-sky Wide-Field Infrared Survey Explorer (WISE; Wright et al. 2010), they found 1317 IFRS fulfilling both selection criteria from Zinn et al. (2011). Whereas some of the IFRS in deep fields are lacking a $3.6\mu\text{m}$ counterpart, all IFRS from the catalogue compiled by Collier et al. have a detected $3.4\mu\text{m}$ counterpart. Also, these sources are on average radio-brighter than the IFRS in deep fields.

Since the first IFRS were identified, it has been argued that these objects might be radio-loud (RL) active galactic nuclei (AGNs) at high redshifts ($z \gtrsim 1$), potentially heavily obscured by dust (Norris et al. 2006, 2011). Whereas other explanations like pulsars have been ruled out (Cameron et al. 2011), the suggested high redshifts of IFRS have been confirmed by Collier et al. (2014) and Herzog et al. (2014); all spectroscopic redshifts are in the range $1.7 \lesssim z \lesssim 3.0$. The first two very long baseline interferometry (VLBI) detections of IFRS were carried out by Norris et al. (2007) and Middelberg et al. (2008b) who targeted six IFRS in total and show that at least some IFRS have high brightness temperatures, indicating the presence of an AGN. Recently, Herzog et al. (2015a) found compact cores in the majority of IFRS based on a large sample of 57 sources. Middelberg et al. (2011) show that IFRS have significantly steeper radio SEDs (median index¹ of -1.4 between 1.4 GHz and 2.4 GHz) than ordinary AGNs.

An overlap between the populations of IFRS on the one hand and GHz peaked-spectrum (GPS) and compact steep-spectrum (CSS) sources on the other hand is suggested and found by Middelberg et al. (2011), Collier et al. (2014) and Herzog et al. (2015a). GPS sources are very compact and powerful AGNs with linear sizes below 1 kpc, showing a turnover in their radio spectral energy distribution (SED) at frequencies of 500 MHz or higher. CSS sources are similarly powerful, but are more extended (linear sizes of a few or a few tens of kpc) and show their turnover at frequencies below 500 MHz (e.g. O’Dea 1998; Randall et al. 2011). Further, CSS sources are characterised by their steep radio SEDs ($\alpha \lesssim -0.5$). GPS and CSS sources are usually considered to be young versions of extended radio galaxies, but it has also been suggested that they are frustrated AGNs confined by dense gas (O’Dea et al. 1991) or dying radio sources (Fanti 2009).

Modelling the multi-wavelength SED of IFRS was accomplished by Garn & Alexander (2008), Huynh et al. (2010), Herzog et al. (2014), and Herzog et al. (2015b), and shows that these sources can only be modelled as high-redshift RL AGNs, potentially suffering from heavy dust extinction. The strong link

¹ The spectral index α is defined as $S \propto \nu^\alpha$ throughout this paper where S is the flux density and ν the frequency.

between IFRS and high-redshift radio galaxies (HzRGs)—first suggested by Huynh et al. and Middelberg et al. (2011) and later emphasised by Norris et al. (2011)—has also been found in the modelling by Herzog et al. (2015b). HzRGs are massive galaxies at high redshifts ($1 \lesssim z \lesssim 5.2$) which are expected to be the progenitors of the most massive elliptical galaxies in the local universe (e.g. Seymour et al. 2007; De Breuck et al. 2010). They host AGNs and undergo heavy star forming activity. IFRS have a significantly higher sky density than HzRGs (a few IFRS per square degree versus around 100 HzRGs known on the entire sky) and are suggested to be higher-redshift or less luminous siblings of these massive galaxies.

The correlation between K band magnitude and redshift has been known for radio galaxies (e.g. Lilly & Longair 1984; Willott et al. 2003; Rocca-Volmerange et al. 2004) for three decades and was used to find radio galaxies at high redshifts. In particular, HzRGs were also found to follow this correlation (Seymour et al. 2007). Although IFRS are on average fainter than HzRGs in the near-IR regime, an overlap between both samples exists. Norris et al. (2011) suggest that IFRS might also follow a correlation between near-IR flux density and redshift. This suggestion has been supported by Collier et al. (2014) and Herzog et al. (2014) who find that those IFRS with spectroscopic redshifts are consistent with this suggested correlation. Similarly, ultra-steep radio spectra ($\alpha \lesssim -1.0$) are known to be successful tracers of high-redshift galaxies (e.g. Tielens et al. 1979; McCarthy et al. 1991; Roettgering et al. 1994). The classes of HzRGs and IFRS were both found to have steep radio spectra (Middelberg et al. 2011).

Studying IFRS in the optical and IR regime is challenging because of their faintness at these frequencies. In contrast, IFRS are relatively bright in the radio regime, making detailed radio studies feasible. Since the radio emission of RL galaxies is dominated by the AGN, radio studies of IFRS can provide insights into the characteristics of the active nucleus, e.g. its age.

This paper aims at studying the broad radio SEDs of IFRS, spanning a frequency range of more than two orders of magnitude. In Sect. 2, we present our sample of 34 IFRS from the ATLAS fields and describe the available data for the ELAIS-S1 and CDFS fields which includes the first data on IFRS below 610 MHz and above 8.6 GHz. Among others, we are using data of two of the new-generation radio telescopes and Square Kilometer Array (SKA; Dewdney et al. 2009) precursors, Murchison Widefield Array (MWA; Lonsdale et al. 2009; Tingay et al. 2013) and Australian Square Kilometer Array Pathfinder (ASKAP; Johnston et al. 2007, 2008; DeBoer et al. 2009). We also describe the Plateau de Bure Interferometer (PdBI) observations—the highest-frequency radio observations of an IFRS so far—and ancillary data of one IFRS in the xFLS field. Based on the available data, we build and fit radio SEDs for the IFRS in the ATLAS fields in Sect. 3 and analyse them with respect to spectral index, turnover, and high-frequency behaviour in Sect. 4. In Sect. 5, we present a multi-wavelength and radio SED modelling for the IFRS observed with the PdBI. Our results are summarised in Sect. 6. The photometric data obtained in Sect. 2 are summarised in Appendix A. Throughout this paper, we use flat Λ CDM cosmological parameters $\Omega_\Lambda = 0.7$, $\Omega_M = 0.3$, $H_0 = 70 \text{ km s}^{-1} \text{ Mpc}^{-1}$, and the calculator by Wright (2006). The linear scale in Λ CDM cosmology is limited in the redshift range $0.5 \lesssim z \lesssim 12$ between 4 kpc/arcsec and 8.5 kpc/arcsec. Following Cameron (2011), we calculate 1σ confidence intervals of binomial population proportions based on the Bayesian approach.

2. Observations and data

Aiming at building the broad radio SEDs of a larger number of IFRS, we based our sample on the IFRS catalogue compiled by Zinn et al. (2011). This catalogue contains 55 IFRS in the ELAIS-S1, CDFS, xFLS and COSMOS fields. Because of the rich radio data set in the ELAIS-S1 and CDFS fields, we limited our study to IFRS in these two fields only. However, we discarded the source ES11 from our sample since it was recently found to be putatively associated with a $3.6\mu\text{m}$ SWIRE source in high-resolution radio observations (Collier et al., in prep.), not fulfilling the selection criteria from Zinn et al. any more. Thus, we used 28 IFRS from the sample presented by Zinn et al. for our study: 14 IFRS in ELAIS-S1, and 14 in CDFS.

Maini et al. (2013) presented a catalogue of IFRS based on the deeper *Spitzer* Extragalactic Representative Volume Survey (SERVS) near- and mid-IR data, also covering parts of the ELAIS-S1 and the CDFS fields. Because of the deeper $3.6\mu\text{m}$ data, Maini et al. were able to identify some IFRS that were not listed in the IFRS catalogue from Zinn et al. (2011). These sources were undetected in the shallower SWIRE survey. However, because of their 1.4 GHz flux densities of around 1 mJy, they did not fulfil criterion (i) from Zinn et al. but meet the criterion based on a SERVS detection below the SWIRE limit. In order to study the less extreme versions of IFRS, Maini et al. lowered the first IFRS selection criterion from Zinn et al. and included sources with a radio-to-IR flux density ratio above 200 in their sample. Aiming at studying the originally very extreme class of IFRS, in our work, we limited our sample to a radio-to-IR flux density ratio of 500 for the definition of IFRS and added only those sources in ELAIS-S1 and CDFS from Maini et al. to our sample that fulfil this stronger criterion. Adding one IFRS in ELAIS-S1 and five IFRS in CDFS, we ended up with a sample size of 34 IFRS for our radio SED study: 15 in ELAIS-S1 and 19 in CDFS. Throughout this paper, we use identifiers from Zinn et al. and Maini et al. which are identical to the identifiers in the first ATLAS data release (DR1) presented by Norris et al. (2006) and Middelberg et al. (2008a).

We describe our radio data in Sects. 2.1 and 2.2 for ELAIS-S1 and CDFS, respectively. All observations are summarised in Tables 1 and 2, listing frequency, telescope, angular resolution, maximum sensitivity, and the number of detected IFRS, undetected IFRS, and IFRS outside the field, respectively. All photometric data are listed in Appendix A in Tables A.1 and A.2 for ELAIS-S1 and CDFS, respectively. We comment on our cross-matching approach in Sect. 2.3 and clarify our way of dealing with flux density uncertainties in Sect. 2.4. Issues arising from different angular resolutions are discussed in Sect. 2.5 and a control sample is introduced in Sect. 2.6. In Sect. 2.7, we present observations of the IFRS xFLS478 with the PdBI, describe the data calibration, and collect ancillary data.

2.1. Radio data for ELAIS-S1

2.1.1. 1.4 GHz ATLAS DR3 data

Since the definition of IFRS is based on the observed 1.4 GHz flux density, all IFRS are detected at this frequency. Zinn et al. (2011) used data from ATLAS DR1 (Norris et al. 2006; Middelberg et al. 2008a) for their IFRS catalogue. Here, we used the recent ATLAS data release 3 (DR3; Franzen et al. 2015). ATLAS DR3 has a resolution of $12 \times 8 \text{ arcsec}^2$ and a sensitivity of $\sim 17 \mu\text{Jy beam}^{-1}$ (up to $100 \mu\text{Jy beam}^{-1}$ at the edges) at 1.4 GHz in ELAIS-S1. Franzen et al. applied three criteria for their com-

ponent catalogue: (1) local rms noise below $100 \mu\text{Jy beam}^{-1}$, (2) sensitivity loss arising from bandwidth smearing below 20%, and (3) primary beam response at least 40% of the peak response. Sources in ATLAS DR3 have been fitted with one or more Gaussians, where each Gaussian is referred to as a single “component”. Thus, a source can consist of one or more components.

We extracted all components from the ATLAS DR3 component catalogue by Franzen et al. (2015) that we deemed to be associated with our 15 IFRS in ELAIS-S1. Eleven component counterparts were found for eight IFRS, fulfilling all three selection criteria from Franzen et al. Seven IFRS did not provide counterparts in ATLAS DR3. These sources are located close to the field edges and the respective sources in the DR3 map do not fulfil the primary beam response criterion (3). Therefore, these components are not listed in the component catalogue presented by Franzen et al. Middelberg et al. (2008a) used different component selection criteria which allowed sources at the field edges to be included in their catalogue.

Component extraction was performed on those seven IFRS without counterpart in the DR3 catalogue in the same way as presented by Franzen et al. (2015), however at the cost of lower beam response and higher local rms noise. Thus, nine component counterparts were found for the seven remaining IFRS, i.e. 1.4 GHz ATLAS DR3 counterparts could be extracted for all IFRS from our sample in ELAIS-S1.

We visually inspected the 1.4 GHz map along with the $3.6\mu\text{m}$ SWIRE map to check whether all components found in our manual cross-matching were associated with the IFRS. If a source is composed of more than one Gaussian component in DR3, these components are clearly separated, and we found a $3.6\mu\text{m}$ counterpart for more than one of these radio components, we disregarded those additional radio components with IR counterparts. Because of their IR counterparts, these components are putatively not radio jets of a spatially separated galaxy. In this approach, we discarded one out of 20 Gaussian components found for our 15 IFRS in ELAIS-S1. Therefore, the grouping of Gaussian components to sources differed from the automatic approach used by Franzen et al. (2015) in some cases.

We extracted integrated flux densities at 1.4 GHz from ATLAS DR3. If the counterpart of an IFRS was confirmed to be composite of more than one component in DR3 as described above, we added the integrated flux densities of the individual components and propagated the errors. Because of discarding components as described above, the 1.4 GHz flux densities of the IFRS in our sample might differ from the respective numbers in the ATLAS DR3 source catalogue.

2.1.2. 610 MHz GMRT data

The ELAIS-S1 field was observed with the Giant Metrewave Radio Telescope (GMRT) at 610 MHz with a resolution of $11 \times 11 \text{ arcsec}^2$ (Intema et al., in prep.) down to a median rms of $100 \mu\text{Jy beam}^{-1}$ over large parts of the field and up to $450 \mu\text{Jy beam}^{-1}$ at the edges. Nine out of our 15 IFRS in ELAIS-S1 were located in the final map of this project. Five more IFRS were also covered by these observations, but are located outside the final map where the primary beam response is low and the beam shape is poorly known, resulting in higher noise and uncertainty. We measured integrated flux densities from the extended map using JMFIT²—also including data with low beam

² JMFIT is a task of the Astronomical Image and Processing System (AIPS); <http://www.aips.nrao.edu/>

Table 1: Characteristics of the observations of the ELAIS-S1 field, covering 15 IFRS from our sample.

Frequency [MHz]	Telescope	Angular resolution [arcsec ²]	Sensitivity [μ Jy beam ⁻¹]	# det	# undet	# outside	Reference
200	MWA	140 × 130	7600	13	2	...	(1)
610	GMRT	11 × 11	100	14	...	1	(2)
843	MOST	62 × 43	600	15	(3)
1400	ATCA	12 × 8	17	15	(4)
2300	ATCA	33.56 × 19.90	70	15	(5)
4800	ATCA	4.6 × 1.7	130	5	1	9	(6)
8640	ATCA	4.6 × 1.7	130	3	3	9	(6)
34 000	ATCA	7 × 7	110	2	1	12	(7)

Notes. Columns 5, 6, and 7 list the number of detected IFRS, undetected IFRS, and IFRS outside the field, respectively.

References. (1) Hurley-Walker et al. (in prep.); (2) Based on the map from Intema et al. (in prep.); (3) Based on the map from Randall et al. (2012); (4) Franzen et al. (2015); (5) Based on the map from Zinn et al. (2012); (6) Middelberg et al. (2011); (7) Emonts et al. (in prep.)

Table 2: Characteristics of the observations of the CDFS field, covering 19 IFRS from our sample.

Frequency [MHz]	Telescope	Angular resolution [arcsec ²]	Sensitivity [μ Jy beam ⁻¹]	# det	# undet	# outside	Reference
150	GMRT	25.2 × 14.7	2000	12	7	...	(1)
200	MWA	135 × 120	6200	10	9	...	(2)
325	GMRT	11 × 7	100	18	1	...	(1)
610	GMRT	7.7 × 3.7	100	10	...	9	(3)
843	MOST	95 × 43	1700	8	9	2	
844	ASKAP-BETA	91 × 56	450	18	1	...	(4)
1400	ATCA	16 × 7	14	19	(5)
2300	ATCA	57.15 × 22.68	70	19	(6)
4800	ATCA	4.6 × 1.7	100	5	3	11	(7)
5500	ATCA	4.9 × 2.0	12	2	...	17	(8)
8640	ATCA	4.6 × 1.7	90	5	3	11	(7)
20 000	ATCA	29.1 × 21.9	40	2 ^a	10	7	(9)
34 000	ATCA	8.2 × 5.1	30	3	...	16	(10)

Notes. Columns 5, 6, and 7 list the number of detected IFRS, undetected IFRS, and IFRS outside the field, respectively. ^(a) These two IFRS were also detected in the follow-up observations by Franzen et al. (2014) at 5.5 GHz, 9 GHz, and 18 GHz.

References. (1) Based on the map from Sirothia et al. (in prep.); (2) Hurley-Walker et al. (in prep.); (3) Based on the map from Intema et al. (in prep.); (4) Based on the map from Marvil et al. (in prep.); (5) Franzen et al. (2015); (6) Based on the map from Zinn et al. (2012); (7) Middelberg et al. (2011); (8) Huynh et al. (2012); (9) Franzen et al. (2014); (10) Emonts et al. (in prep.)

response—for all 14 IFRS covered in these observations and accounted for the higher uncertainty as described in Sect. 2.4. IFRS ES1259 was not targeted by these observations.

2.1.3. 200 MHz GLEAM data

The Galactic and Extragalactic MWA Survey (GLEAM) targeted the entire sky south of +30° declination at 72–231 MHz (Wayth et al. 2015) with the MWA. Here, we used preliminary GLEAM data (Hurley-Walker et al., in prep.) which are reliable but incomplete. The used catalogue has been selected at 200 MHz with 60 MHz bandwidth. The beam size in ELAIS-S1 is around 140 × 130 arcsec² and the rms around 7.6 mJy beam⁻¹. We found counterparts for 13 out of 15 IFRS in ELAIS-S1. For the two IFRS undetected in the GLEAM survey, we set flux density upper limits based on the mean rms in ELAIS-S1. Since the local rms at the position of the undetected IFRS is unknown, we set a conservative 4 σ flux density upper limit—using the mean rms—of 30 mJy beam⁻¹ at 200 MHz.

2.1.4. 843 MHz MOST data

Randall et al. (2012) presented observations of the ELAIS-S1 field at 843 MHz with the Molonglo Observatory Synthesis Telescope (MOST). The data have a resolution of 62 × 43 arcsec² and an rms of around 0.6 mJy beam⁻¹. The observations from Randall et al. use the same frequency and resolution as the Sydney University Molonglo Sky Survey (SUMSS; Bock et al. 1999; Mauch et al. 2003), but are twice as sensitive.

To be consistent with MOST observations of the CDFS described below, we measured flux densities in the same way in both fields using JMFIT. As reported by Randall et al. (2012), there are two types of artefacts in their final map: grating rings and radial spokes, where the former one is relevant for our flux measurements. One of these rings interferes with one of our sources (ES1259) and neither a flux density nor an upper limit could be reliably measured. In SUMSS, this source is also affected by this artefact.

Furthermore, sources in the final map from Randall et al. (2012) are surrounded by a ring of negative pixel values (“holes”). We accounted for this issue by fitting a background level and subtracting this background from the measured flux

densities using JMFIT. We found 843 MHz flux densities for all 15 sources but ES1259. These flux densities were found to be in agreement with those reported by Randall et al. and also in agreement with the SUMSS flux densities for sources listed in that survey catalogue.

2.1.5. 2.3 GHz ATLAS data

The ELAIS-S1 field was observed with the Australia Telescope Compact Array (ATCA) at 2.3 GHz (Zinn et al. 2012) as part of the ATLAS survey. The observations resulted in an rms of $70 \mu\text{Jy beam}^{-1}$ and a resolution of $33.56 \times 19.90 \text{ arcsec}^2$. We cross-matched our IFRS sample with the source catalogue from Zinn et al. and found six out of 15 IFRS in ELAIS-S1 to have a counterpart at 2.3 GHz.

At the positions of all nine IFRS without catalogued 2.3 GHz counterpart by Zinn et al. (2012), unambiguous detections are visible in the 2.3 GHz map. Seven of these IFRS are located close to the edges of the field and their 2.3 GHz counterparts might therefore not be listed by Zinn et al. It is unclear why ES419 and ES427 in the centre of the field do not have catalogued 2.3 GHz counterparts.

Due to these missing 2.3 GHz counterparts, we measured flux densities from the 2.3 GHz map from Zinn et al. (2012) using JMFIT for all IFRS in ELAIS-S1. For the IFRS with 2.3 GHz counterparts listed by Zinn et al., we found that the flux densities measured in our work are in agreement with the flux densities from Zinn et al. For consistency purposes, we used 2.3 GHz flux densities measured in our work for all 15 IFRS in ELAIS-S1.

2.1.6. Higher-frequency radio data

Middelberg et al. (2011) studied the higher-frequency radio SEDs of IFRS and observed nine sources in the ELAIS-S1 field with the ATCA at 4.8 GHz and 8.6 GHz down to an rms of around $130 \mu\text{Jy beam}^{-1}$. Six IFRS from our sample in ELAIS-S1 were observed in this study, resulting in five detections at 4.8 GHz and three detections at 8.6 GHz. The observations had an angular resolution of $4.6 \times 1.7 \text{ arcsec}^2$ at both frequencies. We used the integrated flux densities and flux density upper limits presented by Middelberg et al. in our study.

Three IFRS from our sample in ELAIS-S1 were observed with the ATCA at 34 GHz, resulting in a resolution of around 7 arcsec and an rms of around $110 \mu\text{Jy beam}^{-1}$ (Emonts et al., in prep.). Two of the targeted IFRS were detected and one IFRS was found to be undetected. We used the related flux densities and upper limits in our study.

2.2. Radio data for CDFS

2.2.1. 1.4 GHz ATLAS DR3 data

The 1.4 GHz ATLAS DR3 data (Franzen et al. 2015) of the CDFS field with a resolution of $16 \times 7 \text{ arcsec}^2$ and a sensitivity of $\sim 14 \mu\text{Jy beam}^{-1}$ (up to $100 \mu\text{Jy beam}^{-1}$ at the field edges) was used. We extracted all components from the ATLAS DR3 component catalogue that we deemed to be associated with our 19 IFRS in CDFS as described in Sect. 2.1.1 for the ELAIS-S1 field. We found 29 component counterparts for 17 IFRS. Counterparts in DR3 for the other two IFRS were missing because of the primary beam criterion as mentioned in Sect. 2.1.1. Again, component extraction was performed on the ATLAS DR3 map at the respective positions in the same way as presented by Franzen et al. and three component counterparts were found for these two

IFRS. The resulting component catalogue was analysed and used as described in Sect. 2.1.1. In the visual inspection, we discarded six Gaussian components.

We emphasise that IFRS CS618 is peculiar and differs from all other IFRS in our sample because of its morphology. In the 1.4 GHz ATLAS map, this source appears as a typical double-lobed radio galaxy, consisting of three clearly separated emission regions, which were fitted by four Gaussian components in DR3. In Sect. 4.10, we discuss the characteristics of this source in detail.

2.2.2. 150 MHz, 325 MHz, and 610 MHz GMRT data

The maps of the CDFS at 150 MHz and 325 MHz (Sirothia et al., in prep.) are based on data from the GMRT and have resolutions of $25 \times 15 \text{ arcsec}^2$ and $11 \times 7 \text{ arcsec}^2$, respectively. The sensitivities reach around 2 mJy beam^{-1} and $100 \mu\text{Jy beam}^{-1}$, respectively. We found counterparts for twelve IFRS at 150 MHz and measured their flux densities using JMFIT. Seven IFRS remained undetected at 150 MHz. At 325 MHz, we found counterparts for 18 IFRS using JMFIT. The only undetected IFRS at this frequency is CS94. This source is located in an area where the noise is significantly higher and neither a counterpart nor a flux density upper limit could be reliably determined for this IFRS.

The TIFR GMRT Sky Survey³ (TGSS) aims to observe $37\,000 \text{ deg}^2$ at 150 MHz with a sensitivity of 7 mJy beam^{-1} . TGSS DR5 (November 2012) covers parts of the CDFS at a sensitivity of around 8 mJy beam^{-1} , and is assumed to have an uncertainty of 25% in flux density. Three IFRS from our sample are detected in TGSS DR5 and we found our flux densities measured with JMFIT in agreement with the TGSS results. However, for consistency, we used our flux densities for all sources in our study at 150 MHz and 325 MHz.

Three parts of the CDFS were observed with one pointing each with the GMRT at 610 MHz (Intema et al., in prep.). These pointings were centred on the IFRS CS114, CS194, and CS703. Five additional IFRS (CS97, CS265, CS292, CS618, CS713) are also located in the pointing fields. These observations reach sensitivities of $95 \mu\text{Jy beam}^{-1}$, $150 \mu\text{Jy beam}^{-1}$, and $80 \mu\text{Jy beam}^{-1}$, respectively, at a resolution of around $7.7 \times 3.7 \text{ arcsec}^2$. We measured flux densities from the maps using JMFIT and found 610 MHz counterparts for all eight IFRS.

2.2.3. 200 MHz GLEAM data

We cross-matched our IFRS sample in CDFS with a preliminary GLEAM catalogue (Hurley-Walker et al., in prep.), selected at 200 MHz and covering a bandwidth of 60 MHz as presented in Sect. 2.1.3. This catalogue has an angular resolution of around $135 \times 120 \text{ arcsec}^2$ and an average rms of around $6.2 \text{ mJy beam}^{-1}$ in CDFS. We found counterparts for ten out of 19 IFRS in CDFS. For eight out of the nine IFRS undetected in the GLEAM survey, we set conservative 4σ flux density upper limits of 25 mJy beam^{-1} at 200 MHz as described in Sect. 2.1.3. Since the local rms around CS194 was found to be higher, we set a flux density upper limit of 39 mJy beam^{-1} for this source.

2.2.4. 843 MHz MOST data

The CDFS was observed with MOST at 843 MHz over several epochs in 2008, very similar to the observations of the ELAIS-S1

³ <http://tgss.ncra.tifr.res.in/>

field described in Sect. 2.1.4. In CDFS, the map reaches a sensitivity of around $1.7 \text{ mJy beam}^{-1}$ at a resolution of $95 \times 43 \text{ arcsec}^2$. We measured flux densities in the same way as described for ELAIS-S1 in Sect. 2.1.4. Two IFRS are located outside the field and one IFRS is affected by radial spokes. Of the remaining 16 IFRS from our sample, nine sources provided a counterpart at 843 MHz; all other sources were undetected.

2.2.5. 844 MHz ASKAP-BETA data

The six antennas of the Boolardy Engineering Test Array (BETA; Hotan et al. 2014), a subset of ASKAP⁴, were used by the ASKAP Commissioning and Early Science (ACES) team to observe a region of around 22 deg^2 at 844 MHz (Marvil et al., in prep.). The rms in this field is around $450 \mu\text{Jy beam}^{-1}$ and the angular resolution $91 \times 56 \text{ arcsec}^2$. The field includes the CDFS, i.e. all IFRS in CDFS were covered by these observations and we found counterparts for 18 sources using JMFIT. Flux densities for sources detected both in the MOST observations (Sect. 2.2.4) and in the ASKAP-BETA observations agree within the uncertainties.

2.2.6. 2.3 GHz ATLAS data

The 2.3 GHz survey of the CDFS presented by Zinn et al. (2012) has an rms of $70 \mu\text{Jy beam}^{-1}$ at a resolution of $57.15 \times 22.68 \text{ arcsec}^2$. 13 out of 19 IFRS in the CDFS field have a 2.3 GHz counterpart listed in the source catalogue from Zinn et al. The other six IFRS show 2.3 GHz counterparts in the map, too. Four sources are located close to the field edges and therefore might not be listed in the 2.3 GHz source catalogue. CS265 and CS538 are in the centre of the field and it is unclear why their 2.3 GHz counterparts are not listed in the source catalogue from Zinn et al.

To obtain 2.3 GHz flux densities for all IFRS in CDFS, we measured flux densities of all IFRS as described in Sect. 2.1.5. For the 13 IFRS with 2.3 GHz counterpart presented by Zinn et al. (2012), we found the 2.3 GHz flux densities measured in our work to be consistent with the flux densities listed by Zinn et al. For consistency in our study, we used our own 2.3 GHz flux densities for all IFRS in CDFS.

2.2.7. Higher-frequency radio data

Middelberg et al. (2011) observed eight IFRS from our sample in CDFS with the ATCA at 4.8 GHz and 8.6 GHz at a resolution of $4.6 \times 1.7 \text{ arcsec}^2$ and an rms of around $90 \mu\text{Jy beam}^{-1}$ and $100 \mu\text{Jy beam}^{-1}$, respectively. Five of these IFRS were detected both at 4.8 GHz and 8.6 GHz, the other three IFRS remained undetected at both frequencies. We used the integrated flux densities from these observations in our study.

Huynh et al. (2012) observed the 0.25 deg^2 field of the extended CDFS (eCDFS) with the ATCA at 5.5 GHz at a resolution of $4.9 \times 2.0 \text{ arcsec}^2$, resulting in an rms of $12 \mu\text{Jy beam}^{-1}$. Two of our IFRS—CS520 and CS415—lie in the field covered by this survey and both were detected. We extracted integrated flux densities with respective errors from Huynh et al.

Higher-frequency data used for our study were taken from the Australia Telescope 20 GHz (AT20G) deep pilot survey (Franzen et al. 2014). Among other fields, this survey targeted the CDFS at 20 GHz at resolution of $29.1 \times 21.9 \text{ arcsec}^2$ down to an rms of $0.3 \text{ mJy beam}^{-1}$ or $0.4 \text{ mJy beam}^{-1}$.

Two IFRS—CS265 and CS603—were detected, whereas ten IFRS remained undetected at 20 GHz at this sensitivity and the other seven IFRS were located outside the final AT20G field.

This project also included follow-up observations at 18 GHz, 9 GHz, and 5.5 GHz of the sources detected at 20 GHz. The angular resolutions were around 10 arcsec, 25 arcsec, and 40 arcsec at 18 GHz, 9 GHz, and 5.5 GHz, respectively. The IFRS CS265 and CS603 were both detected at all three follow-up frequencies. We used the integrated flux densities at all four frequencies from the AT20G project (Franzen et al. 2014) for CS265 and CS603 and conservative flux density upper limits at 20 GHz for the undetected IFRS in the survey field.

Three IFRS from our sample (CS114, CS194, CS703) were observed with the ATCA at 34 GHz, resulting in a resolution of $8.2 \times 5.1 \text{ arcsec}^2$ and an rms of around $30 \mu\text{Jy beam}^{-1}$ (Emonts et al., in prep.). All three targeted IFRS were detected.

2.3. Cross-matching of radio data

Cross-matching of data from different catalogues—characterised by different angular resolution, sensitivity, and observing frequency—is a crucial step in order to gain broad-band information about the SEDs of astrophysical objects. Sophisticated methods such as the likelihood ratio (Sutherland & Saunders 1992) or Bayesian approaches (Fan et al. 2015) were unnecessary in our case as we were matching radio data with other radio data, the sky density of objects in these different surveys is comparatively low, and the mean distance between sources is much greater than our beamwidth. Thus, when cross-matching different catalogues, we followed a nearest-neighbour approach and checked by eye whether the cross-matching was correct and unambiguous.

2.4. Flux density uncertainties

Uncertainties on flux densities of radio sources are composed of a number of different contributions, namely errors on gain factors and source fitting, the local background rms noise, CLEANing errors and other errors. Since this work is based on radio data from several projects, a proper derivation of errors for individual flux density measurements is challenging due to the different characteristics of telescopes, surveys, and observations.

For flux densities S measured in this work, we derived the related flux density uncertainties S_{err} using the approach

$$S_{\text{err}} = \sqrt{(a_{\text{calib}} \cdot S)^2 + dS^2 + (a_{\text{edge}} \cdot S)^2}, \quad (1)$$

where a_{calib} is the fractional calibration error, dS is the flux density error obtained from the source fitting using JMFIT, and a_{edge} is an additional fractional error for some observations that applies when a source is located close to the primary beam edges. We note that the error obtained from JMFIT includes exclusively the rms of the image since the error resulting from fitting a Gaussian to the source is tiny and is therefore neglected in this task.

For observations with the GMRT (150 MHz, 325 MHz, 610 MHz), we assumed a calibration uncertainty of 25%, i.e. $a_{\text{calib}} = 0.25$. The quoted accuracy of the 843 MHz flux densities from MOST in ELAIS-S1 is 0.05 (Randall et al. 2012). Since the MOST observations of the CDFS were carried out and calibrated in the same way, we also used an accuracy of 0.05. For the ASKAP-BETA data at 844 MHz, we set $a_{\text{calib}} = 0.1$. At 2.3 GHz, we assumed an accuracy of 0.1. An additional error applies in the GMRT observations at 610 MHz for some sources located at the edges of the respective fields because of pointing

⁴ See <http://www.atnf.csiro.au/projects/askap>

errors. In this case, we set a_{edge} to 0.15. In all other cases, a_{edge} was set to zero.

When using data from published catalogues (1.4 GHz, 4.8 GHz, 5.5 GHz, 8.6 GHz, 9 GHz, 18 GHz, 20 GHz), we used the flux density errors quoted in the respective catalogue. For GLEAM counterparts, we added in quadrature a fractional uncertainty of 0.1 to the catalogued uncertainty since it does not contain the absolute flux density uncertainty.

In case of non-detections, we used flux density upper limits in our study. Since all sources are detected at 1.4 GHz in the ATLAS survey at a confidence of at least 9σ in DR3, all sources can be considered as unambiguous detections at this frequency. Therefore, we used 3σ flux density upper limits in case of non-detections at other wavelengths when using our own flux density measurements. Since flux density upper limits of faint sources are dominated by the local rms of the map and the calibration error hardly contributes, it is valid for our study to neglect the fractional calibration error in case of non-detections. For non-detections at 4.8 GHz, 8.6 GHz, and 34 GHz, we used the 3σ flux density upper limits quoted by Middelberg et al. (2011) and Emonts et al. (in prep.). The 20 GHz catalogue from Franzen et al. (2014) contains sources with S/N higher than 5. Therefore, we used 5σ flux density upper limits for undetected sources at 20 GHz. In case of non-detections at 200 MHz in the GLEAM survey, we set flux density upper limits as discussed in Sects. 2.1.3 and 2.2.3.

2.5. Effects of different angular resolutions on our analysis

In our analysis, we were using data covering a wide frequency range and taken with different telescopes as described in Sects. 2.1 and 2.2. These observations therefore cover a wide range of resolution, from a few arcsec to more than 100 arcsec. We carefully checked that our analysis is not affected by resolution effects.

Most sources from our sample are lacking complex structure and are point-like at any frequency, so there are no significant resolution effects. However, flux densities measured from lower-resolution maps can be increased because of confusing, nearby radio sources. We checked all photometric detections for potentially confusing radio sources—detected at higher resolution in the 610 MHz and 1.4 GHz observations—that might be located in the respective beam covering the IFRS. If a measured flux density is or might be affected by confusion, we did not use this data point in our analysis but considered it as a flux density upper limit. We found potential issues in the 150 MHz map, the 325 MHz map, the 843 MHz maps, the 844 MHz map, and the 2.3 GHz map and discarded one, one, one, four, and three detections, respectively.

Particular caution had to be used with respect to the GLEAM counterparts because of the large beam size. We found seven GLEAM counterparts of IFRS to be potentially confused by other sources inside the GLEAM beam that are visible in the higher-resolution data at 610 MHz and 1.4 GHz. GLEAM flux densities are corrected for the local background, i.e. faint confusing sources of the order of the local GLEAM rms do not contribute to the catalogued 200 MHz flux density. This was the case for three of these seven GLEAM counterparts. The other four GLEAM counterparts, however, have strong closeby sources in the beam and confusion is likely. Therefore, we used the GLEAM flux densities as upper limits on the 200 MHz flux densities of these four IFRS.

All flux density upper limits that were set because of confusion are specially marked in Tables A.1 and A.2. Our data

might also be affected by low surface brightness features that are measured at low frequencies but are resolved out at higher frequencies. This would result in decreasing high-frequency flux densities.

2.6. Control sample

We built a control sample of the broader RL galaxy population—i.e. non-IFRS—to compare the results from our IFRS sample. For this, we randomly selected 15 sources in ELAIS-S1 and 19 sources in CDFS, ensuring that they had similar 1.4 GHz flux densities than the IFRS from our sample described above. Cross-matching with published source catalogues, measuring flux densities, and dealing with flux density errors and confusion issues was carried out in the same way as for the IFRS sample. However, since the observations at 4.8 GHz, 8.6 GHz, and 34 GHz were targeted observations of IFRS, no data are available for the sources in the control sample at these frequencies.

2.7. PdBI observations and ancillary data of IFRS xFLS 478

To complement the cm-wave observations described above, we observed one of the brightest IFRS in the Zinn et al. (2011) catalogue, IFRS xFLS 478 (35.8 mJy at 1.4 GHz), with the PdBI. The source is located in the xFLS (Condon et al. 2003) field at RA 17h11m48.526s and Decl. +59d10m38.87s (J2000). Zinn et al. found an uncatalogued IR counterpart of around $20 \mu\text{Jy}$ at $3.6 \mu\text{m}$, resulting in a radio-to-IR flux density ratio $S_{1.4\text{GHz}}/S_{3.6\mu\text{m}} = 1831$.

2.7.1. PdBI observations

The IFRS xFLS 478 was observed in continuum with the PdBI at 105 GHz (2.9 mm), covering a bandwidth of 3.6 GHz. The observations were carried out on 25-Aug-2013 and 13-Sep-2013 in 5Dq configuration and on 25-Sep-2013 and 02-Oct-2013 in 6Dq configuration. The field of view was $51.2 \times 51.2 \text{ arcsec}^2$ and the synthesised beam was $6.03 \times 3.81 \text{ arcsec}^2$. The seeing varied between $0.95''$ and $2.44''$. The data were correlated with the wide-band correlator WideX.

In all observations, MWC 349 was observed as flux calibrator, while 1637+574 was used as phase and amplitude calibrator. Each of the four observing sessions was divided into different scans. One scan consisted of 30 subscans of 45 sec each, corresponding to a total scan length of 22.5 min. The phase and amplitude calibrator were observed for 45 sec after each scan on the target.

2.7.2. PdBI data calibration, mapping, and flux measurement

Data calibration was carried out using the Grenoble Image and Line Data Analysis Software⁵ (GILDAS) packages. We followed the different tasks in the Standard Calibration section of the CLIC software included in GILDAS. Automatic flagging was applied and phases were corrected for atmospheric effects. We measured the receiver bandpass on 1803+784 (25-Sep-2013) or 3C 454.3 (all other observing dates). In the following, we departed from the standard calibration and calibrated phases and amplitudes by averaging both polarisations, following a recommendation by the PdBI staff. Phases and amplitudes were calibrated based on 1637+574, and the flux density scale was then tied to MWC 349.

⁵ <http://www.iram.fr/IRAMFR/GILDAS>

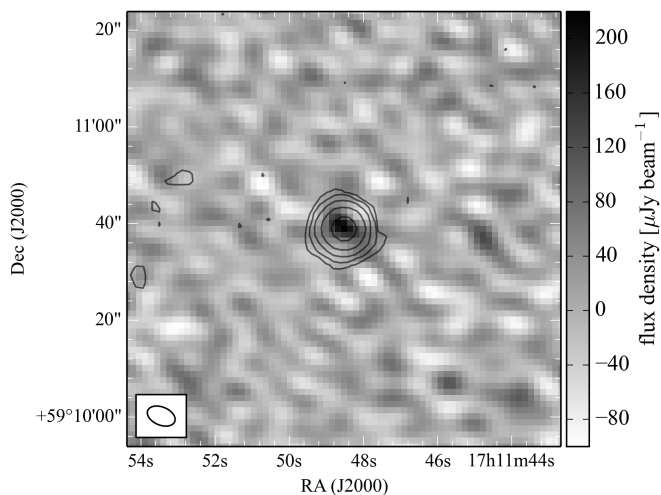


Fig. 1: Plateau de Bure Interferometer map (greyscale) of IFRS xFLS 478 at 105 GHz (2.9 mm) overlaid with the VLA 1.4 GHz radio contours from Condon et al. (2003), starting at 3σ and increasing by factors of 4.

Since the antenna configuration was changed immediately before the observations on 25-Aug-2013, an incorrect baseline solution would have been used by the standard calibration. Therefore, at the beginning of the data calibration, the most suitable baseline solution—taken on 02-Sep-2013—was applied to these data.

We performed a final flagging step on the calibrated data by flagging all visibilities with phase losses $> 40^\circ$ RMS or amplitude losses $> 20\%$ as recommended for a detection experiment. 57 116 visibilities remained after this flagging process, corresponding to an effective on-source time on IFRS xFLS 478 of 11.9 hrs with six antennas. A more strict phase loss criterion in the flagging process did not improve our data.

Data analysis was done using the task MAPPING from the GILDAS software package. We built the dirty image by applying natural weighting and using a pixel size of 0.6 arcsec and subsequently CLEANed the map. The CLEANed map is shown in Fig. 1.

Since the source appeared to be point-like in the CLEANed map, we fitted the uv data with the Fourier transform of a point source and found this fit to be consistent. Based on the fit, we obtained a flux density of $220 \mu\text{Jy beam}^{-1}$ for xFLS 478 at 105 GHz. With a measured rms noise of $36 \mu\text{Jy beam}^{-1}$, this corresponds to a 6.1σ detection. This is the highest-frequency detection of an IFRS in the radio regime. The absolute flux uncertainty is 10%.

2.7.3. Ancillary data of IFRS xFLS 478

Counterparts of xFLS 478 have been detected at 610 MHz (GMRT; Garn et al. 2007), 325 MHz (Westerbork Northern Sky Survey; Rengelink et al. 1997), and 151 MHz (6th Cambridge Survey; Hales et al. 1990). In the near- and mid-IR regime, xFLS 478 was observed with *Spitzer* and detected at $4.5 \mu\text{m}$, but remained undetected at $3.6 \mu\text{m}$, $5.8 \mu\text{m}$, and $8.0 \mu\text{m}$ (Lacy et al. 2005). Furthermore, the source xFLS 478 was observed by the *Herschel* Multi-tiered Extragalactic Survey (HerMES; Oliver et al. 2012) and was detected at $250 \mu\text{m}$, $350 \mu\text{m}$, and $500 \mu\text{m}$. Source xFLS 478 remained undetected in the Sloan Digital Sky Survey data release 10 (SDSS DR10; Ahn

et al. 2014) and also in the *R* band survey (50% completeness at 24.5 Vega mag; Fadda et al. 2004) with the Mosaic-1 camera on the Kitt Peak National Observatory. Hence, the redshift of this source is unknown.

3. Building and fitting the radio SEDs

Using the data presented in Sects. 2.1 and 2.2, we built radio SEDs for all 34 IFRS from our sample in CDFS and ELAIS-S1 based on all photometric detections and flux density upper limits. The resulting radio SEDs are shown in Fig. 2.

- (1) For each source, as the simplest approach, we fitted a single power law based on a least-squared method to all available photometric detections of the radio SED, weighting the data by their respective uncertainties. The resulting fitted single power laws are shown in Fig. 2.

We considered the fitted single power law as an appropriate description of the radio SED if (I) the low-frequency tail (below 1.4 GHz) and (II) the high-frequency (above 1.4 GHz) tail of the radio SED—considering detections and upper limits—were consistent with the fit, and (III) no turnover was seen in the central part of the radio SED. More precisely, for (I) and (II), we required that the lowest-frequency (highest-frequency) data point constraining the SED was consistent with the fit and that the low-frequency (high-frequency) cumulative deviation was below 1σ . In all cases, we considered the 1σ uncertainties of fit and data.

- (2) If the single power law in (1) was rejected because of (I) or (III), we fitted a radio SED model with a turnover to the photometric detections based on a least-squared method and weighting the data points by their uncertainties. The different models explaining this turnover can be divided by the location of the related physical process: internal or external to the synchrotron-emitting region (Kellermann 1966). If an external process is thought to cause the turnover, the physical process is expected to be free-free absorption by ionised gas outside the radio-emitting region. However, if the physical process is internal, synchrotron self-absorption (SSA) in the synchrotron-emitting region itself is usually assumed to cause the turnover. Since we found our data to trace only—if at all—the turnover in the radio SEDs but not the slope towards low frequencies (see Fig. 2), we were not able to study the physical processes causing the turnover. Therefore, the decision which model to use for the fit was not relevant for our study and did not change our results. We decided to use an SSA model (e.g. Tingay & de Kool 2003) given by

$$S_\nu = S_0 \left(\frac{\nu}{\nu_0} \right)^{-\frac{\beta-1}{2}} \frac{1 - e^{-\tau_\nu}}{\tau_\nu}, \quad \tau_\nu = \left(\frac{\nu}{\nu_0} \right)^{-\frac{\beta+4}{2}}, \quad (2)$$

where S_0 denotes the zero flux density, ν the frequency, ν_0 the frequency where the synchrotron optical depth is equal to 1, β the power law index of the relativistic electron energy distribution, and τ_ν the frequency-dependent optical depth. If the low-frequency end of the radio SED was constrained by flux density upper limits and these limits were inconsistent with the fitted single power law, we included these limits in the fitting to obtain a lower limit on the peak frequency since lower flux densities at low frequencies will push the peak towards higher frequencies. Sources fitted by the SSA model are discussed in Sect. 4.6. The fitted SSA model is shown for these sources in Fig. 2.

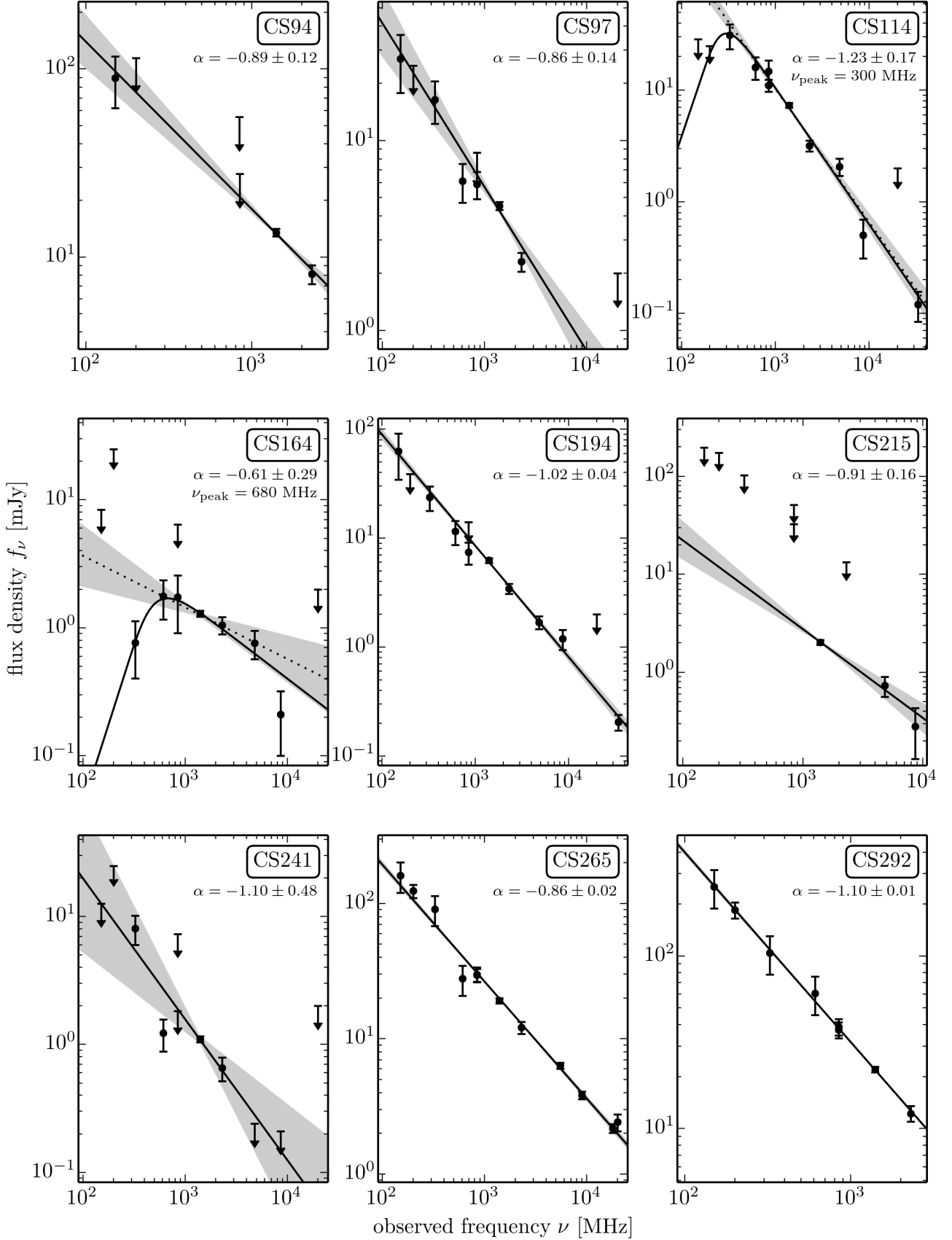


Fig. 2: Radio SEDs of IFRS in CDFS and ELAIS-S1, using all available flux density data points and upper limits. The solid line shows the fit which was found to best describe the photometric detections as discussed in Sect. 3. Spectral index and—if applicable—turnover frequency of the best fit are quoted. We also show the first approach to describe the data—a single power law fitted to all photometric detections—by a dotted line if this fit was discarded later in the analysis. 1σ uncertainties of the single power law fits are represented by the shaded areas. Error bars show 1σ uncertainties. The frequency coverage varies from one IFRS to another and the flux density scales are different.

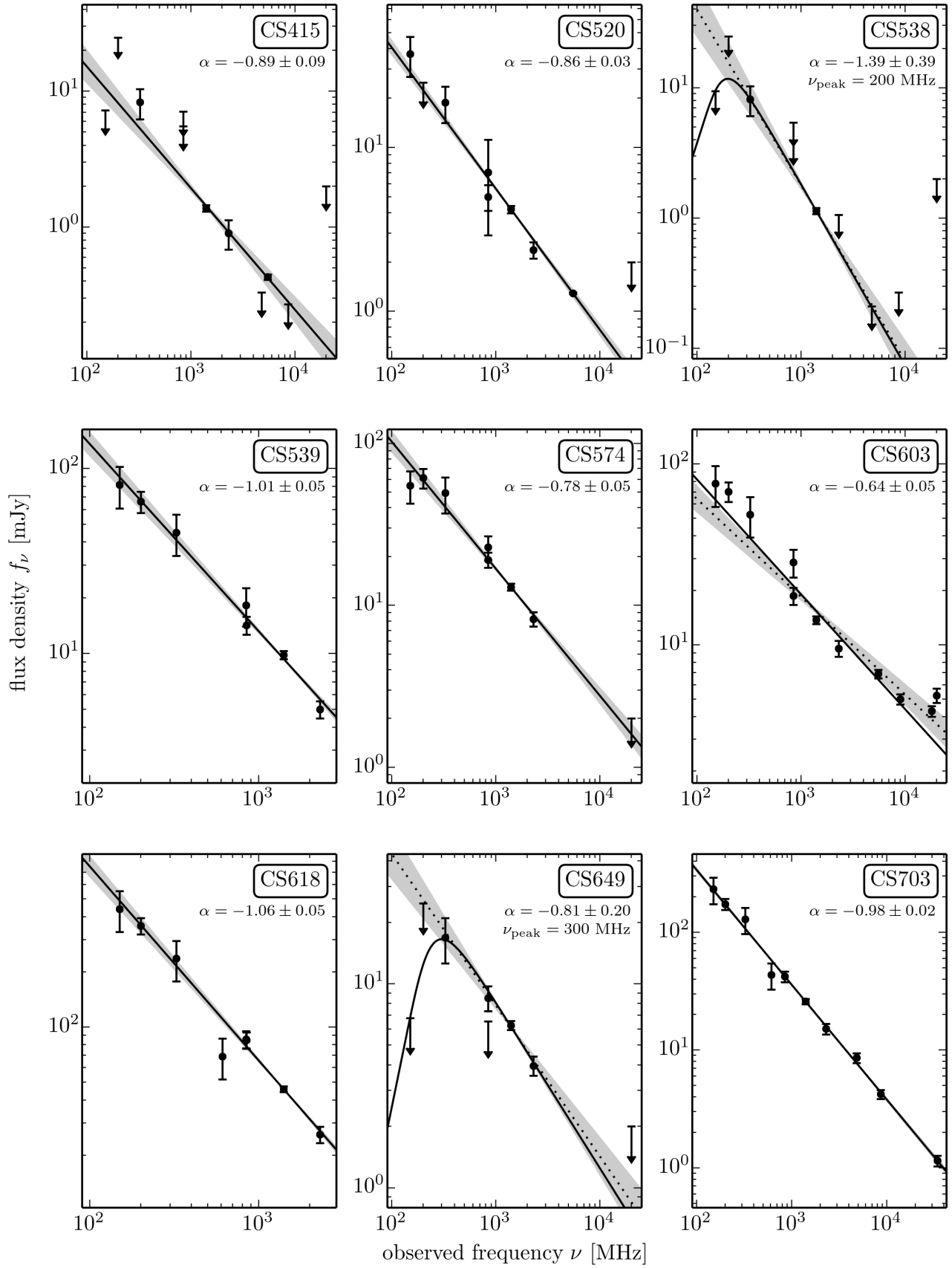


Fig. 2: continued.

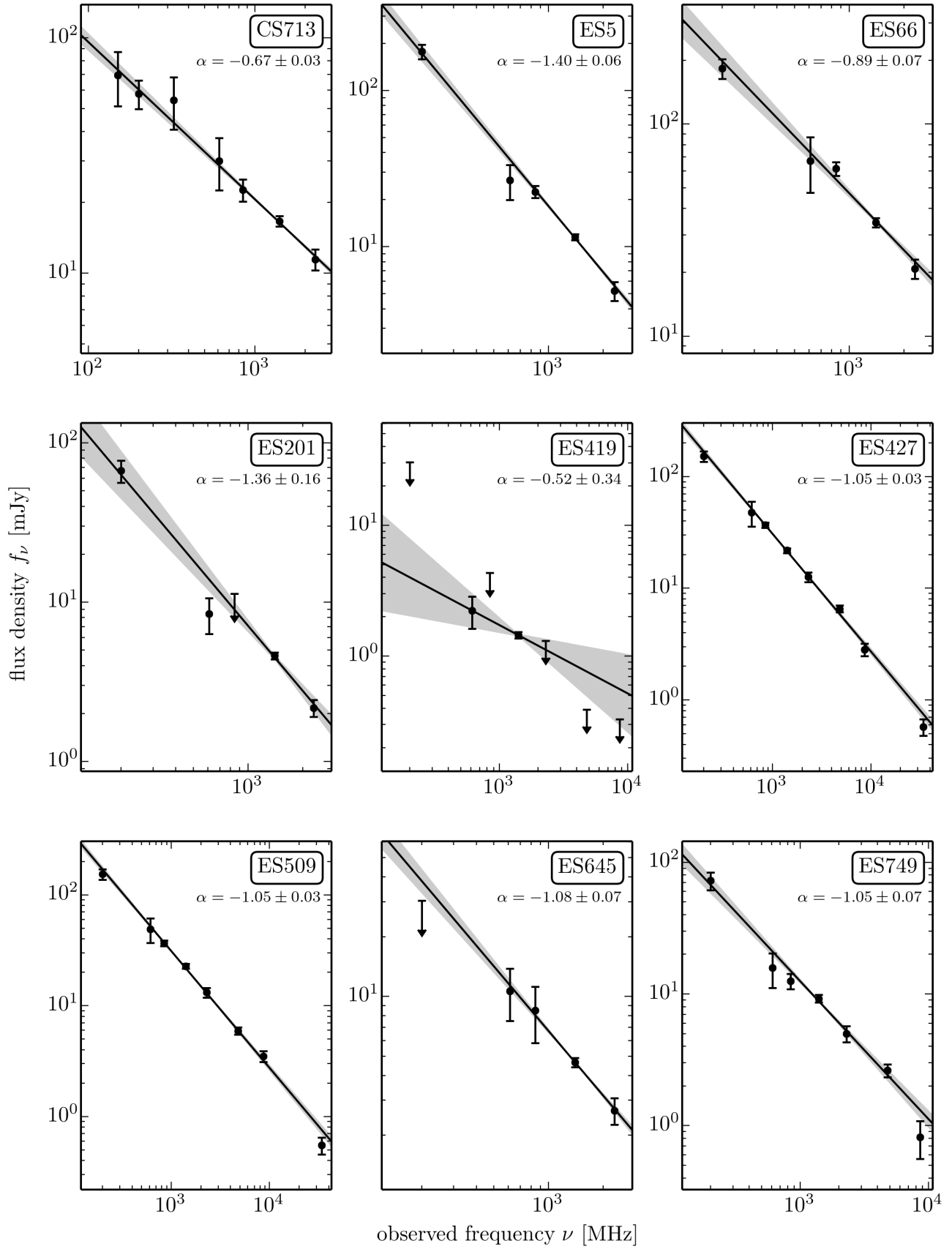


Fig. 2: continued.

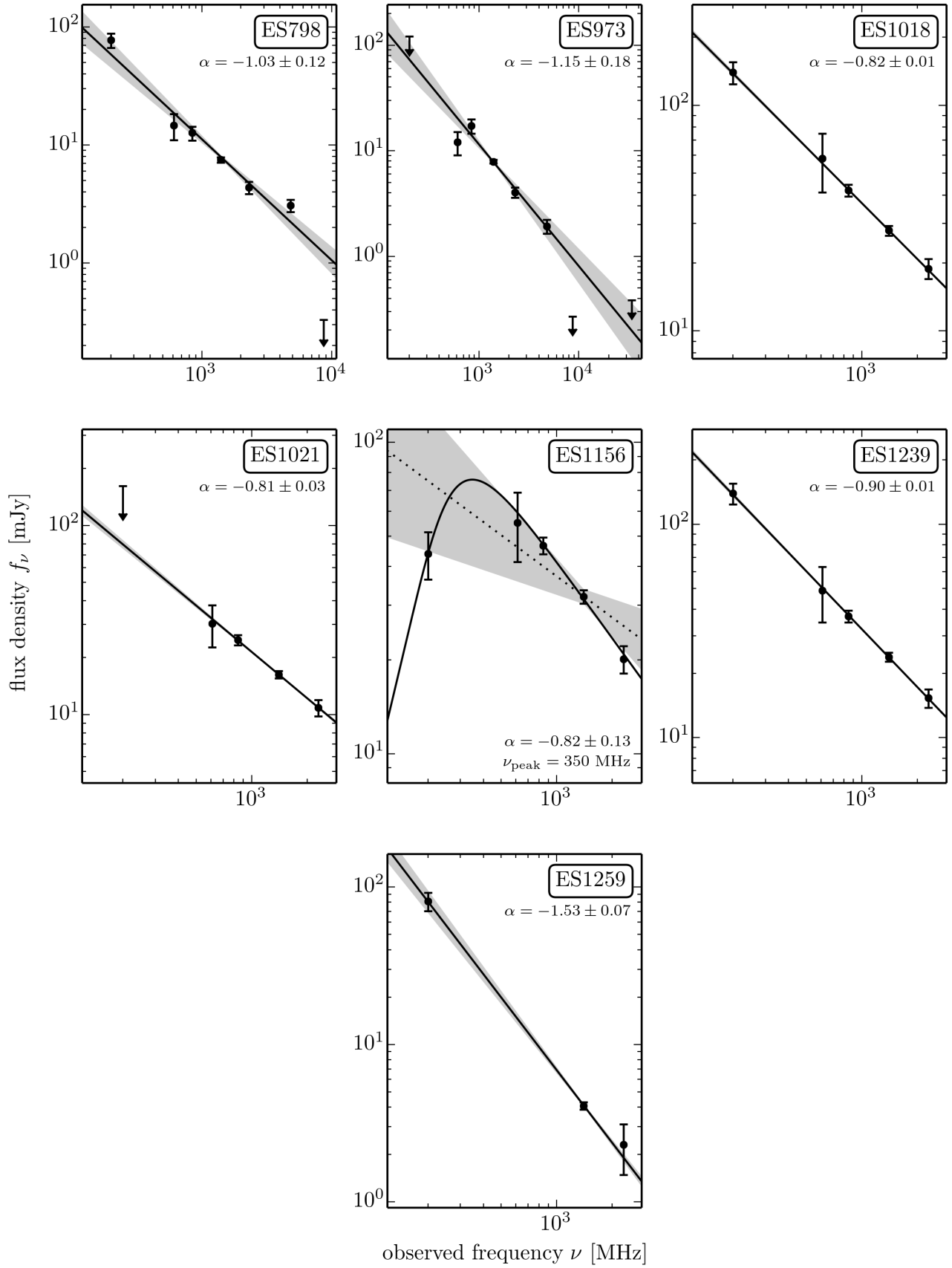


Fig. 2: continued.

(3) Sources that were found to be poorly described by a single power law because of (II) can be divided in two subclasses, depending on the departure of the fitted power law from the SED:

- (a) If the highest frequency data points departed upwards from the fitted single power law, the source was considered as showing an upturn in the radio SED. A new single power law was then fitted to the data of this source, while ignoring the deviating high-frequency data points, and this fit is also shown in Fig. 2. These sources are discussed in Sect. 4.5.
- (b) If high-frequency flux densities or upper limits were found to depart downwards from the fitted single power law, the source was considered to steepen towards higher frequencies. This subclass is discussed in Sect. 4.4.

The classification of each IFRS and the spectral index at the high-frequency side of the synchrotron bump—obtained from the best fit as described above—are summarised in Table 3. Also listed is the IAU designation, the position, and the radio-to-IR flux density ratio from Zinn et al. (2011) or Maini et al. (2013). We do not quote reduced chi-squared numbers for the fits since upper limits were used as constraints in some cases as discussed above. A statistical comparison between the fits based on these numbers would be incorrect.

The SEDs of the sources in our control sample were built and fitted in the same way. We found the SEDs to be self-consistent, i.e. without spectral features that might arise from flux density measurements at different angular resolutions. Since the IFRS and control samples would suffer from the same effects, we are confident that our analysis is not significantly affected by changing resolution. In particular, we found that our approach to classify radio SEDs as described above works for the IFRS sample and for the control sample. In the subsequent analysis, we quote numbers for the control sample in square brackets.

The class of IFRS has not been studied with respect to radio variability. Therefore, variability effects on the radio SEDs presented here cannot be ruled out. In general, long-term variability (of the order of a year) of radio sources is low at 1.4 GHz and lower frequencies (e.g. Ofek & Frail 2011; Thyagarajan et al. 2011; Mooley et al. 2013). However, this is not necessarily the case at higher frequencies ≥ 5 GHz where a significant fraction—a few tens per cent—of sources show variability of the order of 10% or more (e.g. Bolton et al. 2006; Sadler et al. 2006; Franzen et al. 2009; Chen et al. 2013). In particular, flat- or inverted-spectrum radio sources are variable because of their dominating, beamed core emission (e.g. Franzen et al. 2014). These classes of object usually dominate samples selected at ~ 20 GHz. So it is very unlikely that the 1.4 GHz flux densities of our sample are significantly affected by variability, but we have no information about variability at higher frequencies.

4. Discussion: Radio SEDs of IFRS

4.1. Sources following a single power law

Out of our sample of 34 IFRS, the SEDs of 24 IFRS [30 sources from the control sample] were well described by a single power law fitted to all available photometric data as described in Sect. 3. These sources do not show any evidence for a deviation from this fit, neither at low nor high frequencies. However, we note that nine [eight] of these sources are comparatively faint or are affected by confusion in some of the observations, reducing the number of photometric detections and, consequently, the number of data points constraining their radio SEDs. Therefore, we

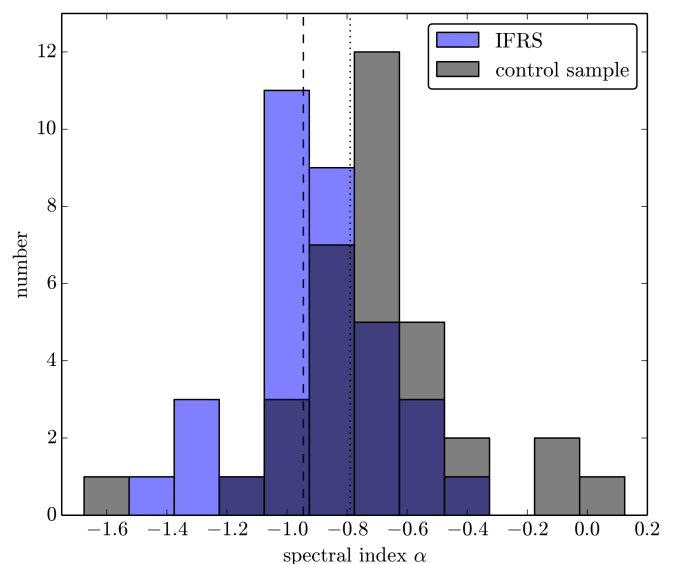


Fig. 3: Histogram of the spectral indices, resulting from the best fit to the radio SED of each individual source in our sample as described in Sect. 3. The IFRS sample is represented by blue bars and the control sample by grey bars. The vertical lines show the median spectral indices of the IFRS sample (-0.95 ; black dashed line) and the control sample (-0.79 ; black dotted line).

were able to exclude a deviation from the fitted single power law—by increasing or decreasing flux density at low or high frequencies—for only 15 [22] of these 24 IFRS [30 sources] based on the available data.

Klamer et al. (2006) studied the radio SEDs of a sample of 37 HzRGs, selected at observed frequencies between 843 MHz and 1.4 GHz. The majority of their sources (89%) were found to be well described by a single power law in the studied frequency range between 843 MHz and 18 GHz. Our frequency coverage extends significantly to lower frequencies compared to theirs. If considering only the radio SEDs above 800 MHz, we found $85^{+4}_{-8}\%$ of our IFRS to be well described by a single power law, consistent with the HzRG sample from Klamer et al. Emonts et al. (2011a) and Emonts et al. (2011b) found three HzRGs to follow single power laws up to frequencies of 36 GHz. This is consistent with all five IFRS with 34 GHz detections presented in our work.

4.2. Radio spectral index

Based on the best fit found for each IFRS as described in Sect. 3, we found spectral indices between -0.52 and -1.53 [between -0.09 and -1.73] on the high-frequency side of the synchrotron bump for the 34 IFRS in our sample. The median index is -0.95 ± 0.05 [-0.79 ± 0.06] and the mean index is -0.97 ± 0.23 [-0.77 ± 0.30]. The histogram of these spectral indices is shown in Fig. 3. We found that the IFRS sample has a steeper median SED than the control sample and that the spectral index distribution of IFRS is shifted towards steeper SEDs compared to the control sample, describing the broader, flux density-matched radio source population. The intrinsic difference between these two populations is also shown by a two-sample Anderson-Darling (A-D) test (Scholz & Stephens 1987). The A-D test measures the sum of the squared deviations of the samples and is more sensitive than a Kolmogorov-Smirnov (K-

Table 3: Characteristics and results of our sample of 34 IFRS in ELAIS-S1 and CDFS.

IFRS ID	IAU designation	RA J2000	Dec J2000	$S_{1.4\text{GHz}}/S_{3.6\mu\text{m}}$	α	Classification
CS94	ATCDFS J032740.72–285413.4	03:27:40.727	–28:54:13.48	801	-0.89 ± 0.12	pl, poss. peak
CS97	ATCDFS J032741.70–274236.6	03:27:41.700	–27:42:36.61	614	-0.86 ± 0.14	pl
CS114	ATCDFS J032759.89–275554.7	03:27:59.894	–27:55:54.73	> 2400	-1.23 ± 0.17	peak
CS164	ATCDFS J032900.20–273745.7	03:29:00.200	–27:37:45.70	640	-0.61 ± 0.29	peak, st
CS194	ATCDFS J032928.59–283618.8	03:29:28.594	–28:36:18.81	> 2033	-1.02 ± 0.04	pl
CS215	ATCDFS J032950.01–273152.6	03:29:50.010	–27:31:52.60	> 733	-0.91 ± 0.16	pl, poss. peak
CS241	ATCDFS J033010.21–282653.0	03:30:10.210	–28:26:53.00	> 908	-1.10 ± 0.48	pl, poss. peak
CS265	ATCDFS J033034.66–282706.5	03:30:34.661	–28:27:06.51	634	-0.86 ± 0.02	pl
CS292	ATCDFS J033056.94–285637.2	03:30:56.949	–28:56:37.29	1842	-1.10 ± 0.01	pl
CS415	ATCDFS J033213.07–274351.0	03:32:13.070	–27:43:51.00	> 1186	-0.89 ± 0.09	pl, poss. peak
CS520	ATCDFS J033316.75–280016.0	03:33:16.754	–28:00:16.02	500	-0.86 ± 0.03	pl
CS538	ATCDFS J033330.20–283511.1	03:33:30.200	–28:35:11.10	> 648	-1.39 ± 0.39	peak
CS539	ATCDFS J033330.54–285428.2	03:33:30.542	–28:54:28.22	640	-1.01 ± 0.05	pl
CS574	ATCDFS J033353.27–280507.3	03:33:53.279	–28:05:07.31	1091	-0.78 ± 0.05	pl, poss. peak
CS603	ATCDFS J033413.75–283547.4	03:34:13.759	–28:35:47.47	709	-0.64 ± 0.05	upturn
CS618	ATCDFS J033429.75–271744.9	03:34:29.754	–27:17:44.95	1660	-1.06 ± 0.05	pl
CS649	ATCDFS J033452.84–275813.0	03:34:52.846	–27:58:13.05	1838	-0.81 ± 0.20	peak
CS703	ATCDFS J033531.02–272702.2	03:35:31.025	–27:27:02.20	> 8700	-0.98 ± 0.02	pl
CS713	ATCDFS J033537.52–275057.8	03:35:37.525	–27:50:57.88	643	-0.67 ± 0.03	pl
ES5	ATELAIS J003709.36–444348.1	00:37:09.365	–44:43:48.11	1082	-1.40 ± 0.06	pl
ES66	ATELAIS J003942.45–442713.7	00:39:42.452	–44:27:13.77	1865	-0.89 ± 0.07	pl
ES201	ATELAIS J003130.06–441510.6	00:31:30.068	–44:15:10.69	> 1683	-1.36 ± 0.16	pl
ES419	ATELAIS J003322.76–435915.3	00:33:22.766	–43:59:15.37	557	-0.52 ± 0.34	pl, poss. peak
ES427	ATELAIS J003411.59–435817.0	00:34:11.592	–43:58:17.04	> 7120	-1.05 ± 0.03	pl
ES509	ATELAIS J003138.63–435220.8	00:31:38.633	–43:52:20.80	> 7400	-1.05 ± 0.03	pl
ES645	ATELAIS J003934.76–434222.5	00:39:34.763	–43:42:22.58	780	-1.08 ± 0.07	pl, poss. peak
ES749	ATELAIS J002905.22–433403.9	00:29:05.229	–43:34:03.94	> 2337	-1.05 ± 0.07	pl
ES798	ATELAIS J003907.93–433205.8	00:39:07.934	–43:32:05.83	> 2597	-1.03 ± 0.12	st
ES973	ATELAIS J003844.13–431920.4	00:38:44.139	–43:19:20.43	> 3046	-1.15 ± 0.18	st, poss. peak
ES1018	ATELAIS J002946.52–431554.5	00:29:46.525	–43:15:54.52	1012	-0.82 ± 0.01	pl
ES1021	ATELAIS J003255.53–431627.1	00:32:55.534	–43:16:27.15	575	-0.81 ± 0.03	pl, poss. peak
ES1156	ATELAIS J003645.85–430547.3	00:36:45.856	–43:05:47.39	2888	-0.82 ± 0.13	peak
ES1239	ATELAIS J003547.96–425655.4	00:35:47.969	–42:56:55.40	1220	-0.90 ± 0.01	pl
ES1259	ATELAIS J003827.17–425133.7	00:38:27.170	–42:51:33.70	> 2063	-1.53 ± 0.07	pl

Notes. The IAU designations and positions are taken from Norris et al. (2006) and Middelberg et al. (2008a), radio-to-IR flux density ratios from Zinn et al. (2011) and Maini et al. (2013). Spectral indices α and classification of the radio SEDs are results of our work as described in Sect. 3. If a source was found to show a turnover, it is classified by “peak” and the quoted spectral index was obtained from fitting the SSA model to the data. Sources with data that are well described by a single power law are labelled as “pl”. The additional classification “poss. peak” indicates sources for which a turnover cannot be ruled out down to 200 MHz, mainly because of their faintness. Sources steepening towards higher frequencies are labelled as “st”. Sources with increasing flux densities at the highest frequencies are indicated by “upturn”. Spectral indices were measured over different frequency ranges as discussed in Sect. 3.

S), in particular at the tails of the distribution (Babu & Feigelson 2006). We rejected the null hypothesis that the spectral indices in the IFRS sample and in the control sample have the same parent distribution (probability $p < 0.001$).

Our median spectral index for IFRS of -0.95 is flatter than the median index of -1.4 for IFRS found by Middelberg et al. (2011). However, we measured the spectral index over a wider frequency range—particularly towards lower frequencies—, whereas the median index from Middelberg et al. has been measured between 1.4 GHz and 2.4 GHz. Middelberg et al. also find a spectral steepening towards higher frequencies which is discussed in detail in Sect. 4.4. They present a median spectral index for HzRGs of $\alpha = -1.02$ between 1.4 GHz and 2.4 GHz which is close to the number found in our study for IFRS. Our median spectral index is steeper than the median spectral index of the entire radio source population ($\alpha = -0.74$) and the AGN population ($\alpha = -0.63$) in the ATLAS fields as

presented by Zinn et al. (2012) between 1.4 GHz and 2.3 GHz. The median spectral index of the broader radio source population presented by Zinn et al. is consistent with the median spectral index of -0.79 found for our control sample.

4.3. Ultra-steep, steep, flat, and inverted radio SEDs

The IFRS in our sample show generally steep radio SEDs. However, there is no generally accepted definition for steep and ultra-steep spectrum (USS) sources and selection criteria differ between studies with respect to frequencies and critical spectral index. Steep radio SEDs might be defined based on a spectral index $\alpha < -0.8$. Following this criterion, 29 ($85^{+4}_{-8}\%$) [14; $41^{+9}_{-8}\%$] out of 34 IFRS can be classified as steep-spectrum sources.

Afonso et al. (2011) point out that a significant number of sources with measured spectral indices steeper than a critical index are likely to be intrinsically flatter due to the long tail of the

spectral index distribution. They argue that $\alpha < -1.0$ is a reasonable definition for USS sources and used a conservative cut $\alpha < -1.3$ between 610 MHz and 1.4 GHz for their sample. We found four IFRS (12 $^{+8}_{-4}$ %; CS538, ES5, ES201, ES1259) [2; 6 $^{+7}_{-2}$ %] in our sample with a spectral index steeper than -1.3 . They are most likely to be USS sources. Further, twelve (35 $^{+9}_{-7}$ %) [3; 9 $^{+7}_{-3}$ %] IFRS have a spectral index in the range $-1.3 \leq \alpha \leq -1.0$. These sources are also good candidates for USS sources. In particular, we found statistically significantly more steep-spectrum sources in the IFRS sample than in the control sample. Based on a Fisher's exact test (e.g. Wall & Jenkins 2012), we found a probability $p < 0.001$ that the subsets of sources with $\alpha < -0.8$ in the IFRS sample and the control sample were obtained from the same parent spectral index distribution and, therefore, rejected this hypothesis.

USS sources in IFRS samples were already found by Garn & Alexander (2008) who classify three (21 $^{+14}_{-7}$ %) IFRS in their sample as USS sources based on a spectral index $\alpha < -1$ between 610 MHz and 1.4 GHz. Collier et al. (2014) find 155 (16 $^{+1}_{-1}$ %) USS sources—defined by $\alpha \lesssim -1.0$ —in their all-sky sample of IFRS.

Steep-spectrum radio sources tend to be at higher redshifts (e.g. Tielens et al. 1979; McCarthy et al. 1991; Roettgering et al. 1994; Chambers et al. 1996; Klamer et al. 2006), although exceptions in both directions are known (see references in Afonso et al. 2011). The suggested high redshifts of IFRS—the highest known redshift is $z = 2.99$ (Collier et al. 2014)—have been confirmed based optical spectroscopy (Collier et al. 2014; Herzog et al. 2014). However, it has been argued that the IR-faintest IFRS might be at even higher redshifts (Norris et al. 2011; Collier et al. 2014; Herzog et al. 2014). Our finding that the fraction of steep-spectrum sources is higher in the IFRS sample than in the control sample can be interpreted that IFRS might be at higher redshifts than ordinary RL AGNs.

Two IFRS from our sample have spectroscopic redshifts: CS265 ($z = 1.84$) and CS713 ($z = 2.13$). They are among the IR and optically brightest IFRS in the ATLAS fields and are therefore expected to be at the lower tail of the redshift distribution of IFRS. Following the connection between steepness of the radio SED and redshift, the radio spectral indices for these sources presented in this work of -0.88 and -0.66 —lower than the median spectral index—suggest that these sources have lower redshifts than the median IFRS in our sample, consistent with the argument based on the IR flux densities.

We found one (3 $^{+6}_{-1}$ %) IFRS in our sample [6; 18 $^{+8}_{-5}$ %] with a flat ($-0.6 \leq \alpha \leq 0$) and none (0 $^{+5}_{-0}$ %) [0; 0 $^{+5}_{-0}$ %] with an inverted ($\alpha > 0$) radio SED. Based on these numbers, we are confident that the radio SEDs presented in this work are not significantly affected by radio variability as discussed in Sect. 3.

4.4. Radio SEDs steepening towards higher frequencies

We found three IFRS (9 $^{+8}_{-3}$ %; CS164, ES798, ES973) [none; 0 $^{+5}_{-0}$ %] in our sample that show a steepening radio SED towards higher frequencies, suggesting that a single power law does not properly describe the data. This spectral behaviour was already found for two of these IFRS by Middelberg et al. (2011) and can be explained by a recently inactive AGN. In a magnetic field, higher-energy electrons lose their energy faster than low-energy electrons. If a region of synchrotron emission is not fed by the continuous injection of new particles, the highest-energy particles are cooled quicker by energy losses than low-energy particles, resulting in a lack of radiated high-energy photons and a

steepening in the SED towards higher frequencies (e.g. Kardashev 1962).

Middelberg et al. (2011) matched the uv coverage of their observations at 4.8 GHz and 8.6 GHz to eliminate the possibility that the observed spectral steepening between 4.8 GHz and 8.6 GHz might be caused by resolution effects. Therefore, this can be ruled out for ES798 and ES973—both detected at 4.8 GHz but undetected at 8.6 GHz—and CS164 which was detected at both frequencies.

Based on their resolution-matched spectral indices between 1.4 GHz and 2.4 GHz on the one hand and between 4.8 GHz and 8.6 GHz on the other hand, Middelberg et al. (2011) find that the radio SEDs of IFRS generally steepen towards higher frequencies. Some IFRS in our sample are also steepening towards higher frequencies. However, our data at high frequencies are generally not sensitive enough to detect or constrain the radio SED of our IFRS. Only four IFRS were detected in the higher-frequency surveys by Huynh et al. (2012) and Franzen et al. (2014); these are the only IFRS from our sample detected at a frequency above 2.3 GHz that were not covered in the observations by Middelberg et al. For these four sources, we did not find evidence for a steepening. In contrast, one of those four IFRS even shows an upturn as discussed in the following Sect. 4.5.

We did not find a steepening radio SED towards higher frequencies for any source in our control sample. However, few high-frequency data are available in the control sample since the observations at 4.8 GHz, 8.6 GHz, and 34 GHz were targeted observations of IFRS and no data are available at these frequencies for the sources in the control sample. Therefore, we cannot exclude the possibility that a steepening occurs for some of the control sources but is not seen in our data because of poor high-frequency coverage and sensitivity. Klamer et al. (2006) did not find any HzRG in their sample of 37 sources that steepens at higher frequencies. If the fraction of steepening sources is higher for IFRS than for HzRGs, this might suggest an intrinsic difference. In that case, IFRS might be recently inactive and restarted RL AGNs, whereas HzRGs do not show any evidence for a changing activity of their active nucleus.

4.5. IFRS with an upturn in their radio SED

The radio SED of IFRS CS603 follows a single power law in the frequency range between 800 MHz and 10 GHz. At higher frequencies, however, the SED departs from this power law, showing an increasing flux density with increasing frequency. This is indicated by the 18 GHz detection and clearly visible from the 20 GHz detection. There are two potential explanations for this behaviour.

A flattening or upturning SED at high frequencies can be explained by a flat or inverted SED of an AGN core that is dominating over the steep synchrotron SED of the lobes at these frequencies. Alternatively, the upturn might be caused by dust. It is known that thermal free-free and dust emission start to dominate over the non-thermal synchrotron emission at rest-frame frequencies above ~ 100 GHz in starburst galaxies (e.g. Murphy 2009; Fig. 2), though thermal dust emission significantly depends on the size and composition of the dust grains. Considering that IFRS are known to be AGNs and that no evidence for heavy dust obscuration in IFRS has been found (Collier et al. 2014), the flat or inverted radio SED of an AGN core seems to be the most plausible explanation. Higher-frequency observations would be needed to add evidence to this hypothesis.

Since we found an upturning SED at high frequencies also for one source in the control sample, this spectral behaviour does

not seem to be a characteristic feature of IFRS, but to occur in the broader RL AGN population, too. The results from Klammer et al. (2006), finding 11% of their HzRGs flattening at higher frequencies, is also consistent. The putative causes for this effect discussed with respect to the IFRS are also valid for HzRGs and ordinary AGNs without IR-faintness.

4.6. Radio SEDs showing a turnover

Covering the frequency regime between 200 MHz and 34 GHz in ELAIS-S1 and between 150 MHz and 34 GHz in CDFS, our data enabled us to detect the turnover in the radio SEDs of IFRS in a wide frequency range. In particular, GPS sources with a turnover frequency above 500 MHz and CSS sources, peaking at frequencies below 500 MHz, should be detectable based on our rich data set. It has been argued by Middelberg et al. (2011) and Herzog et al. (2015a) that an overlap between the population of GPS and CSS on the one hand and IFRS on the other hand might exist. Collier et al. (2014) find that at least a few IFRS are GPS or CSS sources.

The radio SEDs shown in Fig. 2 revealed that CS164 and ES1156 have a turnover in the frequency range of a few hundred MHz [three sources in the control sample]. Based on fitting an SSA model to the data, we found peak frequencies in the observed frame of 350 MHz and 680 MHz [220 MHz – 1 GHz]. In addition to these two IFRS, the radio SEDs of CS114, CS538, and CS649 [no source] also suggest a turnover in the frequency regime covered by our data. However, the putative peak in the radio SEDs of these three sources is indicated only by flux density upper limits. Based on fitting the SSA model to the flux density upper limits, we obtained lower limits of the peak frequencies between 200 MHz and 300 MHz for these three sources.

Summarising, we found five ($15_{-4}^{+8}\%$) IFRS [$3; 9_{-3}^{+7}\%$] in our sample of 34 sources that show a clear turnover in their radio SED based on photometric detections or flux density upper limits. Out of these peaking sources, one IFRS [one] was found to peak at an observed frequency above 500 MHz, fulfilling the selection criterion of GPS sources (note that GPS sources are usually defined based on their observed peak frequency; O’Dea 1998). Based on these numbers, we suggest that $3_{-1}^{+6}\%$ of IFRS [$3_{-1}^{+6}\%$] are GPS sources. Considering that we cannot rule out a turnover in the frequency range above 200 MHz for nine [eight] other sources since their low-frequency regime is only constrained by upper limits, we conclude that between $15_{-4}^{+8}\%$ and $41_{-9}^{+9}\%$ of IFRS [between $9_{-3}^{+7}\%$ and $32_{-7}^{+9}\%$] show a turnover at a frequency above 150 MHz. However, since CSS sources can also have their turnover at frequencies below 150 MHz—i.e. even IFRS following a single power law down to 150 MHz might be CSS sources—we are not able to set an upper limit on the fractional overlap between IFRS and CSS sources. However, we suggest that this overlap is $\geq 9_{-3}^{+7}\%$ [$\geq 6_{-3}^{+7}\%$]. The class of CSS sources (e.g. O’Dea 1998) is defined by steep radio SEDs ($\alpha \lesssim -0.5$) and compact morphology (a few or a few tens of kpc). Since IFRS are known to be compact with linear sizes of not more than a few tens of kpc (e.g. Garn & Alexander 2008; Middelberg et al. 2011) and to have steep radio SEDs (Middelberg et al. 2011; and discussion in Sects. 4.2 and 4.3), IFRS are prototypical for the class of CSS sources. In particular, we found three additional sources (CS415, CS574, ES645) that slightly departed from the fitted single power law at low frequencies and might be CSS sources not represented in our statistics. Therefore, we suggest that the fraction of CSS sources is putatively significantly higher than the observed fraction of $9_{-3}^{+7}\%$.

In our control sample, we found $3_{-1}^{+6}\%$ and $\geq 6_{-3}^{+7}\%$ of the sources to be GPS sources and CSS sources, respectively. These numbers are consistent with those found by O’Dea (1998) in the broader population of RL AGNs ($\sim 10\%$ and $\sim 30\%$, respectively). Comparing these numbers to those found for our IFRS sample, we did not find any evidence for a higher fraction of GPS and CSS compared to samples of ordinary RL AGNs. However, the potentially high redshifts of our IFRS sample might prevent us from picking up the expected peak in the radio SED covered by our data. Although suffering from small number statistics, the lower turnover frequencies found in the IFRS sample compared to the control sample is consistent with putatively higher redshifts of IFRS.

It has already been argued that a significant fraction of IFRS might be young AGNs in their earliest evolutionary stages (Collier et al. 2014; Herzog et al. 2015a). Although our results based on the turnover do not provide evidence for a higher fraction of GPS and CSS sources in the IFRS population, they do not exclude this possibility either. Instead, a high fraction of CSS sources is likely because of the steep radio SEDs and the compact morphology of IFRS. If IFRS are indeed younger—i.e. with turnovers at high rest-frame frequencies—and at higher redshifts than the broader AGN population, these two effects would work against each other. A younger radio galaxy is expected to peak at a higher rest-frame frequency, but a high redshift shifts this peak to a lower frequency, resulting in similar observed fractions of GPS and CSS sources in the IFRS population and in the broader RL AGN population. Since we are lacking redshifts for the vast majority of IFRS in our sample, we are unable to distinguish between these two effects contributing to the observed peak frequency: evolution of the AGN, and cosmology.

4.7. Connection between turnover frequency and linear size

Based on samples of GPS and CSS sources, O’Dea & Baum (1997) presents an anti-correlation between intrinsic turnover frequency and linear size (their Fig. 3). In the evolutionary scenario for AGNs described in Sect. 4.6, this correlation implies a shift of the turnover to lower frequencies while the AGN evolves and the jets expand. Here, we analyse our sample in the context of this scenario.

The typical linear size of fully evolved RL AGNs, i.e. FRI/FRII, is around 100 kpc or higher (Pentericci et al. 2000). Higher resolution data used in our work show that the majority of IFRS are smaller than 100 kpc as already mentioned by Garn & Alexander (2008) and Middelberg et al. (2011). However, generally, the angular resolution of our observational data is not high enough to test whether the correlation between intrinsic turnover frequency and linear size holds for our sources. The plot from O’Dea & Baum (1997) shows sources with linear sizes of around 10 kpc and smaller. Furthermore, the two correlated quantities are redshift-dependent, resulting in an additional uncertainty for the redshift-lacking IFRS sample.

Even for the most compact IFRS, the correlation from O’Dea & Baum (1997) provides only weak constraints. Middelberg et al. (2011) concluded that three IFRS (CS703, ES427, ES509) are even smaller than $4.5 \text{ kpc} \times 2.1 \text{ kpc}$ since they do not show any evidence for being resolved at any of the five frequencies used in their study. Following O’Dea & Baum, a source limited to that linear size is expected to show a turnover at a rest-frame frequency of around 300 MHz or higher. Already at a redshift of $z = 1$, this turnover would have been shifted out of the frequency range covered by our data. This is consistent with our finding, that the radio SEDs of these three sources clearly follow

single power laws down to observed frequencies of 200 MHz or 150 MHz without indicating a turnover.

Going the other way around and using the fitted peak frequencies of 350 MHz and 680 MHz, the rest-frame peak frequencies are above 1 GHz and 2 GHz, respectively, assuming that these sources are at $z \gtrsim 2$. Following the correlation presented by O’Dea & Baum (1997), these objects are expected to be smaller than ~ 300 pc and ~ 100 pc, respectively. In all available maps, CS164 and ES1156 were found to be very compact. In particular, CS164 was observed by Middelberg et al. (2011) at high angular resolution and did not reveal any substructure, suggesting an angular size of less than 1 arcsec, consistent with the linear size estimated from the observed turnover frequency.

4.8. Comparison of peaking and non-peaking sources

As presented above, we found five IFRS that show a turnover in their radio SEDs and 20 IFRS unambiguously without a peak in the frequency range covered by our data. We compared the median properties of these two subsamples and found a 1.4 GHz flux density of 6.3 mJy (13.7 mJy), a $3.6\ \mu\text{m}$ flux density of $< 3\ \mu\text{Jy}$ ($= 11.1\ \mu\text{Jy}$), and a radio-to-IR flux density ratio of ≥ 1838 ($= 1660$) for the peaking (non-peaking) subsample.

Summarising, the peaking subsample is both radio- and IR-fainter than the non-peaking subsample. An A-D test (Scholz & Stephens 1987) with respect to the 1.4 GHz flux density showed that the null hypothesis—the peaking and non-peaking subsamples have the same parent population—can be rejected at a 0.07 significance level. Though not statistically significant, it might indicate an intrinsic difference between those two subsamples. However, we emphasise that this result has to be considered with caution since it is based on small number statistics.

Our subsample of peaking sources putatively contains GPS and young CSS sources, whereas the non-peaking subsample is expected to contain older CSS sources peaking at observed frequencies below 150 MHz. At first glance, a difference in the radio brightness found for the two subsamples is unexpected since O’Dea & Baum (1997) showed that GPS and CSS have similar radio luminosities, i.e. young AGNs do not become radio-brighter while evolving and expanding. Potentially, a different redshift distribution in the two subsamples is responsible for the differences in the 1.4 GHz flux densities. Since we found the peaking subsample to be IR-fainter, we expect these IFRS to be at higher redshifts—following the suggested correlation between $3.6\ \mu\text{m}$ flux density and redshift for IFRS (Norris et al. 2011; Collier et al. 2014; Herzog et al. 2014)—, resulting in 1.4 GHz luminosities potentially similar to those of the non-peaking subsample. On the other hand, the IR faintness and expected higher redshifts of the peaking subsample make a detection of the peak less likely since the turnover would be redshifted out of the frequency regime covered by our data. Redshift information is crucial to disentangle these two effects—evolution and cosmology—, contributing in opposite directions.

4.9. Radio spectral index as a function of IR and radio properties

So far, we have focused on the radio SEDs of our IFRS sample and found that the population of IFRS does not necessarily deviate from the general RL source population with respect to the fraction of GPS and CSS sources. However, IFRS were found to have steeper radio SEDs than the ordinary AGN and star form-

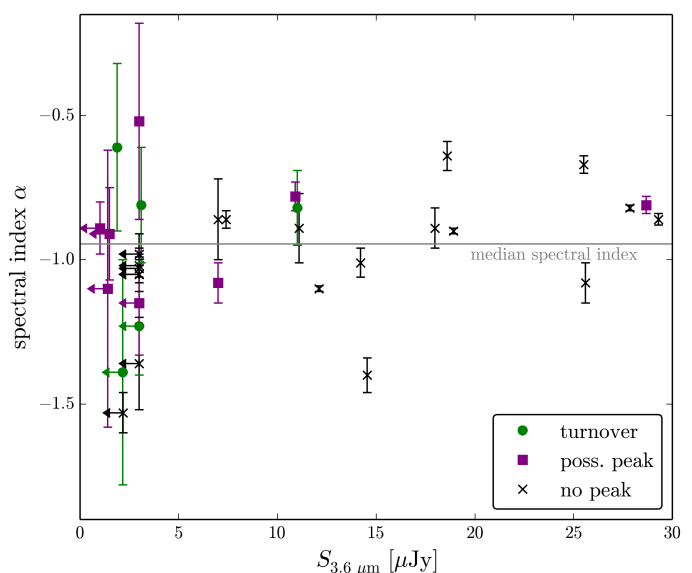


Fig. 4: Radio spectral index α as a function of the $3.6\ \mu\text{m}$ flux density for our sample of 34 IFRS. Green dots represent sources with a detected turnover. Sources with a possible peak are shown by purple squares, and sources without a peak by black crosses. IR flux density upper limits are represented by arrows. The grey horizontal line indicates the median spectral index.

ing galaxy populations. Here, we link the radio SEDs to the IR properties of IFRS.

As discussed in Sect. 4.4, higher-redshift radio galaxies have generally steeper radio SEDs. Connecting this correlation to the suggested relation between $3.6\ \mu\text{m}$ flux density and redshift for IFRS (Norris et al. 2011; Collier et al. 2014; Herzog et al. 2014), IR-fainter IFRS would be expected to have steeper radio SEDs. We tested our data for this potential correlation and show the spectral index as a function of $3.6\ \mu\text{m}$ flux density in Fig. 4. Our data do not exclude a correlation, but do not find statistically significant evidence for it either. When splitting our sample at a $3.6\ \mu\text{m}$ flux density of $15\ \mu\text{Jy}$, we found only one ($13_{-4}^{+20}\%$) out of eight IFRS in the IR-brighter subsample with a radio SED steeper than the median, whereas 16 ($61_{-10}^{+8}\%$) out of 26 IFRS in the IR-fainter subsample have a steeper spectral index than the median. We also tested the data based on a Spearman rank correlation test (e.g. Wall & Jenkins 2012) and found a correlation coefficient r between 0.25 and 0.56, considering the unknown relation between the IR-undetected sources. A coefficient of 1 (−1) corresponds to an ideal (anti-)correlation, whereas 0 indicates a lacking correlation. The probability p that $3.6\ \mu\text{m}$ flux density and spectral index are uncorrelated is between 0.075 and 0.0003. For the control sample, we found a correlation coefficient of -0.04 , indicating no evidence of a strong correlation.

We also looked at the spectral index as a function of 1.4 GHz flux density and found no correlation, neither in the IFRS nor in the control sample. Based on 15.7 GHz data, Franzen et al. (2014) showed that the general radio source population with 15.7 GHz flux densities above ~ 25 mJy and below ~ 1 mJy is dominated by flat ($\alpha > -0.5$) spectrum sources, whereas the intermediate flux density range is dominated by sources with steep ($\alpha < -0.5$) radio SEDs. We did not find any dependence at 1.4 GHz. However, our sample has been selected at lower frequencies and our sample covers only one order of magnitude in 1.4 GHz flux density, in contrast to the sample by Franzen et al.

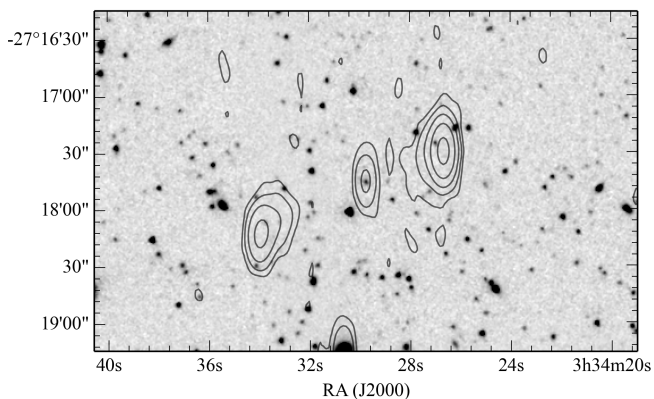


Fig. 5: $3.6\mu\text{m}$ SWIRE map (Lonsdale et al. 2003; greyscale) of CS618 overplotted by the 1.4 GHz ATLAS DR3 (Franzen et al. 2015) contours. Contours start at 3σ and increase by factors of 4. CS618 is an evolved FR II radio galaxy with an unresolved core (centre of the shown map) and two slightly resolved lobes.

4.10. Radio SED of IFRS CS618

The IFRS CS618 is peculiar and has a different morphology than any other source in our IFRS sample. The $3.6\mu\text{m}$ map of CS618 overplotted by the 1.4 GHz ATLAS DR3 contours is shown in Fig. 5. It appears as a double-lobed FR II radio galaxy with an angular size of around 1.7 arcmin. Its total radio SED (containing the core and the two lobes) is well described by a single power law with a spectral index $\alpha = -1.06 \pm 0.05$ (see Fig. 2). All three components are separately detected at 325 MHz, 610 MHz, 1.4 GHz and 2.3 GHz, but are indistinguishable at 200 MHz, 843 MHz, and 844 MHz because of the lower resolution. The radio SEDs of all three individual components are well described by single power laws. The central component (1.6 mJy at 1.4 GHz) is unresolved with a spectral index between 325 MHz and 2.3 GHz of $+0.33 \pm 0.17$, whereas the two lobes are slightly resolved with 1.4 GHz flux densities of 34.5 mJy and 11.4 mJy, and spectral indices between 150 MHz and 2.3 GHz of -1.01 ± 0.09 and -1.23 ± 0.13 . These characteristics are common for FR II radio galaxies (e.g. Hovatta et al. 2014) and so CS618 seems to differ from the majority of IFRS in our sample, which are dominated by more compact and putatively younger radio sources as discussed above.

4.11. Comparison to sources used in broad-band SED modellings

Herzog et al. (2014) presented the first redshift-based SED modelling of IFRS and find all three studied IFRS in agreement with scaled templates of 3C 48 and 3C 273. Two of these three IFRS are also in our sample: CS265 and CS713. The radio SEDs of these IFRS were found to be in good agreement with single power laws with spectral indices of -0.86 ± 0.02 and -0.67 ± 0.03 , respectively. 3C 48 is a CSS source with a spectral index of $\alpha \sim -0.8$, and the core of the RL quasar 3C 273 is known to have a flat radio SED. Based on the spectral index found in our work, the core of 3C 273 seems to provide an inadequate template to explain the characteristics of IFRS CS265. In contrast, the spectral index of CS713 matches the flat radio SED known for 3C 273, whereas the steeper SED of 3C 48 disagrees with the characteristics of CS713.

An extended sample of SED templates was used by Herzog et al. (2015b) to constrain the broad-band SED of six IFRS ob-

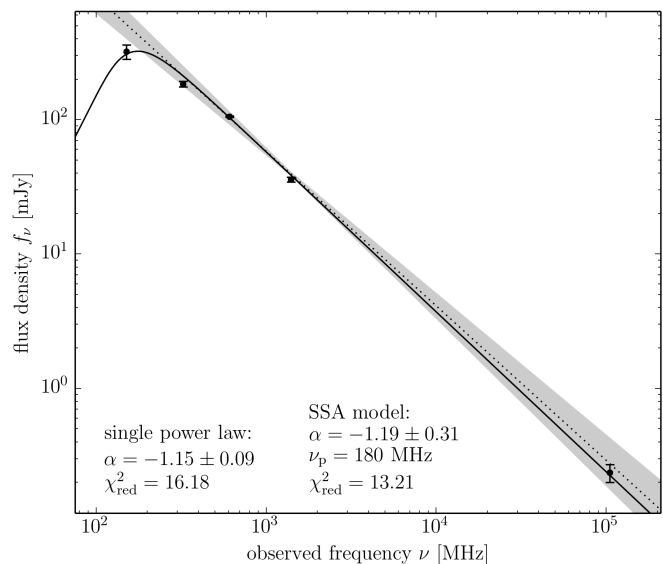


Fig. 6: Radio SED of IFRS xFLS 478. Error bars represent 1σ uncertainties. The black solid line shows the best fit of an SSA model. The fitted single power law is shown as black dotted line. The shaded area represents the 1σ uncertainty of the single power law fit.

served with *Herschel*. All sources are also in our radio sample of IFRS and we found radio spectral indices between -0.98 and -1.15 , i.e. all have steep or ultra-steep SEDs. Herzog et al. find only the redshifted broad-band SED templates of the spiderweb galaxy, Cygnus A, 3C 48, and 3C 273 to be in agreement with the data, even if the templates were scaled in luminosity and extinction was added. The flat radio SED of the core of 3C 273 is in clear disagreement with the steep radio SEDs found for all six sources. Also the radio SED of 3C 48 is flatter than any radio SED in that sample of six IFRS, although an overlap with the flattest sources in the IFRS sample cannot be ruled out. In contrast, both the spiderweb galaxy and Cygnus A are known to have ultra-steep radio SEDs with spectral indices of around -1.3 and -1.2 , respectively. Thus, the radio spectral indices measured in our work add evidence to the conclusion presented by Herzog et al. that the spiderweb galaxy and Cygnus A provide adequate templates to explain the broad-band characteristics of IFRS.

5. The radio and multi-wavelength SED of IFRS xFLS 478

In Sect. 4, we analysed the broad radio SEDs of a large sample of IFRS in the ELAIS-S1 and CDFS fields. To complement this study, we present the detailed analysis of one IFRS (xFLS 478) in the following. This study is not limited to the radio regime, but also links to the far-IR (FIR) detections of this source. IFRS xFLS 478 is particularly suitable for this study since it provides the highest-frequency radio data point of an IFRS (at 105 GHz as presented in Sect. 2.7.2) and ancillary data in the radio and IR regime, described in Sect. 2.7.3.

Figure 6 shows the radio SED of this source—including all available data between 150 MHz and 105 GHz—, similar to the SEDs shown in Fig. 2. To describe the radio emission over this wide frequency range of almost three orders of magnitude, we followed the same approach as described in Sect. 3. Fitting a single power law to the data resulted in a spectral index

$\alpha = -1.15 \pm 0.09$. However, the low-frequency data at 150 MHz and 325 MHz depart from the single power law, indicating a potential turnover. An SSA model was found to better describe the data, resulting in a turnover at 180 MHz and a spectral index of -1.19 ± 0.31 at the high-frequency side of the synchrotron bump. However, a turnover can only be suggested based on the available data; its frequency remains unclear. In any case, IFRS xFLS 478 has a steep radio SED and might—depending on the definition as discussed in Sect. 4.3—be classified as a USS source according to both fits.

If the radio SED of xFLS 478 indeed follows the fitted single power law or the SSA model up to an observed frequency above 100 GHz, this provides interesting new constraints on the properties of IFRS. As shown by Collier et al. (2014) and Herzog et al. (2014), all known redshifts of IFRS are in the range $1.7 \lesssim z \lesssim 3.0$. Assuming that xFLS 478 is at a similar redshift, the observed 105 GHz detection is at a rest-frame frequency ~ 300 GHz. It is known that the thermal free-free and dust emission in star forming galaxies start to dominate over non-thermal synchrotron emission at around 100 GHz (e.g. Murphy 2009) as discussed in Sect. 4.5. This would imply for xFLS 478 that the AGN emission of this source dominates over the emission from star forming activity even in the mm regime despite the *Herschel* detection at $250 \mu\text{m}$. The alternative explanation for a flattening of the radio SED at higher frequencies—a dominating AGN core as discussed in Sect. 4.5—can also be excluded for xFLS 478 up to this frequency.

The same behaviour—following a power law up to the mm regime—was found for the source F00183-7111 (Norris et al. 2012), referred to as 00183. 00183 is one of the most luminous ULIRGs, being heavily obscured and undergoing vigorous star forming activity, at $z = 0.3276$. In VLBI observations, a core-jet structure was found in its centre with an extension of only 1.7 kpc, however the source is radio-loud. Norris et al. suggested that this source is undergoing a transition from a merging starburst with a quasar-mode AGN in its centre to an RL quasar. Emonts et al. (2011a) and Emonts et al. (2011b) found three HzRGs to follow single power laws up to 36 GHz (115 GHz in the restframe).

We emphasise that while the suggested single power law or SSA model for xFLS 478 are the simplest explanation, it is based on only one detection in the mm regime. Other interpretations are also possible, such as a steepening SED above 1.4 GHz, followed by a minimum between 10 GHz and 100 GHz, and increasing thermal dust emission—dominating over synchrotron emission—at 105 GHz. Further high-frequency observations would be required to distinguish between these hypotheses. In Sect. 4.5, we presented one IFRS that did not follow a power law up to high frequencies but showed deviations at observed frequencies around 20 GHz. Most likely, this deviation is caused by the flat or inverted SED of an AGN core.

We now consider the multi-wavelength SED of IFRS xFLS 478, including all ancillary data presented in Sect. 2.7.3 and following the approach used by Herzog et al. (2015b). In this modelling, SED templates of different galaxy classes typically found at high redshifts—including star forming galaxies with and without AGN, Seyfert galaxies, and RL AGNs—were used, shifted in the redshift range $0.5 \leq z \leq 12$, scaled in luminosity, and obscured by additional dust. These templates were then tested whether they are consistent with the photometric data of IFRS. In this comprehensive approach, we did not find any SED template that could reproduce the characteristics of IFRS xFLS 478 in the redshift regime $0.5 \leq z \leq 12$. In particular, the most promising templates—RL AGNs at high redshifts, e.g.

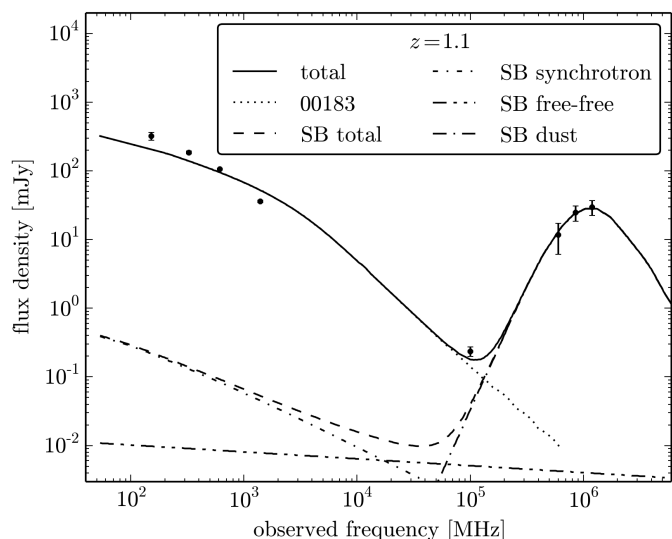


Fig. 7: Modelling the radio-FIR SED of IFRS xFLS 478. The total SED (solid line) is composed of the SED of a star forming galaxy (dashed line) from Murphy (2009) and the radio SED of 00183 (dotted line) from Norris et al. (2012). The star forming SED template is again composed of synchrotron, free-free, and thermal dust components. The best model was found at $z = 1.1$ and is shown in this figure. Black dots represent the photometric data points of xFLS 478 with respective 1σ uncertainties.

HzRGs—were found to be inconsistent with the FIR detections of xFLS 478. Herzog et al. (2015b) observed six IFRS with *Herschel* that are only slightly radio-fainter than xFLS 478 but none was detected; the detection sensitivities were similar to the observed FIR flux densities of xFLS 478.

Consequently, we asked the question what properties a galaxy would need to have to be consistent with the photometric constraints of xFLS 478. To account for the HerMES FIR detections with flux densities of a few tens of mJy, we used the radio-FIR SED template of a star forming galaxy from Murphy (2009). This template is composed of synchrotron, free-free, and thermal dust components as shown in Fig. 7 for $z = 1.1$. However, the observed radio emission of xFLS 478 cannot be explained by star forming activity at any redshift. Therefore, we added the radio emission from an RL AGN, consistent with the finding that the majority of IFRS—if not all—contain AGNs (Herzog et al. 2015a). We used the radio SED of 00183 from Norris et al. (2012). This source is known to host an RL AGN and to show similarities to xFLS 478 as discussed above. We shifted these templates in the redshift range $0.5 \leq z \leq 8.0$ and built the total SED by summing both individual templates, each of them scaled by an individual factor. The best modelling was found at $z = 1.1$ and is shown in Fig. 7. We note that the fractional contributions from synchrotron, free-free, and thermal dust emission to the star forming galaxy template were fixed as described by Murphy and were not varied in our modelling.

The photometric data of the IFRS are well described by the model at $z = 1.1$, particularly in the FIR and mm regimes. The radio SED of xFLS 478 seems to be flatter at higher frequencies than that of 00183. Norris et al. (2012) fitted a broken power law to the radio SED of 00183, finding a break at around 5 GHz and spectral indices of -0.43 and -1.49 at low and high frequencies, respectively. We measured a spectral index of -1.19

for xFLS 478 as described above and did not find clear evidence for a break at higher frequencies.

At $z = 1.1$, the 00183 radio template had to be scaled up in luminosity by a factor of 3.0. The star forming galaxy template had to be scaled up by a factor of 1.9, giving a star formation rate of around $170 M_{\odot} \text{ yr}^{-1}$. This model, if confirmed, makes xFLS 478 the lowest-redshift IFRS known.

6. Conclusion

We built radio SEDs for 34 IFRS in the CDFS and ELAIS-S1 fields, covering the frequency range between 150 MHz and 34 GHz. Based on these SEDs, we found the vast majority of IFRS ($85^{+4}_{-8}\%$) to show steep radio SEDs defined by $\alpha < -0.8$. $12^{+8}_{-4}\%$ of the IFRS in our sample are classified as USS sources ($\alpha < -1.3$) and are therefore good candidates for high-redshift sources. The sample of IFRS shows statistically significantly steeper radio SEDs than the broader RL AGN population. The median spectral index in our IFRS sample is -0.95 .

We found $3^{+6}_{-1}\%$ of our sample are GPS sources and $\geq 9^{+7}_{-3}\%$ are CSS sources. These numbers are consistent with the general fraction of GPS and CSS sources in the RL AGN population. This finding implies that at least some IFRS are young AGNs in the earliest stages of their evolution to powerful and extended FRI/FRII radio galaxies. However, the intrinsic fraction of GPS and CSS sources in the IFRS population might be higher than in the general RL source population if IFRS are at higher redshifts. Generally, IFRS are prototypical for the class of CSS sources because of their steep radio SEDs and their compactness. Our analysis showed that IFRS with an observed peak in their radio SED are radio- and IR-fainter than IFRS without a turnover, putatively explained by higher redshifts in the subsample of peaking IFRS. The complete GLEAM survey (Hurley-Walker et al., in prep.), covering the full bandwidth between 72 MHz and 231 MHz, will provide a clearer picture on the low-frequency turnover of IFRS.

We also carried out a detailed analysis of the broadband SED of IFRS xFLS 478. This source was observed with the PdBI at 105 GHz and provided the highest-frequency radio detection of an IFRS. The source was found to have a steep radio SED, potentially indicating a turnover at around 150 MHz. We did not observe an upturn or flattening in the radio SED at high frequencies, indicating that synchrotron emission dominates over thermal dust emission at least down to a rest-frame frequency of 300 GHz (1 mm) if the source is at $z \geq 2$.

Modified SED templates of known galaxies were found to be inconsistent with the multi-wavelength data of xFLS 478. However, the data are well described by a radio-FIR SED template composed of a star forming galaxy and an RL AGN at $z = 1.1$ which would make this object the lowest-redshift IFRS known. This model suggests a star formation rate of around $170 M_{\odot} \text{ yr}^{-1}$.

Acknowledgements. We thank the IRAM staff for carrying out the PdBI observations and helping with data calibration. NS is the recipient of an ARC Future Fellowship. BE acknowledges funding through the European Union FP7 IEF grant nr. 624351. This research has made use of the NASA/IPAC Extragalactic Database (NED) which is operated by the Jet Propulsion Laboratory, California Institute of Technology, under contract with the National Aeronautics and Space Administration. This research has made use of data from HerMES project (<http://hermes.sussex.ac.uk/>). HerMES is a Herschel Key Programme utilising Guaranteed Time from the SPIRE instrument team, ESAC scientists and a mission scientist. The HerMES data was accessed through the Herschel Database in Marseille (HeDaM - <http://hedam.lam.fr>) operated by CeSAM and hosted by the Laboratoire d'Astrophysique de Marseille. The Australian SKA Pathfinder is part of the Australia Telescope National Facility which is funded by the Commonwealth of Australia for operation as a National Facility managed by CSIRO. This scientific work uses data obtained from the Murchison Radio-astronomy Observatory (MRO), which is jointly funded by the Commonwealth Govern-

ment of Australia and State Government of Western Australia. The MRO is managed by the CSIRO, who also provide operational support to ASKAP. We acknowledge the Wajarri Yamatji people as the traditional owners of the Observatory site. The work was supported by iVEC through the use of advanced computing resources at the Pawsey Advanced Supercomputing Centre. Support for the MWA comes from the U.S. National Science Foundation (grants AST-0457585, PHY-0835713, CAREER-0847753, and AST-0908884), the Australian Research Council (LIEF grants LE0775621 and LE0882938), the U.S. Air Force Office of Scientific Research (grant FA9550-0510247), and the Centre for All-sky Astrophysics (an Australian Research Council Centre of Excellence funded by grant CE110001020). Support is also provided by the Smithsonian Astrophysical Observatory, the MIT School of Science, the Raman Research Institute, the Australian National University, and the Victoria University of Wellington (via grant MED-E1799 from the New Zealand Ministry of Economic Development and an IBM Shared University Research Grant). The Australian Federal government provides additional support via the Commonwealth Scientific and Industrial Research Organisation (CSIRO), National Collaborative Research Infrastructure Strategy, Education Investment Fund, and the Australia India Strategic Research Fund, and Astronomy Australia Limited, under contract to Curtin University. We acknowledge the iVEC Petabyte Data Store, the Initiative in Innovative Computing and the CUDA Center for Excellence sponsored by NVIDIA at Harvard University, and the International Centre for Radio Astronomy Research (ICRAR), a Joint Venture of Curtin University and The University of Western Australia, funded by the Western Australian State government.

References

- Afonso, J., Bizzocchi, L., Ibar, E., et al. 2011, *ApJ*, 743, 122
Ahn, C. P., Alexandroff, R., Allende Prieto, C., et al. 2014, *ApJS*, 211, 17
Babu, G. J. & Feigelson, E. D. 2006, in *Astronomical Society of the Pacific Conference Series*, Vol. 351, *Astronomical Data Analysis Software and Systems XV*, ed. C. Gabriel, C. Arviset, D. Ponz, & S. Enrique, 127
Banfield, J. K., George, S. J., Taylor, A. R., et al. 2011, *ApJ*, 733, 69
Bock, D. C.-J., Large, M. I., & Sadler, E. M. 1999, *AJ*, 117, 1578
Bolton, R. C., Chandler, C. J., Cotter, G., et al. 2006, *MNRAS*, 370, 1556
Cameron, A. D., Keith, M., Hobbs, G., et al. 2011, *MNRAS*, 415, 845
Cameron, E. 2011, *PASA*, 28, 128
Chambers, K. C., Miley, G. K., van Breugel, W. J. M., & Huang, J.-S. 1996, *ApJS*, 106, 215
Chen, X., Rachen, J. P., López-Caniego, M., et al. 2013, *A&A*, 553, A107
Collier, J. D., Banfield, J. K., Norris, R. P., et al. 2014, *MNRAS*, 439, 545
Condon, J. J., Cotton, W. D., Greisen, E. W., et al. 1998, *AJ*, 115, 1693
Condon, J. J., Cotton, W. D., Yin, Q. F., et al. 2003, *AJ*, 125, 2411
De Breuck, C., Seymour, N., Stern, D., et al. 2010, *ApJ*, 725, 36
DeBoer, D. R., Gough, R. G., Bunton, J. D., et al. 2009, *IEEE Proceedings*, 97, 1507
Dewdney, P. E., Hall, P. J., Schilizzi, R. T., & Lazio, T. J. L. W. 2009, *IEEE Proceedings*, 97, 1482
Emonts, B. H. C., Feain, I., Mao, M. Y., et al. 2011a, *ApJ*, 734, L25
Emonts, B. H. C., Norris, R. P., Feain, I., et al. 2011b, *MNRAS*, 415, 655
Fadda, D., Jannuzi, B. T., Ford, A., & Storrie-Lombardi, L. J. 2004, *AJ*, 128, 1
Fan, D., Budavári, T., Norris, R. P., & Hopkins, A. M. 2015, *ArXiv e-prints*
Fanti, R. 2009, *Astronomische Nachrichten*, 330, 303
Franzen, T. M. O., Banfield, J. K., Hales, C. A., et al. 2015, submitted to *MNRAS*
Franzen, T. M. O., Davies, M. L., Davies, R. D., et al. 2009, *MNRAS*, 400, 995
Franzen, T. M. O., Sadler, E. M., Chhetri, R., et al. 2014, *MNRAS*, 439, 1212
Garn, T. & Alexander, P. 2008, *MNRAS*, 391, 1000
Garn, T., Green, D. A., Hales, S. E. G., Riley, J. M., & Alexander, P. 2007, *MNRAS*, 376, 1251
Hales, S. E. G., Masson, C. R., Warner, P. J., & Baldwin, J. E. 1990, *MNRAS*, 246, 256
Herzog, A., Middelberg, E., Norris, R. P., et al. 2014, *A&A*, 567, A104
Herzog, A., Middelberg, E., Norris, R. P., et al. 2015a, *A&A*, 578, A67
Herzog, A., Norris, R. P., Middelberg, E., et al. 2015b, *ArXiv e-prints*
Hotan, A. W., Bunton, J. D., Harvey-Smith, L., et al. 2014, *PASA*, 31, 41
Hovatta, T., Aller, M. F., Aller, H. D., et al. 2014, *AJ*, 147, 143
Huynh, M. T., Hopkins, A. M., Lenc, E., et al. 2012, *MNRAS*, 426, 2342
Huynh, M. T., Norris, R. P., Siana, B., & Middelberg, E. 2010, *ApJ*, 710, 698
Johnston, S., Bailes, M., Bartel, N., et al. 2007, *PASA*, 24, 174
Johnston, S., Taylor, R., Bailes, M., et al. 2008, *Experimental Astronomy*, 22, 151
Kardashev, N. S. 1962, *Soviet Ast.*, 6, 317
Kellermann, K. I. 1966, *Australian Journal of Physics*, 19, 195
Kimball, A. E. & Ivezić, Ž. 2008, *AJ*, 136, 684
Klamer, I. J., Ekers, R. D., Bryant, J. J., et al. 2006, *MNRAS*, 371, 852
Lacy, M., Wilson, G., Masci, F., et al. 2005, *ApJS*, 161, 41
Lilly, S. J. & Longair, M. S. 1984, *MNRAS*, 211, 833

- Lonsdale, C. J., Cappallo, R. J., Morales, M. F., et al. 2009, *IEEE Proceedings*, 97, 1497
- Lonsdale, C. J., Smith, H. E., Rowan-Robinson, M., et al. 2003, *PASP*, 115, 897
- Maini, A., Prandoni, I., Norris, R. P., et al. 2013, submitted to *A&A*
- Mauch, T., Murphy, T., Buttery, H. J., et al. 2003, *MNRAS*, 342, 1117
- McCarthy, P. J., van Breughel, W., Kapahi, V. K., & Subrahmanya, C. R. 1991, *AJ*, 102, 522
- Middelberg, E., Norris, R. P., Cornwell, T. J., et al. 2008a, *AJ*, 135, 1276
- Middelberg, E., Norris, R. P., Hales, C. A., et al. 2011, *A&A*, 526, A8
- Middelberg, E., Norris, R. P., Tingay, S., et al. 2008b, *A&A*, 491, 435
- Mooley, K. P., Frail, D. A., Ofek, E. O., et al. 2013, *ApJ*, 768, 165
- Murphy, E. J. 2009, *ApJ*, 706, 482
- Norris, R. P., Afonso, J., Appleton, P. N., et al. 2006, *AJ*, 132, 2409
- Norris, R. P., Afonso, J., Cava, A., et al. 2011, *ApJ*, 736, 55
- Norris, R. P., Lenc, E., Roy, A. L., & Spoon, H. 2012, *MNRAS*, 422, 1453
- Norris, R. P., Tingay, S., Phillips, C., et al. 2007, *MNRAS*, 378, 1434
- O’Dea, C. P. 1998, *PASP*, 110, 493
- O’Dea, C. P. & Baum, S. A. 1997, *AJ*, 113, 148
- O’Dea, C. P., Baum, S. A., & Stanghellini, C. 1991, *ApJ*, 380, 66
- Ofek, E. O. & Frail, D. A. 2011, *ApJ*, 737, 45
- Oliver, S. J., Bock, J., Altieri, B., et al. 2012, *MNRAS*, 424, 1614
- Pentericci, L., Van Reeve, W., Carilli, C. L., Röttgering, H. J. A., & Miley, G. K. 2000, *A&AS*, 145, 121
- Randall, K. E., Hopkins, A. M., Norris, R. P., & Edwards, P. G. 2011, *MNRAS*, 416, 1135
- Randall, K. E., Hopkins, A. M., Norris, R. P., et al. 2012, *MNRAS*, 421, 1644
- Rengelink, R. B., Tang, Y., de Bruyn, A. G., et al. 1997, *A&AS*, 124, 259
- Rocca-Volmerange, B., Le Borgne, D., De Breuck, C., Fioc, M., & Moy, E. 2004, *A&A*, 415, 931
- Roettgering, H. J. A., Lacy, M., Miley, G. K., Chambers, K. C., & Saunders, R. 1994, *A&AS*, 108, 79
- Sadler, E. M., Ricci, R., Ekers, R. D., et al. 2006, *MNRAS*, 371, 898
- Scholz, F. W. & Stephens, M. A. 1987, *Journal of the American Statistical Association*, 82, 918
- Seymour, N., Stern, D., De Breuck, C., et al. 2007, *ApJS*, 171, 353
- Sutherland, W. & Saunders, W. 1992, *MNRAS*, 259, 413
- Thyagarajan, N., Helfand, D. J., White, R. L., & Becker, R. H. 2011, *ApJ*, 742, 49
- Tielens, A. G. G. M., Miley, G. K., & Willis, A. G. 1979, *A&AS*, 35, 153
- Tingay, S. J. & de Kool, M. 2003, *AJ*, 126, 723
- Tingay, S. J., Goeke, R., Bowman, J. D., et al. 2013, *PASA*, 30, 7
- Wall, J. V. & Jenkins, C. R. 2012, *Practical statistics for astronomers*, Cambridge Observing Handbooks for Research Astronomers (Leiden: Cambridge Univ. Press)
- Wayth, R. B., Lenc, E., Bell, M. E., et al. 2015, *ArXiv e-prints*
- Willott, C. J., Rawlings, S., Jarvis, M. J., & Blundell, K. M. 2003, *MNRAS*, 339, 173
- Wright, E. L. 2006, *PASP*, 118, 1711
- Wright, E. L., Eisenhardt, P. R. M., Mainzer, A. K., et al. 2010, *AJ*, 140, 1868
- Zinn, P.-C., Middelberg, E., & Ibar, E. 2011, *A&A*, 531, A14
- Zinn, P.-C., Middelberg, E., Norris, R. P., et al. 2012, *A&A*, 544, A38
-
- ¹ Astronomisches Institut, Ruhr-Universität Bochum, Universitätsstr. 150, 44801 Bochum, Germany
e-mail: herzog@astro.rub.de
- ² Macquarie University, Sydney, NSW 2109, Australia
- ³ CSIRO Astronomy and Space Science, Marsfield, PO Box 76, Ep-
ping, NSW 1710, Australia
- ⁴ International Centre for Radio Astronomy Research, Curtin Univer-
sity, Bentley, WA 6102, Australia
- ⁵ Australian Astronomical Observatory, PO Box 915, North Ryde,
NSW 1670, Australia
- ⁶ Centro de Astrobiología (INTA-CSIC), Ctra de Torrejón a Ajalvir,
km 4, 28850 Torrejón de Ardoz, Madrid, Spain
- ⁷ Sydney Institute for Astronomy, School of Physics, The University
of Sydney, NSW 2006, Australia
- ⁸ National Radio Astronomy Observatory, P.O. Box O, 1003
Lopezville Road, Socorro, NM 87801, USA
- ⁹ Department of Physics, Chong Yuet Ming Physics Building, The
University of Hong Kong, Pokfulam, Hong Kong
- ¹⁰ National Centre for Radio Astrophysics, TIFR, Post Bag 3, Pune
University Campus, 411007, Pune, India
- ¹¹ SKA SA, 3rd Floor, The Park, Park Road, Pinelands, 7405, South
Africa
- ¹² Department of Physics and Electronics, Rhodes University, PO Box
94, Grahamstown, 6140, South Africa
- ¹³ Harvard-Smithsonian Center for Astrophysics, 60 Garden Street,
Cambridge, MA 02138, USA
- ¹⁴ School of Earth and Space Exploration, Arizona State University,
Tempe, AZ 85287, USA
- ¹⁵ Research School of Astronomy and Astrophysics, Australian Na-
tional University, Canberra, ACT 2611, Australia
- ¹⁶ MIT Haystack Observatory, Westford, MA 01886, USA
- ¹⁷ ARC Centre of Excellence for All-sky Astrophysics (CAASTRO)
- ¹⁸ Raman Research Institute, Bangalore 560080, India
- ¹⁹ International Centre for Radio Astronomy Research, University of
Western Australia, 35 Stirling Hwy, Crawley, WA, 6009, Australia
- ²⁰ Department of Physics, University of Washington, Seattle, WA
98195, USA
- ²¹ School of Chemical & Physical Sciences, Victoria University of
Wellington, PO Box 600, Wellington 6140, New Zealand
- ²² Department of Physics, University of Wisconsin–Milwaukee, Mil-
waukee, WI 53201, USA
- ²³ School of Physics, The University of Melbourne, Parkville, VIC
3010, Australia
- ²⁴ Kavli Institute for Astrophysics and Space Research, Massachusetts
Institute of Technology, Cambridge, MA 02139, USA
- ²⁵ National Centre for Radio Astrophysics, Tata Institute for Funda-
mental Research, Pune 411007, India
- ²⁶ The Netherlands Institute for Radio Astronomy (ASTRON), Postbus
2, 7990 AA Dwingeloo, The Netherlands

Appendix A: Photometric data of IFRS in ELAIS-S1 and CDFS

The photometric data used to study the radio SEDs of 15 IFRS in ELAIS-S1 and 19 IFRS in CDFS are summarised in Tables A.1 and A.2, respectively.

Table A.1: Flux densities used in this work for the IFRS located in the ELAIS-S1 field.

IFRS ID	$S_{200\text{MHz}}$ [mJy]	$S_{610\text{MHz}}$ [mJy]	$S_{843\text{MHz}}$ [mJy]	$S_{1.4\text{GHz}}$ [mJy]	$S_{2.3\text{GHz}}$ [mJy]	$S_{4.8\text{GHz}}$ [mJy]	$S_{8.6\text{GHz}}$ [mJy]	$S_{34\text{GHz}}$ [mJy]
ES5	177 ± 19	26.6 ± 6.7	22.5 ± 2.0	11.51 ± 0.49	5.21 ± 0.72
ES66	183 ± 19	67.0 ± 19.6	61.6 ± 4.5	34.37 ± 1.74	20.84 ± 2.16
ES201	67 ± 11	8.5 ± 2.1	< 11.3*	4.62 ± 0.23	2.18 ± 0.26
ES419	< 30	2.2 ± 0.6	< 4.3*	1.45 ± 0.08	< 1.31*	< 0.39	< 0.33	...
ES427	152 ± 17	47.7 ± 11.9	36.8 ± 2.1	21.82 ± 1.09	12.63 ± 1.26	6.54 ± 0.46	2.83 ± 0.36	0.575 ± 0.098
ES509	153 ± 17	49.2 ± 12.3	36.6 ± 2.2	22.73 ± 1.14	13.18 ± 1.33	5.94 ± 0.45	3.51 ± 0.39	0.550 ± 0.096
ES645	< 30	10.7 ± 3.1	8.5 ± 2.7	4.66 ± 0.25	2.67 ± 0.41
ES749	73 ± 11	15.7 ± 4.7	12.6 ± 1.7	9.22 ± 0.62	4.99 ± 0.69	2.63 ± 0.29	0.82 ± 0.26	...
ES798	77 ± 11	14.6 ± 3.7	12.7 ± 1.7	7.48 ± 0.38	4.37 ± 0.51	3.07 ± 0.37	< 0.33	...
ES973	< 121*	12.1 ± 3.0	17.2 ± 2.6	7.88 ± 0.32	4.05 ± 0.44	1.93 ± 0.29	< 0.27	< 0.385
ES1018	140 ± 16	58.0 ± 16.9	42.0 ± 2.5	27.87 ± 1.40	18.89 ± 1.92
ES1021	< 162*	30.3 ± 7.6	24.8 ± 1.6	16.31 ± 0.74	10.88 ± 1.09
ES1156	44 ± 8	55.1 ± 13.8	46.6 ± 2.9	31.92 ± 1.60	20.13 ± 2.02
ES1239	140 ± 16	48.9 ± 14.3	37.1 ± 2.3	23.88 ± 1.19	15.31 ± 1.54
ES1259	81 ± 11	...	af	4.08 ± 0.22	2.31 ± 0.82

Notes. Flux density upper limits resulting from confusion are marked by (*). Sources for which the flux density could not be measured at the respective frequency because of image artefacts are marked by “af”. Sources that were outside the survey fields or not targeted by the observations at the respective frequency are represented by ellipsis dots (...).

Table A.2: Flux densities used in this work for the IFRS located in the CDFS..

IFRS ID	$S_{150\text{MHz}}$ [mJy]	$S_{200\text{MHz}}$ [mJy]	$S_{325\text{MHz}}$ [mJy]	$S_{610\text{MHz}}$ [mJy]	$S_{843\text{MHz}}$ [mJy]	$S_{844\text{MHz}}$ [mJy]	$S_{1.4\text{GHz}}$ [mJy]	$S_{2.3\text{GHz}}$ [mJy]
CS94	89 ± 27	< 114*	af	...	< 55.6	< 27.7*	13.49 ± 0.64	8.12 ± 0.93
CS97	27 ± 9	< 25	16.4 ± 4.1	6.1 ± 1.4	< 8.6	5.9 ± 1.0	4.53 ± 0.23	2.11 ± 0.26
CS114	< 29	< 25	31.1 ± 7.8	16.1 ± 3.7	14.8 ± 3.6	11.1 ± 1.4	7.34 ± 0.38	3.02 ± 0.36
CS164	< 8	< 25	0.8 ± 0.4	1.8 ± 0.6	< 6.4	1.7 ± 0.8	1.29 ± 0.07	0.81 ± 0.16
CS194	63 ± 28	< 39	23.8 ± 6.0	11.5 ± 2.9	< 14.1	7.4 ± 1.7	6.26 ± 0.32	3.10 ± 0.37
CS215	< 195*	< 174*	< 102.4*	...	< 32.6*	< 51.0*	2.03 ± 0.11	< 13.29*
CS241	< 13	< 25	8.1 ± 2.1	1.2 ± 0.3	< 7.3	< 1.8	1.10 ± 0.06	0.43 ± 0.14
CS265	161 ± 41	124 ± 14	91.0 ± 22.7	27.8 ± 7.0	29.9 ± 3.8	29.7 ± 3.2	19.13 ± 0.83	12.10 ± 1.22
CS292	252 ± 63	185 ± 20	104.2 ± 26.1	60.7 ± 15.2	38.9 ± 4.3	37.3 ± 3.9	21.99 ± 0.80	12.22 ± 1.27
CS415	< 7	< 25	8.3 ± 2.1	...	< 5.5	< 7.1*	1.38 ± 0.08	0.90 ± 0.22
CS520	37 ± 10	< 25	18.8 ± 4.7	...	7.0 ± 4.1	5.0 ± 0.9	4.19 ± 0.22	2.17 ± 0.27
CS538	< 9	< 25	8.2 ± 2.1	...	< 5.4	< 3.9*	1.14 ± 0.06	< 1.06*
CS539	82 ± 21	66 ± 9	45.0 ± 11.3	...	18.3 ± 4.3	14.2 ± 1.6	9.82 ± 0.50	4.72 ± 0.53
CS574	55 ± 12	61 ± 9	49.4 ± 12.3	...	22.9 ± 3.9	19.1 ± 2.0	12.95 ± 0.65	8.24 ± 0.84
CS603	78 ± 20	70 ± 9	52.5 ± 13.1	...	28.5 ± 5.0	18.6 ± 2.0	13.71 ± 0.69	9.55 ± 0.97
CS618	441 ± 111	357 ± 37	236.3 ± 59.1	69.2 ± 17.3	85.8 ± 9.2	84.8 ± 8.6	45.86 ± 1.66	25.90 ± 2.65
CS649	< 7	< 25	16.8 ± 4.2	...	< 6.5	8.5 ± 1.2	6.26 ± 0.32	3.88 ± 0.43
CS703	232 ± 58	173 ± 18	128.5 ± 32.1	43.5 ± 10.9	...	42.1 ± 4.3	25.89 ± 1.30	15.18 ± 1.56
CS713	69 ± 18	58 ± 8	54.4 ± 13.6	30.0 ± 7.5	...	22.6 ± 2.4	16.62 ± 0.85	11.42 ± 1.18

Notes. Flux density upper limits resulting from confusion are marked by (*). Sources for which the flux density could not be measured at the respective frequency because of image artefacts are marked by “af”. Sources that were outside the survey fields or not targeted by the observations at the respective frequency are represented by ellipsis dots (...).

Table A.2: continued.

IFRS ID	$S_{4.8\text{ GHz}}$ [mJy]	$S_{5.5\text{ GHz}}$ [mJy]	$S_{8.6\text{ GHz}}$ [mJy]	$S_{9\text{ GHz}}$ [mJy]	$S_{18\text{ GHz}}$ [mJy]	$S_{20\text{ GHz}}$ [mJy]	$S_{34\text{ GHz}}$ [mJy]
CS94
CS97	< 2.0	...
CS114	2.07 ± 0.36	...	0.50 ± 0.19	< 2.0	0.120 ± 0.036^a
CS164	0.76 ± 0.19	...	0.21 ± 0.11	< 2.0	...
CS194	1.69 ± 0.23	...	1.19 ± 0.25	< 2.0	0.205 ± 0.034
CS215	0.73 ± 0.17	...	0.28 ± 0.15
CS241	< 0.24	...	< 0.21	< 2.0	...
CS265	...	6.33 ± 0.34	...	3.83 ± 0.25	2.18 ± 0.16	2.42 ± 0.34	...
CS292
CS415	< 0.33	0.429 ± 0.020	< 0.27	< 2.0	...
CS520	...	1.292 ± 0.013	<	...
CS538	< 0.21	...	< 0.27	<	...
CS539
CS574	< 2.0	...
CS603	...	6.90 ± 0.39	...	5.00 ± 0.32	4.30 ± 0.29	5.25 ± 0.48	...
CS618
CS649	< 2.0	...
CS703	8.60 ± 0.82	...	4.22 ± 0.37	1.150 ± 0.118
CS713

Notes. ^(a) Detection at 33 GHz.

6

Conclusion and outlook

Are IFRSs a class of high-redshift RL AGNs? That was the pressing question about these sources when this PhD project was started. Former studies suggest these characteristics. However, direct evidence had not been found.

This thesis presents new and direct evidence which supports the hypothesis that IFRSs are high-redshift RL AGNs. All three IFRSs with optical spectra in the ATLAS fields have redshifts $z > 1.8$, showing the suggested high redshifts of this class of objects (chapter 2; Herzog et al., 2014). Adding the 18 spectroscopic redshifts presented in chapter 3, spectroscopic redshift information is known for 40 IFRS. 38 of them are in the redshift range $1.8 \leq z \leq 3.6$. The remaining two are at very low redshifts and might be misidentifications. Although all redshifts of IFRSs are at $z \leq 3.6$, there are reasons to suggest that other IFRSs might be at higher redshifts. The sources with spectroscopic information are amongst the near-IR brightest IFRSs. Extrapolating the correlation between near-IR flux density and redshift and using their near-IR flux densities, it is suggested that the near-IR faintest IFRSs are at even higher redshifts ($z \sim 5$). All spectroscopic redshifts of IFRSs are found to be

consistent with this correlation. However, the alternative hypothesis that all IFRSs are in the given redshift range cannot be discarded based on the available data.

Measuring redshifts for some of the IR-faintest IFRSs is one of the key challenges in future work on this extreme class of objects. Such data would directly test the hypothesis that the population of IFRSs extends to redshifts of 5 or 6 and the suggested correlation between near-IR flux density and redshift holds at higher redshifts. However, such a project is hardly feasible with optical telescopes because of the IR and optical faintness of the desired targets. Therefore, searching for molecular emission lines like CO in the mm regime with ALMA might be a more promising and more efficient way of measuring redshifts for the most extreme sources in the class of IFRSs.

Strong evidence is found in this thesis (chapter 3; Herzog et al., 2015a) for the hypothesis that the majority of IFRSs contain AGNs. VLBI observations of a large sample of IFRSs increase the number of IFRSs with detected compact radio emission from 2 to 37 and show that most—if not all—IFRSs have AGNs in their centres. Further, these data suggest that IFRSs might be a class of young AGNs, potentially overlapping with the populations of GPS and CSS sources. Currently, additional observations with the VLBA are being carried out, increasing the sample size of VLBI-observed IFRSs and enabling a deeper study of the compact emission characteristics of IFRSs, in particular linked to optical ancillary data and photometric redshifts.

Based on studying the radio SEDs of IFRSs (chapter 5; Herzog et al., 2015c), the suggested overlap between this class of objects and the populations of GPS and CSS sources has been directly shown for the first time. Using observational data covering more than two orders of magnitude in frequency—significantly extending the explored radio regime of IFRSs towards lower and higher frequencies—, the turnover in the radio SED has been traced for several IFRSs. Redshift information for this sample of IFRSs is needed to draw final conclusions on the observationally unbiased abundance of young AGNs in the population of IFRSs. The Multifrequency Snapshot Sky Survey (MSSS; Heald and LOFAR Collaboration, 2014) using the LOw Frequency ARray (LOFAR; van Haarlem et al., 2013) will provide low-frequency radio data for the IFRS sample presented by Collier et al. (2014), putatively unveiling the turnover for more IFRSs and potentially for some IFRSs with redshift information.

The highest-frequency observations of IFRSs in the radio regime presented in chapter 5

(Herzog et al., 2015c) show that the data of this particular source can be explained by a combined AGN-starburst SED template. Disentangling the contribution of AGN activity on the one hand and starburst activity on the other hand—the former definitely, the latter potentially contributing to the emission of IFRSs—was also the aim of the first FIR observations of this class of objects (chapter 4; Herzog et al., 2015b). Though all six targeted sources remain undetected in all wavebands, a comprehensive multi-wavelength SED modelling—making use of the measured FIR flux density upper limits—shows that only HzRGs can reproduce the emission characteristics of IFRSs, strengthening the suggested link to these massive galaxies. In a separate analysis (chapter 5), one IFRS is found to be detected in the FIR regime based on recently released survey data. These data from HerMES (Oliver et al., 2012), the PACS Evolutionary Probe (PEP; Lutz et al., 2011), and the Cosmic Assembly Near-infrared Deep Extragalactic Legacy Survey (CANDELS; Grogin et al., 2011) cover more IFRS and enable further FIR studies of IFRSs.

Recalling the list of remaining potential explanations for the “IFRS phenomenon” given in section 1.3.6, the multi-frequency data and analyses presented in this thesis increase the knowledge of IFRSs. Strong direct evidence is found that IFRSs are high-redshift RL AGNs with massive black holes in the centres. Further, the analyses finally dispose of some originally suggested explanations. In particular, the redshift distribution found in chapters 2 (Herzog et al., 2014) and 3 shows that IFRSs are extragalactic objects, eliminating pulsars and ultracool dwarf stars. The observed redshifts also rule out radio lobes and misidentifications as explanation for the majority of IFRSs. Heavily obscured star forming galaxies are eliminated based on the redshift distribution and the high detection fraction of IFRSs in VLBI observations. Also, medium-redshift ($z \sim 1$) RL AGNs suffering from heavy dust extinction are unlikely to explain the class of IFRSs because of the observed redshift distribution. Generally, significant dust extinction cannot be ruled out to cause the IR-faintness of IFRSs, however no evidence is found to support this hypothesis. Although it is now established based on the work presented in this thesis that the vast majority of IFRSs are high-redshift RL AGNs, it cannot be ruled out that a few individual sources in the sample of IFRSs may be caused by other phenomena. In particular, no evidence is found that the population of IFRSs is an inhomogeneous class, consisting of more than one type of object as originally suggested.

Table 6.1 summarises the current status of research of the class of IFRSs in the ATLAS

Table 6.1: Median broadband characteristics of the sample of IFRSs in the ATLAS fields. The subsamples of IFRSs used to derive the median characteristics vary and are potentially affected by different selection biases.

References: (1) Zinn et al. (2011), (2) Norris et al. (2006), (3) Middelberg et al. (2008a), (4) Herzog et al. (2014), (5) Norris et al. (2011a), (6) Herzog et al. (2015b), (7) Maini et al. (2013), (8) Norris et al. (2007), (9) Middelberg et al. (2008b), (10) Middelberg et al. (2011), (11) Herzog et al. (2015c). Work that is part of this thesis is indicated by (*).

Regime	Quantity	Median IFRS characteristic	Reference
X-ray	$F_{0.5-2.0\text{keV}}$	$\lesssim 5.5 \times 10^{-19} \text{ W m}^{-2}$	(1)
optical	R band	$\lesssim 24.5 \text{ mag (Vega)}$	(2), (3)
optical	emission line width	broad	(4)*
near-IR	$S_{3.6\mu\text{m}}$	$\lesssim 0.63 \mu\text{Jy}$	(5)
mid-IR	$S_{24\mu\text{m}}$	$\lesssim 90 \mu\text{Jy}$	(6)*
far-IR	$S_{100\mu\text{m}}$	$\lesssim 2.3 \text{ mJy}$	(6)*
radio	$S_{1.4\text{GHz}}$	$\sim 9 \text{ mJy}$	(1), (2), (3), (7)
radio	compact (VLBI) emission	$\lesssim 0.62 \text{ mJy}$	(8), (9)
radio	spectral index	steep ($\alpha \lesssim -1.0$)	(10), (11)*
radio	SED shape	power law down to 200 MHz	(10), (11)*
radio	linear scale	smaller than FRI/II	(10), (11)*
radio-IR	$S_{1.4\text{GHz}}/S_{3.6\mu\text{m}}$	$\gtrsim 1100$	(1), (7)
	redshift	$\gtrsim 2$	(4)*
	sky density	$\sim 5 \text{ deg}^{-2}$	(1), (7)

fields. The IFRSs in these fields are the best studied objects of their class and provide a broad wavelength coverage, significantly extended by this thesis. Although the median IFRS is only constrained by flux density upper limits in most wavelength regimes, IFRSs are now established as a relatively new class of RL AGNs at high redshifts.

Analysing more detailed characteristics of IFRSs, all spectroscopically observed IFRSs are found to have radio luminosities of FR II galaxies and to have broad optical emission lines, showing that these IFRSs are type I AGNs. Since the class of IFRSs has been missed in former AGN studies, this class—showing a sky density of around five per square degree in the deep fields—increases the number of RL AGNs in the early universe. The cosmological relevance of IFRSs would be even higher if the redshift distribution extends to $z \sim 5$ or 6 as hypothesised in this thesis and other studies. If the entire IFRS population contains only type I AGNs as suggested by the findings presented in chapter 3—i.e. all IFRSs are

RL quasars—the class of IFRSs would considerably increase the known quasar sky density which is around 26 deg^{-2} ($\sim 18 \text{ deg}^{-2}$ with $z > 2.15$) in the latest SDSS quasar catalogue (Pâris et al., 2014).

Based on all available data, IFRSs and HzRGs are believed to be identical with one characteristic difference. All IFRSs with redshift information meet the selection criteria of HzRGs and the broad-band SED modelling shows that results—including estimated limits on SFR and black hole accretion rate—for the class of IFRSs are consistent with those of HzRGs, although the IFRSs have lower luminosities, lower stellar masses, and lower-mass black holes than HzRGs. The only difference between IFRSs and HzRGs is the optical emission line width. HzRGs are known to be type II AGNs, whereas all IFRSs with optical spectra show broad emission lines, classifying the latter as type I AGNs and raising the question why no type II IFRS has been found yet. If type II IFRSs do not exist, it would be challenging to include this class of objects in the unified AGN model which is already experiencing problems with unifying some classes of AGNs as discussed in chapter 1.2.1 (see Tadhunter, 2008 and Netzer, 2015). However, so far, spectroscopic data are only available for the optically brightest IFRSs, preventing a generalisation of the finding that all spectroscopically observed IFRSs have broad emission lines. Spectroscopic information on the IR-faintest IFRSs is needed to test whether these most extreme IFRSs show the same characteristics than HzRGs with respect to redshift, luminosity, and emission line width.

Following the finding that the populations of IFRSs and HzRGs are similar, the class of IFRSs significantly increases the number of known HzRGs because of its sky density which is around two orders of magnitude higher than that of HzRGs. Whilst radio galaxies at high redshifts are often selected based on their faintness in K band, the class of IFRSs might establish the faintness at $3.6 \mu\text{m}$ as a new tool to select high-redshift objects. However, spectroscopic observations of IR-fainter IFRSs are needed to confirm the relation between $3.6 \mu\text{m}$ flux density and redshift.

High-redshift radio galaxies are crucial objects when studying the link between AGN and starburst activity (“feedback”), one of the most pressing, open questions in current astrophysical research (see references e.g. in Zinn et al., 2013 and Karouzos et al., 2014). Since IFRSs are found to be similar to HzRGs—as lower luminosity or more distant siblings as discussed in chapter 4—, IFRSs might be interesting objects in order to find answers to the controversially discussed feedback question. However, the faintness of IFRSs at all wavelengths

outside the radio regime makes studying these objects challenging. In particular, conclusions on the host galaxies harbouring the AGNs of IFRSs is hardly possible. Therefore, the faintness of IFRSs might prevent insights into galaxy evolution and the putative interplay between AGN and host galaxy from this class of objects in the near future. However, it is suggested that IFRSs are AGNs at the beginning of their evolution to extended radio galaxies (chapter 3).

References

- Afonso, J., Bizzocchi, L., Ibar, E., et al., 2011, Ultra Steep Spectrum Radio Sources in the Lockman Hole: SERVS Identifications and Redshift Distribution at the Faintest Radio Fluxes, *ApJ*, 743, 122.
- Ahn, C. P., Alexandroff, R., Allende Prieto, C., et al., 2012, The Ninth Data Release of the Sloan Digital Sky Survey: First Spectroscopic Data from the SDSS-III Baryon Oscillation Spectroscopic Survey, *ApJS*, 203, 21.
- Ahn, C. P., Alexandroff, R., Allende Prieto, C., et al., 2014, The Tenth Data Release of the Sloan Digital Sky Survey: First Spectroscopic Data from the SDSS-III Apache Point Observatory Galactic Evolution Experiment, *ApJS*, 211, 17.
- Antonucci, R., 1993, Unified models for active galactic nuclei and quasars, *ARA&A*, 31, 473.
- Antonucci, R. R. J. and Miller, J. S., 1985, Spectropolarimetry and the nature of NGC 1068, *ApJ*, 297, 621.
- Appleton, P. N., Fadda, D. T., Marleau, F. R., et al., 2004, The Far- and Mid-Infrared/Radio Correlations in the Spitzer Extragalactic First Look Survey, *ApJS*, 154, 147.
- Archibald, E. N., Dunlop, J. S., Hughes, D. H., et al., 2001, A submillimetre survey of the star formation history of radio galaxies, *MNRAS*, 323, 417.
- Armus, L., Charmandaris, V., Bernard-Salas, J., et al., 2007, Observations of Ultraluminous Infrared Galaxies with the Infrared Spectrograph on the Spitzer Space Telescope. II. The IRAS Bright Galaxy Sample, *ApJ*, 656, 148.
- Bahcall, J. N., Kirhakos, S., Schneider, D. P., et al., 1995, Hubble Space Telescope and MERLIN Observations of the Jet in 3C 273, *ApJ*, 452, L91.
- Banfield, J. K., George, S. J., Taylor, A. R., et al., 2011, Polarized Radio Sources: A Study of Luminosity, Redshift, and Infrared Colors, *ApJ*, 733, 69.
- Barthel, P. D., 1989, Is every quasar beamed?, *ApJ*, 336, 606.
- Beckmann, V. and Shrader, C. R., 2012, *Active Galactic Nuclei*, Wiley-VCH, Weinheim/Berlin.
- Begelman, M. C., Blandford, R. D., and Rees, M. J., 1984, Theory of extragalactic radio sources, *Reviews of Modern Physics*, 56, 255.
- Bell, E. F., 2003, Estimating Star Formation Rates from Infrared and Radio Luminosities: The Origin of the Radio-Infrared Correlation, *ApJ*, 586, 794.

- Bell Burnell, J., 2009, Reflections on the discovery of pulsars, in *Proceedings of the special session "Accelerating the Rate of Astronomical Discovery" of the 27th IAU General Assembly. August 11-14 2009. Rio de Janeiro, Brazil*, page 14.
- Best, P. N. and Heckman, T. M., 2012, On the fundamental dichotomy in the local radio-AGN population: accretion, evolution and host galaxy properties, *MNRAS*, 421, 1569.
- Bianchi, S., Maiolino, R., and Risaliti, G., 2012, AGN Obscuration and the Unified Model, *Advances in Astronomy*, 2012, 782030.
- Blandford, R. D. and Koenigl, A., 1979, A model for the knots in the M87 jet, *Astrophys. Lett.*, 20, 15.
- Bouwens, R. J., Illingworth, G. D., Blakeslee, J. P., Broadhurst, T. J., and Franx, M., 2004, Galaxy Size Evolution at High Redshift and Surface Brightness Selection Effects: Constraints from the Hubble Ultra Deep Field, *ApJ*, 611, L1.
- Bouwens, R. J., Illingworth, G. D., Blakeslee, J. P., and Franx, M., 2006, Galaxies at $z \sim 6$: The UV Luminosity Function and Luminosity Density from 506 HUDF, HUDF Parallel ACS Field, and GOODS i-Dropouts, *ApJ*, 653, 53.
- Brammer, G. B., van Dokkum, P. G., and Coppi, P., 2008, EAZY: A Fast, Public Photometric Redshift Code, *ApJ*, 686, 1503.
- Bridle, A. H., Fomalont, E. B., Palimaka, J. J., and Willis, A. G., 1981, VLA observation of radio/optical knots in 3C 277.3 = Coma A, *ApJ*, 248, 499.
- Calzetti, D., Armus, L., Bohlin, R. C., et al., 2000, The Dust Content and Opacity of Actively Star-forming Galaxies, *ApJ*, 533, 682.
- Cameron, A. D., Keith, M., Hobbs, G., et al., 2011, Are the infrared-faint radio sources pulsars?, *MNRAS*, 415, 845.
- Cappelluti, N., Hasinger, G., Brusa, M., et al., 2007, The XMM-Newton Wide-Field Survey in the COSMOS Field. II. X-Ray Data and the logN-logS Relations, *ApJS*, 172, 341.
- Chambers, K. C., Miley, G. K., van Breugel, W. J. M., and Huang, J.-S., 1996, Ultra-Steep-Spectrum Radio Sources. I. 4C Objects, *ApJS*, 106, 215.
- Cirasuolo, M., Celotti, A., Magliocchetti, M., and Danese, L., 2003, Is there a dichotomy in the radio loudness distribution of quasars?, *MNRAS*, 346, 447.
- Collier, J. D., Banfield, J. K., Norris, R. P., et al., 2014, Infrared-faint radio sources: a new population of high-redshift radio galaxies, *MNRAS*, 439, 545.
- Condon, J. J., Cotton, W. D., Greisen, E. W., et al., 1998, The NRAO VLA Sky Survey, *AJ*, 115, 1693.
- Condon, J. J., Huang, Z.-P., Yin, Q. F., and Thuan, T. X., 1991, Compact starbursts in ultra-luminous infrared galaxies, *ApJ*, 378, 65.
- Cowie, L. L., Songaila, A., Hu, E. M., and Cohen, J. G., 1996, New Insight on Galaxy Formation and Evolution From Keck Spectroscopy of the Hawaii Deep Fields, *AJ*, 112, 839.

- Croton, D. J., Springel, V., White, S. D. M., et al., 2006, The many lives of active galactic nuclei: cooling flows, black holes and the luminosities and colours of galaxies, *MNRAS*, 365, 11.
- Daddi, E., Bournaud, F., Walter, F., et al., 2010, Very High Gas Fractions and Extended Gas Reservoirs in $z = 1.5$ Disk Galaxies, *ApJ*, 713, 686.
- Daddi, E., Cimatti, A., Renzini, A., et al., 2004, A New Photometric Technique for the Joint Selection of Star-forming and Passive Galaxies at $1.4 \lesssim z \lesssim 2.5$, *ApJ*, 617, 746.
- Daddi, E., Dickinson, M., Morrison, G., et al., 2007, Multiwavelength Study of Massive Galaxies at $z \sim 2$. I. Star Formation and Galaxy Growth, *ApJ*, 670, 156.
- Dallacasa, D., 2003, High Frequency Peakers, *PASA*, 20, 79.
- Dallacasa, D., Stanghellini, C., Centonza, M., and Fanti, R., 2000, High frequency peakers. I. The bright sample, *A&A*, 363, 887.
- De Breuck, C., Seymour, N., Stern, D., et al., 2010, The Spitzer High-redshift Radio Galaxy Survey, *ApJ*, 725, 36.
- de Jong, T., Klein, U., Wielebinski, R., and Wunderlich, E., 1985, Radio continuum and far-infrared emission from spiral galaxies - A close correlation, *A&A*, 147, L6.
- DeBoer, D. R., Gough, R. G., Bunton, J. D., et al., 2009, Australian SKA Pathfinder: A High-Dynamic Range Wide-Field of View Survey Telescope, *IEEE Proceedings*, 97, 1507.
- Dewdney, P. E., Hall, P. J., Schilizzi, R. T., and Lazio, T. J. L. W., 2009, The Square Kilometre Array, *IEEE Proceedings*, 97, 1482.
- Dey, A., Soifer, B. T., Desai, V., et al., 2008, A Significant Population of Very Luminous Dust-Obscured Galaxies at Redshift $z \sim 2$, *ApJ*, 677, 943.
- Dickey, J. M. and Salpeter, E. E., 1984, 1.4 GHz continuum sources in the Hercules cluster, *ApJ*, 284, 461.
- Draine, B. T. and Lee, H. M., 1984, Optical properties of interstellar graphite and silicate grains, *ApJ*, 285, 89.
- Drouart, G., De Breuck, C., Vernet, J., et al., 2014, Rapidly growing black holes and host galaxies in the distant Universe from the Herschel Radio Galaxy Evolution Project, *A&A*, 566, A53.
- Ekers, R. D., 2009, Big and Small, in *Proceedings of the special session "Accelerating the Rate of Astronomical Discovery" of the 27th IAU General Assembly. August 11-14 2009. Rio de Janeiro, Brazil*, page 7.
- El Boucheffry, K., 2009, X-ray identifications of FIRST radio sources in the XBoötes field, *MNRAS*, 396, 2011.
- Elitzur, M. and Ho, L. C., 2009, On the Disappearance of the Broad-Line Region in Low-Luminosity Active Galactic Nuclei, *ApJ*, 701, L91.

- Elvis, M., Wilkes, B. J., McDowell, J. C., et al., 1994, Atlas of quasar energy distributions, *ApJS*, 95, 1.
- Emonts, B. H. C., Feain, I., Mao, M. Y., et al., 2011a, Molecular CO(1-0) Gas in the $z \sim 2$ Radio Galaxy MRC 0152-209, *ApJ*, 734, L25.
- Emonts, B. H. C., Norris, R. P., Feain, I., et al., 2011b, CO observations of high- z radio galaxies MRC 2104-242 and MRC 0943-242: spectral-line performance of the Compact Array Broadband Backend, *MNRAS*, 415, 655.
- Emonts, B. H. C., Norris, R. P., Feain, I., et al., 2014, CO(1-0) survey of high- z radio galaxies: alignment of molecular halo gas with distant radio sources, *MNRAS*, 438, 2898.
- Fanaroff, B. L. and Riley, J. M., 1974, The morphology of extragalactic radio sources of high and low luminosity, *MNRAS*, 167, 31P.
- Fanti, C., Fanti, R., Dallacasa, D., et al., 1995, Are compact steep-spectrum sources young?, *A&A*, 302, 317.
- Fanti, R., 2009, CSS and GPS research: A status report, *Astronomische Nachrichten*, 330, 303.
- Fath, E. A., 1909, The spectra of some spiral nebulae and globular star clusters, *Lick Observatory Bulletin*, 5, 71.
- Fernandes, C. A. C., Jarvis, M. J., Rawlings, S., et al., 2011, Evidence for a maximum jet efficiency for the most powerful radio galaxies, *MNRAS*, 411, 1909.
- Fine, S., Croom, S. M., Miller, L., et al., 2006, The evolution of host mass and black hole mass in quasi-stellar objects from the 2dF QSO Redshift Survey, *MNRAS*, 373, 613.
- Franceschini, A., 2000, High-Redshift Galaxies: The Far-Infrared and Sub-Millimeter View, *ArXiv e-prints*: 0009121.
- Franceschini, A., Vercellone, S., and Fabian, A. C., 1998, Supermassive Black Holes in Early-Type Galaxies: Relationship with Radio Emission and Constraints on the Black Hole Mass Function, *MNRAS*, 297, 817.
- Franzen, T. M. O., Banfield, J. K., Hales, C. A., et al., 2015, ATLAS – I. Third Release of 1.4 GHz Mosaics and Component Catalogues, submitted to *MNRAS*.
- Gaibler, V., Khochfar, S., Krause, M., and Silk, J., 2012, Jet-induced star formation in gas-rich galaxies, *MNRAS*, 425, 438.
- Garn, T. and Alexander, P., 2008, Deep 610-MHz Giant Metrewave Radio Telescope observations of the Spitzer extragalactic First Look Survey field - III. The radio properties of infrared-faint radio sources, *MNRAS*, 391, 1000.
- Gilli, R., Comastri, A., and Hasinger, G., 2007, The synthesis of the cosmic X-ray background in the Chandra and XMM-Newton era, *A&A*, 463, 79.
- Griffin, M. J., Abergel, A., Abreu, A., et al., 2010, The Herschel-SPIRE instrument and its in-flight performance, *A&A*, 518, L3.

- Grogin, N. A., Kocevski, D. D., Faber, S. M., et al., 2011, CANDELS: The Cosmic Assembly Near-infrared Deep Extragalactic Legacy Survey, *ApJS*, 197, 35.
- Hales, C. A., Norris, R. P., Gaensler, B. M., et al., 2014, ATLAS 1.4 GHz Data Release 2 - I. Observations of the CDF-S and ELAIS-S1 fields and methods for constructing differential number counts, *MNRAS*, 441, 2555.
- Hao, H., Elvis, M., Civano, F., and Lawrence, A., 2011, Hot-dust-poor Quasars in Mid-infrared and Optically Selected Samples, *ApJ*, 733, 108.
- Hardcastle, M. J., Evans, D. A., and Croston, J. H., 2007, Hot and cold gas accretion and feedback in radio-loud active galaxies, *MNRAS*, 376, 1849.
- Harrison, C. M., Alexander, D. M., Mullaney, J. R., et al., 2012, No Clear Submillimeter Signature of Suppressed Star Formation among X-Ray Luminous Active Galactic Nuclei, *ApJ*, 760, L15.
- Hasinger, G., 2008, Absorption properties and evolution of active galactic nuclei, *A&A*, 490, 905.
- Hasinger, G., Miyaji, T., and Schmidt, M., 2005, Luminosity-dependent evolution of soft X-ray selected AGN. New Chandra and XMM-Newton surveys, *A&A*, 441, 417.
- Hatziminaoglou, E., Omont, A., Stevens, J. A., et al., 2010, HerMES: Far infrared properties of known AGN in the HerMES fields, *A&A*, 518, L33.
- Heald, G. and LOFAR Collaboration, 2014, The LOFAR Multifrequency Snapshot Sky Survey (MSSS): Status and Results, in *American Astronomical Society Meeting Abstracts #223*, volume 223 of *American Astronomical Society Meeting Abstracts*, page 236.07.
- Herzog, A., Middelberg, E., Norris, R. P., et al., 2014, Infrared-faint radio sources are at high redshifts. Spectroscopic redshift determination of infrared-faint radio sources using the Very Large Telescope, *A&A*, 567, A104.
- Herzog, A., Middelberg, E., Norris, R. P., et al., 2015a, Active galactic nuclei cores in infrared-faint radio sources. Very long baseline interferometry observations using the Very Long Baseline Array, *A&A*, 578, A67.
- Herzog, A., Norris, R. P., Middelberg, E., et al., 2015b, Infrared-faint radio sources remain undetected at far-infrared wavelengths. Deep photometric observations using the Herschel Space Observatory, *A&A*, 580, A7.
- Herzog, A., Norris, R. P., Middelberg, E., et al., 2015c, The radio spectral energy distribution of infrared-faint radio sources, submitted to *A&A*.
- Higdon, J. L., Higdon, S. J. U., Weedman, D. W., et al., 2005, Spitzer Observations of Optically “Invisible” Radio and X-Ray Sources: High-Redshift Active Galactic Nuclei, *ApJ*, 626, 58.
- Higdon, J. L., Higdon, S. J. U., Willner, S. P., et al., 2008, Radio and Infrared Selected Optically Invisible Sources in the Boötes NDWFS, *ApJ*, 688, 885.

- Hopkins, P. F., Cox, T. J., Kereš, D., and Hernquist, L., 2008a, A Cosmological Framework for the Co-evolution of Quasars, Supermassive Black Holes, and Elliptical Galaxies. II. Formation of Red Ellipticals, *ApJS*, 175, 390.
- Hopkins, P. F., Hernquist, L., Cox, T. J., and Kereš, D., 2008b, A Cosmological Framework for the Co-Evolution of Quasars, Supermassive Black Holes, and Elliptical Galaxies. I. Galaxy Mergers and Quasar Activity, *ApJS*, 175, 356.
- Huang, Z. P., Thuan, T. X., Chevalier, R. A., Condon, J. J., and Yin, Q. F., 1994, Compact radio sources in the starburst galaxy M82 and the Sigma-D relation for supernova remnants, *ApJ*, 424, 114.
- Huynh, M. T., Jackson, C. A., Norris, R. P., and Prandoni, I., 2005, Radio Observations of the Hubble Deep Field-South Region. II. The 1.4 GHz Catalog and Source Counts, *AJ*, 130, 1373.
- Huynh, M. T., Norris, R. P., Siana, B., and Middelberg, E., 2010, Evidence for Infrared-faint Radio Sources as $z > 1$ Radio-loud Active Galactic Nuclei, *ApJ*, 710, 698.
- Ivezić, Ž., Axelrod, T., Brandt, W. N., et al., 2008, Large Synoptic Survey Telescope: From Science Drivers To Reference Design, *Serbian Astronomical Journal*, 176, 1.
- Ivezić, Ž., Menou, K., Knapp, G. R., et al., 2002, Optical and Radio Properties of Extragalactic Sources Observed by the FIRST Survey and the Sloan Digital Sky Survey, *AJ*, 124, 2364.
- Iverson, R. J., Smail, I., Amblard, A., et al., 2012, Gas-rich mergers and feedback are ubiquitous amongst starbursting radio galaxies, as revealed by the VLA, IRAM PdBI and Herschel, *MNRAS*, 425, 1320.
- Jarvis, M. J., Rawlings, S., Eales, S., et al., 2001, A sample of 6C radio sources designed to find objects at redshift $z > 4$ - III. Imaging and the radio galaxy K-z relation, *MNRAS*, 326, 1585.
- Jiang, L., Fan, X., Brandt, W. N., et al., 2010, Dust-free quasars in the early Universe, *Nature*, 464, 380.
- Johnston, S., Bailes, M., Bartel, N., et al., 2007, Science with the Australian Square Kilometre Array Pathfinder, *PASA*, 24, 174.
- Johnston, S., Taylor, R., Bailes, M., et al., 2008, Science with ASKAP. The Australian square-kilometre-array pathfinder, *Experimental Astronomy*, 22, 151.
- Kaiser, M. E., Bradley, L. D., II, Hutchings, J. B., et al., 2000, The Resolved Narrow-Line Region in NGC 4151, *ApJ*, 528, 260.
- Karouzos, M., Im, M., Trichas, M., et al., 2014, A Tale of Two Feedbacks: Star Formation in the Host Galaxies of Radio AGNs, *ApJ*, 784, 137.
- Kaspi, S., Maoz, D., Netzer, H., et al., 2005, The Relationship between Luminosity and Broad-Line Region Size in Active Galactic Nuclei, *ApJ*, 629, 61.

- Kaspi, S., Smith, P. S., Netzer, H., et al., 2000, Reverberation Measurements for 17 Quasars and the Size-Mass-Luminosity Relations in Active Galactic Nuclei, *ApJ*, 533, 631.
- Kauffmann, G., Heckman, T. M., Tremonti, C., et al., 2003, The host galaxies of active galactic nuclei, *MNRAS*, 346, 1055.
- Kellermann, K. and Owen, F., 1988, Radio galaxies and quasars, in Verschuur, G. and Kellermann, K. (editors), *Galactic and Extragalactic Radio Astronomy*, Astronomy and Astrophysics Library, pages 563–602, Springer New York.
- Kellermann, K. I., Sramek, R., Schmidt, M., Shaffer, D. B., and Green, R., 1989, VLA observations of objects in the Palomar Bright Quasar Survey, *AJ*, 98, 1195.
- Kettenis, M., van Langevelde, H. J., Reynolds, C., and Cotton, B., 2006, ParselTongue: AIPS Talking Python, in Gabriel, C., Arviset, C., Ponz, D., and Enrique, S. (editors), *Astronomical Data Analysis Software and Systems XV*, volume 351 of *Astronomical Society of the Pacific Conference Series*, page 497.
- Kewley, L. J., Heisler, C. A., Dopita, M. A., et al., 2000, Compact Radio Emission from Warm Infrared Galaxies, *ApJ*, 530, 704.
- Kimball, A. E. and Ivezić, Ž., 2008, A Unified Catalog of Radio Objects Detected by NVSS, First, WENSS, GB6, and SDSS, *AJ*, 136, 684.
- Kimball, A. E. and Ivezić, Ž., 2014, An Updated Version of the Unified Radio Catalog: A Multi-Wavelength Radio and Optical Catalog of Quasars and Radio Galaxies, *ArXiv e-prints*: 1401.1535.
- Kimball, A. E., Kellermann, K. I., Condon, J. J., Ivezić, Ž., and Perley, R. A., 2011, The Two-component Radio Luminosity Function of Quasi-stellar Objects: Star Formation and Active Galactic Nucleus, *ApJ*, 739, L29.
- Klamer, I. J., Ekers, R. D., Bryant, J. J., et al., 2006, A search for distant radio galaxies from SUMSS and NVSS - III. Radio spectral energy distributions and the z - α correlation, *MNRAS*, 371, 852.
- Klamer, I. J., Ekers, R. D., Sadler, E. M., and Hunstead, R. W., 2004, Molecular Gas at High Redshift: Jet-induced Star Formation?, *ApJ*, 612, L97.
- Kormendy, J. and Bender, R., 2011, Supermassive black holes do not correlate with dark matter haloes of galaxies, *Nature*, 469, 377.
- Kormendy, J. and Richstone, D., 1995, Inward Bound—The Search For Supermassive Black Holes In Galactic Nuclei, *ARA&A*, 33, 581.
- Krolik, J. H. and Begelman, M. C., 1988, Molecular tori in Seyfert galaxies - Feeding the monster and hiding it, *ApJ*, 329, 702.
- La Franca, F., Fiore, F., Comastri, A., et al., 2005, The HELLAS2XMM Survey. VII. The Hard X-Ray Luminosity Function of AGNs up to $z = 4$: More Absorbed AGNs at Low Luminosities and High Redshifts, *ApJ*, 635, 864.

- Lacy, M., Laurent-Muehleisen, S. A., Ridgway, S. E., Becker, R. H., and White, R. L., 2001, The Radio Luminosity-Black Hole Mass Correlation for Quasars from the FIRST Bright Quasar Survey and a “Unification Scheme” for Radio-loud and Radio-quiet Quasars, *ApJ*, 551, L17.
- Laing, R. A., Riley, J. M., and Longair, M. S., 1983, Bright radio sources at 178 MHz - Flux densities, optical identifications and the cosmological evolution of powerful radio galaxies, *MNRAS*, 204, 151.
- Laor, A., 2000, On Black Hole Masses and Radio Loudness in Active Galactic Nuclei, *ApJ*, 543, L111.
- Lawrence, A. and Elvis, M., 2010, Misaligned Disks as Obscurers in Active Galaxies, *ApJ*, 714, 561.
- Ledlow, M. J. and Owen, F. N., 1996, 20 CM VLA Survey of Abell Clusters of Galaxies. VI. Radio/Optical Luminosity Functions, *AJ*, 112, 9.
- Lilly, S. J. and Longair, M. S., 1984, Stellar populations in distant radio galaxies, *MNRAS*, 211, 833.
- Lintott, C. J., Schawinski, K., Slosar, A., et al., 2008, Galaxy Zoo: morphologies derived from visual inspection of galaxies from the Sloan Digital Sky Survey, *MNRAS*, 389, 1179.
- Lonsdale, C. J., Smith, H. E., Rowan-Robinson, M., et al., 2003, SWIRE: The SIRTf Wide-Area Infrared Extragalactic Survey, *PASP*, 115, 897.
- Luo, B., Bauer, F. E., Brandt, W. N., et al., 2008, The Chandra Deep Field-South Survey: 2 Ms Source Catalogs, *ApJS*, 179, 19.
- Lutz, D., Poglitsch, A., Altieri, B., et al., 2011, PACS Evolutionary Probe (PEP) - A Herschel key program, *A&A*, 532, A90.
- Magorrian, J., Tremaine, S., Richstone, D., et al., 1998, The Demography of Massive Dark Objects in Galaxy Centers, *AJ*, 115, 2285.
- Maini, A., Prandoni, I., Norris, R. P., et al., 2013, Searching for Infrared-Faint Radio Sources in the SERVS deep fields, submitted to *A&A*.
- Marr, J. M., Perry, T. M., Read, J., Taylor, G. B., and Morris, A. O., 2014, Multi-frequency Optical-depth Maps and the Case for Free-Free Absorption in Two Compact Symmetric Radio Sources: The CSO Candidate J1324 + 4048 and the CSO J0029 + 3457, *ApJ*, 780, 178.
- Mauduit, J.-C., Lacy, M., Farrah, D., et al., 2012, The Spitzer Extragalactic Representative Volume Survey (SERVS): Survey Definition and Goals, *PASP*, 124, 714.
- McLure, R. J. and Dunlop, J. S., 2001, The black hole masses of Seyfert galaxies and quasars, *MNRAS*, 327, 199.
- McLure, R. J. and Jarvis, M. J., 2002, Measuring the black hole masses of high-redshift quasars, *MNRAS*, 337, 109.

- Middelberg, E., Norris, R. P., Cornwell, T. J., et al., 2008a, Deep Australia Telescope Large Area Survey Radio Observations of the European Large Area ISO Survey S1/Spitzer Wide-Area Infrared Extragalactic Field, *AJ*, 135, 1276.
- Middelberg, E., Norris, R. P., Hales, C. A., et al., 2011, The radio properties of infrared-faint radio sources, *A&A*, 526, A8.
- Middelberg, E., Norris, R. P., Tingay, S., et al., 2008b, The first VLBI image of an infrared-faint radio source, *A&A*, 491, 435.
- Miley, G., 1980, The structure of extended extragalactic radio sources, *ARA&A*, 18, 165.
- Miley, G. and De Breuck, C., 2008, Distant radio galaxies and their environments, *A&A Rev.*, 15, 67.
- Miniutti, G., Sanfrutos, M., Beuchert, T., et al., 2014, The properties of the clumpy torus and BLR in the polar-scattered Seyfert 1 galaxy ESO 323-G77 through X-ray absorption variability, *MNRAS*, 437, 1776.
- Moretti, A., Campana, S., Lazzati, D., and Tagliaferri, G., 2003, The Resolved Fraction of the Cosmic X-Ray Background, *ApJ*, 588, 696.
- Narayan, R. and Yi, I., 1995, Advection-dominated Accretion: Underfed Black Holes and Neutron Stars, *ApJ*, 452, 710.
- Nenkova, M., Ivezić, Ž., and Elitzur, M., 2002, Dust Emission from Active Galactic Nuclei, *ApJ*, 570, L9.
- Nesvadba, N. P. H., De Breuck, C., Lehnert, M. D., et al., 2011, The black holes of radio galaxies during the “Quasar Era”: masses, accretion rates, and evolutionary stage, *A&A*, 525, A43.
- Netzer, H., 2006, Active Galactic Nuclei: Basic Physics and Main Components, in Alloin, D. (editor), *Physics of Active Galactic Nuclei at all Scales*, volume 693 of *Lecture Notes in Physics*, Berlin Springer Verlag, page 1.
- Netzer, H., 2015, Revisiting the unified model of active galactic nuclei, *ARA&A*, 53(1), null.
- Nicastro, F., 2000, Broad Emission Line Regions in Active Galactic Nuclei: The Link with the Accretion Power, *ApJ*, 530, L65.
- Norris, R. P., Afonso, J., Appleton, P. N., et al., 2006, Deep ATLAS Radio Observations of the Chandra Deep Field-South/Spitzer Wide-Area Infrared Extragalactic Field, *AJ*, 132, 2409.
- Norris, R. P., Afonso, J., Cava, A., et al., 2011a, Deep Spitzer Observations of Infrared-faint Radio Sources: High-redshift Radio-loud Active Galactic Nuclei?, *ApJ*, 736, 55.
- Norris, R. P., Hopkins, A. M., Afonso, J., et al., 2011b, EMU: Evolutionary Map of the Universe, *PASA*, 28, 215.
- Norris, R. P., Huynh, M. T., Jackson, C. A., et al., 2005, Radio Observations of the Hubble Deep Field-South Region. I. Survey Description and Initial Results, *AJ*, 130, 1358.

- Norris, R. P., Lenc, E., Roy, A. L., and Spoon, H., 2012, The radio core of the ultraluminous infrared galaxy F00183-7111: watching the birth of a quasar, *MNRAS*, 422, 1453.
- Norris, R. P., Tingay, S., Phillips, C., et al., 2007, Very long baseline interferometry detection of an Infrared-Faint Radio Source, *MNRAS*, 378, 1434.
- Obreschkow, D. and Rawlings, S., 2009, The Cosmic Decline in the H₂/H I Ratio in Galaxies, *ApJ*, 696, L129.
- O’Dea, C. P., 1998, The Compact Steep-Spectrum and Gigahertz Peaked-Spectrum Radio Sources, *PASP*, 110, 493.
- O’Dea, C. P. and Baum, S. A., 1997, Constraints on Radio Source Evolution from the Compact Steep Spectrum and GHz Peaked Spectrum Radio Sources, *AJ*, 113, 148.
- O’Dea, C. P., Baum, S. A., and Stanghellini, C., 1991, What are the gigahertz peaked-spectrum radio sources?, *ApJ*, 380, 66.
- Oesch, P. A., Bouwens, R. J., Carollo, C. M., et al., 2010, Structure and Morphologies of $z \sim 7 - 8$ Galaxies from Ultra-deep WFC3/IR Imaging of the Hubble Ultra-deep Field, *ApJ*, 709, L21.
- Ogle, P., Davies, J. E., Appleton, P. N., et al., 2012, Ultraluminous Star-forming Galaxies and Extremely Luminous Warm Molecular Hydrogen Emission at $z = 2.16$ in the PKS 1138-26 Radio Galaxy Protocluster, *ApJ*, 751, 13.
- Ogle, P., Whysong, D., and Antonucci, R., 2006, Spitzer Reveals Hidden Quasar Nuclei in Some Powerful FR II Radio Galaxies, *ApJ*, 647, 161.
- Oliver, S. J., Bock, J., Altieri, B., et al., 2012, The Herschel Multi-tiered Extragalactic Survey: HerMES, *MNRAS*, 424, 1614.
- Orienti, M. and Dallacasa, D., 2014, Physical properties of young radio sources: VLBA observations of high-frequency peaking radio sources, *MNRAS*, 438, 463.
- Ott, S., 2010, The Herschel Data Processing System — HIPE and Pipelines — Up and Running Since the Start of the Mission, in Mizumoto, Y., Morita, K.-I., and Ohishi, M. (editors), *Astronomical Data Analysis Software and Systems XIX*, volume 434 of *Astronomical Society of the Pacific Conference Series*, page 139.
- Owen, F. N. and White, R. A., 1991, Surface photometry of radio galaxies. II - Cluster sources, *MNRAS*, 249, 164.
- Page, M. J., Symeonidis, M., Vieira, J. D., et al., 2012, The suppression of star formation by powerful active galactic nuclei, *Nature*, 485, 213.
- Pâris, I., Petitjean, P., Aubourg, É., et al., 2014, The Sloan Digital Sky Survey quasar catalog: tenth data release, *A&A*, 563, A54.
- Penzias, A. A. and Wilson, R. W., 1965, A Measurement of Excess Antenna Temperature at 4080 Mc/s., *ApJ*, 142, 419.
- Perlmutter, S., Aldering, G., Goldhaber, G., et al., 1999, Measurements of Ω and Λ from 42 High-Redshift Supernovae, *ApJ*, 517, 565.

- Peterson, B. M., 2006, The Broad-Line Region in Active Galactic Nuclei, in Alloin, D. (editor), *Physics of Active Galactic Nuclei at all Scales*, volume 693 of *Lecture Notes in Physics*, Berlin Springer Verlag, page 77.
- Pilbratt, G. L., Riedinger, J. R., Passvogel, T., et al., 2010, Herschel Space Observatory. An ESA facility for far-infrared and submillimetre astronomy, *A&A*, 518, L1.
- Planck Collaboration, Ade, P. A. R., Aghanim, N., et al., 2015, Planck 2015 results. XIII. Cosmological parameters, ArXiv e-prints: 1502.01589.
- Poglitsch, A., Waelkens, C., Geis, N., et al., 2010, The Photodetector Array Camera and Spectrometer (PACS) on the Herschel Space Observatory, *A&A*, 518, L2.
- Polsterer, K. L., Zinn, P.-C., and Gieseke, F., 2013, Finding new high-redshift quasars by asking the neighbours, *MNRAS*, 428, 226.
- Puccetti, S., Fiore, F., D'Elia, V., et al., 2006, The XMM-Newton survey of the ELAIS-S1 field. I. Number counts, angular correlation function and X-ray spectral properties, *A&A*, 457, 501.
- Randall, K. E., Hopkins, A. M., Norris, R. P., and Edwards, P. G., 2011, An unbiased sample of bright southern compact steep spectrum and gigahertz peaked spectrum sources, *MNRAS*, 416, 1135.
- Readhead, A. C. S., Taylor, G. B., Pearson, T. J., and Wilkinson, P. N., 1996, Compact Symmetric Objects and the Evolution of Powerful Extragalactic Radio Sources, *ApJ*, 460, 634.
- Rees, M. J., 1978, The M87 jet - Internal shocks in a plasma beam, *MNRAS*, 184, 61P.
- Rees, M. J., 1984, Black Hole Models for Active Galactic Nuclei, *ARA&A*, 22, 471.
- Reuland, M., Röttgering, H., van Breugel, W., and De Breuck, C., 2004, Dust and star formation in distant radio galaxies, *MNRAS*, 353, 377.
- Ricci, C., Walter, R., Courvoisier, T. J.-L., and Paltani, S., 2011, Reflection in Seyfert galaxies and the unified model of AGN, *A&A*, 532, A102.
- Richards, E. A., Fomalont, E. B., Kellermann, K. I., et al., 1999, Optically Faint Microjansky Radio Sources, *ApJ*, 526, L73.
- Rieke, G. H., Alonso-Herrero, A., Weiner, B. J., et al., 2009, Determining Star Formation Rates for Infrared Galaxies, *ApJ*, 692, 556.
- Riess, A. G., Filippenko, A. V., Challis, P., et al., 1998, Observational Evidence from Supernovae for an Accelerating Universe and a Cosmological Constant, *AJ*, 116, 1009.
- Rocca-Volmerange, B., Le Borgne, D., De Breuck, C., Fioc, M., and Moy, E., 2004, The radio galaxy $K - z$ relation: The $10^{12} M_{\odot}$ mass limit. Masses of galaxies from the L_K luminosity, up to $z > 4$, *A&A*, 415, 931.
- Rybicki, G. B. and Lightman, A. P., 1979, *Radiative processes in astrophysics*, Wiley-Interscience, New York.

- Schawinski, K., Koss, M., Berney, S., and Sartori, L. F., 2015, Active galactic nuclei flicker: an observational estimate of the duration of black hole growth phases of $\sim 10^5$ yr, MNRAS, 451, 2517.
- Schmidt, M., 1963, 3C 273 : A Star-Like Object with Large Red-Shift, Nature, 197, 1040.
- Seyfert, C. K., 1943, Nuclear Emission in Spiral Nebulae., ApJ, 97, 28.
- Seymour, N., Altieri, B., De Breuck, C., et al., 2012, Rapid Coeval Black Hole and Host Galaxy Growth in MRC 1138-262: The Hungry Spider, ApJ, 755, 146.
- Seymour, N., Stern, D., De Breuck, C., et al., 2007, The Massive Hosts of Radio Galaxies across Cosmic Time, ApJS, 171, 353.
- Smith, H. E., Lonsdale, C. J., Lonsdale, C. J., and Diamond, P. J., 1998, A Starburst Revealed—Luminous Radio Supernovae in the Nuclei of ARP 220, ApJ, 493, L17.
- Snellen, I. A. G., Schilizzi, R. T., Miley, G. K., et al., 2000, On the evolution of young radio-loud AGN, MNRAS, 319, 445.
- Springel, V., White, S. D. M., Jenkins, A., et al., 2005, Simulations of the formation, evolution and clustering of galaxies and quasars, Nature, 435, 629.
- Stanghellini, C., Dallacasa, D., and Orienti, M., 2009, High Frequency Peakers: The faint sample, Astronomische Nachrichten, 330, 223.
- Stoughton, C., Lupton, R. H., Bernardi, M., et al., 2002, Sloan Digital Sky Survey: Early Data Release, AJ, 123, 485.
- Strauss, M. A., Huchra, J. P., Davis, M., et al., 1992, A redshift survey of IRAS galaxies. VII - The infrared and redshift data for the 1.936 Jansky sample, ApJS, 83, 29.
- Tacconi, L. J., Genzel, R., Neri, R., et al., 2010, High molecular gas fractions in normal massive star-forming galaxies in the young Universe, Nature, 463, 781.
- Tadhunter, C., 2008, An introduction to active galactic nuclei: Classification and unification, New Astronomy Reviews, 52, 227.
- Thorburn, W. M., 1915, Occam's Razor, Mind, 24(2), 287.
- Tielens, A. G. G. M., Miley, G. K., and Willis, A. G., 1979, Westerbork Observations of 4C Sources with Steep Radio Spectra, A&AS, 35, 153.
- Tody, D., 1986, The IRAF Data Reduction and Analysis System, in Crawford, D. L. (editor), *Instrumentation in astronomy VI*, volume 627 of *Society of Photo-Optical Instrumentation Engineers (SPIE) Conference Series*, page 733.
- Trakhtenbrot, B. and Netzer, H., 2012, Black hole growth to $z = 2$ - I. Improved virial methods for measuring M_{BH} and L/L_{Edd} , MNRAS, 427, 3081.
- Ueda, Y., Akiyama, M., Ohta, K., and Miyaji, T., 2003, Cosmological Evolution of the Hard X-Ray Active Galactic Nucleus Luminosity Function and the Origin of the Hard X-Ray Background, ApJ, 598, 886.

- Urry, C., 2004, AGN Unification: An Update, in Richards, G. T. and Hall, P. B. (editors), *AGN Physics with the Sloan Digital Sky Survey*, volume 311 of *Astronomical Society of the Pacific Conference Series*, page 49.
- Urry, C. M. and Padovani, P., 1995, Unified Schemes for Radio-Loud Active Galactic Nuclei, *PASP*, 107, 803.
- van Breugel, W., Fragile, C., Anninos, P., and Murray, S., 2004, Jet-Induced Star Formation, in Duc, P.-A., Braine, J., and Brinks, E. (editors), *Recycling Intergalactic and Interstellar Matter*, volume 217 of *IAU Symposium*, page 472.
- van Haarlem, M. P., Wise, M. W., Gunst, A. W., et al., 2013, LOFAR: The LOW-Frequency ARray, *A&A*, 556, A2.
- Veilleux, S., Goodrich, R. W., and Hill, G. J., 1997, Infrared Spectroscopy of Seyfert 2 Galaxies: A Look through the Obscuring Torus? II., *ApJ*, 477, 631.
- Weinberg, S., 2008, *Cosmology*, Cosmology, Oxford University Press, Oxford.
- Willott, C. J., Rawlings, S., Jarvis, M. J., and Blundell, K. M., 2003, Near-infrared imaging and the K-z relation for radio galaxies in the 7C Redshift Survey, *MNRAS*, 339, 173.
- Wright, E. L., 2006, A Cosmology Calculator for the World Wide Web, *PASP*, 118, 1711.
- Wright, E. L., Eisenhardt, P. R. M., Mainzer, A. K., et al., 2010, The Wide-field Infrared Survey Explorer (WISE): Mission Description and Initial On-orbit Performance, *AJ*, 140, 1868.
- Xue, Y. Q., Luo, B., Brandt, W. N., et al., 2011, The Chandra Deep Field-South Survey: 4 Ms Source Catalogs, *ApJS*, 195, 10.
- Yin, Q. F. and Heeschen, D. S., 1991, Two radio supernovae in the unusual galaxy Markarian 297, *Nature*, 354, 130.
- York, D. G., Adelman, J., Anderson, J. E., Jr., et al., 2000, The Sloan Digital Sky Survey: Technical Summary, *AJ*, 120, 1579.
- Yun, M. S., Reddy, N. A., and Condon, J. J., 2001, Radio Properties of Infrared-selected Galaxies in the IRAS 2 Jy Sample, *ApJ*, 554, 803.
- Zinn, P.-C., Middelberg, E., and Ibar, E., 2011, Infrared-faint radio sources: a cosmological view. AGN number counts, the cosmic X-ray background and SMBH formation, *A&A*, 531, A14.
- Zinn, P.-C., Middelberg, E., Norris, R. P., and Dettmar, R.-J., 2013, Active Galactic Nucleus Feedback Works Both Ways, *ApJ*, 774, 66.
- Zinn, P.-C., Middelberg, E., Norris, R. P., et al., 2012, The Australia Telescope Large Area Survey: 2.3 GHz observations of ELAIS-S1 and CDF-S. Spectral index properties of the faint radio sky, *A&A*, 544, A38.

Scientific curriculum vitae

Personal details

name Andreas Herzog
address Joachimstraße 12, 44789 Bochum, Germany
nationality German
date of birth 15 March 1987 in Bochum (Germany)

Education

1993 – 1997 Gemeinschaftsgrundschule in der Vöde, Bochum
1997 – 2006 Hildegardis-Schule Bochum
07/2006 Abitur (A level)
2007 – 2012 Studies of Physics at Ruhr-Universität Bochum
07/2010 Bachelor of Science (B.Sc.) in Physics
Thesis title: Über den Einfang von kleinen Schwarzen Löchern durch astronomische Objekte
03/2012 Master of Science (M.Sc.) in Physics
Thesis title: Multimessenger studies of nearby gamma-ray bursts
2012 – 2015 PhD student in Physics at Ruhr-Universität Bochum / Macquarie University, co-supervised by CSIRO Astronomy & Space Science
Thesis title: The broadband spectra of infrared-faint radio sources

Professional experience

2006 – 2007 Community service at Christopherus-Haus in Bochum
2008 – 2011 Student assistant at the Faculty of Mathematics and Faculty of Physics & Astronomy, Ruhr-Universität Bochum
2011 – 2012 Research assistant at the chair of Theoretical Space- and Astrophysics, Ruhr-Universität Bochum
2012 — 2014 Research assistant at the chair of Astronomy, Ruhr-Universität Bochum

List of publications

- Herzog, A., Middelberg, E., Norris, R. P., Sharp, R., Spitler, L. R., Parker, Q. A., 2014, Infrared-faint radio sources are at high redshifts. Spectroscopic redshift determination of infrared-faint radio sources using the Very Large Telescope, *A&A*, 567, A104.
- Herzog, A., Middelberg, E., Norris, R. P., Spitler, L. R., Deller, A. T., Collier, J. D., Parker, Q. A., 2015, Active galactic nuclei cores in infrared-faint radio sources: Very long baseline interferometry observations using the Very Long Baseline Array, *A&A*, 578, A67.
- Herzog, A., Norris, R. P., Middelberg, E., Spitler, L. R., Leipski, C., Parker, Q. A., 2015, Infrared-faint radio sources remain undetected at far-infrared wavelengths: Deep photometric observations using the *Herschel* Space Observatory, *A&A*, 580, A7.
- Franzen, T. M. O., Banfield, J. K., Hales, C. A., Hopkins, A., Norris, R. P., Seymour, N., Chow, K. E., Herzog, A., Huynh, M. T., Lenc, E., Mao, M. Y., Middelberg, E., 2015, ATLAS – I. Third Release of 1.4 GHz Mosaics and Component Catalogues, submitted to *MNRAS*.
- Herzog, A., Norris, R. P., Middelberg, E., Seymour, N., Spitler, L. R., Emonts, B. H. C., Franzen, T. M. O., Hunstead, R., Intema, H. T., Marvil, J., Parker, Q. A., Sirothia, S. K., Hurley-Walker, N., Bell, M., Bernardi, G., Bowman, J. D., Briggs, F., Cappallo, R. J., Callingham, J. R., Deshpande, A. A., Dwarakanath, K. S., For, B.-Q., Greenhill, L. J., Hancock, P., Hazelton, B. J., Hindson, L., Johnston-Hollitt, M., Kapińska, A. D., Kaplan, D. L., Lenc, E., Lonsdale, C. J., McKinley, B., McWhirter, S. R., Mitchell, D. A., Morales, M. F., Morgan, E., Morgan, J., Oberoi, D., Offringa, A., Ord, S. M., Prabu, T., Procopio, P., Udaya Shankar, N., Srivani, K. S., Staveley-Smith, L., Subrahmanyan, R., Tingay, S. J., Wayth, R. B., Webster, R. L., Williams, A., Williams, C. L., Wu, C., Zheng, Q., Bannister, K. W., Chippendale, A. P., Harvey-Smith, L., Heywood, I., Indermuehle, B., Popping, A., Sault, R. J., Whiting, M. T., 2015, The radio spectral energy distribution of infrared-faint radio sources, submitted to *A&A*.